TECHNISCHE UNIVERSITÄT WIEN

VIENNA UNIVERSITY OF TECHNOLOGY

Dissertation

Computational Materials Science: Oxide-Semiconductor Interfaces and Atomic Fragments for the Description of Condensed Matter

ausgeführt zum Zwecke der Erlangung des
akademischen Grades eines Doktors der Naturwissenschaften

unter der Leitung von

Univ. Prof. Dr. phil. Karlheinz Schwarz
Institut für Materialchemie
TU Wien

Univ. Prof. Dr. rer. nat. Peter Blöchl
Institut für Theoretische Physik
TU Clausthal

eingereicht an

der Technischen Universität Wien
Fakultät für Chemie

der Technischen Universität Clausthal
Gemeinsame Mathematisch-
Naturwissenschaftliche Fakultät

von

Mag. Clemens Först
Voglweg 1,
2620 Neunkirchen
Matrikelnummer:
9550496 (Wien) 319476 (Clausthal)

Wien, September 2004

Kurzfassung

Die vorliegende Dissertation beschäftigt sich mit grundlagentheoretischen und anwendungsorientierten Aspekten von computerunterstützter Materialwissenschaft. Die Entwicklung verlässlicher Modelle sowie das exponentielle Wachstum der Rechenleistung haben dazu geführt, dass Computersimulationen, gleichberechtigt mit Experimenten und analytischer Theorie, die Basis moderner Forschung bilden.

Der erste Teil dieser Arbeit gibt einen Überblick über die grundlegenden Konzepte von Modellbildung und Simulation im Bereich der Festkörperphysik. Der Schwerpunkt wird dabei auf jene Aspekte gelegt, die im Rahmen zweier durchgeführter Projekte benötigt werden.

Das erste Projekt beschäftigt sich mit dem Aufwachsen von Strontiumtitanat auf Silizium. Eine weitere Beschleunigung, also Verkleinerung von Halbleiterbauelementen macht es notwendig, das bisher als Isolatormaterial in Transistoren verwendete Siliziumdioxid durch Übergangsmetalloxide zu ersetzen. Auf der Basis von ab-initio Molekulardynamiksimulationen konnte erstmals die Grenzfläche zwischen Silizium und einem solchen Oxid anhand von Strontiumtitanat aufgeklärt werden. Die Simulationen sind mit experimentellen Ergebnissen kompatibel, resultieren jedoch in einem neuen Wachstumsprinzip von Oxiden auf Halbleitern. Aus dem Verständnis der Grenzflächenchemie konnte weiterhin eine Methode vorgeschlagen werden, um den Bandkantenabstand, eine wesentliche elektrische Eigenschaft, gezielt zu beeinflussen.

Das zweite Projekt befasst sich mit der Berechnung von atomaren Fragmentladungsdichten. Die Einführung eines neuen atomaren Basissatzes von knotenlosen Wellenfunktionen ermöglicht es erstmals, die Pauli-Repulsion von Atomen durch ab-initio Potentialterme zu beschreiben. Dadurch lässt sich die Verformung eines freien Atoms in einem Molekül- oder Kristallverband berechnen. Die resultierenden deformierten Orbitale bilden einen an die Geometrie angepassten, lokalisierten Basissatz, der für viele Anwendungen wie Analyse der Elektronenstruktur, tight-binding Verfahren oder order-N Methoden geeignet ist.

Abstract

This thesis deals with theoretical and practical aspects of computational materials science. The development of reliable models as well as the exponential growth of microprocessor performance has led to a situation where simulation, next to experiment and analytical theory, constitutes a third field of modern research.

The first part of this thesis gives an overview of the basic concepts of atomistic modeling and simulation for condensed matter applications. Emphasis is given to those aspects needed for the two projects pursued in the course of this thesis.

The first project deals with the growth of strontium titanate on silicon. Further miniaturization of semiconductor devices, necessary to produce faster microprocessors, requires the replacement of silicon dioxide as the insulating material in transistors by transition metal oxides. Based on ab-initio molecular dynamics simulations, the interface structure and chemistry between silicon and such an oxide could be unraveled for strontium titanate. While the simulations are compatible with experimental results, they provide a new picture of the chemical binding between silicon and oxides. From the understanding of the interface chemistry we can propose a method of how the band offsets, a crucial parameter for device applications, can be engineered.

The second project is concerned with the calculation of atomic fragment orbitals. The introduction of a novel atomic basis-set composed of nodeless wave-functions enables us to describe the Pauli-repulsion of atoms by ab-initio potentials. This allows us to compute the deformation of an isolated atom upon transfer into a molecule or solid. The resulting orbitals consitute a geometry-adapted and localized basis which is suitable for many applications including the analysis of the electronic structure as well as tight-binding calculations or order-N methods.

Acknowledgments

I want to express my gratitude to my two supervisors, Peter Blöchl (Clausthal University of Technology, Germany) and Karlheinz Schwarz (Vienna University of Technology, Austria). They have believed in my potential and provided me with a great environment in terms of an outstanding scientific as well as social atmosphere which was a strong motivation for me during my Ph. D. time.

I also want to especially mention Peter Blaha and Dieter Kvasnicka. While not being my direct supervisors, both of them have always been ready to help me and I took extensive advantage thereof. Their role was taken over by Jürgen Noffke during my stays in Clausthal. Furthermore I want to thank Christopher Ashman and Alex Poddey for our fruitful cooperation. Philip Walther rendered the life at the institute a lot more enjoyable.

During these last three years, I have also been grateful to enjoy the scientific and social interaction with many colleagues in the research groups of Peter Blöchl and Karlheinz Schwarz, including—in alphabetical order—Johannes Kästner, Robert Laskowski, Joachim Luitz, Georg Madsen, Bernd Olejnik as well as Johannes Schweifer.

My ultimate thanks, however, belong to my family, Hans, Monika and Christina Först, for their neverending support which is the solid basis on which I can build my scientific career.

Clemens Först

Contents

Chapter 1

Introduction: Materials science at the nanoscale

Nanotechnology, nanoengineering, nanocrystals, nanowires, ... – "nano" (greek for "very small") is, besides "bio" and "quantum", *the* buzzword which characterizes interesting and novel research and is frequently used to "sex up" proposals, reports or publications these days.

A nanometer corresponds to 10^{-9} meter or around 1/10 000 of the diameter of a human hair. More importantly, one nanometer gives the order of magnitude of atom–atom distances in solids and molecules, where typical bond lengths are in the range of 0.2–0.3 nanometers. Nanotechnology is a branch of engineering that deals with objects smaller than 100 nanometers or around 500 nearest neighbor atomic distances. It therefore involves the manipulation of matter on the atomic scale. Due to the small dimensions of the components, aspects that are of secondary importance in many fields of traditional engineering, as for example surface and interface properties, decisively influence device functionality and performance.

The following sections give a brief overview of the experimental and theoretical approaches in nano-technology that are relevant to my work and motivate the two projects pursued in the course of this thesis. The examples given are mainly taken from the field of semiconductor physics with a focus on the growth of heterostructures. While nanotechnology is used in many fields of engineering, microelectronics is probably the most important sector motivating its development.

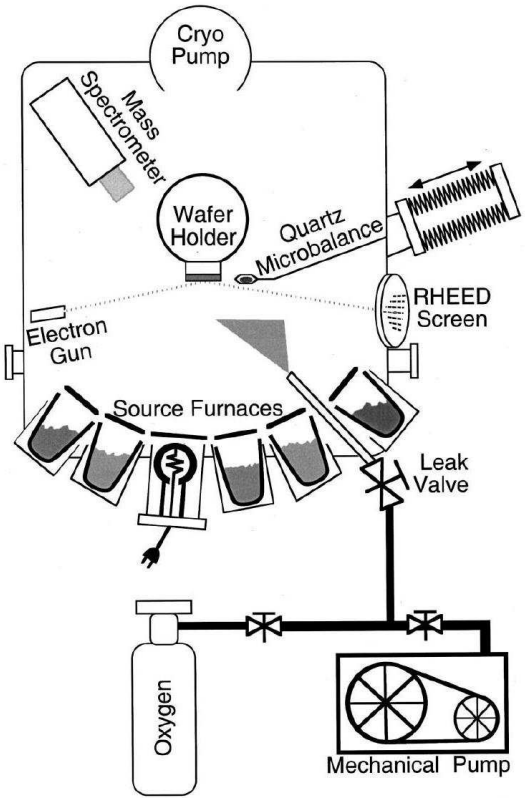

Figure 1.1: Schematic drawing of an MBE reaction chamber (picture taken from [1]). The effusion cells are visualized on the bottom. Behind the wafer holder there is the vacuum pump and a so-called cryo-panel which condenses the flux that has passed by the sample.

1.1 Experimental status

In the last decades, a series of new experimental techniques has allowed scientists to gain atomic control during device manufacturing. Physical and chemical vapor deposition methods enable experimentalists to control the amount of matter deposited on a substrate to sub-monolayer accuracy. A monolayer (ML) is thereby characterized by the number of atoms in the surface layer of the substrate.

The most precise technique is Molecular Beam Epitaxy (MBE, compare figure 1.1 and reference [2] for a review article). During MBE, different types of material can be evaporated from so called effusion cells or sources. When the shutters are open, the atomic or molecular beam can reach the substrate. The amount of matter deposited can be measured for example by an oscillating quartz membrane. Basic in-situ analysis is mainly done via Reflection High Energy Electron Diffraction (RHEED).

The deposition process is performed in an ultra-high vacuum (UHV) chamber to prevent a contamination of the sample. UHV corresponds to partial pressures below 10^{-11} bar. These are the lowest pressures achievable today. It is, however, important to realize that even at a low pressure of 10^{-11} bar, there is still a density of around 10^8 particles per cubic centimeter in the chamber which means that around 10^{12} particles per square centimeter hit a surface per second at a temperature of 300 K. This corresponds to approximately one monolayer every hundred seconds. These numbers scale approximately linearly with pressure.

A milestone in the context of growing semiconductor–oxide heterostructures has been the work by McKee and co-workers at the Oak Ridge National Laboratory [3]. Using MBE they were able to demonstrate for the first time, that an atomically well defined interface between silicon and a transition metal oxide can be grown (compare figure 1.2b and chapter 5 for the technological background). Another prominent example demonstrating the power of experimental techniques comes from Bell Laboratories [4]. There scientists grew heterostructures in which a well defined number of a few lanthanum titanate layers is sandwiched between strontium titanate. They found interesting phenomena due to the interplay of valence discontinuities at the interfaces.

A series of other examples exists in literature demonstrating the sub-monolayer control of the matter deposited. Unfortunately, the experimental means to analyze the atomic processes occurring at a surface in the course of a growth process turn out to be much less accurate. As long as the deposition process is not affected by competing reactions, this does not constitute a serious problem. However, the initial growth steps of transition metal oxides on silicon, the central issue of part II of this thesis, is plagued by a series of competing reactions including silicide formation and metal desorption. While McKee et. al. have managed to prove an epitaxial relationship [3], our simulations indicate that they have misinterpreted the silicon and strontium content at the interface by up to 1/2 ML.

The experimental analysis techniques can be grouped by their information content. A first group gives real-space information. Here, the most prominent examples are scanning tunneling microscopy (STM) or atomic force microscopy (AFM) for analyzing surfaces as well as transmission electron microscopy (TEM) and Z-contrast imaging for bulk and interfacial properties. Figure 1.2 shows an STM and a Z-contrast image which are related to the simulations performed in the context of this thesis (compare chapters 5 and 6). Despite the fact that those images are usually very clear, there is still some ambiguity in the interpretation.

Figure 1.2a shows an STM image of a silicon surface after the deposition of 1/2 ML of Ba [5]. A model of buckled Ba dimers has been devised to explain the recorded image. Alternatively, our simulations show (publication 2, section 6.2), that this image corresponds to a coverage of 1/4 ML. The discrepancy can be

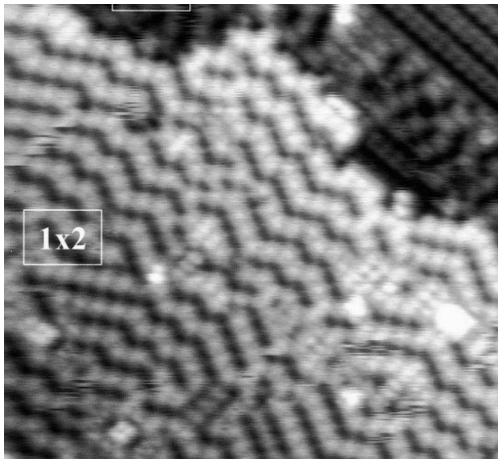

(a) STM image of a Sr-covered silicon surface[5]. Experimentally, this picture has been attributed to 1/2 monolayer coverage. Our simulations show that this is at a coverage of 1/4 monolayer.

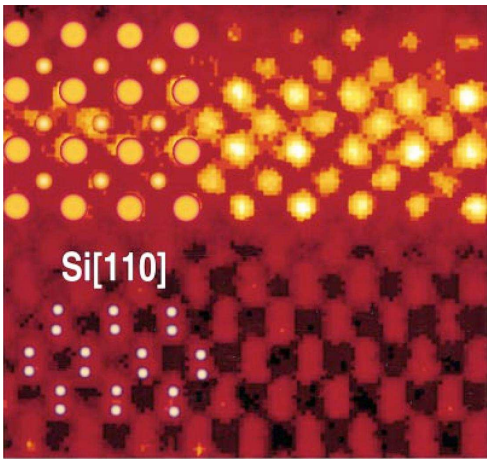

(b) Z-contrast image of the Si-$SrTiO_3$ interface as published by McKee et al.[3] Only atom columns are visible, the silicon atoms near the interface cannot be resolved.

Figure 1.2: Typical experimental results in the context of metal adsorption (a) and oxide growth on silicon (b).

explained by Sr desorption at the deposition temperature. In the course of the deposition of 1/2 ML, a full 1/4 ML has apparently been desorbed. This example nicely shows that a competing reaction, in this example desorption, can lead to a significant decrease of control over the deposition process. Also another recent publication highlights the necessity for computer simulations to back up results from STM images in the context of hydrogen adsorption on rhodium [6]. The Z-contrast image of the interface between silicon and $SrTiO_3$ of figure 1.2b shows that light elements in the oxide and near the interface, such as silicon, oxygen or hydrogen, cannot be resolved due to the presence of the heavy Sr atoms. It is thus not possible to determine the interface stoichiometry and geometry, which is, however, probably the most important piece of information.

The second group of analysis methods is based on diffraction patterns of an incident beam which usually consists of photons (X-ray), electrons (RHEED, LEED) or neutrons. The diffraction patterns give information about two- or three-dimensional periodicities of the sample, information corresponding to reciprocal space.

Finally, spectroscopy gives us information about the electronic and vibrational structure of the sample. Photons of different energy can be used to excite core electrons (X-ray), valence electrons (UV, visible) and vibrational modes (IR).

This allows to extract information about the chemical environment and the atomic species involved.

Despite the wealth of analysis techniques available, it is probably fair to use the following picture of an experimentalist trying to analyze his results: a person who tries to get all the information about complex developments in a big room by looking through one or several keyholes. Even worse, in many cases it is not even clear if the available "keyholes" correspond to the same room, since many of the analysis techniques destroy the sample and thus different samples must be used. This scenario of the experimental situation calls for theoretical approaches since experimental analysis techniques do not keep up with the progress in deposition and growth techniques.

1.2 Analytical theory

Besides experiment, analytical theory is the second traditional pillar of materials science. The complex character of the processes happening at the atomic scale, however, makes it impossible to find reliable and at the same time simple and thus exactly solvable models. Typical examples for analytical models are the ideal gas or the Einstein solid. While analytical theory is a valuable tool to obtain estimates, it is forced to introduce idealizations, which require severe approximations whose implications on the results cannot be foreseen in many cases.

1.3 Simulation as the missing link

Simulations close the gap between analytical theory as well as experiment and constitute a third field of modern materials research. They allow to explore models which cannot be solved analytically and therefore contain fewer approximations than analytical theory. Atomistic simulations, which will be the focus of this thesis, give information about the position and momentum of individual atoms in molecules, on surfaces or in bulk materials and allow to calculate the electronic structure. Computational materials scientists can furthermore perform computer experiments under any imaginable condition or stoichiometry, which enables them to explore situations that are not accessible experimentally. For example it is possible to explore transition states which, due to their short life-times, are not easily detectable via experiment. Knowledge about transition states, however, is crucial for the understanding of chemical processes.

Computational simulation is a rather new and novel field in materials science. The first approaches towards simulation were done during World War II in the

context of the Manhattan project. It then took several decades until computer simulations became "everyday's business", which was mainly due to the limited computer capabilities in previous decades, but also to the non-availability of reliable models and efficient numerical techniques.

Nowadays computer simulations span a wide range of approaches and methodologies and have entered almost all fields of science – from nuclear physics to crash simulations in the automobile industry or simulations of the genesis of our universe to all aspects of materials science. Nevertheless, simulations are only a complement to experiment, having their strengths where the experimental techniques encounter problems and vice versa.

1.4 Outlook

This thesis covers theoretical and practical aspects of computational materials science. Part I introduces the basic concepts of modeling and simulation with an emphasis on the approaches needed in part II. The second part deals with an application project, namely the growth of so-called high-k oxides on silicon. This topic is of uppermost importance for the semiconductor industry. In this context, our simulations have lead to a new picture of oxide–semiconductor interfaces. Part III introduces a novel concept of atomic fragments. Potentials are derived, which mimic the Pauli repulsion of neighboring atoms and allow to calculate geometry adapted, localized orbitals. They can be used for analysis purposes, tight-binding models and non-selfconsistent DFT calculations.

Part I

Concepts – Computational Materials Science

Chapter 2

Modeling

The basis of every simulation is a reliable model, that is a simplified description of the system. Since nanotechnology corresponds to dealing with atomic scale structures, appropriate models will have to describe the interactions between individual atoms. Such models provide us with energies as a function of atomic configurations, and maybe also other parameters such as volume, temperature or electronic structure, as indicated by the dots:

$$E_{\text{tot}} = E_{\text{tot}}[R_i, \ldots]. \tag{2.1}$$

For a given set of atoms, the thermodynamically stable configuration is defined as the one yielding the minimum (free) energy. Therefore, a good model should correctly predict total energies and, upon minimization with respect to the atomic positions, yield the equilibrium geometries as a function of the other parameters entering the model (compare equation 2.1).

2.1 Parametrized energy functionals

The most intuitive way to think of a total energy functional is probably in terms of short-ranged atomic interactions. Such an approach is closely related to our chemical picture of solids and molecules being composed of "balls" and "sticks". The so-called empirical energy functionals define the total energy as a sum of contributions expressed in terms of deviations from the equilibrium bond distances, bond angles, torsional angles, and other suitable geometrical parameters as well as of non-bonding interactions such as Coulomb or Van der Waals interactions (figure 2.1):

$$E_{\text{tot}} = E_{\text{bond}} + E_{\text{angle}} + E_{\text{torsion}} + \ldots + E_{\text{non-bonded}}.$$

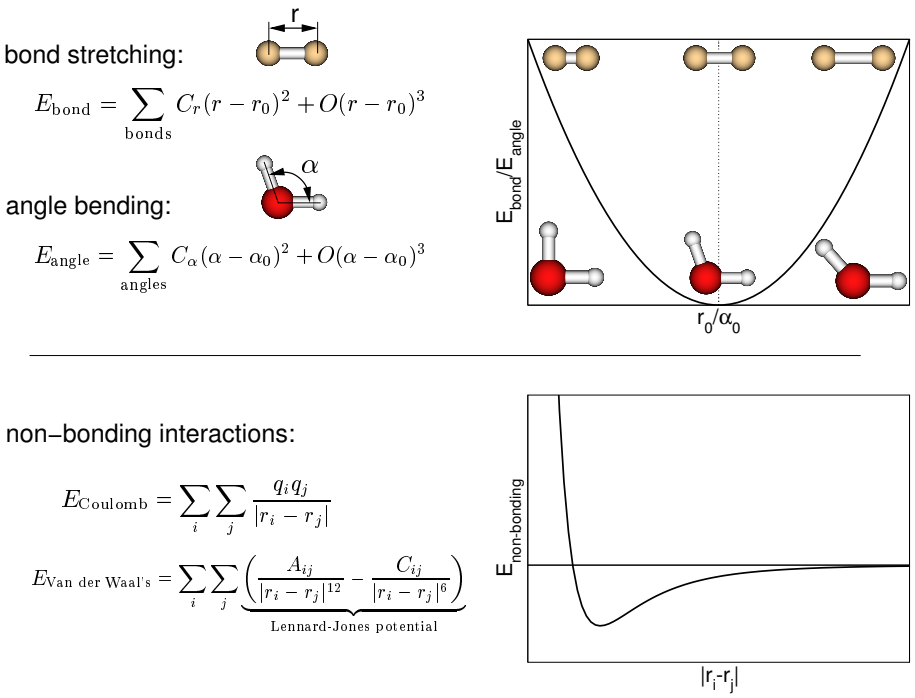

Figure 2.1: Typical functional representation of selected contributions to an empirical total energy functional. Higher order terms can of course be included in the expansions at the price of increased computational effort.

Each of these contributions is expanded in a functional form. In many cases these are Taylor or Fourier expansions. Such an expansion, however, requires the introduction of parameters. In the example of figure 2.1, these are the equilibrium bond lengths r_0 or bond angles α_0 on the one side, but also parameters characterizing the energy dependence upon deviation, C_r and C_α. For the non-bonding interactions we need to parametrize the atomic charges q_i as well as the parameters of the Lennard-Jones potential, A_{ij} and C_{ij}.

Unfortunately, these parameters are not only element-specific, but also depend on the chemical environment. This results in a trade-off between accuracy and reliability on the one hand and the need to fit the parameters for every new system on the other hand. The parameters are usually fitted to reproduce experimental or higher-level theoretical results.

This type of methods has the advantage to be computationally easy to evaluate and thus allows to treat system sizes up to billions of atoms. However, when the behavior of new materials should be studied, for which experimental data is rare, this approach does not have sufficient predictive power. Even for seemingly "easy going" elements like silicon, severe limitations have been encountered [7]: A fairly general three-body potential has been fitted to a large number of different silicon structures. However, as soon as these fitted potentials were used to study

defects with a local atomic arrangement which differs from those included in the database, the results turned out to be unreliable and inaccurate. This illustrates that the transferability of the parameters is limited.

So far we have considered the positions of the nuclei entering the total energy functional as continuous variables. A second class of parametrized energy functionals can be applied, wherever it is possible to map the processes in the system onto some kind of grid. This is most straightforward in applications related to crystalline bulk systems, surface adsorption or epitaxial growth. The energy of a particle is evaluated as a function of the occupancies of lattice sites in the vicinity. These approaches are called lattice-gas Hamiltonians, Ising models or cluster expansions. Due to the discrete character of these total energy functionals, a more efficient and reliable parametrization, also via quantum mechanical calculations, is possible. An concise introduction together with an overview of recent research in this field is found in reference [8]. A parametrized energy functional has been used for Monte-Carlo simulations in the context of Sr adsorption on silicon (compare section 5.3.3).

2.2 Density functional theory

The proper physical framework in microscopic systems is quantum mechanics. So-called *ab-initio* or *first principles* models are purely based on the theorems of quantum mechanics and do not require any experimental input parameters except the chemical composition and charge state of the system. In principle, a full quantum mechanical treatment would require solving the Schrödinger equation for all particles involved – nuclei and electrons. However, with a few exceptions such as hydrogen, helium or lithium, the nuclei can be treated as classical particles, since they have vanishing tunneling probabilities due to their masses. In addition one employs the so-called Born-Oppenheimer approximation, which assumes that the electronic degrees of freedom adapt instantaneously to any change in nuclear geometry. Since protons and neutrons are heavier than electrons by roughly a factor of 1 800, this approximation does not introduce significant errors in most cases. The resulting Hamiltonian for the N electrons in the presence of N_{at} nuclei with atomic charge Z_i is therefore given by (in Hartree atomic units, see appendix A.1)

$$\mathcal{H} = -\frac{1}{2}\sum_{n=1}^{N}\nabla_i^2 - \sum_{n=1}^{N}\sum_{i=1}^{N_{at}}\frac{Z_i}{|r_n - R_i|} + \sum_{n=1}^{N}\sum_{m>n}^{N}\frac{1}{|r_n - r_m|}, \tag{2.2}$$

where r_n and R_i denote the coordinates of the corresponding electrons and nuclei. The first two terms represent the kinetic energy of the electrons and their

Coulomb interaction with the nuclei assuming a frozen geometry in the context of the Born-Oppenheimer approximation. Both terms are straightforward to evaluate. The last term, however, the electrostatic interaction between pairs of electrons constitutes a so-called many-body problem already known from classical mechanics.

Historically the many-body problem arose in connection with the trajectories of planets, which experience a gravitational attraction not only from the sun but also from other planets. The single particle problem (one particle in a constant field) is straightforward to solve. The two-particle problem (two particles exerting forces on each other) was solved by Isaac Newton in his well known *Principia*. For more than two particles, however, no analytical solutions can be found, except for special cases.

Quantum mechanics adds additional complexity to the problem since electrons, being fermions, must obey Pauli's exclusion principle. It is often quoted in the form that it is not possible for two fermions to exist at the same point in space with the same set of quantum numbers. This requirement which has no classical analogue, originates from the many-body wave-function, which must be anti-symmetric under permutation of two particle coordinates (r_i, r_j):

$$\psi = \psi(r_1, r_2, \ldots, r_i, \ldots, r_j, \ldots, r_N) = -\psi(r_1, r_2, \ldots, r_j, \ldots, r_i, \ldots, r_N).$$

For N electrons, the many-body wave-function is $3N$-dimensional, neglecting spin degrees of freedom. Imagine a system with N electrons and suppose we want to represent the many-body wave-function on a regular grid with, say, 10 grid points for each dimension. For the $3N$-dimensional wave-function we thus need 10^{3N} grid points. Using double precision (that is eight bytes for a floating point number) this requires $8 \cdot 10^{3N}$ bytes of memory. A compact disc can store approximately $8 \cdot 10^8$ bytes and we therefore fill 10^{3N-8} CDs storing the data. We can furthermore assume that a CD is about 1 mm thick, which results in a pile of CDs of 10^{3N-11} meters. Performing a calculation on the nitrogen molecule N_2 we have to deal with 10 valence electrons and the pile of CDs needed to save the many-body wave-function is 10^{19} meters high. This corresponds to the unbelievable number of roughly 66 million times the distance from earth to the sun.

While this example is of course highly overemphasized since efficient numerical methods have been developed that dramatically reduce the effort involved, it nevertheless gives a feeling of what is required when dealing with many-body wave-functions. So called wave-function approaches (refer to references [9] and [10] for an overview) are still heavily used but are restricted to atomic systems and small molecules.

In 1964, Hohenberg and Kohn [11] proved that the full many-body ground-state energy and thus also the many-body wave-function is fully determined by the electron density $\rho(r)$. The density only depends on the three spatial coordinates, independent of the number of electrons involved:

$$\rho(r) = \int \cdots \int \psi^*(r_1, \ldots, r_N) \cdot \psi(r_1, \ldots, r_N) \cdot \left\{ \sum_{n=1}^{N} \delta(r_n - r) \right\} dr_1 \cdots dr_N,$$

where ψ^* denotes the complex conjugate of ψ.

In the wave-function approaches, the external potential $v_{\text{ext}}(r)$, that is – in the most simple case – the attractive electrostatic potential exerted by the positive nuclei, as well as the number of electrons, N, determine the Hamiltonian and thus the many-body wave-function (compare equation 2.2). Hohenberg and Kohn [11] and later, in a more general way, Levy [12] proved that the density $\rho(r)$ determines not only the number of electrons via the simple integration

$$N = \int \rho(r) dr,$$

but also exhibits a one-to-one correspondence to the external potential $v_{\text{ext}}(r)$ within an additive constant. Thus, the density fully determines the Hamiltonian and therefore also the many-body wave-function and the ground state energy.

The ground state total energy can be written as the sum of a universal functional $F[\rho]$, which is independent of the external potential, as well as the interaction of the charge density with the external potential:

$$E^{\text{DFT}}[\rho(r)] \;=\; F[\rho(r)] + \int v_{\text{ext}}(r)\rho(r) dr, \tag{2.3}$$

where $F[\rho]$ contains the energy contributions due to the kinetic energy and the many-body electron-electron interaction (compare equation 2.2). Hohenberg and Kohn furthermore established a variational principle: Minimization of $E^{\text{DFT}}[\rho]$ with respect to the density yields the ground state energy:

$$E_0 = \min_{\rho(r)} \left[F[\rho(r)] + \int v_{\text{ext}}(r)\rho(r) dr - \mu \left(\int \rho(r) dr - N \right) \right], \tag{2.4}$$

where the last term ensures that the number of electrons is preserved during the minimization and μ is the associated Lagrange multiplier.

The first implementation of density functional theory (DFT) had already been introduced almost forty years earlier by Thomas and Fermi [13, 14]. Without theoretical justification they had also introduced a universal functional $F[\rho]$, which turns out to be an approximation to the Hohenberg-Kohn functional of equation 2.3:

$$F^{\mathrm{TF}}[\rho(r)] = C_F \int \rho^{5/3}(r)dr + \frac{1}{2}\iint \frac{\rho(r_1)\rho(r_2)}{|r_1 - r_2|}dr_1 dr_2.$$

The first term approximates the kinetic energy based on the assumption of a uniform, non-interacting electron gas. The second term is the classical expression for the Coulomb interaction of a charge density. Dirac later included the exchange energy, resulting from Pauli's exclusion principle, for a uniform electron gas (Thomas–Fermi–Dirac formalism) [15].

The Thomas–Fermi–Dirac theory, however, never made it beyond a simple model. It does not predict chemical binding and also the accuracy for single atoms was below that of other methods. The reason is the error made by approximating the kinetic energy of the many-body wave-function by the non-interacting electron gas.

On the basis of the Hohenberg-Kohn theorems, Kohn and Sham [16] introduced orbitals to improve the approximation of the kinetic energy compared to the Thomas-Fermi approach. The orbitals correspond to a reference system of non-interacting quasi-particles (electrons) $\{\phi_n(r)\}$ in an effective potential $v_{\mathrm{eff}}(r)$:

$$\left[-\frac{1}{2}\nabla^2 + v_{\mathrm{eff}}(r) - \varepsilon_n\right]\phi_n(r) = 0, \tag{2.5}$$

where $v_{\mathrm{eff}}(r)$ is constructed in such a form that the $\{\phi_n(r)\}$ yield the same density as the true many-body wave-function:

$$\rho(r) = \int \cdots \int \psi^*\psi \cdot \left\{\sum_{n=1}^{N} \delta(r_n - r)\right\} dr_1 \cdots dr_N \overset{!}{\equiv} \sum_{n=1}^{N} \int \phi_n^*(r)\phi_n(r)dr. \tag{2.6}$$

The kinetic energy of this non-interacting reference system $T_s[\{\phi_n\}] = -\frac{1}{2}\sum_{n=1}^{N}\int \phi_n^*(r)\nabla^2\phi_n(r)dr$ is already a good approximation to the many-body kinetic energy $T[\psi]$. The difference is due to many-body effects of exchange and correlation. Heine provided an intuitive picture for these effects:

> *On a ship people tend to take a walk after dinner. If they all walk in one direction around the ship, they never meet. If they walk in opposite directions they meet everybody twice. This increases Coulomb*

repulsion for the uncorrelated motion and favors the correlated motion.

Electronic correlation decreases the electron-electron interaction energy but increases the kinetic energy. The kinetic as well as electron-electron interaction energy contributions due to exchange and correlation are transferred into a term called exchange and correlation energy E_{xc}. The total energy in the Hohenberg-Kohn-Sham (HKS) scheme is thus given by

$$\begin{aligned} E^{\mathrm{HKS}}[\rho(r)] &= -\frac{1}{2}\sum_{n=1}^{N}\int \phi_n^*(r)\nabla^2\phi_n(r)dr + \underbrace{\frac{1}{2}\iint \frac{\rho(r_1)\rho(r_2)}{|r_1-r_2|}dr_1dr_2}_{E_H[\rho(r)]} \\ &\quad + \int v_{\mathrm{ext}}(r)\rho(r)dr + E_{\mathrm{xc}}[\rho(r)]. \end{aligned} \tag{2.7}$$

This energy expression, at the same time, defines the exchange and correlation energy $E_{xc}[\rho]$ as

- the difference between the kinetic energy of the non-interacting system $T_s[\rho]$ and that of the many-body wave-function as well as
- the difference between the classical coulomb interaction of the density ($E_H[\rho(r)]$) and the true many-body electron–electron interaction including exchange and correlation.

The three terms $T_s[\rho]$, $E_{xc}[\rho]$ and the so-called Hartree energy E_{H} (second term) define the universal functional $F[\rho]$ of equations 2.3 and 2.4.

The effective potential $v_{\mathrm{eff}}(r)$ of equation 2.5 is obtained by applying the variational principle proven by Hohenberg and Kohn. Inserting the HKS total energy functional (equation 2.7) into equation 2.4 and minimizing with respect to $\rho(r)$ yields

$$\frac{\delta E^{\mathrm{HKS}}[\rho(r)]}{\delta\rho(r)} = 0 \quad \Rightarrow \quad \frac{\delta T_s[\rho(r)]}{\delta\rho(r)} + v_{\mathrm{ext}}(r) + \underbrace{\int \frac{\rho(r)}{|r-r'|}dr'}_{v_{\mathrm{H}}(r)} + \underbrace{\frac{\delta E_{xc}[\rho(r)]}{\delta\rho(r)}}_{v_{xc}(r)} = \mu, \tag{2.8}$$

introducing the Hartree as well as the exchange and correlation potentials $v_{\mathrm{H}}(r)$ and $v_{xc}(r)$, respectively.

Equating the minimum condition of equation 2.8 with the same expression for electrons in an effective potential:

$$\frac{\delta E^{\text{non-interacting}}[\rho(r)]}{\delta\rho(r)} = \frac{\delta T_s[\rho(r)]}{\delta\rho(r)} + v_{\text{eff}}(r) = \mu,$$

defines $v_{\text{eff}}(r)$ of equation 2.5 as

$$v_{\text{eff}}(r) = v_{\text{ext}}(r) + v_{\text{H}}(r) + v_{\text{xc}}(r). \tag{2.9}$$

Since the effective potential entering the Hamiltonian of equation 2.5 depends on the density, the Kohn-Sham equations have to be solved iteratively.

The re-introduction of wave-functions adds again a degree of complexity to the DFT formalism. The decisive difference between the Kohn-Sham and the many-body approach, however, is that in the Kohn-Sham scheme the effort is reduced to dealing with N single-particle wave-functions which is a clear advantage over handling a single N-body wave-function. Instead of 10^{3N} we only have to store and manipulate $N \cdot 10^3$ data points. In the example of the nitrogen molecule this corresponds to 80 kB or 10^{-4} CDs.

It is important to note that the HKS scheme produces the exact many-body ground state, provided that the exact exchange and correlation energy E_{xc} is known. In practical calculations the exchange and correlation energy E_{xc} must be approximated by a local or semi-local functional of the density and its first derivative. Details about approximations to the exchange and correlation functional as well as more extensive reviews of the development of density functional theory can be found in references [17, 18, 19, 20].

The reliability of an electronic structure method for chemical and physical applications is determined by its error bars relative to the "chemical accuracy", defined as 1 kcal/mol or 0.04 eV/atom. For DFT, Becke has performed a broad screening of atomization energies for small molecules and obtained an average error of between 3.9 and 5.7 kcal/mol [21, 22]. While this is decisively above the chemical accuracy, it is important to realize that in practical application we are mostly interested in energy differences of rather similar structures as for example different adsorption sites on a surface. In that case we calculate the energy per bond and not per molecule and the errors are correspondingly smaller. As a rule of thumb, relative energies are said to be reliable to within 0.05 eV. Bond lengths are predicted to within 1–3 %.

Systems with up to a few hundred atoms can be treated on modern computer architectures using density functional theory. The numerical effort scales between N^2 and N^3, where N denotes the number of atoms. The exact scaling behavior depends on the algorithm used (see for example reference [23]).

An important issue in electronic structure calculations is the choice of basis set to represent the wave-functions and densities. An overview over current approaches with an emphasis on the Projector Augmented Wave (PAW) method [24] used for the calculations in part II is given in our publication 5 (section 6.5). Density functional theory has been the model used for the simulations of metal adsorption and oxide growth described in part II.

2.3 Beyond Kohn-Sham density functional theory

From today's point of view, density functional theory is a very well explored tool to calculate total energies. A series of commercial and free software packages exist (CP-PAW [25], Wien2k [26], Vasp [27], ABINIT [28], SFHIngX [29], Castep [30], SIESTA [31] ...) which can almost be used as a "black box". Active research in terms of improving the available electronic structure methods focuses on three domains

- improvements of existing (semi-) local exchange-correlation functionals;
- domains where the (semi-) local approximations of the exchange and correlation energy fail.
- non-ground-state calculations;

The only approximation in terms of ground state energies in Density Functional theory is the exchange and correlation functional. It is implemented as a functional depending only on the local value of the density (local density approximation, LDA) or on the local value and the first derivative (generalized gradient approximation, GGA). For a homogeneous electron gas, LDA is an exact choice. Given a slowly varying electron density, the error introduced is still very small. Errors, however, become large, that is clearly above the chemical accuracy, for highly localized and therefore non-uniform electron densities as well as for electron densities decaying into the vacuum. In the latter case the exchange and correlation potential decreases exponentially whereas the true behavior should be $1/r$. For that reason, the use of gradient corrected functionals is mandatory for calculations on atoms, molecules or surfaces, since the inclusion of the gradient improves the description in these cases.

The error in the exchange and correlation energy can easily be seen by analyzing one-electron systems such as for example hydrogen. Since there is only one electron, the exchange and correlation energy must exactly cancel the Coulomb energy. In LDA, these terms differ by up to 0.6 eV, whereas GGA reduces the error to about 0.05 eV [32].

Another central issue for materials science is the field of so-called "highly correlated materials", transition metal compounds with partially filled d and f shells. Especially the $3\,d$ and $4\,f$ shells are highly localized around the nucleus. They are the first shell of their symmetry and the Coulomb singularity of the nucleus is thus not screened as effectively as for the lower angular momenta. A prominent example of a failure of DFT in this respect is the prediction of late transition metal oxides being metallic. A partially filled band within DFT may split into so-called lower and upper Hubbard bands if orbital information is included in the exchange and correlation energy [33]. In standard DFT, such a multiplet formation is averaged out.

Approaches like self interaction correction (SIC) [34, 35], LDA+U [36] and dynamical mean field theory (DMFT) [37, 38] , where potentials are applied to selected orbitals, as well as exact exchange are used to augment the DFT exchange and correlation functional with non-local, that is orbital-dependent, effects. Exact exchange calculates the exact exchange energy in terms of the KS orbitals, whereas SIC only uses this Hartree-Fock like approach for selected localized orbitals. A brief introduction into these approaches is given in reference [39].

The proof of the Hohenberg-Kohn theorem as well as the construction of the Kohn-Sham total energy functional is restricted to so-called ground-state properties. However, in many applications, such as defects or photochemistry, it is important to have access to excitation energies. Strictly speaking however, the problem starts already when plotting band-structures, since the Kohn-Sham eigenvalues (compare equation 2.5) do not have a clear physical meaning. Janack's theorem [40] only connects the eigenvalues to the partial derivative of the DFT total energy with respect to the occupation number of the corresponding KS orbital:

$$\varepsilon_i = \frac{\partial E^{\mathrm{HKS}}}{\partial f_i}.$$

The only eigenvalue with a physical meaning is the one corresponding to the highest occupied eigenstate which is identical to the negative ionization energy [41]. Therefore it is in principle invalid to identify the Kohn-Sham eigenvalues with excitation energies, which, however, is widely done and proves to be useful from a pragmatic point of view. Kohn himself refers to the DFT-eigenvalues as "illegitimate children" of DFT [42].

Green's Function theory provides means to calculate quasi-particle energies [39]:

$$\left[-\frac{1}{2}\nabla_r^2 + v_{\mathrm{ext}}(r) + v_{\mathrm{H}}(r)\right]\phi_i(r) + \int \sum(r, r'; \varepsilon_i)\phi_i(r')dr' = \varepsilon_i\phi_i(r), \qquad (2.10)$$

where $v_{\mathrm{H}}(r)$ is the Hartree potential (compare equation 2.8) and $\sum(r, r'; \varepsilon_i)$ is the so-called self-energy, a non-local and energy-dependent operator for exchange and correlation. It can be shown, that the different single-particle approaches to the many-body problem are approximations to the self-energy operator [39]. The GW method [43] is an extended Hartree-Fock approximation with a dynamically screened exchange. It is computationally demanding but still the most simple working approximation beyond Hartree-Fock [39].

Recently, there have been also attempts to combine DFT and wave-function calculations (configuration interaction, CI [9]) to obtain the excitation spectrum of a defect [44].

The well known inability of density functional theory to reproduce experimental band gaps is, however, not due to limitations regarding excitation energies. The band gap can be expressed in terms of ground state energies of the system with N, $N-1$ and $N+1$ electrons

$$\begin{aligned} E_g &= \Big(E^{\mathrm{HKS}}(N+1) - E^{\mathrm{HKS}}(N)\Big) - \Big(E^{\mathrm{HKS}}(N) - E^{\mathrm{HKS}}(N-1)\Big) \\ &= -I(N+1) + I(N) \\ &\stackrel{!}{\equiv} \varepsilon_{N+1}(N+1) - \varepsilon_N(N). \end{aligned} \tag{2.11}$$

Recall that the eigenvalue of the highest occupied state is equal to the negative ionization energy I [41]. This allows us to equate the Kohn-Sham eigenvalues $\varepsilon_{N+1}(N+1)$ and $\varepsilon_N(N)$ to the energy differences $E(N+1) - E(N)$ and $E(N) - E(N-1)$. The band gap obtained when analyzing the Kohn-Sham bandstructure is, however, given by $\varepsilon_{N+1}(N) - \varepsilon_N(N)$, that is the difference in eigenvalues between the lowest unoccupied and highest occupied state of the N-electron system.

Perdew and Levy as well as Sham and Schlüter have shown independently [45, 46], that the exchange and correlation potential $v_{\mathrm{xc}}(r)$ (compare equation 2.8) exhibits a discontinuity at an integer number of electrons. The eigenvalue $\varepsilon_{n+1}(N+1)$ is thus given as $\varepsilon_{N+1}(N) + \Delta_{\mathrm{xc}}$, where Δ_{xc} denotes the discontinuity which is not accessible within the standard Kohn-Sham scheme. The true gap is therefore given by the gap of the Kohn-Sham bandstructure plus the discontinuity Δ_{xc}. Perdew and Levy [45] argued that only an energy-dependent approximation to the self-energy operator can cure this problem.

The developments mentioned so far can be summarized by a trend which has already been started by Kohn and Sham [16], namely to increase the extent of non-locality in order to enhance accuracy. Hohenberg and Kohn [11] have proven that there exists an exact ground state energy functional depending entirely on the

density. Because of the large error introduced in the kinetic energy by Thomas-Fermi-like functionals, Kohn and Sham introduced orbitals, that is non-locality, in the kinetic energy functional. Consequently, the resulting Hohenberg-Kohn-Sham approach provides sufficient accuracy for a wide range of applications in materials science. Aiming at going beyond that accuracy, the new schemes partly incorporate non-locality and energy dependence in the exchange and correlation part of the energy and thus move applied DFT again closer to the wave-function approaches.

Time-dependent density-functional-theory was constructed to study the response of a system to a time-dependent potential, such as for example laser pulses. The basis is the Runge-Gross theorem [47], an analogue to the Hohenberg-Kohn theorem, which establishes a one-to-one mapping between time-dependent densities and potentials via the so-called density response function.

Chapter 3

Atomistic Simulation

Choosing an appropriate model for the system of interest is only the first, but nevertheless crucial step. After this choice we have to deal with a high $(3N)$-dimensional space if we only consider the degrees of freedom of the N nuclei in the system. The high dimensionality, however, is only one of the problems. It is even more cumbersome that for a given position in this space, the only information we can extract with a reasonable numerical effort is the total energy and the gradient thereof, at least in ab-initio models [48, 49].

Since analytic solutions to the models of interest are not available, the only way to obtain information about the system, such as for example equilibrium geometries or finite temperature behavior, is via the use of numerical minimization and simulation techniques which will be introduced in this chapter. In-depth information about all flavors of simulation techniques can be found in references [50, 51, 52].

3.1 Gradient based minimization schemes

Several methods use the negative gradients g_i of the total energy with respect to the atomic position R_i,

$$g_i = -\frac{\partial E_{\text{tot}}}{\partial R_i},$$

to find the ground-state atomic configuration. Probably the most intuitive approach is the so-called "steepest descent" method [53]. The gradient of an initial configuration, that is the direction where the energy increases most rapidly, is calculated and the energy is minimized along the direction of the negative gradient (search direction). At the minimum the next gradient is computed and another

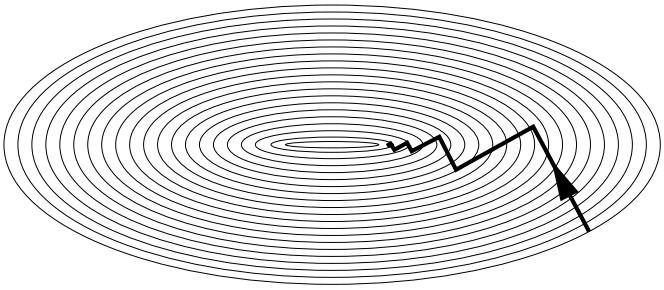

Figure 3.1: Minimization path of the steepest descent approach in a simple, two-dimensional potential. Only the first seven iterations are drawn.

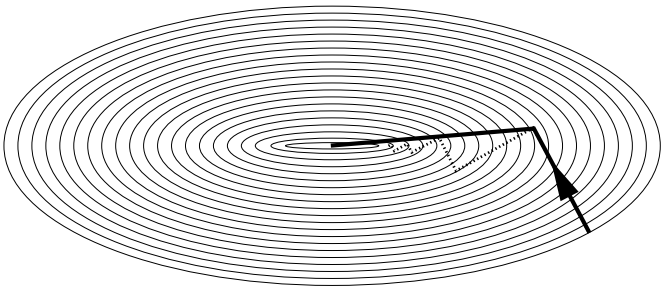

Figure 3.2: Conjugate gradient versus steepest descent (compare figure 3.1). The conjugate gradient algorithm reaches the minimum of the two-dimensional harmonic potential after two iterations. The steepest descent path is indicated by the dotted lines.

minimization along the negative gradient is performed as illustrated in figure 3.1. The gradient at the minimum of a line-search, however, is – by definition – orthogonal to the search direction. This implies that the search direction changes by 90° in each time-step which usually is not the optimum choice, since this leads to a zig-zag path approaching the minimum. Furthermore, the convergence speed slows down considerably upon approaching the minimum. For a general starting point the minimum will not be reached in a finite number of iterations.

Conjugate gradient methods [54, 55, 23, 56] circumvent this problem by mixing a fraction of the old into the new gradient. The mixing factor is defined as the ratio of the lengths squared of the new and old gradient. For an N-dimensional harmonic potential

$$E(r_0 + \Delta r) = E(r_0) + \frac{1}{2}\sum_{i=1}^{N} \left.\frac{\partial^2 E(r)}{\partial r_i^2}\right|_{r_0} (\Delta r_i)^2,$$

the conjugate gradient method finds the minimum in N steps. Each conjugate gradient step minimizes along one degree of freedom. In practical calculations, reasonable convergence is usually achieved much earlier. An in-depth discussion of the conjugate gradient scheme can be found in appendix C. A conjugate gradient minimizer has been developed and employed in the context of the calculation of atomic fragment orbitals introduced in part III.

In the case of anharmonic potentials with several local minima, gradient minimization schemes converge to the next local minimum. This behavior constitutes a major drawback which is partly cured in molecular dynamics approaches introduced in the next section.

3.2 Molecular dynamics

In contrast to the purely mathematical interpretation of the gradient in the last section, molecular dynamics (MD) provides a more physical approach and identifies the negative gradient of the total energy with the force acting on an atom. The force is then related to the acceleration via Newton's second law:

$$m_i \ddot{R}_i = F_i \ = -\frac{\partial E_{\text{tot}}}{\partial R_i} \ (= g_i),$$

where R_i and $\ddot{R}_i$ denote the position and acceleration of the atom with index i. The remaining difficulty is to translate the knowledge of the acceleration into the path of the atom, the so-called trajectory. The most intuitive approach is

the so called Verlet algorithm [57]. The acceleration, the second derivative of the position with respect to time, is replaced by the second difference quotient in Newton's second law:

$$F_i = m_i \cdot \ddot{R}_i \approx m_i \cdot \frac{R_i(+) - 2R_i(0) + R_i(-)}{\Delta^2}, \tag{3.1}$$

where $R_i(+)$, $R_i(0)$ and $R_i(-)$ correspond to the positions at three consecutive time-steps, namely the next, this and the last time-step, respectively. Δ is the time-step chosen and enters the simulation as a parameter. Equation 3.1 can be reformulated to yield the position for the next time-step as a function of the position at this and the last time-step as well as of the force at this time-step:

$$R_i(+) = 2R_i(0) - R_i(-) + \Delta^2 \frac{F_i}{m_i}. \tag{3.2}$$

Equation 3.2 results in an energy conserving molecular dynamics simulation. The inclusion of a friction term in this equation – proportional to the velocity of atom i – can be used to damp the motion and "cool" the atomic configuration towards the minimum energy configuration. Negative friction terms are used to heat up the system. So-called thermostats can be coupled to the system and control the temperature via the friction by accelerating or damping the motion of the nuclei [58, 59].

For infinitesimal short time-steps ($\lim_{\Delta \to 0}$), the Verlet algorithm is exact. Practical calculations, however, require finite time-steps Δ and are a compromise between numerical accuracy (difference quotient) and efficiency (number of time-steps). In order to sample a simple sinus wave with a period of T, the time-step must be smaller than T/π [60]. Realistic trajectories in more general potentials usually require time-steps in the order of $T/10$ to get a reliable sampling. In this case the error in the frequencies is in the region of 1 %.

Typical vibrational frequencies in solids are in the order of 10 to 100 tera-Hertz (THz $= 10^{12}$ Hz) which corresponds to a period between 10 and 100 femto-seconds (fs $= 10^{-15}$ seconds). This would result in a typical time-step in the order of one to ten femto-seconds. In the so-called Car-Parrinello approach [61] one also has to sample the dynamical evolution of the electronic degrees of freedom, which, however, is offset by a reduced numerical effort per time-step. A typical time-step for Car-Parrinello simulations is 0.25 fs.

Irrespective of these details, the maximum simulation length for ab-initio molecular dynamics simulations is in the order of hundred pico-seconds for systems of, say, hundred atoms. Using parametrized energy functionals, the numerical effort for the energy and force evaluations is dramatically reduced. At the same

time, the systems usually studied are significantly larger. Simulation lengths up to one nano-second are typically seen as an upper bound. These estimates are of course highly dependent on the system size and should just give a feeling of the time-scales involved.

The maximum simulation length below one nano-second is probably the most severe limitation of molecular dynamics simulations since many important events, for example diffusion, happen on a longer time-scale and thus cannot be studied by MD. Whether or not an event is suitable for MD simulations can be decided by estimating the waiting time τ, that is the average time between two such events, using

$$\tau = \tau_0 e^{\frac{\Delta E}{k_B T}},$$

where τ_0 is the attempt period, that is one over the attempt frequency, and ΔE the energy barrier. An energy barrier of 0.5 eV is typical for diffusion processes on moderately corrugated surfaces. Taking the above estimate for τ_0 of 100 femto-seconds and a temperature of 1000 K, the time-frame is about 33 pico-seconds (10^{-12} seconds). In this example, a single hop of an ad-atom on a surface can be observed at the given temperature using a molecular dynamics run.

However, the simulation of ad-atom diffusion on surfaces phases involving millions of such hops, or the simulation of growth is far beyond the capabilities of molecular dynamics. In the course of this thesis, molecular dynamics has been used for geometry relaxations as well as finite temperature simulations in the context of metal adsorption and oxide growth on silicon.

3.3 (Kinetic) Monte Carlo

The main limitation of molecular dynamics simulations are the short time-steps that have to be used in order to properly integrate the atomic motion (compare equation 3.2). In Monte Carlo simulations this problem is circumvented by not considering the trajectories of individual atoms but by sampling events, like for example a hop from one surface adsorption site to another. One Monte Carlo step, and thus one energy evaluation, corresponds to an event which might have taken several thousand molecular dynamics time-steps.

Historically, kinetic Monte Carlo simulations were the first atomistic simulations performed. During World War II a group of scientists around Nicholas Metropolis used the first electronic computer (ENIAC) for their simulations in the context of the Manhattan project to develop the atomic bomb [62].

In order to study phenomena mentioned above, such as surface ordering or phase transitions, large simulation cells are needed to minimize the effects from periodic boundary conditions which are usually applied to study extended systems. In praxis, Monte Carlo methods are often used with parametrized Hamiltonians to allow for a larger system size as discussed in section 2.1.

The aim of equilibrium Monte Carlo simulations is to calculate expectation values

$$\langle A(T) \rangle = \int P(X,T) A(X) dX, \tag{3.3}$$

where X refers to an atomic configuration, $P(X,T)$ is the probability that this configuration is observed at a given temperature T and $A(X)$ is the eigenvalue of some operator $\mathcal{A}$ for that configuration. The use of a regular "grid" of configurations to compute the integral of equation 3.3 would be prohibitively expensive due to the high dimensionality of phase space and the large variation of $P(X)$ which would require fine grids. So-called "importance sampling" schemes like the famous Metropolis algorithm [63] concentrate on the "relevant" parts of phase space where $P(X)$ has finite values:

1. it starts from an initial configuration X_i with an energy E_i;
2. an event is chosen at random which leads to the structure X_{i+1} (e.g., an atom A hops from one adsorption site to another);
3. the new total energy E_{i+1} is evaluated;
4. if $E_{i+1} \leq E_i$ the event is accepted, if $E_{i+1} > E_i$ the event is only accepted with a probability
$$0 \leq \exp\left(-\frac{E_{i+1} - E_i}{k_B T}\right) < 1. \tag{3.4}$$
In the case of a rejection, the initial configuration X_i is restored;
5. continue with step 2.

The Metropolis algorithm is designed to fulfill the key criterion for importance sampling schemes, namely the detailed balance [63]:

$$P(X_i,T) P(X_i \rightarrow X_j, T) = P(X_j,T) P(X_j \rightarrow X_i, T).$$

The probability that configuration X_i is observed ($\propto \exp(E_i/k_B T)$) times the probability for a transition from X_i to X_j must be equal to the probability that X_j is observed times the probability for a transition from X_j to X_i. This condi-

tion guarantees that, in the limit of a large number of steps N, the equilibrium probability of an atomic configuration X_i is given by

$$P^{\text{Metropolis}}(X_i, T) = \frac{n_{X_i}(T)}{N} \overset{\lim_{N\to\infty}}{=} P^{\text{equilibrium}}(X_i, T),$$

where n_{X_i} denotes the number of times structure X_i occurred in the series of $\{X_k\}$. The expectation value $\langle A \rangle$ can now be computed to be

$$\langle A(T) \rangle = \int P^{\text{equilibrium}}(X, T) A(X) dX \approx \sum_i P^{\text{Metropolis}}(X_i, T) A(X_i).$$

Via equation 3.4, there is an explicit temperature dependence of the probabilities $P(X, T)$ and the expectation value.

In the importance sampling schemes, the events are chosen at random. This has the advantage, that one does not have to determine the actual rates which would involve the knowledge about the transition barrier and the attempt frequency. On the negative side one looses the dynamical information. These schemes are therefore only applicable in equilibrium situations, such as for example a surface in contact with a gas of constant pressure (see also discussion in chapter 4). In the context of this thesis, an equilibrium Monte Carlo simulation code based on a simple empirical energy functional has been used to simulate adsorption structures of Sr on silicon as described in section 5.3.3.

For non-equilibrium processes, such as for example the growth of a material, the actual rates of various processes like ad-atom deposition or diffusion are important and have to be taken into account. So-called kinetic Monte Carlo schemes do not only choose events at random but also weigh the occurrence of events according to their rates. In that way a correspondence between a kinetic Monte Carlo step and real-time can be established [64].

3.4 Finding transition states

This section brings us again back to the beginning of this chapter and the picture of the highly-dimensional configuration space. Transition state theory is probably the most focused way of exploring the energy landscape around a (local) minimum or between two minima.

The knowledge of the position of transition states as well as their energetics is crucial to understand reaction mechanisms and their kinetics. Reliable and accurate transition state energies are furthermore necessary as input parameters to kinetic Monte Carlo simulations.

The most widely used approach to calculate transition states is the so-called "drag"-method. Given an initial and a final state, we can determine a one-dimensional connection in configuration space. The system is then forced to move in a $3N - 1$ dimensional hyperplane which is orthogonal to the one-dimensional connection and is itself "dragged" from the initial to the final state along that connection. The highest energy position along that path is identified with the transition state. This method can only be applied for simple cases since it can give wrong results when several paths are available [65].

The nudged elastic band scheme [66, 65] and variations thereof [67] are more versatile. A string of equispaced images is spanned between two minima. The individual images are connected by "springs" and are relaxed including the forces from the "springs". In the limit of a large number of images they mark the lowest energy path between the two minima. The highest point along that path corresponds to the transition state.

A recent and more flexible approach is the so-called dimer method introduced by Henkelman and Jonsson [68]. Two images of the system, a so-called dimer, are constrained to have a fixed distance in configuration space. Inversion of the force on each image along the connection vector makes the dimer ascend along the softest accessible mode. Depending on the starting orientation this leads to one of the first order saddle points, that is transition states, surrounding a minimum. The dimer method is currently being reformulated to be used in connection with Car-Parrinello [61] molecular dynamics by A. Poddey and P. E. Blöchl [69].

Chapter 4

Total energies in a chemical environment

Density functional theory provides us with the total energy as a function of the number of atoms $\{N_i\}$ of each species i, the unit cell volume V, the charge state q and other parameters:

$$E^{\mathrm{DFT}} = E^{\mathrm{DFT}}[\{N_i\}, V, q, \ldots] = \min_{\{R_n\},\{|\phi_m\rangle\}} E^{\mathrm{DFT}}[\{R_n\}, \{|\phi_m\rangle\}, \{N_i\}, V, q, \ldots].$$

From now on we will assume that the electronic $\{|\phi_m\rangle\}$ and ionic $\{R_i\}$ degrees of freedom have been minimized, by one of the simulation techniques introduced in the previous chapter.

This chapter deals with questions of the type:

- Is diamond or graphite the ground state configuration of carbon?
- Is $SrSi_2$ or SrSi lower in energy?
- What is the charge state of an oxygen vacancy in $SrTiO_3$?

Questions of this kind arose frequently in the course of the simulations performed in part II. They cannot be answered by simply comparing DFT energies, since this would imply to relate total energies of systems, which differ in the number of atoms, the volume or the number of electrons. In order to create an absolute energy scale we have to introduce the concept of reservoirs.

4.1 Reservoirs

Thermodynamics teaches us to distinguish between extensive and intensive variables. Extensive variables, such as for example the energy, the particle number or the volume scale with the system size. Intensive variables such as temperature, the chemical potential or pressure are independent thereof.

We can identify pairs of intensive and extensive variables, the product of which are energies:

extensive variable	intensive variable
volume (V)	negative pressure ($-p$)
particle number (N_i)	chemical potential (μ_i)
entropy (S)	temperature (T)
magnetization ($\vec{M}$)	magnetic field ($\vec{H}$)
$\vdots$	$\vdots$

A reservoir is fully characterized by an intensive variable. Consider for example a volume reservoir (VR), for which the corresponding intensive variable is the negative pressure and the energy of the reservoir is given as

$$E^{\mathrm{VR}} = -p^{\mathrm{VR}} V.$$

For a given reservoir, there is thus a linear dependence of the energy on the extensive quantity, in this example the volume. A reservoir is considered to be large compared to the system we are studying, so that effects from the system do not change its properties, that is the intensive variable. An example for a volume reservoir is our atmosphere. The pressure will not change noticeably if we perform a laboratory experiment which results in a change of volume.

Analogously, the energy of a particle reservoir (PR) is given by $\mu_i^{\mathrm{PR}} N_i$. Again the value of μ_i^{PR} is considered to be independent of the number of particles we add to or remove from the reservoir in the course of studying our system. A heat bath (HB) is defined by its temperature T^{HB}, the energy is given by $T^{\mathrm{HB}} S$.

4.2 Free energy of formation

Consider now the following thought experiment illustrated in figure 4.1: At a given point in time, where our system of interest does not yet exist, we imagine having a series of reservoirs at our disposal. Amongst others, we have a heat bath

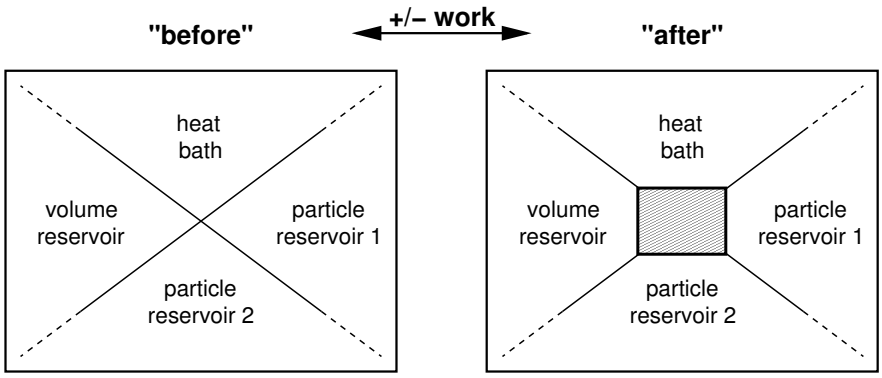

Figure 4.1: Formation of a system (shaded region) out of a set of reservoirs. The reservoirs must not necessarily be in thermodynamic equilibrium.

(e.g. a bath of silicone oil), particle reservoirs (in most cases a gas or a solid) and a volume reservoir (e.g. our atmosphere). The reservoirs must not necessarily be in equilibrium with each other. We furthermore assume that the extensive variables of the set of reservoirs cannot be exchanged with the environment. In our case this corresponds to an isochor, closed and adiabatically decoupled set of reservoirs. It is, however, possible to exchange work between the set of reservoirs and the environment.

The total energy at this point of time, labeled "before", is given by

$$\begin{aligned} E^{\text{before}} &= E^{\text{HB}} + E^{\text{PR's}} + E^{\text{VR}} \\ &= T^{\text{HB}} S^{\text{tot}} + \sum_i \mu_i^{\text{PR}} N_i^{\text{tot}} - p^{\text{VR}} V^{\text{tot}}. \end{aligned}$$

S^{tot}, N_i^{tot} and V^{tot} denote the total entropy, the total number of particles and the total volume available in the reservoirs, respectively. Since the whole arrangement is isochor, closed and adiabatically decoupled, all these quantities are conserved.

Having access to all reservoirs, we are now free to collect the building blocks for our system. In the example of figure 4.1 these are atoms, volume and heat. We assume that we can control the amount of extensive variables exchanged. After our system is assembled, the total energy is given by the internal energy of the system $U(S, V, \{N_i\})$, a function of the extensive variables, and the initial energy of reservoirs minus the amount of volume, particles and heat we have extracted:

$$E^{\text{after}} = U(S, V, \{N_i\}) + T^{\text{HB}}(S^{\text{tot}} - S) - p^{\text{VR}}(V^{\text{tot}} - V) + \sum_i \mu_i^{\text{PR}}(N_i^{\text{tot}} - N_i).$$

We will later see that the internal energy U at zero Kelvin can be related to the total energy of density functional theory. In the energy difference between "before" and "after", which is identified with the free energy of formation F, the extensive variables characterizing the initial extent of the reservoirs drop out:

$$\begin{aligned} \Delta E &= F(T^{\mathrm{HB}}, p^{\mathrm{VR}}, \{\mu_i^{\mathrm{PR}}\}; S, V, \{N_i\}) \\ &= U(S, V, \{N_i\}) - T^{\mathrm{HB}} S - \sum_i \mu_i^{\mathrm{PR}} N_i + p^{\mathrm{VR}} V. \end{aligned} \tag{4.1}$$

The free energy of formation F now depends on the intensive of the reservoirs and the extensive variables of our system. The intensive and extensive variables are independent. Knowing F allows us to explore ΔE, the energy gain or cost to assemble an arbitrary system out of a given set of reservoirs.

Equation 4.1 furthermore allows us to compare the free energy of formation of two different systems a and b assembled from the same set of reservoirs:

$$\begin{aligned} \Delta F(T^{\mathrm{HB}}, p^{\mathrm{VR}}, \{\mu_i^{\mathrm{PR}}\}; \Delta S, \Delta V, \{\Delta N_i\}) &= F^a - F^b \\ &= \Delta U(\Delta S, \Delta V, \{\Delta N_i\}) \\ &\quad -T^{\mathrm{HB}} \Delta S - \sum_i \mu_i^{\mathrm{PR}} \Delta N_i + p^{\mathrm{VR}} \Delta V, \end{aligned} \tag{4.2}$$

where ΔU, ΔS, ΔN_i and ΔV denote the difference in internal energies, entropies, particle numbers and volumes of systems a and b, respectively.

Which of the two systems is more stable, depends apparently not only on the difference in internal energies, but also on the difference in extensive variables weighted by the intensive variables of the reservoirs. Thermodynamic stability is thus only defined in the context of a series of reservoirs. Different structures or stoichiometries can be stable at different conditions, that is coupled to different reservoirs. This dependence of the thermodynamic stability on the environment is captured in the form of phase-diagrams as will be discussed in sections 4.4 and 4.5. The above expressions can of course be extended to include any possible reservoir.

We can now, as a special case, assume thermodynamic equilibrium between our system and some or all of the reservoirs. Thermodynamic equilibrium corresponds to a steady state, that is a coexistence of the reservoir and the system without a driving force to exchange extensive quantities. This translates into the condition that F is minimized with respect to the corresponding extensive quantity and gives us the equilibrium conditions for our three reservoirs:

$$
\begin{aligned}
0 = \frac{\partial F}{\partial S} = \frac{\partial U}{\partial S} - T^{\mathrm{HB}} = T^{\mathrm{system}} - T^{\mathrm{HB}} \quad &\longrightarrow \quad T^{\mathrm{system}} = T^{\mathrm{HB}}; \\
0 = \frac{\partial F}{\partial V} = \frac{\partial U}{\partial V} - p^{\mathrm{VR}} = p^{\mathrm{system}} - p^{\mathrm{VR}} \quad &\longrightarrow \quad p^{\mathrm{system}} = p^{\mathrm{VR}}; \\
0 = \frac{\partial F}{\partial N_i} = \frac{\partial U}{\partial N_i} - p^{\mathrm{VR}} = \mu_i^{\mathrm{system}} - \mu_i^{\mathrm{PR}} \quad &\longrightarrow \quad \mu_i^{\mathrm{system}} = \mu_i^{\mathrm{PR}}.
\end{aligned}
$$

At thermodynamic equilibrium between the system and one or more reservoirs, the corresponding intensive quantities must be identical.

4.3 Relation to thermodynamic potentials

In the last section, we have used the concept of reservoirs and intensive variables to create an absolute energy scale, which allows us to compare internal energies (the relation to DFT energies will be established later in this chapter) with different values of the extensive variables (compare equation 4.2). Experimentalists experience quite similar problems when analyzing measured energetics. This has led to the introduction of the well-known thermodynamic potentials such as the enthalpy, the Helmholtz free energy and the Gibb's free energy:

– The enthalpy is used whenever it does not make sense or it is simply not possible to keep the volume fixed. Alternatively one measures the free energy of formation in connection with a volume reservoir, that is at constant pressure, which yields the enthalpy:

$$H(S, p^{\mathrm{VR}}, \{N_i\}) = F^{\mathrm{Enthalpy}} = U(S, V, \{N_i\}) + p^{\mathrm{VR}} V.$$

Going back to equation 4.1, the enthalpy thus only contains the energy difference due to adding or removing atoms and heat to or from the system. The volume dependence of U has been transformed into a pressure dependence of H:

$$
\begin{aligned}
H(S, p^{\mathrm{VR}}, \{N_i\}) &= U(S, V, \{N_i\}) + p^{\mathrm{VR}} V \\
&= F(T^{\mathrm{HB}}, p^{\mathrm{VR}}, \{\mu_i^{\mathrm{PR}}\}; S, V, \{N_i\}) + T^{\mathrm{HB}} S + \sum_i \mu_i^{\mathrm{PR}} N_i.
\end{aligned}
$$

– Following the above picture, the Helmholtz free energy is the appropriate potential for comparing the free energy of formation, where the entropy

content cannot be compared. In this case one constrains the temperature to be constant by connecting to a heat bath:

$$F(T^{\mathrm{HB}}, V, \{N_i\}) = F^{\mathrm{Helmholtz}} = U(S, V, \{N_i\}) - T^{\mathrm{HB}}S.$$

– Finally, the Gibbs free energy is suited for conditions, where entropy and volume changes cannot be controlled:

$$G(T^{\mathrm{HB}}, p^{\mathrm{VR}}, \{N_i\}) = F^{\mathrm{Gibbs}} = U(S, V, \{N_i\}) - T^{\mathrm{HB}}S + p^{\mathrm{VR}}V.$$

4.4 Zero-Kelvin phase diagrams

Using equation 4.2 we now have a tool to compare energies of systems with a different number of atoms, a different volume or a different charge state. The internal energy U at $T = 0\,\mathrm{K}$ is directly related to the DFT total energy by

$$U(0\,K, V, \{N_i\}) = E^{\mathrm{DFT}}(V, \{N_i\}) + \text{zero point vibrations}.$$

Since all common simulations schemes treat the nuclei classically (Born-Oppenheimer approximation), the ground-state energy does not include the zero point vibrations which are quantum-mechanical effects consistent with Heisenberg's uncertainty principle. For a typical vibrational frequency of an atom in a solid of 10 THz, the zero point vibrational energy ($3/2 \cdot h\nu$) amounts to 0.06 eV per atom. This is the error range of density functional theory.

Furthermore, the difference in vibrational frequency for a given atomic species in two compounds is usually small. This further reduces the error when comparing total energies of systems that have the same number of atoms. In most cases, zero point vibrational energies are not considered.

Figure 4.2 shows as an example the phase diagram for oxygen at the interface between silicon and $SrTiO_3$. The lines correspond to the free energy of formation at $T = 0\,\mathrm{K}$ as a function of the oxygen chemical potential for interface structures between $SrTiO_3$ and Si(001) with different oxygen content. The free energies are plotted relative to a reference system, the unoxidized interface (compare equation 4.2).

The unoxidized interface does not contain oxygen at the interface and thus the free energy does not show a dependence on the oxygen chemical potential. The other lines in figure 4.2 correspond to oxygen contents at the interface of 0.25, 0.75, 1.0, 1.25 and 1.50 monolayers. The lower envelope of the free energy lines

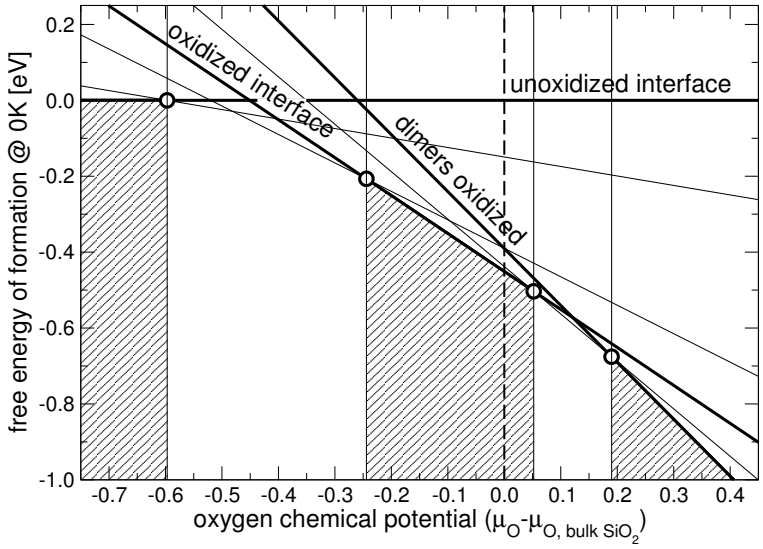

Figure 4.2: Zero Kelvin phase diagram for oxygen at the interface between $SrTiO_3$ and Si(001). Depending on the oxygen chemical potential, different interface structures are thermodynamically stable. For details see our publication 1, in chapter 6.1.

defines the thermodynamically stable phases as a function of the oxygen chemical potential. A crossing of two free energy lines corresponds to a phase boundary. The phase boundaries of the three stoichiometric interface structures (compare our publication 1) have been marked by vertical lines, the corresponding stability regions are shaded. In the publication we left out the energy information and arrived at the one-dimensional phase-diagram which can be seen in Figure 2 of publication 1. The pV-term of the free energy has been neglected since the introduction of oxygen to the interface has negligible effects on the volume of the sample.

4.5 Finite temperatures

At finite temperatures we additionally have to consider a series of internal energy and entropy contributions from

- translational,
- vibrational,
- rotational and
- electronic

degrees of freedom. Configurational degrees of freedom only contribute to the entropy which is calculated by Boltzmann's formula

$$S = -k_B \ln \Omega,$$

where Ω is the number of microstates, that are different atomic configurations yielding the same total energy. A typical example are vacancies in a solid. In the independent vacancy approximation there are

$$\Omega = \frac{M!}{N!(M-N)!}$$

ways to arrange N vacancies on M lattice sites. Especially for vacancies, the configurational entropy has sizable effects, whereas it is small for ordered surface structures.

The standard way to access finite temperature effects is to take 0 K DFT total energies and then use approaches from statistical mechanics to calculate the internal energy and entropy contributions. The internal energy at a given temperature T is thus written as

$$U(T,\ldots) = \underbrace{U(0\,K,\ldots)}_{E^{\mathrm{DFT}}} + \Delta U(T,\ldots).$$

Analytical expressions for the contributions to $\Delta U(T)$ can be found in most textbooks on statistical mechanics [70, 71, 72, 73]. Note that the zero-point vibrational energy has to be subtracted from $U(0\,K,\ldots)$ when using classical expressions for the vibrational free energy.

4.6 Relating chemical potentials to experimental parameters

While the phase diagram of figure 4.2 provides valuable insight into the thermodynamic stability, it does not directly give us practical information in terms of experimental parameters.

Sticking to the example of the oxygen content at the interface between $SrTiO_3$ and Si(001), the interesting parameter would be the oxygen partial pressure corresponding to a given chemical potential. Within the ideal gas approximation, however, it is straightforward to relate a chemical potential to a partial pressure

and temperature for simple molecules. Similarly, chemical potentials can also be related to bulk particle reservoirs [70, 71, 72, 73].

4.7 Summary

The concepts introduced in the last sections allow us to answer the questions raised at the beginning of this chapter. All of them were related to comparing the energetics of systems with different values of the extensive variables such as particle number (SrSi vs. $SrSi_2$), volume (graphite vs. diamond) or charge state (vacancy in $SrTiO_3$). Using reservoirs we are able to place the DFT energies on an absolute energy scale. Depending on the chemical environment, that is intensive variables defined by the reservoirs, it is now possible to compare the energetics.

Part II

Application – Growth of High-K Oxides

Chapter 5

Interfacing silicon with high-k oxides

Microelectronics is probably the most important field of engineering which has driven us into nanotechnology. Today, microprocessors with an unbelievable number of forty million transistors on an area of 214 square millimeters (14.6×14.6 mm) are mass-produced. Aiming at ever faster processor generations, the industry keeps pushing the limits of engineering and, lately, also physics.

This chapter focuses on the industry's biggest problem at the moment which is the replacement of silicon dioxide as the insulating material in transistors. Simulations of the growth of alternative oxides on silicon in the course of this thesis have led to a new binding principle at silicon–oxide interfaces.

5.1 A short review of 50 years microelectronics

Transistors are switches for electric current with an "on" or "1" state, where current can flow, and a non-conducting "off" or "0" state. The first transistor, a so-called bipolar transistor, was built by the group of William Shockley of Bell Laboratories in 1947 marking the onset of microelectronics. In 1958, Jack Kilby of Texas Instruments was able to produce all circuit elements such as diodes, resistors, capacitors and transistors of the same material which allowed him to put them on a single chip. Both inventions were awarded with the Nobel prize in physics.

In 1965, Gordon Moore, a scientist from Intel, summarized the young history of component densities in integrated circuit devices in a graph which became

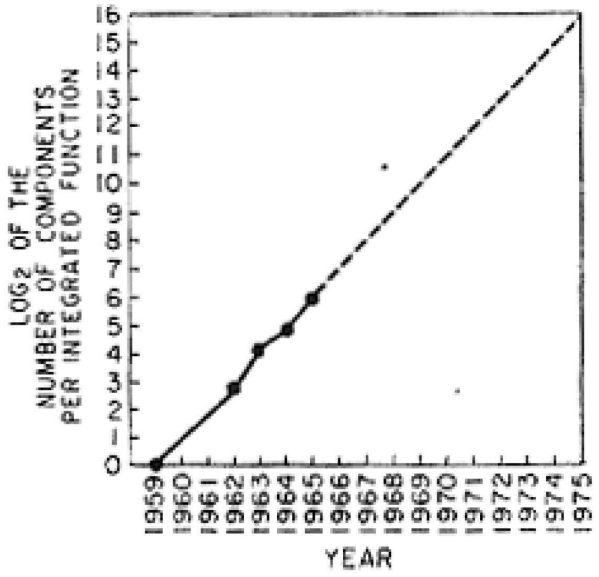

Figure 5.1: The five data points Gordon Moore used to extrapolate microprocessor performance and formulate his famous law. Picture taken from [74]. For continuation see figure 5.2.

famous (compare figure 5.1). Based on five data-points available at that time, he predicted that

the number of components per integrated circuit doubles every year.

Now, almost forty years later, this exponential growth as predicted by Moore still takes place as is evident from figure 5.2 which shows as an example the development of the familiar processor generations from Intel. There is only a small deviation from the initial prediction in that the doubling of the component density only occurs every eighteen and not every twelve months.

The first MOSFET (Metal Oxide Semiconductor – Field Effect Transistor), the type of transistor employed in today's devices, was fabricated in 1960 at Bell Laboratories. It was, however, not before 1970 when the bipolar transistors were in the course of being replaced by the new technology mainly due to cost factors [75].

The functionality of a MOSFET transistor is visualized in figure 5.3. Each junction between two semiconductor regions with different doping constitutes a diode. Therefore, no current can flow between the two contacts, source and drain terminal, in the arrangement shown due to the two opposing diodes. If, however, a positive voltage is applied to the gate terminal, one attracts electrons into the channel region. This effect is called inversion as electrons become the majority charge carriers. As a result there are no diodes anymore and current can flow

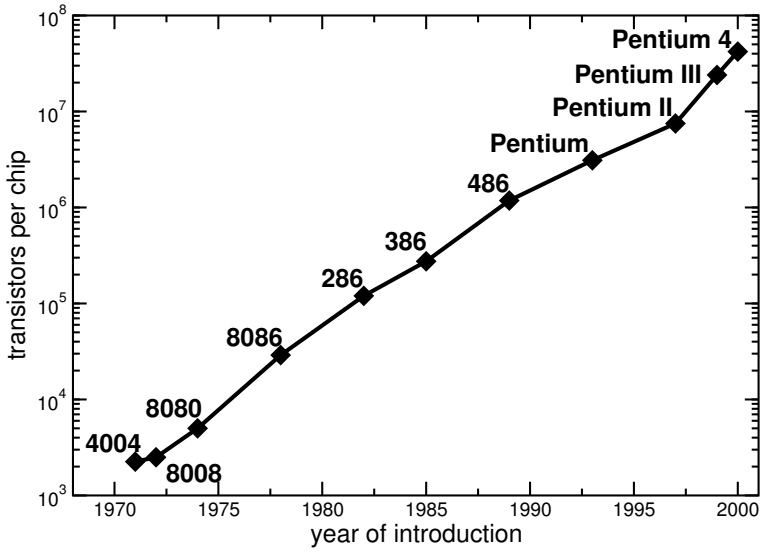

Figure 5.2: Transistors per chip for the processor generations of Intel since 1970. Data taken from www.intel.com.

between the two contacts, provided a voltage is applied. Central to the functionality of a MOSFET is a thin, insulating layer, the gate oxide. It separates the gate electrode from the silicon substrate.

The final breakthrough for the MOSFET technology came with the discovery of the scaling law for MOSFET's by Bob Dennard of IBM in 1972 [76]: If all dimensions and voltages are scaled down by a given factor and the substrate doping is increased by the same factor, all performance parameters improve while the device dimensions decrease. Scaling a 65 nm gate length transistor (production year 2003) to 45 nm (production year 2005) corresponds to a factor of roughly 1.4. This will reduce the required operating voltage and the circuit delay by a factor of 1.4 and also results in a correspondingly larger operating frequency. So 3 GHz at a gate length of 65 nm are scaled up to 4.3 GHz at 45 nm. At the same time, the space per transistor is reduced by the factor squared. A 45 nm transistor is thus roughly 2 times smaller which allows to double the number of transistors per chip. For bipolar transistors there is no analogue to this scaling law.

5.2 The need for high-k

Following Dennard's scaling law, the channel length has been reduced from 10 μm to 65 nm since 1970 and, at the same rate, also the gate oxide thickness from 200 nm to between 1 and 2 nm [75, 77]. Over the years on has observed a constant factor of about 45 between channel length and gate oxide thickness [75]. So far,

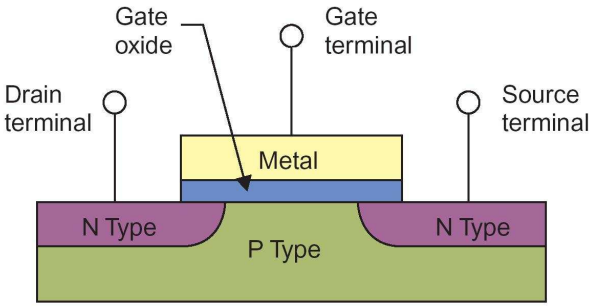

Figure 5.3: Schematic drawing of an (NMOS) MOSFET transistor. The substrate is p-doped silicon. Two contacts, called "*source*" and "*drain*" are implanted as highly n-doped regions. The substrate between these contacts is called "*channel*". Above the channel there is a thin, insulating layer, the "*gate oxide*" and a metallic electrode, the "*gate*". Picture taken from http://www.icknowledge.com/.

the gate oxide (compare figure 5.3) consists of silicon dioxide (SiO_2) or silicon oxynitride (SiO_xN_y). SiO_2 is actually one of the main reasons that silicon is today's semiconductor of choice. Other candidates such as for example gallium arsenide do not have a "native" oxide with, as in case of SiO_2, almost perfect properties in terms of growth as well as interface and bulk properties.

The process of gradually reducing the SiO_2 film thickness (following Dennard's scaling law) is now approaching unsurmountable physical barriers ("red brick wall" in the language of the semiconductor engineers [77]) as the gate oxide thickness approaches atomic dimensions. Two nanometers correspond to only a few layers of oxide and one nanometer is considered to be the thickness below which quantum mechanical leakage currents from the channel to the gate electrode will become intolerable.

A solution to the problem is in principle easily found when analyzing the physics of MOSFET transistors. The main reason behind the required downscaling of the gate oxide thickness is the resulting increase of the capacitance per unit area of the capacitor formed by the metal gate, the gate oxide and the semiconducting substrate (MOS-capacitor, compare figure 5.3):

$$\frac{C}{A} \propto \frac{\epsilon}{t},$$

where ϵ is the dielectric constant of the oxide and t its thickness. An increased capacitance per unit area increases the drain current which improves the switching time of the device. The dielectric constant ϵ (3.9 for SiO_2) is a materials property. Therefore the route taken so far to increase C/A was to decrease t according to Dennard's scaling law. Having reached the limits using this approach, one now

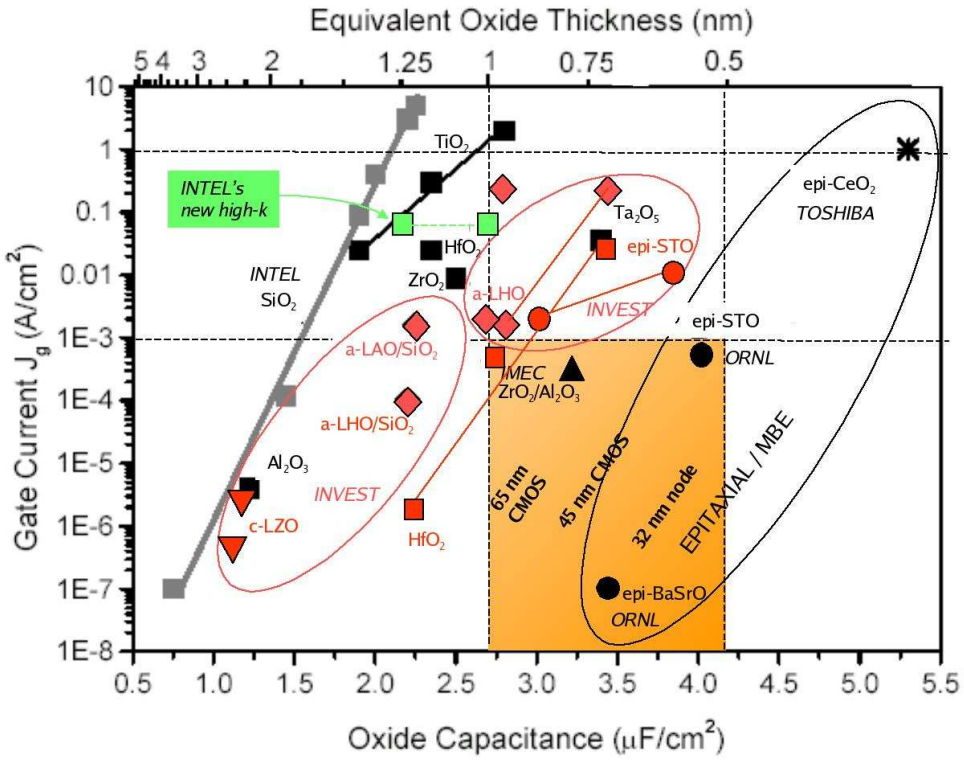

Figure 5.4: The high-k materials map in mid-2004. The leakage current per area is plotted versus the capacitance per unit area (bottom) and the corresponding SiO_2 film thickness (top). The exponential dependence of the gate current on the film thickness for SiO_2 nicely fits with a quantum mechanical leakage current. Figure courtesy of Athanasis Dimoulas, Demokritos, Athens.

has to increase ϵ which, however, translates into introducing a new oxide. In this context, oxides with a larger dielectric constant compared to silicon are called "high-k oxides".

An inability to replace SiO_2 is considered to be a showstopper for device scaling and therefore also the further exponential increase in computer performance. A deviation from Moore's law, however, will inevitably affect the economic success not only of the semiconductor industry but also of related branches such as the software industry.

Figure 5.4 introduces the main contenders for replacing SiO_2 within the next years. All candidates contain transition metals which have a high tendency to form metallic silicides in contact with silicon. A first generation of high-k oxides around ZrO_2 and HfO_2 will therefore still have a very thin SiO_2 layer to separate the transition metal from the substrate. These oxides will be grown by chemical vapor deposition.

As the required capacitances per unit area are further increased, this interfacial SiO_2 layer will no more be tolerable since the smallest capacitance dominates in a series of capacitances (SiO_2 and high-k oxide). In a second step, around 2010 to 2015, industry will then require oxides with an atomically well defined interface with silicon. So far, such a heteroepitaxial relationship has only been proven for oxides around $SrTiO_3$ and SrO [3, 78] using molecular beam epitaxy (compare section 1.1) which is, however, a more expensive method with only moderate throughput at the moment.

5.3 Results

Despite the experimental evidence of an atomically well defined interface, the interfacial stoichiometry and structure remained elusive. Decisive process parameters as well as the electronic properties at the interface are still under debate. Using ab-initio molecular dynamics simulations we could unravel the growth process of $SrTiO_3$ on Si(001). In the following sections the main results obtained, starting with metal deposition on the clean silicon surface, are briefly reviewed. Detailed information is found in our publications in chapter 6. Additional information about computational procedures is given in appendix B.

5.3.1 The substrate: Si(001)

Prior to considering oxide growth we must understand the substrate, namely the technologically relevant (001) oriented surface of silicon. Silicon crystallizes in the diamond structure. Each atom is tetrahedrally coordinated and forms four covalent bonds. Cleaving the crystal along a (001) plane initially creates a surface with a quadratic (1×1) array of silicon atoms (compare figure 5.5a). On the surface, each atom is now lacking the two "upper" bonding partners. Only the two covalent bonds to the silicon atoms in the lower plane remain. As a result there are two singly occupied dangling bonds per atom pointing out of the surface. This situation is energetically highly unfavorable and leads to the probably most famous surface reconstruction: the (4×2) buckled dimer row reconstruction of the silicon (001) surface.

In a first step, two neighboring silicon atoms approach each other and form the so-called dimer bond which is parallel to the surface. The result is the (2×1) dimer row reconstructed silicon surface (compare figure 5.5b). This first reconstruction step still leaves one singly occupied orbital per surface silicon atom. The bonding and anti-bonding states of the dimer bonds move out of the center of the gap and approach the bulk silicon band edges.

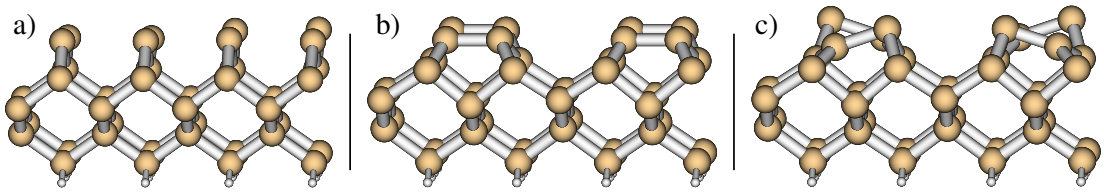

Figure 5.5: The reconstruction of the Si(001) surface. Panel a: the unreconstructed (1×1) surface; panel b: the (2×1) reconstruction; panel c: the (4×2) reconstruction.

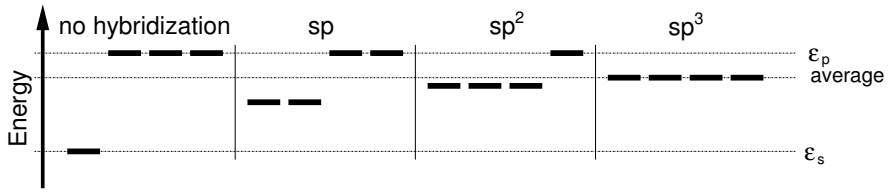

Figure 5.6: Schematic evolution of the atomic energy levels of silicon as a result of sp, sp^2 and sp^3 hybridization. The average energy is identical in all four cases.

The half-filled dangling bond band is then, in a second step, split into two subbands, one fully occupied, the other empty. The reason for this lift in degeneracy is a geometrical distortion, namely the tilt of the dimer bond. One silicon atom moves up and adopts a quasi-tetrahedral, sp^3-like bonding arrangement, the other one moves down and ends up in a planar, sp^2-like bonding environment. This process is called "buckling". Along a row, the dimer buckling is strongly correlated in an anti-parallel manner. Across the rows, the correlation is comparably weak. This second step results in the final $c(4 \times 2)$ reconstruction of the silicon surface (compare figure 5.5c).

The p_z orbital of an sp^2 hybridization is higher in energy compared to an sp^3 orbital (compare figure 5.6). The half filled dangling bond band of the (2×1) reconstruction therefore splits into a fully occupied band formed from the sp^3-orbitals of the upper silicon atoms and an empty band with p_z character from the lower silicon atoms. The upper silicon atoms are thus formally "1−" and the lower silicon atoms "1+" charged.

It is important to note that despite this reconstruction processes, the silicon surface is still considered to be a highly reactive surface. The presence of oxygen or transition metals leads to oxidation and silicidation even at ambient conditions. A widely used approach to passivate the surface is by saturation via a monolayer of hydrogen. The dangling bond states are then saturated by Si–H bonds. Hydrogen saturation again removes the dimer buckling since all surface silicon atoms are then tetrahedrally coordinated.

5.3.2 Metal adsorption on Si(001)

The main problem in the context of growing high-k oxides on silicon is silicide and silicate formation as soon as transition metals get in contact with the substrate. Controlled growth should, however, start with metal deposition to at least some extent, since introducing oxygen too early leads to the similarly unwanted formation of silicon dioxide. Therefore, we have investigated the deposition of metal ions out of the three most relevant groups in the context of high-k oxides. These are the divalent earth-alkali metals and the three- and the four-valent transition metals at the examples of strontium (Sr), lanthanum (La) and zirconium (Zr). The detailed results can be found in our publications 2, 3 and 4 in the corresponding sections of chapter 6.

Figure 5.7 summarizes the main results for Sr and La. It shows the energy per (1×1) surface unit cell versus coverage. Each point corresponds to a surface reconstruction. The reconstructions connected by line segments are the thermodynamically stable phases and the slope of the line segments gives the chemical potential at which the phases coexist. A detailed discussion of these graphs is given in appendix B.1. The energies and thus also the chemical potentials are plotted relative to the corresponding lowest energy silicide. A positive chemical potential, that is a positive slope, thus implies that the corresponding phase transition is thermodynamically unstable with respect to bulk silicide formation.

While in case of Sr (figure 5.7(a) and our publication 2, section 6.2) coverages up to 2/3 monolayer (ML) are thermodynamically stable, we observe that La surface reconstructions are only stable up to the coverage of 1/3 ML (figure 5.7(b) and our publication 3, section 6.3). In case of Zr (our publication 4, section 6.4) and also Hf, all surface reconstructions are unstable with respect to silicide formation which excludes the possibility of metal pre-deposition. Zr-silicide formation has also been observed experimentally [79].

The surface reconstructions found for Sr and La are driven by the atomic and electronic topology of the Si(001) surface. The basic principle will be shortly summarized at the example of Sr. La behaves conceptually similar at low coverages and, due to a change in oxidation state from 3+ to 2+ above 1/3 ML, even identical to Sr at high coverages (for details refer to our publication 3, section 6.3).

The chemistry of Si and Sr is probably best understood in terms of bulk Sr silicides. These structures can be explained by a very simple scheme, the so-called Zintl-Klemm concept, which was initially formulated in 1939 [80, 81, 82]. At the rise of solid state chemistry, scientists started to investigate the correspondence between structure and stoichiometry. They discovered that they can explain a wide range of compounds between electronegative elements, essentially groups

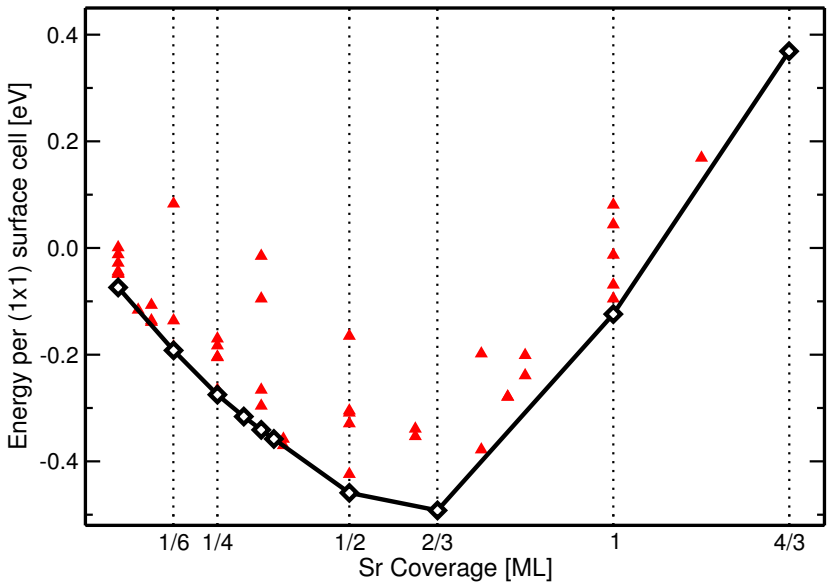

(a) Surface energy versus coverage for Sr

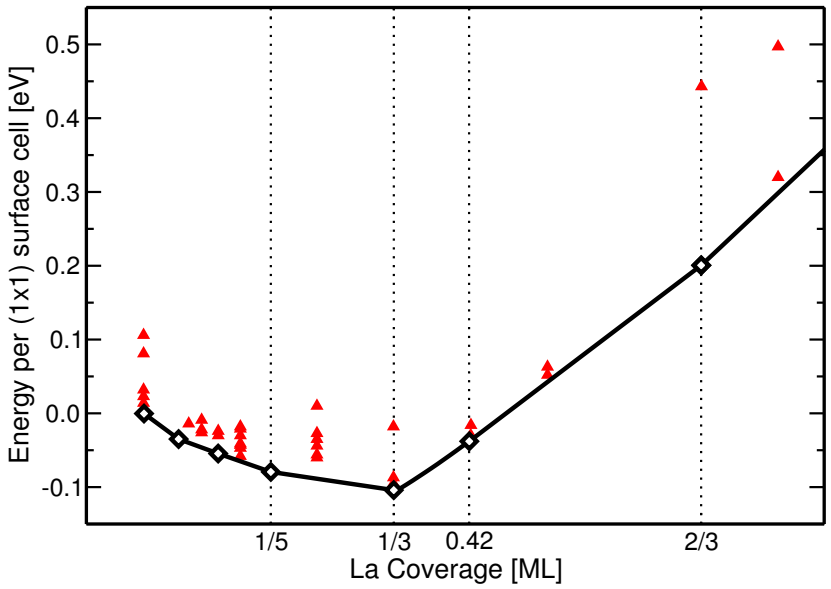

(b) Surface energy versus coverage for La

Figure 5.7: Surface energy versus coverage for Sr and La. The open diamonds represent thermodynamically accessible structures, the triangles correspond to metastable structures. Mind that the coverage-axes are scaled differently.

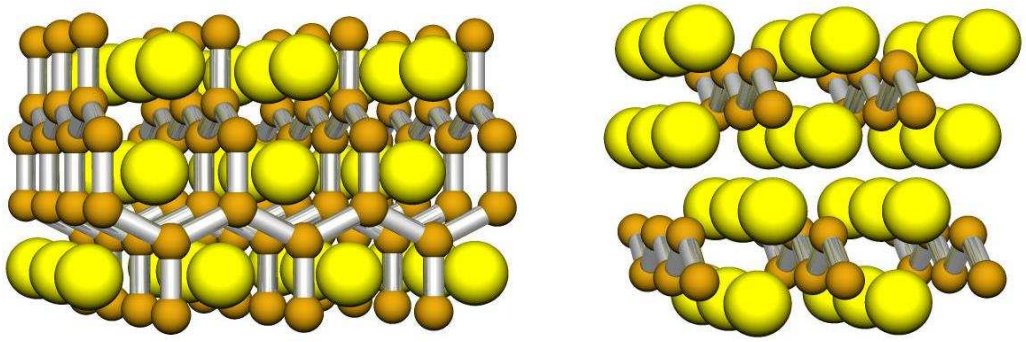

(a) The bulk $SrSi_2$ structure.

(b) The bulk SrSi structure.

Figure 5.8: Two typical bulk Sr silicides (Si: small spheres connected by sticks; Sr: big spheres).

IV to VII, and electropositive elements, mainly groups I and II, in a simple ionic picture.

The electropositive element, we will take Sr as an example from now on, donates all its valence electrons to the electronegative element, silicon in our context. Upon accepting an electron, silicon saturates one of its four valences. Silicon in the oxidation states of Si^{-}, Si^{2-}, Si^{3-} and Si^{4-} is thus able to form 3, 2, 1 and 0 covalent bonds, respectively. Furthermore it turned out that, from a structural point of view, the acceptance of one electron results in a quasi-shift of silicon one position to the right in the periodic table of elements. Si^{-}, Si^{2-}, Si^{3-} and Si^{4-} are thus found to be isosteric to P, S, Cl and Ar.

This stunningly simple concept can easily be demonstrated right at the example of two bulk Sr silicides shown in figure 5.8. In panel (a) we observe that each Si atom forms three covalent bonds. This leaves one valency per Si atom which has to be saturated via electron donation from Sr. Since Sr donates two valence electrons, the final stoichiometry, according to Zintl-Klemm, must be $SrSi_2$ ($Sr^{2+}Si_2^{-}$), which is indeed correct. In the example of figure 5.8(b), each Si atom forms two covalent bonds which corresponds to two valences that need to be saturated via electron donation or, in other words, formal Si^{2-} ions. The stoichiometry is indeed SrSi ($Sr^{2+}Si^{2-}$). SrSi with its chain structures is furthermore a nice example showing that Si^{2-} is isosteric to sulfur which is known for forming chain structures. This simple principle of relating the number of covalent bonds per Si atom to its charge state and furthermore to the stoichiometry works reliably for all experimentally known Sr silicide structures.

Translated to the silicon (001) surface, the two valence electrons from one Sr will saturate the dangling bonds of a dimer. A saturated dimer looses its buckling,

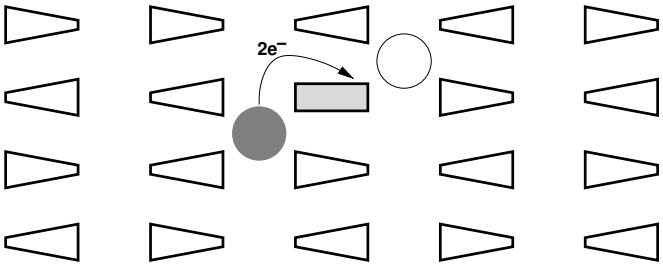

Figure 5.9: Schematic representation of the isolated Sr ad-atom at the preferred adsorption site position. The filled circle represents the Sr ad-atom, the rectangle represents a filled and therefore unbuckled Si dimer. The triangles represent buckled dimers. The flat side of a buckled dimer indicates the upper Si atom with a filled dangling bond, whereas the pointed side indicates the lower Si atom with the empty dangling bond. The charge transfer from the Sr ad-atom to one of the surrounding dimers is indicated by the arrow, the preferred adsorption site in the neighboring valley by the open circle.

since all dangling bonds are filled and both Si atoms prefer the tetrahedral sp^3 configuration (compare figure 5.6). The atomic structure around a singe ad-atom is visualized in figure 5.9. The preferred adsorption site is in the center of four dimers. One of the neighboring Si dimers is unbuckled due to the electron donation from the ad-atom. The other three dimers are orientated such that the upper, and thus negatively charged Si atom points towards the Sr^{2+} ion. Reversing the buckling of one dimer and thus placing a positively charged Si atom next to Sr results in an energy penalty of roughly 0.4 eV.

The filled dimer offers a preferred adsorption site in the next valley as indicated by the open circle in figure 5.9. As a result, diagonal and zig-zag chain structures turn out to be the thermodynamically stable reconstructions at dilute coverages. At 1/6 ML these chains condense (figure 5.10(a)). It is not possible to stack them closer since that would mean that a lower and thus positively charged Si atom points towards a Sr ion which involves a large energy penalty as indicated above. The next phase are therefore double chains at 1/4 ML shown in figure 5.10(b) (compare also figure 1.2a and corresponding text).

At one half monolayer the Sr ad-atoms occupy all favorable positions in the center of four dimers. We labeled this coverage as the "canonical coverage" since all the dangling bond states are saturated and we do not observe any surface states deep in the gap of silicon anymore. This surface is isoelectronic to a hydrogen terminated silicon surface and is thus expected to be chemically comparably inert. Above 1/2 ML, the electrons from Sr enter the dimer anti-bonds leading to a partial breakup of the dimer bonds. At 2/3 ML we observe a (3×1) reconstruction with alternating rows of Si dimers and isolated Si atoms.

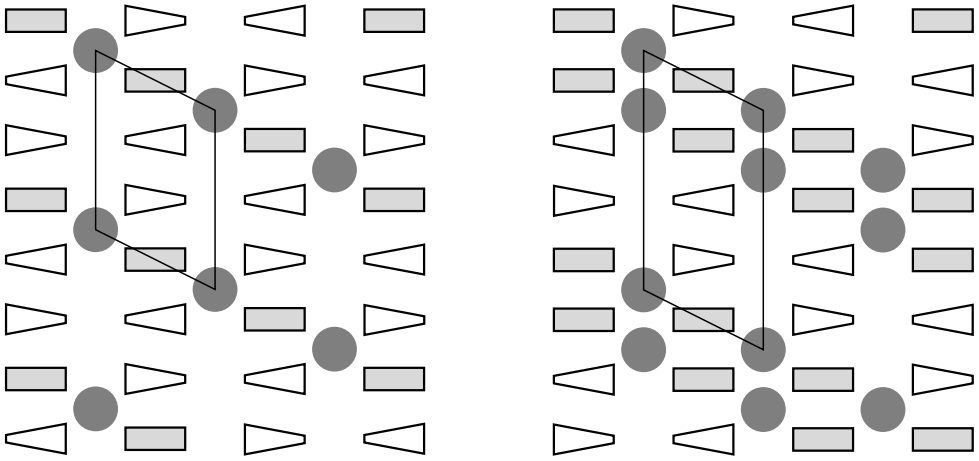

(a) Condensed diagonal chains of Sr at a coverage at 1/6 ML.

(b) Diagonal double chains of Sr at a coverage of 1/4 ML.

Figure 5.10: Chain structures of Sr ad-atoms at low coverages. The symbols are explained in figure 5.9. The surface unit cells are outlined.

Our studies on Sr adsorption have led to a unified picture of the processes and has helped to interpret a series of experimental results. The phase diagram we propose on the basis of the surface energies is compatible with recent experimental results [83]. Unlike most experimental papers, however, we clearly identify a phase at 1/2 ML. This "canonical" surface reconstruction plays a crucial role as a template for oxide growth.

5.3.3 Monte Carlo simulations of low-coverage surface ordering

In the course of our ab-initio study on Sr adsorption on Si(001) we have screened a large variety of possible surface reconstructions. This not only allowed us to identify the thermodynamically stable phases but also to quantify energy penalties for deviations from the ideal structural principles derived. These principles are:

1. Each Sr atom is electrostatically stabilized by four negatively charged silicon atoms located next to it. Negative silicon atoms have two electrons in their dangling bond and are in a raised, sp^3-like bonding configuration (compare figure 5.9 and 5.10).

   Violation of this rule raises the energy by roughly 0.4 eV per positively charged Si atom next to a Sr ion. At this level of abstraction we do not

distinguish between a negatively charged Si atom of a buckled and an unbuckled dimer.

2. There are no reversals of the dimer buckling in the Sr-free regions of the surface. Such a reversal would result in two neighboring dimers buckled in the same direction. The energy penalty for this has been calculated to be about 0.1 eV. This is a consequence of the anti-correlated coupling of the dimer buckling within one row (see section 5.3.1).

3. Sr atoms on neighboring adsorption sites within one valley, that is between two dimer rows, experience a mutual electrostatic repulsion. This is the reason why we do not observe patches or islands of Sr ad-atoms but separated chain structures. As a result of this repulsion, the adsorption energies, which are nearly constant below 1/6 ML, increase by 0.23 eV per atom when increasing the coverage to 1/2 ML, where all adsorption sites are filled. The energy penalty as a function of the number of neighboring Sr atoms along a valley has been parametrized.

Analysis of these three basic rules reveals, that rules 1 and 2 are almost automatically fulfilled by considering Sr "double-vacancies". In the chain structures of figure 5.10 we see that the Sr chains are separated by two empty adsorption sites, a "double-vacancy". This guarantees that rule 1 is fulfilled, except for the case of two double vacancies at the same position in neighboring valleys. This configuration leads to a positive Si atom neighboring a Sr. We have thus devised an energy functional which checks whether

– double-vacancies are on the same position in neighboring valleys (energy penalty of $0.38\,eV$), and

– Sr ad-atoms occupy neighboring sites within one valley (energy penalty between 0.06 and 0.23 eV depending on the number of neighboring atoms)

According to this model, the alternative surface reconstruction at 1/4 ML of figure 5.11 would be isoenergetic to figure 5.10b since all rules are fulfilled in both cases. Our ab-initio calculations show that the structure of figure 5.10b is more stable by 0.04 eV. This value is close to the DFT error bar as well as to k_BT at room temperature. In the standard implementation, our model does therefore not include this energy penalty for interrupting double-vacancy chain structures. We have, however, performed some tests to check the influence of such a penalty on the resulting structure.

Based on this simple parametrized model, I have developed an equilibrium Monte Carlo simulation code (refer to section 3.3 for the basic principle) in order to cross-check whether we have missed any surface reconstructions in the small-scale ab-initio screening. For this purpose, the crude nature of our model is even

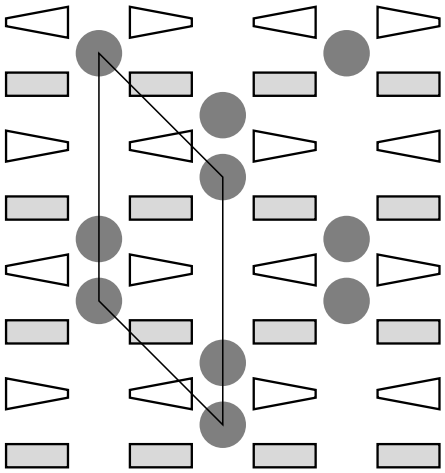

Figure 5.11: Alternative structure at 1/4 ML (compare figure 5.10b). The energy difference is just 0.04 eV. The surface unit cell is outlined.

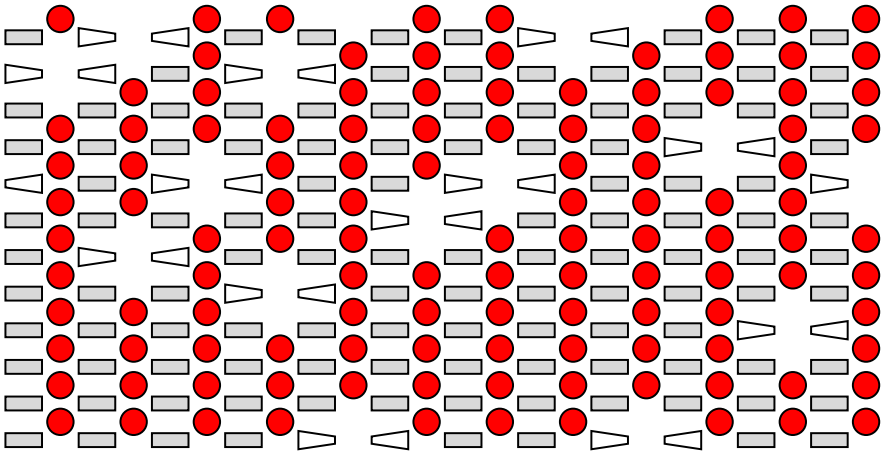

Figure 5.12: Typical ad-atom geometry at a coverage of 0.4 ML as a result of the Monte Carlo simulation. The simulation cell consists of 16×16 silicon dimers.

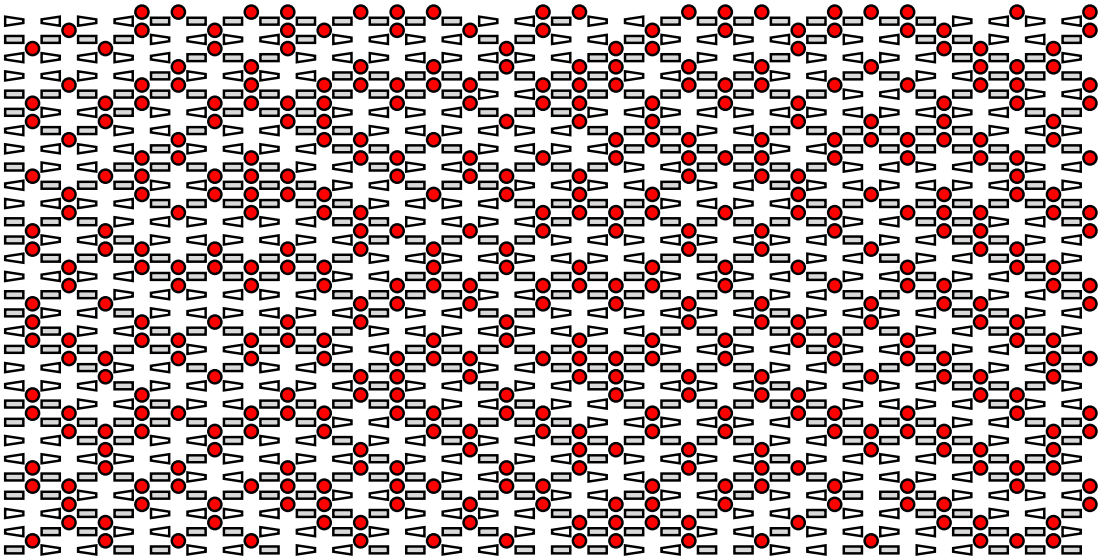

Figure 5.13: Typical ad-atom geometry at a coverage of 1/4 ML as a result of the Monte Carlo simulation. The simulation cell consists of 30×30 silicon dimers.

an advantage since it only includes the unambiguous, "hard" rules. "Soft" rules easily introduce hidden assumptions and can thus bias the results.

At coverages close to 1/2 ML we observe, as also expected from the ab-initio results, an array of randomly distributed double vacancies as visualized in figure 5.12. Interestingly, a simulation of 1/4 ML, however, shows a relatively well ordered reconstruction based on double chain structures. Figure 5.13 shows a typical adsorbate structure at 1/4 ML in a 30×30 dimers simulation cell. This simulated reconstruction pattern exhibits a rather close resemblance to an STM image taken at the same coverage (figure 1.2a). Inclusion of the 0.04 eV energy penalty for deviations from chain structures as mentioned above, results in perfect double chains across the unit cell even at 500 K. Figure 5.14 shows a typical atomic arrangement at 1/8 ML as an example for dilute coverages. We observe chain structures as anticipated from the ab-initio results.

The Monte Carlo simulations have thus not lead to the discovery of relevant surface reconstructions which had not already been identified in the course of the ab-initio calculations. Due to the very coarse model, including only a small number of unambiguous rules, we are thus confident to fully understand Sr adsorption on Si(001). The close resemblance of our simulated reconstruction at 1/4 ML with available STM images furthermore indicates that the simple model employed is sufficient to describe the essential physics. These results are unpublished.

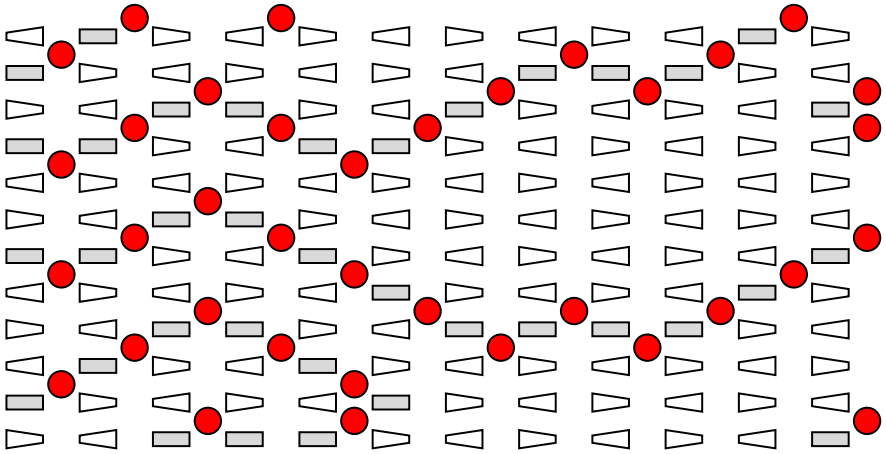

Figure 5.14: Typical ad-atom geometry at a coverage of 1/8 ML as a result of the Monte Carlo simulation. The simulation cell consists of 16×16 silicon dimers.

5.3.4 Growth of $SrTiO_3$ on Si(001)

With the Sr adsorption on Si(001) understood, we can now turn to oxide growth. The main problem is connected to the fact that the chemical bonding in silicon and $SrTiO_3$ is fundamentally different. While silicon is a covalently bonded material, $SrTiO_3$ is an ionic crystal with some covalent character in the Ti–O bonds. More specifically, $SrTiO_3$ crystallizes in the perovskite structure with Ti being octahedrally coordinated by oxygen and Sr placed in a cubic oxygen cage. The (001) planes of $SrTiO_3$ are alternating SrO and TiO_2 planes and therefore electronically saturated, that is unable to form covalent bonds. The SrO terminated surface does not exhibit states in the band gap.

In order to make an electronically saturated Si–$SrTiO_3$ stack we need to create an interfacial layer with the ability to form covalent bonds in one direction to saturate the valences of the silicon surface and, on the other hand, provide an ionic template compatible with $SrTiO_3$.

Based on the understanding of the Sr surface reconstructions we have identified the canonical 1/2 ML covered silicon surface as the only surface reconstruction which fulfills these requirements. It is the only one which saturates all silicon dangling bonds. The quasi-ionic interaction of Sr with Si furthermore prepares an ionic template with a formal charge distribution as visualized in figure 5.16. The resulting two-dimensional ionic layer is compatible with the NaCl–type charge pattern of a SrO–terminated $SrTiO_3$ crystal.

Using molecular dynamics we simulated the "deposition" of $SrTiO_3$ on top of this template. While the first SrO layer still reconstructs significantly, we observe a recrystallization if we deposit two more $SrTiO_3$ layers. The resulting structure,

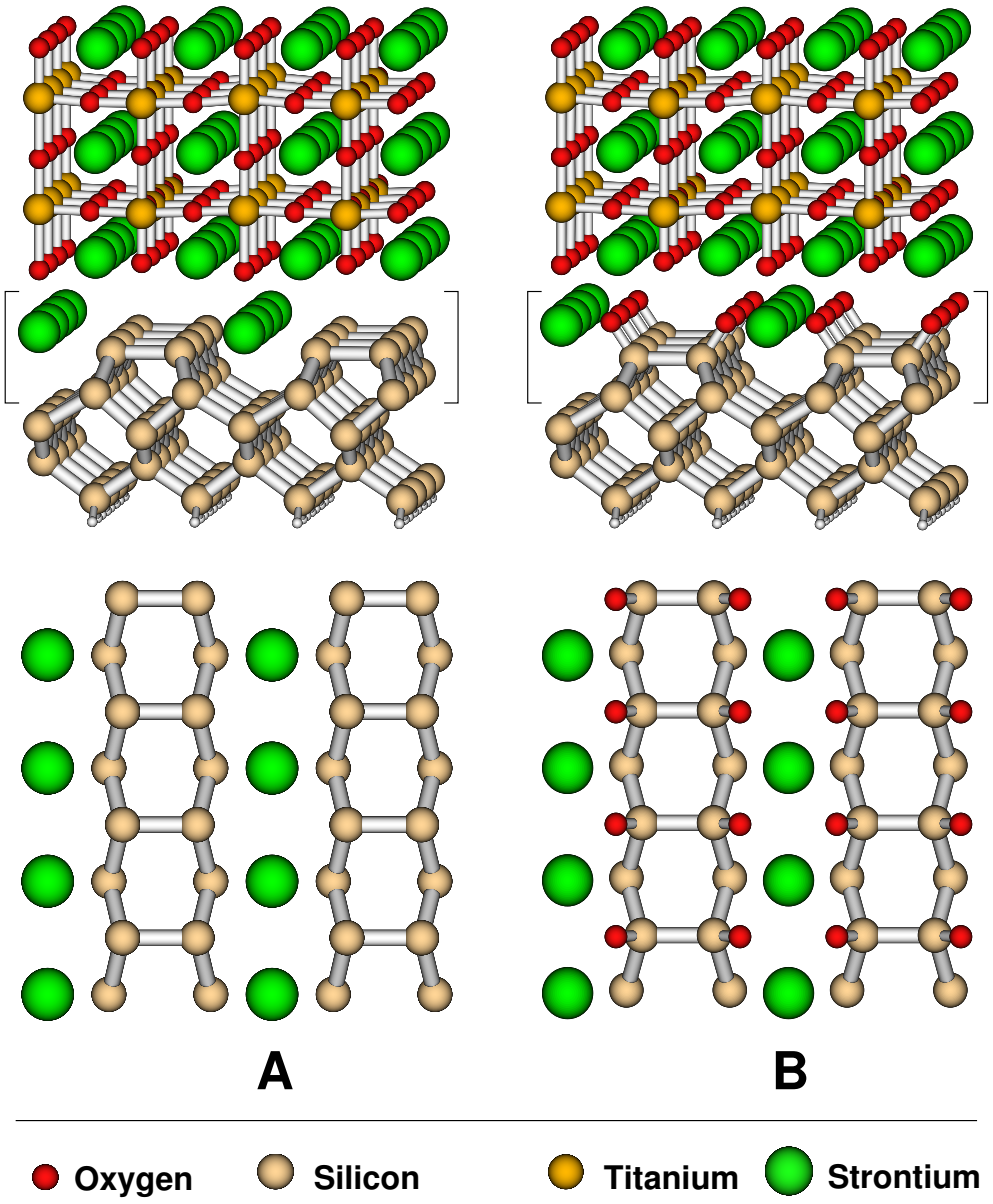

Figure 5.15: The two relevant interface structures between silicon and $SrTiO_3$ taken from publication 1.

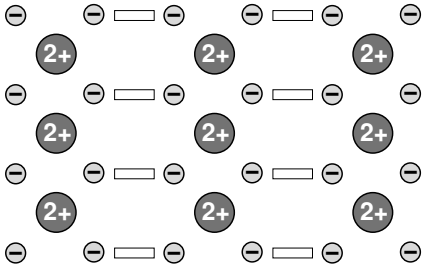

Figure 5.16: Charge pattern of the silicon surface covered by 1/2 ML of Sr. The Sr ions have a formal charge of 2+, Si of 1− due to the filled dangling bond. The empty rectangles denote the dimer bonds to ease comparison with the lower left panel of figure 5.15.

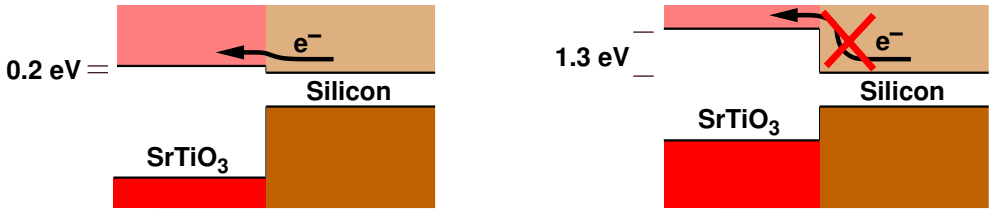

(a) Interface A (b) Interface B

Figure 5.17: Schematic band-gap evolution at the interface for interfaces A and B as shown in figure 5.15.

visualized in two modifications in figure 5.15, has proved to be stable during molecular dynamics simulations at 800 Kelvin.

Unfortunately, a good interface structure does not yet make a good high-k oxide. Many promising candidates for example fail because they do not have sufficiently large band-offsets relative to silicon. For device applications, the conduction and valence band offsets have to be in the region of 1 eV. This is necessary to prevent electrons and holes from entering the oxide. For the interface just introduced (left panel of figure 5.15), the conduction band offset is, however, just 0.2 eV as visualized in figure 5.17. This excludes the use of this interface in device application – at least for n-doped substrates.

The stability analysis of the interface with respect to oxidation, however, revealed, that oxygen first attacks the filled dangling bonds of the dimer silicon atoms. Exactly one monolayer of oxygen can be selectively introduced at the interface this way which leads to the interface structure shown in the right panel of figure 5.15. This introduction of oxygen, possible without running the risk of creating interfacial silicon dioxide (for details see our publication 1, section 6.1), results in a major charge redistribution at the interface. While we had formal

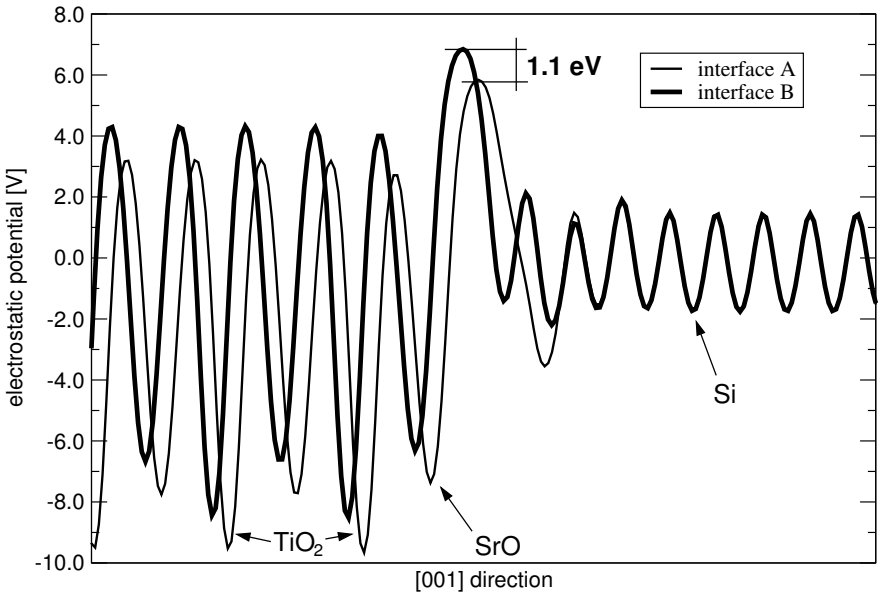

Figure 5.18: Layer-averaged electrostatic potential (plane-wave part, compare our publication 5) in planes parallel to the interface for the unoxidized (A) and oxidized (B) interface. The potential curve of the silicon substrate is on the right hand side (sinusoidal behavior), $SrTiO_3$ on the left hand side. The potential exhibits minima at the positions of atomic planes, maxima in the interstitial. In the $SrTiO_3$ region, the TiO_2 layers produce a deeper potential. At the interface both potential curves start to deviate. The important difference is the shift of the potential of interface B towards higher values by 1.1 V in the oxide region. This shift can be clearly observed at the extrema.

Si^- ions in the case of the initial interface, we now have formal Si^+ and O^{2-} ions which corresponds to creating an interfacial dipole relative to the initial interface. This dipole causes a shift of the electrostatic potential in the oxide to higher values by around 1.1 eV as seen in figure 5.18. As a result, also the band-structure of the oxide is shifted upwards and the oxidized interface therefore has a conduction band offset of 1.3 (= 0.2+1.1) eV, which is well within the technologically required range. A detailed description on how to obtain band offsets of hetero-junctions within DFT is given in appendix B.2.

In summary we succeeded in understanding metal deposition of groups II to IVa on silicon. In the case of Sr this has directly led to an understanding of the interface between silicon and $SrTiO_3$, a very promising candidate to replace SiO_2 as a gate dielectric. To the best of our knowledge, this is the first interface between silicon and a high-k oxide which has been unraveled. The interface between silicon and $SrTiO_3$ furthermore constitutes a new class of interfaces. It combines a covalently and an ionically bonded crystal and is thus conceptually different from the well-known Si–SiO_2 interface which consists of Si–O–Si bridges.

Chapter 6

Publications

This chapter contains the publications which have been written during the work on this thesis.

- Section 6.1:
  "The interface between silicon and a high-k oxide",
  Nature **427**, 53 (2004);
- Section 6.2:
  "First-principles calculations of strontium on Si(001)",
  Phys. Rev. B **69**, 75309 (2004);
- Section 6.3:
  "The chemistry of La on the Si(001) surface: ab-initio electronic structure calculations",
  Phys. Rev. B **70**, in press;
- Section 6.4:
  "Heteroepitaxial growth of high-k gate oxides on silicon: insights from first-principles calculations on Zr on Si(001)",
  Comp. Mat. Sci. **27**, 70 (2003);
- Section 6.5:
  "Electronic structure methods: Augmented Waves, Pseudopotentials and the Projector Augmented Wave Method",
  to appear in: Handbook of Materials Modeling; Volume 1: Methods and Models, Sidney Yip (Ed.); Kluwer Academic Publishers.

6.1 Nature 427, 53 (2004): The interface between silicon and a high-k oxide

This paper deals with the interface between silicon and $SrTiO_3$. Based on the understanding of Sr adsorption (compare publication 2) we propose an interface structure as well as a method to engineer the band-offsets between silicon and the oxide.

11. Pfeffer, P. Effect of inversion asymmetry on the conduction subbands in GaAs-$Ga_{1-x}Al_xAs$ heterostructures. *Phys. Rev. B* **59,** 15902–15909 (1999).
12. Lommer, G., Malcher, F. & Rossler, U. Spin splitting in semiconductor heterostructures for B → 0. *Phys. Rev. Lett.* **60,** 728–731 (1988).
13. Das, B., Datta, S. & Reifenberger, R. Zero-field spin splitting in a two-dimensional electron gas. *Phys. Rev. B* **41,** 8278–8287 (1990).
14. Luo, J., Munekata, H., Fang, F. F. & Stiles, P. J. Effects of inversion asymmetry on electron energy band structures in GaSb/InAs/GaSb quantum wells. *Phys. Rev. B* **41,** 7685–7693 (1990).
15. Dresselhaus, P. D., Papavassiliou, C. M. A., Wheeler, R. G. & Sacks, R. N. Observation of spin precession in GaAs inversion layers using antilocalization. *Phys. Rev. Lett.* **68,** 106–109 (1992).
16. Knap, W. *et al.* Weak antilocalization and spin precession in quantum wells. *Phys. Rev. B* **53,** 3912–3924 (1996).
17. Jusserand, B., Richards, D., Peric, H. & Etienne, B. Zero-magnetic-field spin splitting in the GaAs conduction band from Raman scattering on modulation-doped quantum wells. *Phys. Rev. Lett.* **69,** 848–851 (1992).
18. Nitta, J., Akazaki, T., Takayanagi, H. & Enoki, T. Gate control of spin-orbit interaction in an inverted $In_{0.53}Ga_{0.47}As/In_{0.52}Al_{0.48}As$ heterostructure. *Phys. Rev. Lett.* **78,** 1335–1338 (1997).
19. Kalevich, V. K. & Korenov, V. L. Effect of electric field on the optical orientation of 2D electrons. *JETP Lett.* **52,** 230–235 (1990).
20. Gossard, A. C. Growth of microstructures by molecular beam epitaxy. *IEEE J. Quant. Electron.* **QE-22,** 1649–1655 (1986).
21. Crooker, S. A., Awschalom, D. D., Baumberg, J. J., Flack, F. & Samarth, N. Optical spin resonance and transverse spin relaxation in magnetic semiconductor quantum wells. *Phys. Rev. B* **56,** 7574–7588 (1997).
22. Kikkawa, J. M. & Awschalom, D. D. Lateral drag of spin coherence in gallium arsenide. *Nature* **397,** 139–141 (1999).
23. Kikkawa, J. M. & Awschalom, D. D. Resonant spin amplification in *n*-type GaAs. *Phys. Rev. Lett.* **80,** 4313–4316 (1998).
24. Flatté, M. E. & Byers, J. M. Spin diffusion in semiconductors. *Phys. Rev. Lett.* **84,** 4220–4223 (2000).
25. La Rocca, G. C., Kim, N. & Rodriguez, S. Effect of uniaxial stress on the electron spin resonance in zinc-blende semiconductors. *Phys. Rev. B* **38,** 7595–7601 (1988).
26. Rashba, E. I. & Sheka, V. I. Combinational resonance of zonal electrons in crystals having a zinc blende lattice. *Sov. Phys. Solid State* **3,** 1257–1267 (1961).
27. Rashba, E. I. & Efros, A. L. Orbital mechanisms of electron-spin manipulation by an electric field. *Phys. Rev. Lett.* **91,** 126405 (2003).
28. Kato, Y. *et al.* Gigahertz electron spin manipulation using voltage-controlled g-tensor modulation. *Science* **299,** 1201–1204 (2003).
29. Salis, G. *et al.* Electrical control of spin coherence in semiconductor nanostructures. *Nature* **414,** 619–622 (2001).
30. Gupta, J. A., Knobel, R., Samarth, N. & Awschalom, D. D. Ultrafast manipulation of electron spin coherence. *Science* **292,** 2458–2461 (2001).

Supplementary Information accompanies the paper on **www.nature.com/nature**.

Acknowledgements We thank A. M. Andrews, E. L. Hu, P. M. Petroff and J. S. Speck for discussions. This work was supported by the DARPA SPINS and QuIST programmes.

Competing interests statement The authors declare that they have no competing financial interests.

Correspondence and requests for materials should be addressed to D.D.A. (awsch@physics.ucsb.edu).

The interface between silicon and a high-*k* oxide

Clemens J. Först[1,2], Christopher R. Ashman[1], Karlheinz Schwarz[2] & Peter E. Blöchl[1]

[1]*Clausthal University of Technology, Institute for Theoretical Physics, Leibnitzstrasse 10, D-38678 Clausthal-Zellerfeld, Germany*
[2]*Vienna University of Technology, Institute for Materials Chemistry, Getreidemarkt 9/165-TC, A-1060 Vienna, Austria*

The ability of the semiconductor industry to continue scaling microelectronic devices to ever smaller dimensions (a trend known as Moore's Law[1]) is limited by quantum mechanical effects: as the thickness of conventional silicon dioxide (SiO_2) gate insulators is reduced to just a few atomic layers, electrons can tunnel directly through the films. Continued device scaling will therefore probably require the replacement of the insulator with high-dielectric-constant (high-*k*) oxides[2], to increase its thickness, thus preventing tunnelling currents while retaining the electronic properties of an ultrathin SiO_2 film. Ultimately, such insulators will require an atomically defined interface with silicon without an interfacial SiO_2 layer for optimal performance. Following the first reports of epitaxial growth of AO and ABO_3 compounds on silicon[3–7], the formation of an atomically abrupt crystalline interface between strontium titanate and silicon was demonstrated[8–10]. However, the atomic structure proposed for this interface is questionable because it requires silicon atoms that have coordinations rarely found elsewhere in nature. Here we describe first-principles calculations of the formation of the interface between silicon and strontium titanate and its atomic structure. Our study shows that atomic control of the interfacial structure by altering the chemical environment can dramatically improve the electronic properties of the interface to meet technological requirements. The interface structure and its chemistry may provide guidance for the selection process of other high-*k* gate oxides and for controlling their growth.

Interfacing a new oxide with silicon is a major challenge. A gate oxide has to fulfil a number of requirements in addition to intrinsic properties such as the high dielectric constant and low defect concentrations. The gate oxide must also be chemically stable in contact with silicon, it must have a sufficiently large injection barrier, and it must not have interface states in the bandgap of silicon. Oxides related to silicon dioxide, used in today's transistors, uniquely fulfil these requirements owing to their strong bonds to silicon and their flexible bonding network. They fail only because of their low dielectric constant. Retaining the same beneficial properties for high-*k* oxides has turned out to be very difficult. The first high-*k* oxides introduced technologically are likely to be amorphous oxides or silicates of Hf and Zr with an interfacial SiO_2 layer. By around 2010, however, the projected miniaturization of transistors will mean that an interfacial SiO_2 layer will no longer be tolerable and oxides with an atomically well-defined interface with silicon will be required.

Before discussing the formation of the interface, we need to review the clean (001) surface of silicon and describe its changes due to Sr adsorption. On the unreconstructed silicon surface the atoms form a square array. Owing to a lack of upper bonding partners, each atom has two singly occupied dangling bonds pointing out of the surface. Pairs of silicon atoms dimerize, using up one dangling bond per atom to form the dimer bond. This is called the 'dimer row' reconstruction. A second rearrangement leads to the 'buckled dimer' reconstruction, in which one atom of each dimer lifts up and the other shifts down, resulting in a buckled dimer. This buckling causes both electrons to localize in the upper silicon atom of a dimer, whereas the other silicon atom with the empty dangling bond prefers a more planar arrangement.

By depositing various amounts of Sr atoms onto the Si(001) surface we explored the structural complexity of Sr adlayers[11]. This enables us to attribute atomic structures to the periodicities observed experimentally[10,12]. Here we summarize only the findings relevant for the present topic: initially each Sr atom donates two electrons into the empty dangling bonds of the surface. As Sr is added, the dimer buckling vanishes because both dangling bonds of a Si dimer become filled with electrons. Similar to Ba (refs 13, 14), Sr first occupies the trough between the dimer rows, in the centre of four dimers. At a coverage of half a monolayer all positions in the trough are occupied and each dimer dangling bond is filled with two electrons. This (2×1) structure is the only Sr-covered surface without surface states in the bandgap of silicon. Therefore, it is a suitable building block for an interface without states in the gap, as required for device applications. The finding of a sizeable bandgap also explains why this surface is fairly resistant to oxidation[15].

Thus we found that the substrate surface can be chemically

saturated by half a monolayer of Sr. Such a surface is 'isoelectronic' to an H-terminated silicon surface. Hydrogen is known to be very effective at passivating silicon. In the following, we therefore refer to the Si surface covered with half a monolayer of Sr as the Sr-passivated substrate.

After having gained insight into the metal overlayers, we investigated the formation of an oxide layer. We start from the Sr-passivated substrate and simulate the deposition of one layer of SrO. During a heating cycle to 600 K this single oxide layer reconstructs significantly. However, after placing two or more layers of SrO or $SrTiO_3$ on top of the reconstructed SrO layer, the oxide layers crystallize into the perfect bulk structure. Thus we obtain an atomically abrupt interface between the silicon substrate and the high-*k* oxide. This interface structure, denoted A and shown in Fig. 1, corresponds to the Sr-passivated silicon surface matched to the nonpolar SrO layer of the oxide.

After the chemical saturation of the substrate surface with half a monolayer of Sr, the second-most-important property is the matching of the charge patterns of the oxide and the Sr-passivated substrate surfaces joined at the interface. Whereas the SiO_2/Si interface relies on strong covalent bonds across the interface and a flexible bond network of the oxide, the interface described here is based on the chemical saturation of the silicon surface with an alkaline earth metal, so that a template for the deposition of a matching oxide is obtained.

In a device the interface is exposed to a number of chemical influences that affect the stability of the stack. The most critical question is the stability of the interface with respect to oxidation. Oxygen ions can diffuse out of the gate oxide to the interface.

To explore how the interface changes upon oxidation, we have added oxygen atoms to a wide range of different sites. Oxygen first attacks the surface silicon atoms at their vacant coordination sites. After introducing one monolayer of oxygen into the interface all these sites are consumed. The resulting structure, denoted B, is shown in Fig. 1. Additional oxygen atoms, up to a total oxygen content of 1.5 monolayers, insert into the dimer bonds. As explained below, structure B and the dimer-oxidized variant of structure B are the optimum choices for device applications.

Figure 2 illustrates the phase boundaries of the interfaces as a function of the oxygen chemical potential. The chemical potential is defined as the energy required to add a single oxygen atom to the system. It is the driving force for oxidation, which can be controlled externally, for example, by choosing the appropriate temperature

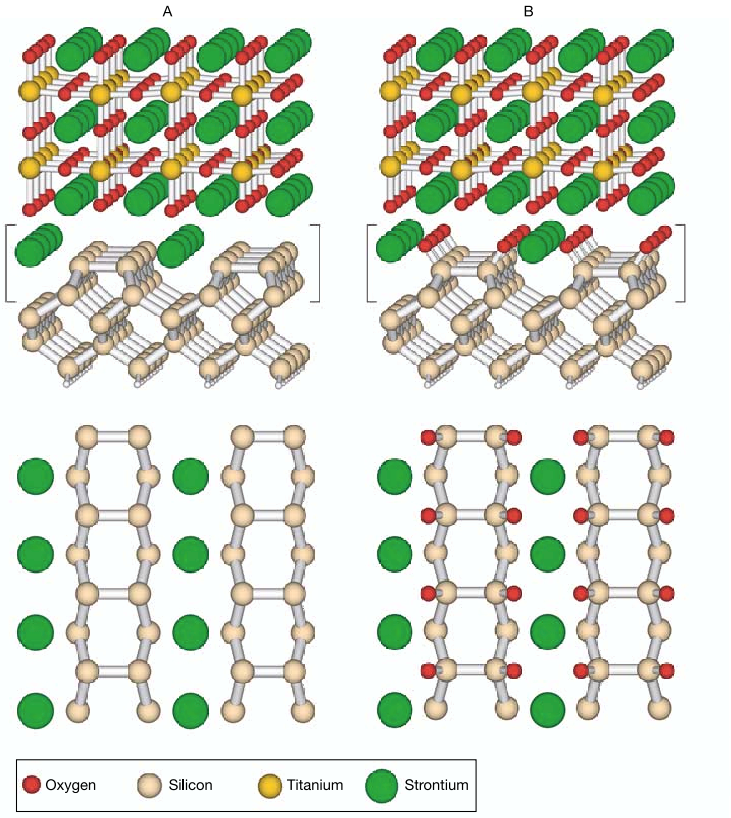

Figure 1 Atomic structures of the $SrTiO_3$/Si(001) interfaces: structure A (on left), unoxidized interface; structure B (on right), oxidized interface. Top, view slightly off the [110] direction of silicon, which is parallel to the [100] direction of the oxide. The topmost layer corresponds to the oxide surface of our slab calculation. Bottom, view along the interface normal of the interface layer.

and oxygen partial pressure during growth. In thermal equilibrium the chemical potential is related to the partial pressure and temperature of the growth chamber. It should be noted, however, that the formation of the stack mostly involves non-equilibrium processes, so that the chemical potential at the interface lags behind the value reached in the growth chamber. The oxygen chemical potential needs to be sufficiently low to avoid formation of an interfacial SiO_2 layer but high enough to avoid a large oxygen vacancy concentration in the gate oxide, which may cause trap-assisted leakage currents.

Our results indicate that structures A and B can be formed selectively in the absence of an interfacial SiO_2 layer. The processing window—the stability region of interface B—extends from −0.24 to 0.05 eV and corresponds to a range of partial pressures of nearly three orders of magnitude at 1,000 K. This region lies almost entirely below the coexistence line of Si and SiO_2.

In addition, we find indications of sizeable thin-film effects, which delay the formation of an interfacial SiO_2 layer. This can be inferred from the fact that the oxidation of all dimer bonds requires a chemical potential of 0.19 eV, and subsurface oxidation starting from interfaces A or B requires energies in excess of 0.91 eV above the coexistence line of Si and SiO_2.

The interface structure proposed in this work is quite different and much simpler than previously assumed: it was believed that an interfacial silicide[8,9] or silicate[16,17] layer must be formed. Such a layer is not present in the interface that emerged from our simulations. Nevertheless, our simulated $SrTiO_3$/Si(001) interfaces reproduce the undisputed features of the *Z*-contrast images of ref. 8, such as the pattern of interfacial Sr atoms and the oxide-substrate registry. Thus the lateral alignment of the columns of Sr and Ti atoms relative to the Si substrate and the (2×1) periodicity can clearly be identified.

We also performed calculations on the interfaces proposed by McKee and co-workers[8,9,10] and by Wang and co-workers[16,17]. As also shown previously[18], the former interface[8,9] is metallic, which is detrimental for device applications. The same applies for the latter structural proposal[16,17], which reconstructs significantly upon relaxation.

On the basis of electron-count arguments, Robertson and Peacock recently proposed a structure[18] that is related to our dimer-oxidized variant of structure B. It differs in that the oxide starts with the TiO_2 layer instead of a SrO layer and it is derived from a $c(2 \times 2)$ dimer reconstruction of the silicon surface. If we modify our interface by terminating the oxide with a TiO_2 layer instead of a SrO layer, it is more stable than Robertson's proposal by 0.19 eV per (1×1) surface unit cell. Having an oxide terminated by SrO is, however, favourable compared to TiO_2 terminated oxides, because the TiO_2 layer and the substrate in direct contact are expected to react, as pointed out[18]. Conceptually similar interfaces with a TiO_2 interface layer have been investigated[19], ruling out their use in devices on the basis of their electronic properties.

A critical parameter for gate stacks is the injection barrier, which is the offset between the conduction band edges of the silicon substrate and the oxide. It prevents electrons from entering the oxide conduction band, where they can cross the gate oxide. For device applications the injection barrier should be larger than 1 eV (ref. 3). There are indications[20,21] that the injection barriers for most high-*k* oxides are too low.

Before we discuss our results on the band offsets we need to briefly touch upon the bandgap problem of density functional theory (DFT)[22,23]: typically the one-particle energies obtained in these calculations underestimate the bandgap. Therefore, there is an uncertainty in our calculated injection barriers. Assuming that the error of the valence band edge is negligible, as required in exact DFT, and using the experimental bandgaps of silicon and $SrTiO_3$ (ref. 24), we anticipate that our calculations underestimate the injection barrier by 0.7–0.8 eV.

For interface A we obtain an injection barrier that is negative by 0.6 eV. Including our correction, we estimate the injection barrier to lie at 0.1–0.2 eV. The injection barrier lies below the technologically required minimum.

For interface B, however, we obtain a positive injection barrier of 0.5 eV. Adding the correction, our final estimate yields a positive injection barrier of 1.2–1.3 eV, which fulfils the criterion. The margin is sufficiently large that a reasonable error in the band-offset correction does not lead to an unacceptably low injection barrier. Most important is the ability to influence the injection barrier by carefully choosing the processing conditions.

Note that band offsets are frequently derived from the properties of the two bulk materials alone[21], disregarding the interface structure and composition in detail. The interface between silicon and $SrTiO_3$ is an example where the band offset can be engineered by controlling the chemical environment. The change of the band offset due to oxidation is about 1.1 eV, and is thus sizeable. It results from a dipole created when the electrons are transferred from the filled dangling bonds of the surface silicon atoms to the oxygen atoms that attach to the vacant coordination sites.

The injection barrier of interface B is fairly insensitive to additional oxidation of the dimer bonds. An amorphous interfacial SiO_2 layer is likely to destroy these restrictions and thus lead to a lower injection barrier. □

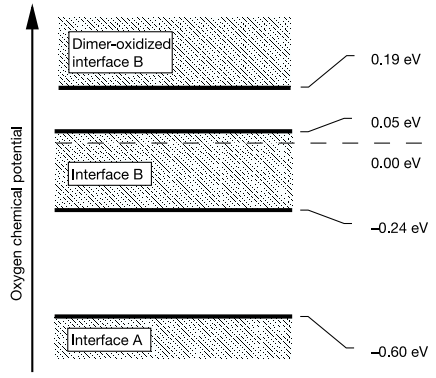

Figure 2 Phase diagram for interface oxidation. Shaded areas indicate the stability regions of the defect-free interfaces A and B and the dimer-oxidized variant of interface B. The blank regions separating them correspond to disordered structures with an oxygen content that increases with increasing chemical potential. The external parameter is the oxygen chemical potential. The zero of the chemical potential corresponds to the coexistence of bulk Si and SiO_2 (α-quartz) in thermal equilibrium.

Methods

We performed state-of-the-art electronic structure calculations and *ab initio* molecular dynamics simulations[25] based on density functional theory[22,23,26] and the projector augmented wave method[27].

The calculations have been done on 5-layer slabs of silicon. The slab calculations included a vacuum region of at least 6 Å between repeated slabs. The relevant calculations of the interfaces are done in a (2×2) supercell. All structures are relaxed without symmetry constraints. The hydrogen-terminated silicon back plane has been kept frozen.

Our calculations used a plane wave cutoff of 30 Ry for the plane wave part of the wave function. We used the frozen-core approximation. Semi-core states of Sr and Ti have, however, been treated as valence electrons. We used the following sets of projector functions per angular momentum: 2*s*2*p*1*d* for oxygen, 2*s*2*p*1*d* for silicon, 3*s*2*p*2*d* for strontium and 2*s*2*p*2*d* for titanium.

For all calculations of Sr adsorption we used a grid with about 64 lateral *k*-points per

(1 × 1) surface unit cell. For the interfaces we used a grid corresponding to 16 *k*-points per (1 × 1) unit cell. For metallic structures we used the Mermin functional with a temperature of 1,000 K and the extrapolation to zero Kelvin proposed in ref. 28.

The band offsets have been derived by relating the plane wave part of the potential, averaged laterally, to band edges. The relative displacement between potential and band edges has been obtained from the epitaxially strained bulk materials.

The phase diagram in Fig. 2 was obtained from the total energies as a function of the oxygen chemical potential. A number of different, stoichiometric and non-stoichiometric, interface structures with varying oxygen content have been considered. The regions where one of the stoichiometric interfaces (A, B or the dimer-oxidized variant of B) is most stable are shaded. Tests for the upper boundary of interface A with larger, that is (4 × 4), unit cells confirmed that the phase boundaries obtained in (2 × 2) unit cell are reliable to about 0.03 eV.

Received 28 February; accepted 10 November 2003; doi:10.1038/nature02204.

1. Moore, G. E. Cramming more components onto integrated circuits. *Electronics* **38,** 114–117 (1965).
2. Semiconductor Industry Association. *International Technology Roadmap for Semiconductors* at ⟨http://public.itrs.net/⟩ (International SEMATECH, Austin, TX, 2001).
3. Ishiwara, H. & Azuma, K. Oriented growth of $SrTiO_3$ films on Si(100) substrates using in-situ cleaning by excited hydrogen. *Mater. Res. Soc.* **116,** 369–374 (1988).
4. Kado, Y. & Arita, Y. Heteroepitaxial growth of SrO films on Si substrates. *J. Appl. Phys.* **61,** 2398–2400 (1987).
5. Mori, H. & Ishiwara, H. Epitaxial growth of $SrTiO_3$ films on Si(001) substrates using a focused electron beam evaporation method. *J. Appl. Phys.* **30,** 1415–1417 (1991).
6. Kim, T. W. *et al.* Structural properties and interfacial layer formation mechanisms of $PbTiO_3$ thin films grown on p-Si substrates. *Appl. Phys. Lett.* **64,** 2676–2678 (1994).
7. Alexe, M. Measurement of interface trap states in metal ferroelectric silicon heterostructures. *Appl. Phys. Lett.* **72,** 2283–2285 (1998).
8. McKee, R. A., Walker, F. J. & Chisholm, M. F. Crystalline oxides on silicon: the first five monolayers. *Phys. Rev. Lett.* **81,** 3014–3017 (1998).
9. McKee, R.A. & Walker, F.J. Process for depositing an oxide epitaxially onto a silicon substrate and structures prepared with the process. US patent 5,225,031 (United States Patent Office, 1993).
10. McKee, R. A., Walker, F. J. & Chisholm, M. F. Physical structure and inversion charge at a semiconductor interface with a crystalline oxide. *Science* **293,** 468–471 (2001).
11. Ashman, C., Först, C. J., Schwarz, K. & Blöchl, P. E. First-principles calculations of strontium adsorption on Si(001). *Phys. Rev. B* **69** (in the press).
12. Fan, W. C., Wu, N. J. & Ignatiev, A. Observation of ordered structures of Sr on the Si(001) surface. *Phys. Rev. B* **42,** 1254–1257 (1990).
13. Yao, X. *et al.* Initial stages of Ba adsorption on the Si(100)-(2 × 1) surface at room temperature. *Phys. Rev. B* **59,** 5115–5119 (1999).
14. Wang, J. *et al.* Bonding and diffusion of Ba on a Si(001) reconstructed surface. *Phys. Rev. B* **60,** 4968–4971 (1999).
15. Liang, Y., Gan, S. & Engelhard, M. First step towards the growth of single-crystal oxides on Si: formation of a two-dimensional crystalline silicate on Si(001). *Appl. Phys. Lett.* **79,** 3591–3593 (2001).
16. Wang, J., Ooms, W. J. & Hallmark, J. A. Semiconductor structure having a crystalline alkaline earth metal oxide interface with silicon. US patent 6,238,459 (United States Patent Office, 2001).
17. Droopad, R. *et al.* Epitaxial oxides on silicon grown by molecular beam epitaxy. *J. Cryst. Growth* **227–228,** 936–943 (2001).
18. Robertson, J. & Peacock, P. W. Atomic structure, band offsets and hydrogen in high k oxide:silicon interfaces. *Mater. Res. Soc. Symp. Proc.* **747,** 99–111 (2002).
19. Zhang, X., Demkov, A. A., Li, H., Hu, X. & Wei, Y. Atomic and electronic structure of the $Si/SrTiO_3$ interface. *Phys. Rev. B* **68,** 125323 (2003).
20. Chambers, S. A. *et al.* Band offset and structure of $SrTiO_3/Si(001)$ heterojunctions. *J. Vac. Sci. Technol. A* **19,** 934–939 (2001).
21. Robertson, J. Band offsets of wide-band-gap oxides and implications for future electronic devices. *J. Vac. Sci. Technol. B* **18,** 1785–1791 (2000).
22. Hohenberg, P. & Kohn, W. Inhomogeneous electron gas. *Phys. Rev. B* **136,** 864–871 (1964).
23. Kohn, W. & Sham, L. J. Self-consistent equations including exchange and correlation effects. *Phys. Rev. A* **140,** 1133–1138 (1965).
24. Noland, T. A. Optical absorption of single-crystal strontium titanate. *Phys. Rev.* **94,** 724 (1954).
25. Car, R. & Parrinello, M. Unified approach for molecular dynamics and density-functional theory. *Phys. Rev. Lett.* **55,** 2471–2474 (1985).
26. Perdew, J. P., Burke, K. & Ernzerhof, M. Generalized gradient approximation made simple. *Phys. Rev. Lett.* **77,** 3865–3868 (1996).
27. Blöchl, P. E. Projector augmented-wave method. *Phys. Rev. B* **50,** 17953–17979 (1994).
28. Gillan, M. G. Calculation of the vacancy formation energy in aluminum. *J. Phys. Condens. Matter* **1,** 689–711 (1989).

Acknowledgements We thank S. Chambers, M. Chisholm, W. Daum, A. Dimoulas, J. Fompeyrine, J.-P. Loquet, R.A. McKee, G. Norga and S. Stemmer for discussions. This work has been funded by the European Commission in the project 'Integration of Very High-k Dielectrics with CMOS Technology' (INVEST) and by the AURORA project of the Austrian Science Fund. Parts of the calculations have been performed on the computers of the 'Norddeutscher Verbund für Hoch- und Höchstleistungsrechnen' (HLRN).

Competing interests statement The authors declare competing financial interests: details accompany the paper on **www.nature.com/nature**.

Correspondence and requests for materials should be addressed to P.E.B. (peter.bloechl@tu-clausthal.de).

High-latitude controls of thermocline nutrients and low latitude biological productivity

J. L. Sarmiento[1], N. Gruber[2], M. A. Brzezinski[3] & J. P. Dunne[4]

[1]*Atmospheric and Oceanic Sciences Program, Princeton University, Princeton, New Jersey 08544, USA*
[2]*IGPP and Department of Atmospheric Sciences, University of California at Los Angeles, Los Angeles, California 90095, USA*
[3]*Department of Ecology, Evolution and Marine Biology and the Marine Science Institute, University of California, Santa Barbara, California 93106, USA*
[4]*NOAA/Geophysical Fluid Dynamics Laboratory, PO Box 308, Forrestal Campus B Site, Princeton, New Jersey 08542, USA*

The ocean's biological pump strips nutrients out of the surface waters and exports them into the thermocline and deep waters. If there were no return path of nutrients from deep waters, the biological pump would eventually deplete the surface waters and thermocline of nutrients; surface biological productivity would plummet. Here we make use of the combined distributions of silicic acid and nitrate to trace the main nutrient return path from deep waters by upwelling in the Southern Ocean[1] and subsequent entrainment into subantarctic mode water. We show that the subantarctic mode water, which spreads throughout the entire Southern Hemisphere[2,3] and North Atlantic Ocean[3], is the main source of nutrients for the thermocline. We also find that an additional return path exists in the northwest corner of the Pacific Ocean, where enhanced vertical mixing, perhaps driven by tides[4], brings abyssal nutrients to the surface and supplies them to the thermocline of the North Pacific. Our analysis has important implications for our understanding of large-scale controls on the nature and magnitude of low-latitude biological productivity and its sensitivity to climate change.

The classical explanation for the observed nutrient distribution of the ocean in the low latitudes is that the downward flux of biogenic material from the surface of the ocean is balanced by upwelling of dissolved inorganic nutrients driven by vertical mixing in the main thermocline. This essentially one-dimensional view grew out of early theories of thermocline and thermohaline circulation that are no longer tenable. Estimates of the magnitude of vertical mixing in the main thermocline are about an order of magnitude smaller than required to explain the vertical profiles of tracers within this feature[5]. In addition, ocean model simulations of radiocarbon distribution show that balancing the formation of deep waters by upwelling through the main thermocline gives results that are inconsistent with observations[1]. Instead, these studies suggest that a more likely return path for the deep water to the surface is in the Southern Ocean[1].

Subantarctic Mode Water (SAMW) has been identified as the main conduit of nutrients from the Southern Ocean to the upwelling regions of the equatorial Pacific and off South America[6]. The SAMW is a pycnostad (a layer of relatively uniform density) that originates in the thick wintertime mixed layers that ring the Southern Ocean[7] (Fig. 1d). This belt, which is particularly strong eastward of the central Indian Ocean to the western South Atlantic, coincides with the Subantarctic Zone (SAZ) between the Subtropical Front at about 40–45° S and the Subantarctic Front at about 45–55° S, and appears to also include the Polar Front Zone (PFZ) between the Subantarctic Front and Polar Front just to the south (Fig. 1d). The SAMW pycnostad increases in density from $\sigma_\theta = 26.5$ (equivalent to $1{,}026.5\,kg\,m^{-3}$) in the western Atlantic to $\sigma_\theta = 27.1$ in the southeast Pacific[8] as it flows in an eastward circuit around the Southern Ocean.

6.2 Phys. Rev. B 69, 75309 (2004): First-principles calculations of strontium on Si(001)

This publication provides a consistent picture of the chemistry of Sr on the Si(001) surface. Starting from an isolated Sr ad-atom, we explore the adsorption structures up to a coverage of 4/3 ML and propose a surface phase-diagram which is compatible with recent experimental results.

PHYSICAL REVIEW B **69**, 075309 (2004)

First-principles calculations of strontium on Si(001)

Christopher R. Ashman,[1] Clemens J. Först,[1,2] Karlheinz Schwarz,[2] and Peter E. Blöchl[1,*]
[1]*Clausthal University of Technology, Institute for Theoretical Physics, Leibnizstraße 10, D-38678 Clausthal-Zellerfeld, Germany*
[2]*Vienna University of Technology, Institute for Materials Chemistry, Getreidemarkt 9/165-TC, A-1060 Vienna, Austria*
(Received 29 August 2003; published 17 February 2004)

This paper reports state-of-the-art electronic structure calculations on the deposition of strontium on the technologically relevant, (001) orientated silicon surface. We identified the surface reconstructions from $0-\frac{4}{3}$ monolayers and relate them to experimentally reported data. A phase diagram is proposed. We predict phases at $\frac{1}{6}$, $\frac{1}{4}$, $\frac{1}{2}$, $\frac{2}{3}$, and 1 monolayers. Our results are expected to provide valuable information in order to understand heteroepitaxial growth of a prominent class of high-K oxides around $SrTiO_3$. The insight obtained for strontium is expected to be transferable to other alkaline-earth metals.

DOI: 10.1103/PhysRevB.69.075309 PACS number(s): 68.43.Fg, 68.47.Fg, 71.15.Mb, 73.20.−r

I. INTRODUCTION

Device scaling has been the engine driving the microelectronics revolution as predicted by Moore's law.[1] By reducing the size of transistors, processors become faster and more power efficient at an exponential rate. Currently the main challenge in device scaling is the integration of high-K oxides as gate oxides into silicon technology.

The gate oxide is the dielectric of a capacitor, which is used to attract charge carriers into the channel region. Thus a current can flow from source to drain, provided a voltage is applied to the gate electrode. With a thickness[2] of only 1–2 nm the gate dielectric is the smallest structure of a transistor. As the thickness of the gate oxide is further reduced, its insulating property is lost due to direct tunneling through the ultrathin oxide. The results are intolerable leakage currents and a large power consumption.

A remedy to this problem is the replacement of the current SiO_2 based gate oxides with an insulator having a larger dielectric constant, a so-called high-K oxide. A high-K oxide gate with the same capacity as an ultrathin SiO_2 based one will be thicker and should therefore exhibit smaller leakage currents due to direct tunneling. The integration of new oxides into the semiconductor technology has, however, proven to be a major problem. Hence an enormous research effort is underway to understand growth of high-K oxides onto silicon.

Currently, HfO_2 and ZrO_2 are the main contenders for the first generation of high-K oxides to be introduced in fabrication. These oxides still exhibit an interfacial SiO_2 layer and therefore do not form a direct interface with silicon. As scaling proceeds, an interfacial SiO_2 layer cannot be tolerated anymore. The existence of an atomically abrupt interface between silicon and a high-K oxide has been demonstrated by McKee *et al.*[3,4] for $Ba_xSr_{1-x}TiO_3$ on Si(001), after an epitaxial relationship has been reported in the late 1980's.[5,6]

A detailed understanding of metal adsorption is crucial to control oxide growth on Si. The growth process is guided by the sequence of structures that develop as the metal is deposited on the silicon surface.[3] The nature of these structures as well as the interface between Si and a high-K oxide is, however, still under debate.

The adsorption of the alkaline-earth metals Sr and Ba on Si(001) has been extensively studied. Most of the studies of Sr on Si(001) are diffraction studies such as low-energy electron diffraction[7–12] (LEED) and reflection high-energy electron diffraction[13–16] (RHEED) or scanning tunneling microscopy[8,9,12] (STM) experiments. The STM studies have been most valuable because these contribute detailed real-space information on the atomic scale. Similar LEED,[17–19] RHEED,[20] and STM (Refs. 21–25) as well as x-ray photoemission studies[26,19] (XPS) have been performed for Ba. X-ray standing-wave experiments provide valuable restrictions on the structures with coverages of 1/2 and 1/3 monolayer (ML).[27] The photoemission[28,11] studies provide insight into the ionization state of Sr, and show a qualitative change of the Fermi-level pinning as a function of coverage.[11]

Diffraction studies suffer from the fact that these average over several structures and terraces. Here STM experiments provide valuable clues. One of the major experimental difficulties is the determination of the coverage at which the data are collected.[11]

Theoretical investigations of isolated Ba atoms adsorbed on Si(001) have been performed by Wang *et al.*[29]

In this work we address the deposition of Sr on Si(001) using state-of-the-art electronic structure calculations. We attempt to provide a complete set of adsorption structures, their energetics, chemical binding and electronic structure. We will categorize the reconstructions by pointing out the driving forces that lead to the various ordered structures. This provides a unified picture of Sr adsorption from low coverage up to 4/3 ML.

II. COMPUTATIONAL DETAILS

The calculations are based on density-functional theory[30,31] (DFT) using a gradient corrected functional.[32] The electronic structure problem was solved with the projector augmented wave method,[33] an all-electron electronic structure method using a basis set of plane waves augmented with partial waves that incorporate the correct nodal structure. The frozen core states were imported from the isolated atom. For the silicon atoms, we used a set with two projector functions per angular momentum for s and p character and one projector per angular momentum with d character. The hy-

drogen atoms of the back surface had only one *s*-type projector function. For strontium we treated the $4s$ and $4p$ core shells as valence electrons. Per angular momentum we used three *s*-type and two *p*- and *d*-type projector functions. The augmentation charge density has been expanded in spherical harmonics up to $\ell=2$. The kinetic-energy cutoff for the plane-wave part of the wave functions was set to 30 Ry and that for the electron density to 60 Ry.

A slab of five silicon layers was used as silicon substrate. Wang *et al.*[29] report that the adsorption energy of a Sr atom on the surface changes by 0.05 eV when between a 4-layer slab and a 6-layer slab of silicon. In our calculations the energy per additional silicon atom agrees to within 0.06 eV with that of bulk silicon between a 4-layer and a 5-layer slab. The dangling bonds of the unreconstructed back surface of the slab have been saturated by hydrogen atoms. The lateral lattice constant was chosen as the experimental lattice constant $a=5.4307$ Å of silicon,[34] which is 1% smaller than the theoretical lattice constant. Since we always report energies of adsorbate structures relative to the energy of a slab of the clean silicon surface, the lateral strain due to the use of the experimental lattice constant cancels out. The slabs repeat every 16 Å perpendicular to the surface, which results in a vacuum region of 9.5 Å for the clean silicon surface.

The Car-Parrinello *ab initio* molecular dynamics[35] scheme with damped motion was used to optimize the electronic and atomic structures. All structures were fully relaxed without symmetry constraints. The atomic positions of the back plane of the slab and the terminating hydrogen atoms were frozen.

Many of the Sr adsorption structures are metallic, which requires a sufficiently fine grid in k space. We used an equivalent to 8×8 points per (1×1) surface unit cell. This value has been chosen after careful convergence tests for surface structures, bulk silicon, and bulk Sr silicides (Fig. 1). In cases where this k mesh is incommensurate with the size of the unit cell we selected the closest, finer commensurate k mesh.

For metallic systems, the orbital occupations were determined using the Mermin functional[37] which produces a Fermi distribution for the electrons in its ground state. The electron temperature was set to 1000 K. In our case this temperature should not be considered as a physical temperature but rather as a broadening scheme for the states obtained with a discrete set of k points. The Mermin functional adds an entropic term to the total energy, which is approximately canceled by taking the mean of the total energy $U(T)$ and the Mermin-free energy $F(T)=U(T)-TS(T)$ as proposed by Gillan:[38]

$$U(T=0)\approx\tfrac{1}{2}[F(T)+U(T)]. \tag{1}$$

The forces are, however, derived from the free energy $F(T)$. Relaxation of the (3×1) 4/3 ML reconstruction at 0 K and 1000 K shows that the atomic positions at the two temperatures differ by less than 0.06 Å or 1.5% of the nearest-neighbor bond length.

In order to express our energies in a comprehensible manner, we report all energies relative to a set of reference energies. This set is defined by bulk silicon and the lowest-energy polymorph of $SrSi_2$ ($P4_332$). The reference energies are listed in Table I. The reference energy $E_0[\mathrm{Sr}]$ for a Sr atom, corresponding to the coexistence of bulk silicon and bulk $SrSi_2$, is extracted from the energy $E[\mathrm{SrSi_2}]$ of the disilicide calculated with a $(8\times8\times8)$ k mesh and the reference energy of bulk silicon $E_0[Si]$ as

$$E_0[\mathrm{Sr}]=E[\mathrm{SrSi_2}]-2E_0[\mathrm{Si}]. \tag{2}$$

The bulk calculation for silicon was performed in the two-atom unit cell with a $(10\times10\times10)$ k mesh and at the experimental lattice constant of 5.4307 Å.[34]

For the surface calculation, we always subtracted the energy of a clean (4×2) silicon surface of the same slab thickness, to account for the slab including hydrogen termination.

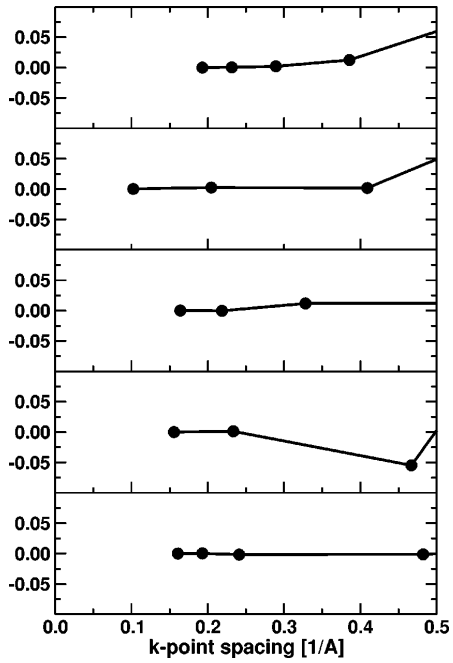

FIG. 1. *k*-point convergence: Energy in eV relative to the converged value vs characteristic *k*-point spacing (Ref. 36). From top to bottom: bulk silicon per atom; adsorption energy per Sr atom for a coverage of 1/2 ML; bulk silicides SrSi $Cmcm$, $SrSi_2I4_1/amd$, and $SrSi_2P4_332$ per atom. Our surface calculations used a *k*-point spacing of 0.2 Å^{-1} or the closest commensurate mesh.

TABLE I. Reference energies used in this paper without frozen core energy. See text for details of the calculation.

	Energy [H]
E_0 [Si]	−4.0036
E_0 [Sr]	−31.1441
E_0 [5-layer Si slab]	−21.1140
E_0 [4-layer Si slab]	−17.1083

For the surfaces with $\frac{1}{2}$ ML coverage of silicon we assumed that the corresponding reservoir for the silicon atoms is a silicon terrace. Hence, the reference energy for the 4.5 layer silicon slab is the average energy of a 4-layer slab and a 5-layer slab. The terrace energy itself does not enter the limit of an infinitely dilute step density.

In some of our structures the choice of unit cell has an impact on the dimer buckling. We estimated the energy of a buckling reversal from the energy difference of a (2×2) and a (5×2) supercell. The cell with an odd number of dimers contains one buckling reversal. The calculated energy for such a buckling reversal is 0.06 eV.

III. BULK SILICIDES

Before studying the adsorption of Sr on silicon, we investigated the bulk silicides of Sr. The energetics of bulk silicides provide us with the driving force to go from ordered surface structures to silicide grains on the surface. Our calculations on early transition metals on silicon indicate that silicide formation is a major problem for layer-by-layer growth of an oxide.[39]

The binding characteristics of the bulk silicides provide us with insight into the favored structural templates which might be anticipated for the Sr-covered silicon surface.

Sr silicides are typical Zintl compounds. According to the Zintl-Klemm concept,[40] atoms with an increased number of electrons form similar structures as atoms with the correspondingly increased atomic number. Consequently, a charge transfer of one electron to silicon will result in a preferred bonding environment similar to phosphorous with three or five covalent bonds. Addition of two electrons will result in chainlike structures like sulfur. After addition of three electrons, one anticipates formation of dimers and once four electrons are transferred, isolated ions are expected. In other words, for every added electron one covalent bond will be missing.

Due to the large difference in electronegativity, Sr formally donates its two valence electrons to the silicon substrate.

(1) In $SrSi_2$ one electron is transferred per silicon atom. Hence threefold coordinated silicon networks are formed as shown in the top two structures of Fig. 2.

(2) Two electrons are transferred in SrSi so that the silicon network is similar to that of elemental sulfur with two-coordinated silicon atoms forming Si chains as seen in the middle left panel of Fig. 2. The middle right panel shows another modification of SrSi. The average number of covalent bonds per silicon atom is, however, still 2.

(3) In Sr_5Si_3 there is a charge transfer of ten electrons to three silicon atoms, which can be used to form two Si^{3-} ions and one Si^{4-} ion. The two Si^{3-} combine to form dimers and the Si^{4-} is no more able to form covalent bonds. Hence we observe an equal number of Si dimers and single Si ions in the structure of Sr_5Si_3 as shown in the lower left panel of Fig. 2.

(4) In Sr_2Si four electrons are transferred to each silicon atom. As a consequence, the Si atoms in the structure on the bottom right of Fig. 2 do not form covalent bonds.

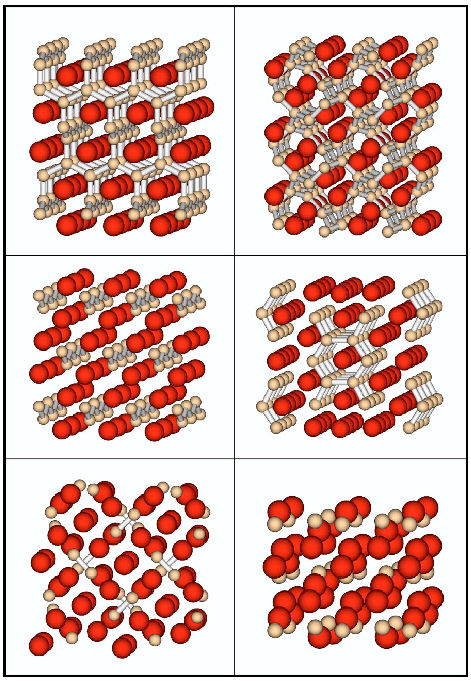

FIG. 2. (Color online) Bulk silicide structures. Top left, $SrSi_2(I4_1/amd)$ (Ref. 41); top right; $SrSi_2(P4_332)$ (Ref. 42); middle left, SrSi $(Cmcm)$ (Ref. 43); middle right, SrSi $(Immm)$ (Ref. 44); bottom left, $Sr_5Si_3(I4/mcm)$ (Ref. 45); bottom right, Sr_2Si $(Pnma)$ (Ref. 46). The large, dark (red) spheres represent Sr atoms; the smaller, light (beige) spheres represent Si atoms. Energies are listed in Table II.

We find $SrSi_2$ $(P4_332)$ to be the most stable phase of silicides per Sr atom (Table II). Therefore we have chosen this material to define, together with bulk Si, the reference energy for Sr.

As a side remark, we note that a lower energy of a Sr atom in a bulk silicide compared to the adsorbed Sr on the surface does not automatically indicate the formation of silicide grains during growth: The silicide formation may be suppressed by the strain due to an epitaxial constraint by the silicon lattice constant. Thus the formation of silicides is expected to be delayed for thin films, because the bulk sili-

TABLE II. Energies per Sr atom of bulk silicides relative to our reference energies.

	E [Sr] [eV]
$SrSi_2$ $(P4_332)$	0.00
$SrSi_2$ $(I4_1/amd)$	0.01
SrSi $(Cmcm)$	0.09
SrSi $(Immm)$	0.20
Sr_5Si_3 $(I4/mcm)$	0.39
Sr_2Si $(Pnma)$	0.45

cides have a large mismatch with the silicon substrate. This argument does not refer to the thermodynamic equilibrium of large samples, but it indicates that nucleation of silicide grains will have to overcome a large barrier.

IV. THE CLEAN SILICON SURFACE

The clean (001) silicon surface has a $c(4\times2)$ dimer-row reconstruction. We briefly summarize the driving forces towards this reconstruction in order to understand the adsorption structures of Sr on silicon.

An unreconstructed surface of silicon (001) is terminated by a square, (1×1) array of atoms. Each silicon atom on the surface is connected by two bonds to the subsurface. Consequently, there are two half-occupied dangling bonds on each silicon sticking out of the surface.

Each pair of surface silicon atoms forms a dimer bond which saturates one of the two dangling bonds on each atom. The dimers arrange in rows. This is the so-called (2×1) dimer-row reconstruction which results in an energy gain of 0.65 eV per (1×1) unit cell according to our calculations.

In a second reconstruction, both electrons in the dangling bonds localize on one atom of each dimer, resulting in a dimer buckling. The buckling is driven by the fact that an sp^3 hybridization is favored for a five-electron species such as the negative Si atom, while an sp^2 hybridization is favored for a three-electron species such as the positive silicon atom. The sp^2 hybridization in turn favors a planar bonding environment, whereas three-coordinated sp^3 bonded atoms form an umbrellalike environment. In the buckled-dimer row reconstruction, the electrons are localized on the atoms sticking out farthest from the surface. The dimer buckling can be considered as a Peierl's distortion which splits the half-filled energy bands resulting from the dimer bonds into a filled and an empty band, with a band gap in between. The energy gain due to this distortion is 0.12 eV per (1×1) cell.

The energies quoted here are in reasonable agreement with previously published local-density approximation pseudopotential calculations.[47] The dimer reconstruction can be considered to be fairly stable. Even at 1500 K only 3% of the dimer bonds are broken, as estimated from the Boltzmann factor with $\Delta E=0.65+0.12$ eV.

Two neighboring buckled dimer rows interact only weakly. We obtain an energy difference of 1.2 meV per dimer between the $c(4\times2)$ reconstruction with antiparallel buckling and the $p(2\times2)$ reconstruction with parallel buckling on neighboring dimer rows. This indicates that the buckling patterns of different rows are fairly independent of each other.

Within a row, however, the buckling of the dimers is coupled in an anticorrelated manner. This can, at least partly, be explained by the fact that the lower silicon atom of a dimer pushes the two adjacent subsurface silicon atoms apart. For the equivalent silicon atom of the next dimer, it is therefore favorable to be in the higher, sp^3-like configuration.[48]

There has been an intense debate as to whether there is dimer buckling or not. STM images reveal a 2×1 structure. They exhibit the buckling only at rather low temperatures and near defects. The theoretical predictions depend strongly on the approach chosen (cluster calculations with configuration interaction or density-functional calculations with periodic boundary conditions). The most conclusive results have been produced by quantum Monte Carlo simulations,[49] indicating that the buckling is present and density-functional calculations just overestimate the energy difference.

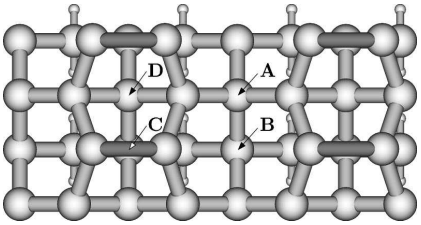

FIG. 3. Top view of the Si(001) surface and the four high-symmetry positions spanning the surface irreducible (2×1) unit cell. The dimer buckling is not shown. The energies are listed in Table III.

The fact that STM experiments cannot resolve the dimer buckling may be due to thermal averaging of the two buckled configurations. We believe that the mechanism is due to the migration of a solitonlike defect in the anticorrelated buckling pattern of a dimer row. The calculated energy for this defect is 0.06 eV (see Sec. II). Thus we predict a concentration of one such defect per 11 dimers at room temperature. Typical tunnel currents in STM experiments are around 1 nA, which corresponds to six electrons per nanosecond.

Thus even a soliton migration barrier as large as 0.05 eV would imply that the buckling changes once during the transfer of a single electron. These estimates should be taken with caution, since the small energy difference of 0.06 eV carries a large relative error bar.

From the comparison between DFT and quantum Monte Carlo calculations one can deduce an error bar of 0.05 eV per (1×1) unit cell due to electron correlations.[49] We verified that this correction does not qualitatively affect the findings reported in this paper.

V. ISOLATED Sr ON SILICON

In order to determine the low-coverage limit of Sr adsorption, we investigated the energy as a function of the lateral position of a Sr adatom on the surface. The total energy as a function of the lateral position of Sr is obtained by constraining the lateral movement of the Sr atom relative to the rigid back plane of the slab. The calculations were performed in a (4×4) surface supercell. We considered the high-symmetry points of the (2×1) surface shown in Fig. 3 and the midpoint between the local minima. The energies of the high-symmetry positions are given in Table III.

Sr has the global minimum at position **A** as defined in Fig. 3. Sr is located in the trench between the dimer rows and in the center of 4 surrounding dimers. The Sr atoms are slightly elevated above the plane of the surface dimers.

A metastable position, **D** of Fig. 3, is located in between two dimers on top of a dimer row. It is 0.29 eV higher in

TABLE III. Relative energies of isolated Sr on the Si(001) surface at the high-symmetry points of the surface irreducible unit cell as well as the **A**–**D** midpoint. The labels refer to Fig. 3.

Position	ΔE [eV]
A	0.00
B	0.55
C	0.75
D	0.29
A–**D** midpoint	0.61

energy than the global minimum. We will see that the structures **A** and **D** are repeating motifs in a range of different adsorption structures.

The diffusion of Sr on the silicon surface proceeds about equally fast parallel and perpendicular to the dimer rows, with a slight preference for the parallel direction. The diffusion barrier along the valley is equal to the energy difference between sites **A** and **B**, namely, 0.55 eV, the one across the row is 0.61 eV and is estimated by the midpoint between the sites **A** and **D**

It should be noted that in our analysis we ignored the reduced symmetry due to dimer buckling. As a result, different versions of the high-symmetry points quoted here exist with slightly different energies. For the structure **A**, we found two versions which differ in energy by 0.15 eV. In these cases the lowest-energy structure has been chosen.

In contrast to Sr, there has been a lot of work related to isolated Ba atoms adsorbed on Si(001).[29,21] Our results are in line with previous calculations for isolated Ba on Si(001).[29] We believe that both atoms behave in a similar fashion. Ba has been found mostly on sites **A** in the trenches, and also on sites **D** on top of the dimer rows. The main difference between Ba and Sr lies in the energy difference between the two metastable sites **A** and **D**. For Ba the difference is 0.88 eV (Ref. 29) which is substantially larger than 0.29 eV for Sr.

The chemical binding can be well understood in an ionic picture as suggested by the chemical binding of the silicides. The two electrons of the Sr atom are donated into an unoccupied dangling bond of a Si dimer. Interestingly we find this electron pair to be localized at a single dimer. This is evident from the dimer buckling, which vanishes when both dangling bonds are occupied.

The Sr atom experiences an additional electrostatic stabilization from the remaining three buckled dimers next to it. They are buckled such that the negative, and therefore raised, silicon atoms are located next to the Sr atom. The local configuration is shown in Fig. 4. This arrangement significantly affects the buckling of the two dimer rows adjacent to the Sr atom: (1) the buckling gets pinned and is therefore observed in STM images in the vicinity of a Sr atom whereas it is thermally averaged out on the bare surface; (2) the dimer buckling within one row is reversed as already pointed out by Wang *et al.*[29] This becomes apparent by looking at the row left to the Sr atom in Fig. 4.

From the static structure shown in Fig. 4 it is not evident why *both* dimer rows contain a buckling reversal as observed

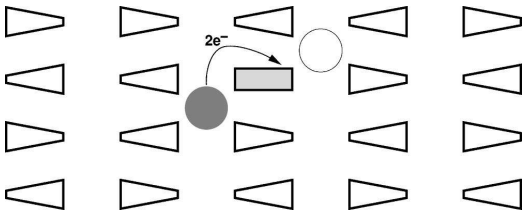

FIG. 4. Schematic representation of the isolated Sr adatom at position **A**. The filled circle represents the Sr adatom; the rectangle represents a filled and therefore unbuckled Si dimer. The triangles represent buckled dimers. The flat side of a buckled dimer indicates the upper Si atom with a filled dangling bond, whereas the pointed side indicates the lower Si atom with the empty dangling bond. The charge transfer from the Sr adatom to one of the surrounding dimers is indicated by the arrow; the preferred adsorption site (see Sec. VI) in the neighboring valley by the open circle.

in Fig. 1(b) of Yao *et al.*[21] We attribute the experimental observation to a dynamical effect: One electron pair can rapidly migrate from the filled dimer to one of the three buckled dimers next to the Sr adatom. If this fluxional motion occurs on a time scale faster than the time scale for a buckling reversal of the entire chain, the buckling will appear pinned in both dimer rows.

In our supercell with an even number of dimers in a row, every reversal of the buckling must be compensated by a second one, thus artificially destabilizing site **A**. This adds an uncertainty of up to 0.12 eV to all energies for the isolated Sr. Even taking this uncertainty into account, isolated Sr adatoms do not form a thermodynamically stable phase at any coverage as will be demonstrated in the following section.

VI. CHAIN STRUCTURES AT DILUTE COVERAGES

The Sr atoms on the surface tend to arrange in chains, as seen in the STM experiments.[8,9] Similar results have been obtained for Ba on Si(001).[22]

Our calculations predict random, single-chain structures up to a coverage of $\frac{1}{6}$ ML. Between $\frac{1}{6}$ ML and $\frac{1}{4}$ ML we find condensed, single- and double-chain structures. Above $\frac{1}{4}$ ML the multiple-chain structures convert into disordered arrays of double vacancies as will be discussed below. We investigated chain structures with coverages of $\frac{1}{16}$, $\frac{1}{10}$, $\frac{1}{8}$, $\frac{1}{6}$, $\frac{1}{4}$, $\frac{3}{10}$, $\frac{1}{3}$, $\frac{5}{14}$, and $\frac{6}{16}$ ML. We find an energy gain of 0.3–0.4 eV per Sr atom when single chains are formed from isolated Sr adatoms on **A** sites.

The chain formation is driven by the electrostatic attraction between the positively charged Sr ions, located at **A** sites, and the negatively charged dimers: An isolated Sr ion located at an **A** site, with the lone pairs of the four neighboring dimers pointing towards it, donates its two valence electrons into a silicon dangling bond adjacent to a neighboring valley. Thus it offers a preferred binding site for a Sr atom in that valley, namely next to this filled dangling bond as seen in Fig. 4. This second atom in turn donates its electron pair to the dimer row which does not already contain a negatively charged dimer and all four surrounding dimers will rearrange

to point their lone pairs towards the new adatom. This process continues to form chains of Sr atoms. The filled dimers are clearly identified by the absence of any buckling.

Two nearest Sr ions of one chain are displaced parallel to the dimer row by one lattice constant in order to position the filled dimer in between. Since the favorable Sr positions are staggered with respect to the dimers, the chains run at an angle of 30 deg relative to the direction of a dimer or 60 deg with respect to the dimer rows. The small energy difference of 0.02 eV per Sr ion between diagonal and zigzag chains at, e.g., $\frac{1}{8}$th ML cannot be considered as a hard number due to the systematic errors of DFT calculations. It does, however, indicate that the energy cost for changing the direction of such a chain is negligible so that these chains may meander on the surface.

As for the isolated Sr adatom, an additional stabilization occurs due to the dimer buckling of the surrounding silicon dimers. The negatively charged, raised part of an adjacent dimer is located next to the Sr ion, stabilized by electrostatic and covalent interactions. Reversing the buckling of one of the dimers next to a Sr ion raises the energy by 0.38 eV.[50] This ordering induces a freezing of the dimer buckling, which reaches far out into the clean silicon surface, as can be clearly seen in the STM images by Hu *et al.*[22]

At first sight one might think that there is a second preferred binding site in Fig. 4, right next to the initial adatom on the **A** site below the open circle. This configuration is, however, only possible for a pair of Sr atoms. A further continuation of such a chain perpendicular to the dimer row will make it impossible to rearrange dimers in a way that only filled dangling bonds are oriented towards the adatoms. Such chains are therefore destabilized with respect to diagonal or zigzag ones.

A favorable registry between two Sr chains is obtained if the Sr atoms are either in contact or separated by an even number of vacant **A** sites along each valley of the Si surface. This follows from a simple building principle which is an extension of what is already known from isolated chains.

(1) Each Sr atom is electrostatically stabilized by four negatively charged silicon atoms located next to it. Negative silicon atoms have two electrons in their dangling bond and are in a raised, sp^3-like bonding configuration. Violation of this rule raises the energy by 0.38 eV per empty dangling bond next to the Sr atom. At this level of abstraction we do not distinguish between a negatively charged Si atom of a buckled and an unbuckled dimer.

(2) There are no reversals of the dimer buckling in the Sr free regions on the surface. A buckling reversal increases energy by 0.06 eV. This is a consequence of the anticorrelated coupling of the dimer buckling within one row (see Sec. IV).

When the chains approach the shortest possible distance before they collapse into double chains, we obtain a partially ordered structure at $\frac{1}{6}$ ML as shown in Figs. 5(c) and 5(d). It should be noted that our calculations indicate that also the condensed chains at $\frac{1}{6}$ ML change their directions frequently, even though synchronized with the neighboring chains running in parallel.

As the coverage increases, Sr atoms arrange themselves into double chains as shown in Fig. 5(e), resulting in a partially ordered surface structure at $\frac{1}{4}$ ML. The "1×2" areas in Fig. 4 of Ojima *et al.*[24] can be explained by double chains at a $\frac{1}{4}$ ML. Their interpretation that buckled Ba dimers at $\frac{1}{2}$ ML coverage are responsible for this "wavy structure" cannot be supported by our calculations.

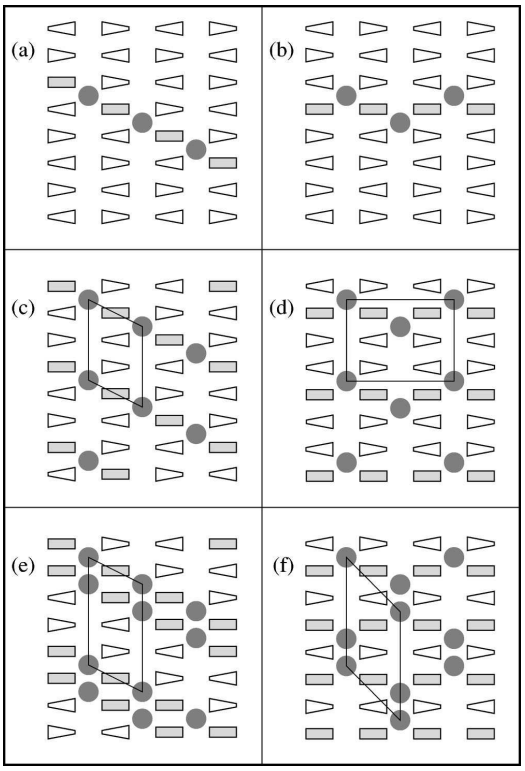

FIG. 5. Schematic representation of a set of chain structures. Isolated chains are shown in the top row. The ordered single-chain structures at 1/6 ML are shown in the middle row. The bottom row shows the ordered structures at $\frac{1}{4}$ ML. The left-hand side shows straight (diagonal) chains running at an angle of 60° to the dimer rows, while the right column shows zigzag chains perpendicular to the dimer rows. See Fig. 4 for a description of structural elements. The surface unit cells are outlined. The energies are listed in Table IV.

If we continue this building principle beyond $\frac{1}{4}$ ML, we will obtain sequences of triple, quadruple, etc., chains of Sr atoms separated by double vacancies. However, the positions of the double vacancies of different valleys are then only weakly correlated. Double vacancies of neighboring valleys can arrange themselves almost arbitrarily except that they do not line up perpendicular to the dimer rows. This implies a new building principle of double vacancies that do not necessarily arrange in chains. Note that a multiple-chain structure of Sr atoms can also be interpreted as a chain structure of double Sr vacancies. This building principle can already be observed in Figs. 5(e) and 5(f) for $\frac{1}{4}$ ML, which show that

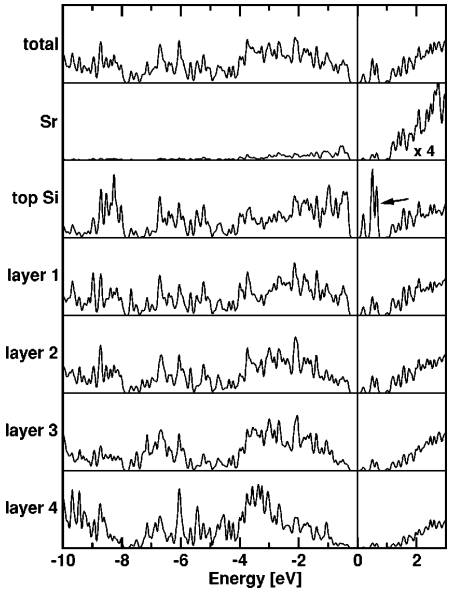

FIG. 6. Layer-projected density of states of the single-chain structure at 1/6 ML. Values are divided by the number of atoms in the layer. The vertical line at 0 eV indicates the Fermi level, the arrow points at the characteristic surface band in the band gap of silicon.

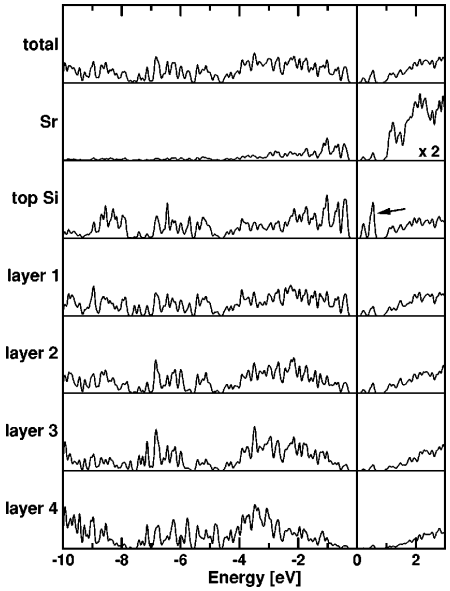

FIG. 7. Layer-projected density of states of the double-chain structure at $\frac{1}{4}$ ML. Values are divided by the number of atoms in the layer. The vertical line at 0 eV indicates the Fermi level, the arrow points at the characteristic band states in the band gap of silicon.

double vacancies in neighboring valleys can assume three out of four relative positions. While the energy difference between the structures in Figs. 5(e) and 5(f) is as small as 0.04 eV per Sr atom, it decreases further for the analogous structural patterns for wider Sr chains. For coverages close to $\frac{1}{2}$ ML, when the concentration of double vacancies is dilute, we therefore expect a nearly random arrangement of double vacancies instead of multiple chains.

TABLE IV. Energies per Sr adatom relative to our reference energies for all structures graphically represented in the figures unless not already tabulated elsewhere in the paper.

Sr coverage	Figure number	Energy/Sr [eV]
1/∞	5(a)	just schematic
1/∞	5(b)	just schematic
1/6	5(c)	−1.15
1/6	5(d)	−1.15
$\frac{1}{4}$	5(e)	−1.10
$\frac{1}{4}$	5(f)	−1.06
$\frac{1}{4}$	14 bottom	−0.30
$\frac{1}{4}$	14 top	0.44
$\frac{1}{2}$	9	−0.92
$\frac{2}{3}$	11 left	−0.74
1	10 left	0.04
1	10 right	0.08
1	11 right	−0.12
4/3	13	0.28

The reciprocal lattice vectors for the diagonal chain structures are $(\frac{1}{2},0)$ and $(\pm\frac{1}{2n},\frac{1}{n})$, where n is the periodicity of the the real-space unit cell [compare Figs. 5(c) and 5(e)] along the dimer-row direction. It should be noted that there is some structural disorder due to frequent changes in the chain direction. For zigzag chains the corresponding reciprocal lattice is spanned by the vectors $(\frac{1}{4},0)$ and $(0,\frac{1}{n})$. The actual diffraction pattern observed in experiment will contain a mixture of both reciprocal lattices.

The density of states of the single-chain structure at $\frac{1}{6}$ ML is shown in Fig. 6. The states on the Sr atom, which appear in the valence band, can be attributed to the tails of the Si dangling bonds, which hybridize with the Sr-*s* orbital. We observe states in the Si band gap, which are assigned to the empty dangling bonds on the buckled dimers. These states actually form a single band that is separated from the valence and conduction bands. The fact that they appear as individual states is an artifact of our discrete sampling of the Brillouin zone. This band pins the Fermi level in the lower part of the band gap. This feature remains nearly unchanged in the density of states of the double-chain structure at $\frac{1}{4}$ ML (Fig. 7). It disappears, however, with the absence of the half-occupied dimers at $\frac{1}{2}$ ML as seen in Fig. 8. Thus the gap states remain approximately in their position as the coverage increases, but the density of states is reduced. Hence the Fermi level will remain pinned in the lower part of the silicon band gap up to a coverage of $\frac{1}{2}$ ML. At this point the Fermi level becomes unpinned. In the following we will see that for coverages above $\frac{1}{2}$ ML states from the conduction band are pulled into

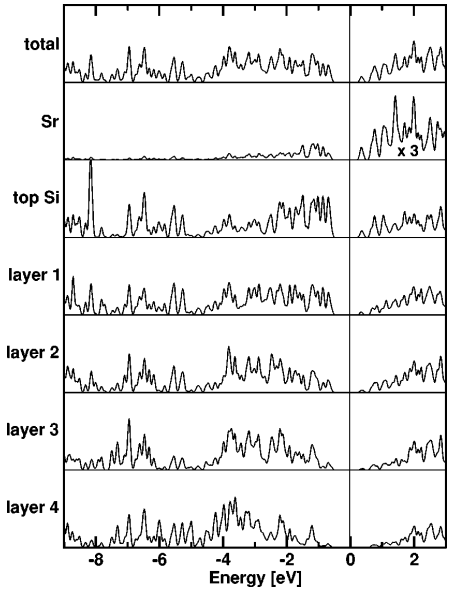

FIG. 8. Layer-projected density of states of the (2×1) structure at $\frac{1}{2}$ ML. Values are divided by the number of atoms in the layer. The vertical line at 0 eV indicates the Fermi level.

the band gap of silicon, and pin the Fermi level in the upper part of the band gap.

This finding explains the discontinuity of the band bending as observed by Herrera-Gomez *et al.*[11] Their XPS studies show that the Fermi level shifts up by almost 0.5 eV when the coverage is increased from below $\frac{1}{2}$ ML to above. However, it should be noted that such a discontinuity in Fermi-level pinning is not specific to detailed structures: also higher-energy structures exhibit a similar behavior.

VII. THE (2×1) RECONSTRUCTION AT $\frac{1}{2}$ ML

At a coverage of $\frac{1}{2}$ ML all dangling bonds of the surface dimers are fully occupied (Fig. 9). It can be considered as the canonical Sr covered Si surface. It is the only Sr covered surface structure without states in the band gap of silicon. This structure is "isoelectronic" to a hydrogen terminated silicon surface and is therefore expected to be comparably inert. The increased resistance to oxidation has already been observed experimentally.[12] A (2×1) reconstruction at $\frac{1}{2}$ ML has already been reported by several authors.[7,51,17,11,14]

This structural template has been proposed to be the basic

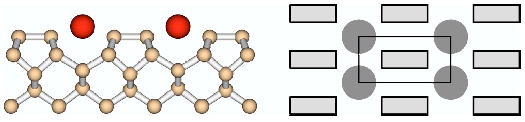

FIG. 9. (Color online) The (2×1) reconstructed surface at $\frac{1}{2}$ ML coverage. The energy is listed in Table IV.

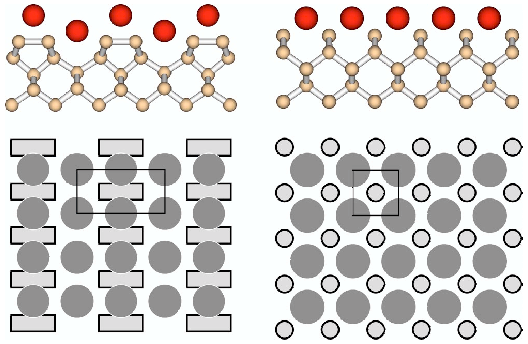

FIG. 10. (Color online) Building blocks for the surface structure with 1 ML coverage having a (2×1) (left) and a (1×1) (right) reconstruction. The outlined circles represent single Si atoms in the first layer. The energies are listed in Table IV.

building block of the interface between silicon and $SrTiO_3$.[52]

VIII. FROM $\frac{1}{2}$ ML TO 1 ML

For coverages between $\frac{1}{2}$ ML and 1 ML, we find structures built up from three structural templates: (1) the (2×1) reconstruction at $\frac{1}{2}$ ML (Fig. 9), (2) the (2×1) reconstruction at 1 ML (Fig. 10 left), and (3) the (1×1) reconstruction at 1 ML (Fig. 10 right)

When we increase the coverage above $\frac{1}{2}$ ML, the additional atoms occupy the **D** sites, since all **A** sites are already occupied. When all **A** sites and all **D** sites are occupied, as shown in the left panel of Fig 10, the coverage is that of 1 ML. At this coverage, two electrons are transferred to each silicon atom instead of only one as in the case of the $\frac{1}{2}$ ML. These electrons can fill the dimer antibonding states and thus break up the dimer bond. When all dimer bonds are broken at 1 ML, we obtain a (1×1) reconstructed silicon surface with a Sr ion above the center of each square of silicon atoms (Fig. 10 right). This structure is, however, never realized in its pure form due to the large strain in the top layer. An indication for the strain is the difference between the spacing of Sr atoms in bulk SrSi (Fig. 2) and that of this hypothetical surface structure. The former is larger by 25%. Nevertheless, this pattern is found as a building block in a number of low-energy structures between coverages of $\frac{1}{2}$ ML and 1

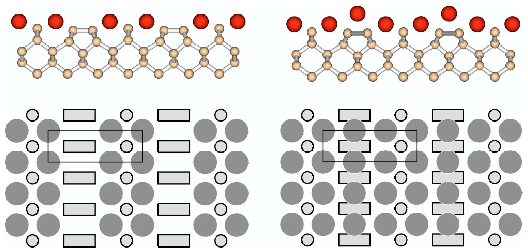

FIG. 11. (Color online) The (3×1) structures for coverages 2/3 ML (left) and 1 ML (right). Energies are listed in Table IV.

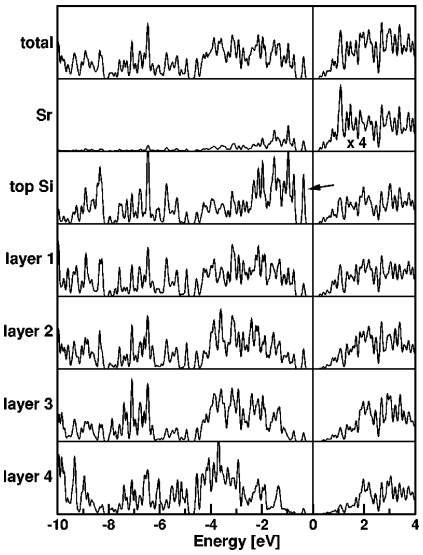

FIG. 12. Layer-projected density of states for the (3×1) surface at 2/3 ML coverage. Values are divided by the number of atoms in the layer. Note that the characteristic peak just below the Fermi level is not a single state, but the top of a surface band extending into the continuum of the valence band states. The vertical line at 0 eV indicates the Fermi level.

ML. The (1×1) reconstruction at 1 ML is unfavorable by 0.04 eV per Sr atom compared to the corresponding (2×1) structure.

By combining the (2×1) structure at $\frac{1}{2}$ ML (Fig. 9) and the (1×1) structure at 1 ML (right panel of Fig. 10), a series of structures with increasing coverage and periodicity can be formed: dimer rows are separated by stripes of the (1×1)/1 ML structure with increasing width. This leads to a series of $(n\times1)$ structures at a coverage of $\frac{(n-1)}{n}$ ML. We have investigated these structures from $n=3$ to $n=6$.

The first structure in the series is the 3×1 reconstructed surface at a coverage of $\frac{2}{3}$ ML shown in the left panel of Fig. 11. It consists of dimer rows separated by a stripe of two Sr atoms in the (1×1)/1 ML configuration. According to our calculations, this structure is present as a distinct phase between $\frac{1}{2}$ ML and 1 ML.

In order to form this structure the dimer row pattern needs to reconstruct. This process is facilitated by the additional electrons in the conduction band which weaken the dimer bonds: beyond a coverage of $\frac{1}{2}$ ML, Sr is likely to act as a catalyzer for dimer bond rearrangement.

The density of states for this (3×1) structure (Fig. 12) exhibits a surface band that ranges from the continuum of the valence band of bulk silicon into its band gap. The surface band is localized on the dangling bonds of the silicon dimers and the undimerized silicon atoms. The Fermi level is pinned between this band and the conduction band of silicon (see also discussion in Sec. VI).

For coverages greater than $\frac{2}{3}$ ML, that is, $n>3$, the structures can be interpreted as stripes with coverage of 1 ML with a (1×1) reconstruction separated by dimer rows without Sr, as discussed above. As the stripes with (1×1)/1 ML increase in width, they build up strain, which can be released by forming dimer rows with Sr atoms on top (Fig. 10 left). This corresponds to a transition between both 1 ML structures shown in Fig 10. Since the energy difference between these structural variants is smaller than 0.04 eV per Sr atom, it is likely that they do not form distinct phases but transform into each other in a fluxional fashion.

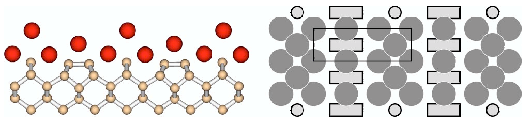

FIG. 13. (Color online) 4/3 ML coverage showing a 3×1 silicide layer. The energy is listed in Table IV.

At a coverage of 1 ML we find a series of structures built from the two structural templates in Fig. 10. In our calculations the (3×1) (Fig. 11) and (4×1) reconstructions are most stable and, within the theoretical error bar, degenerate. There is a slow increase in energy towards the (5×1) and (6×1) reconstructions which are less than 0.11 eV per Sr atom higher in energy.

IX. BEYOND 1 ML

Beyond 1 ML additional Sr atoms deposit on top of the silicon atoms in the (1×1) stripes. The first commensurate structure is the (3×1) structure at a coverage of $\frac{4}{3}$ ML shown in Fig. 13.

Fan *et al.* have observed a (3×1) reconstruction at a coverage of 1.3 ML, Bakhtizin *et al.*[8,9] have published STM images with a (3×1) periodicity for a coverage of 1.2 ML. There, alternating bright and dark stripes have been observed, which we attribute to the Sr atoms on top of the dimer rows (darker stripes) and those on top of the twofold coordinated Si atoms (more prominent stripes).

X. THE (3×2) STRUCTURE AT $\frac{1}{3}$ ML

Diffraction and STM studies identify a (3×2) reconstruction at $\frac{1}{3}$ ML.[7,51,8,9,19,22,27,12,23,24] The diffraction studies (LEED, RHEED) did not distinguish between the orientations parallel and perpendicular to the dimer rows as they average over multiple terraces. Most previous studies assumed that the $3\times$ direction of the (3×2) surface unit cell is orientated parallel to the dimer rows.[8,9,27,53] However, the STM images of Hu *et al.*[22] (Fig. 5) and Ojima *et al.*[24] (Fig. 4) clearly show that the $3\times$ axis is orthogonal to the dimer-row direction. This is particularly evident from the images showing the phase boundaries between the (3×2) reconstructed domains and chain structures. This observation implies that the dimer row pattern is disrupted.

Our lowest-energy structures for this coverage are variants of the quadruple chain as described in Sec. VI. We have been unable to determine a thermodynamically stable structure with a (3×2) diffraction pattern at $\frac{1}{3}$ ML.

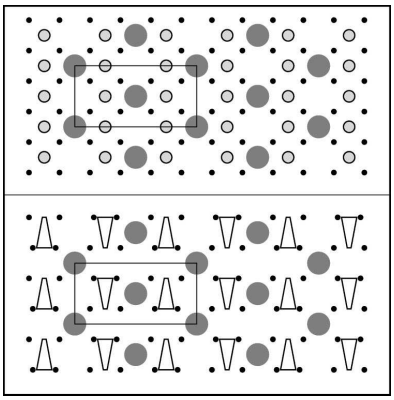

FIG. 14. Silicide structures with a $c(4\times2)$ reconstruction at $\frac{1}{4}$ ML: The $\frac{1}{4}$ ML $c(4\times2)$ structure as proposed by McKee *et al.* (Ref. 3) (top) and the lowest-energy structure we find for that chemical composition (bottom). The large dark circles correspond to Sr, the smaller, outlined ones to Si in the silicide layer (only in the top figure) and the small black dots to Si atoms in the first full layer. In the lower graph the Si atoms of the silicide layer have formed dimers indicated by the triangles. Energies are listed in Table IV.

Hu *et al.*[22] suggested two (3×2) structures for $\frac{1}{6}$ and $\frac{1}{3}$ ML. We simulated both of them and found them energetically unfavorable compared to the corresponding chain structures by more than 0.61 eV per Sr atom. Despite various other attempts, we failed to arrive at a thermodynamically stable surface structure with this reconstruction.

This failure may be attributed to our inability to scan the entire phase space. However, one should also consider the possibility of coadsorption of other elements such as hydrogen or oxygen, which may help to tie up the dangling bonds created by disrupting the dimer-row pattern. These effects have not been considered in the present study.

For the sake of completeness we also studied the model for the $\frac{1}{3}$ ML coverage with the $3\times$ direction parallel to the dimer row. It was lower in energy than the structures suggested by Hu *et al.*[22] Nevertheless, it turned out 0.23 eV per Sr atom higher in energy than the quadruple chain structure.

XI. $SrSi_2$ SURFACE LAYER

So far, we have discussed structures on a stoichiometric Si surface. The atomic model for the interface between Si and $SrTiO_3$ by McKee *et al.*,[3] which can be seen in the top panel of Fig. 14, has inspired us to also investigate reconstructions with only $\frac{1}{2}$ ML of silicon in the surface layer. Such a structure can, in principle, be formed by the migration of Si atoms or dimers from step edges onto the terraces. For a clean surface this process is clearly not energetically favorable. However, it cannot be excluded *a priori* that the presence of Sr stabilizes a surface with $\frac{1}{2}$ ML of silicon.

We started from the structure proposed by McKee *et al.*[3] which consists of $\frac{1}{4}$ ML of Sr and $\frac{1}{2}$ ML of Si. In this structure the Sr atoms occupy every second **A** site in the valleys,

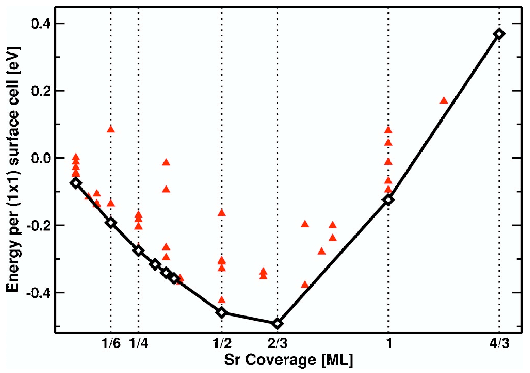

FIG. 15. (Color online) The adsorption energy (Ref. 55) per (1×1) unit cell as a function of Sr coverage. The open diamonds represent thermodynamically accessible structures, the triangles correspond to metastable structures.

while the Si atoms deposit on top of the center of four subsurface Si atoms. We restricted our search to the $c(4\times2)$ periodicity reported by McKee *et al.*

We find a number of metastable structures, the most stable one (Fig. 14 bottom) differs substantially from the proposal by McKee *et al.* The $\frac{1}{2}$ ML of silicon on the surface combines into dimers, a behavior already known from Si adatoms on Si(001).[54] The Sr atoms occupy positions in the center of four such dimers.

The energy of this structure is, however, still higher by 0.80 eV per Sr adatom than our lowest-energy structure at this coverage, namely, double chains of Sr atoms. The energy was evaluated relative to the average of a 4-layer and a 5-layer slab, representing a terrace. This energy thus describes the process of adsorption of Sr and the decomposition of two terraces into a single terrace with an additional $\frac{1}{2}$ ML of silicon.

We consider the difference in formation energy of 0.80 eV per Sr atom, relative to our lowest-energy structure at this coverage, as too large for this structure to be physically relevant.

XII. PHASE DIAGRAM

We now investigate which of the reported structures form at given experimental conditions. The thermodynamic stability is determined by the zero-Kelvin Gibbs free energy $G(\mu)=E-\mu N$, where E is the energy per Sr atom and N is the number of Sr atoms. μ is the chemical potential of the Sr atom relative to our reference energy for Sr. The extrinsic quantities, such as energies G and E, as well as the atom numbers are measured per (1×1) unit cell of the silicon surface. In Fig. 15 we show the adsorption energy E per (1×1) surface unit cell.

The thermodynamically stable phases are determined by connecting the points in Fig. 15 by line segments and forming the lower envelope. Each line segment corresponds to the coexistence of two phases, denoted by a and b, at the ends of the line segment with energies E_a and E_b and N_a and N_b Sr

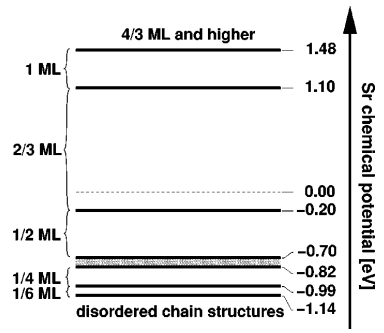

FIG. 16. One-dimensional phase diagram of Sr on Si(001) as a function of the Sr chemical potential. The shaded region between the $\frac{1}{4}$ and $\frac{1}{2}$ ML phases indicates disordered surface structures as described in Sec. VI. Above the dashed line at a chemical potential of 0 eV bulk Sr silicides are thermodynamically stable compared to surface structures.

atoms per (1×1) unit cell. For a coverage N per (1×1) unit cell between N_a and N_b, the energy is $E(N)=E_a+(E_b-E_a)/(N_b-N_a)(N-N_a)$. The slope of the line segment, namely, $\mu=dE(N)/dN=(E_a-E_b)/(N_a-N_b)$, is the chemical potential at which both phases a and b coexist. All structures not contributing to the lower envelope are not thermodynamically stable at low temperatures. At higher temperatures they may be stabilized due to entropic effects.

The one-dimensional phase diagram is shown in Fig. 16. The region in between two lines corresponds to the different surface phases. The lines indicate the coexistence of the two neighboring phases.

We find thermodynamically stable phases at $\frac{1}{6}$ ML and $\frac{1}{4}$ ML. We did not fully explore the phase diagram below $\frac{1}{6}$ ML. In this region we find single-chain structures as shown in Figs. 5(a) and 5(b). Entropic effects disorder the arrangement of chains at room temperature.

At $\frac{1}{4}$ ML we find an ordered structure of double chains. Beyond $\frac{1}{4}$ ML we predict nearly random arrangements of double vacancies. The double vacancy is stabilized relative to the single vacancy due to a favorable dimer buckling.

The structure at $\frac{1}{2}$ ML is a clear phase boundary for a wide range of chemical potentials.

The next phase boundary is found at a coverage of $\frac{2}{3}$ ML with a (3×1) reconstructed surface. Above $\frac{2}{3}$ ML there are a number of low-energy structures with various coverages and an $(n\times1)$ periodicity.

Within the phase region of the $\frac{2}{3}$ ML coverage, bulk Sr silicides become thermodynamically stable as indicated by the dashed line in Fig. 16. As mentioned above, we expect the onset of silicide formation to be significantly delayed due to thin-film effects as the bulk Sr silicides are highly incommensurate with the Si(001) substrate.

It is of interest to compare our phase diagram with that obtained by McKee *et al.*[16] At around 600 C they determine three line compounds at $\frac{1}{6}$ ML, $\frac{1}{4}$ ML, and $\frac{5}{8}$ ML. Our calculations reproduce phase boundaries at $\frac{1}{6}$ ML and $\frac{1}{4}$ ML. The next phase with a (3×1) diffraction pattern is seen at $\frac{5}{8}=0.625$ ML, which is close to the coverage of $\frac{2}{3}$, where our calculations predict a phase with the identical periodicity. The difference in coverage corresponds to a change by 1 in 16 adatoms or $\frac{1}{24}$ ML. This difference may be attributed to occasional Sr vacancies, which help to release strain. It seems surprising that no phase boundary is seen at $\frac{1}{2}$ ML. This may be due to the fact that, on the one hand, the (2×1) structure develops continuously out of the multiple chains structures below $\frac{1}{2}$ ML and, on the other hand, it can be transformed continuously into the (3×1) structure by introducing thin stripes with local coverage of 1 ML.

The multiplicity of structures with low energy above a coverage of $\frac{2}{3}$ ML suggests the presence of disordered structures at elevated temperatures. McKee reports incommensurate structures beyond a coverage of $\frac{5}{8}$ ML.[16]

A similar multiplicity of structures is found for 1 ML. Our calculation predicts a (3×1) structure as the most favorable. However, we find also (4×1), (5×1), and (6×1) reconstructions within a window of 0.11 eV per Sr atom.

We did not extend our calculations beyond $\frac{4}{3}$ ML, where an overlayer of metallic Sr is formed. Therefore, our data do not necessarily indicate the presence of a phase boundary at 4/3 ML.

XIII. CONCLUSIONS

In this paper we have investigated the surface structures of Sr adsorbed on Si(001) as a function of coverage. We propose a theoretical phase diagram by relating the phase boundaries at zero temperature to chemical potentials, which can be converted into partial pressure and temperature in thermal equilibrium. We predict phases at $\frac{1}{6}$ ML, $\frac{1}{4}$ ML, $\frac{1}{2}$ ML, $\frac{2}{3}$ ML, and 1 ML. Structural models are discussed for all experimentally observed reconstructions except a (3×2) reconstructed layer attributed to a coverage of $\frac{1}{3}$ ML. The models are explained in terms of structural templates and rationalized in terms of their electronic structure.

Our findings elucidate the chemistry of alkaline-earth metals on Si(001) and the phases of Sr on Si(001), which is expected to provide critical information for the growth of one of the most promising high-K gate oxides to date, namely, $SrTiO_3$.

ACKNOWLEDGMENTS

We thank A. Dimoulas, J. Fompeyrine, J.-P. Loquet, R.A. McKee, and G. Norga for useful discussions. This work was funded by the European Commission in the project "INVEST" (Integration of Very High-K Dielectrics with CMOS Technology) and by the AURORA project of the Austrian Science Fund. Parts of the calculations have been performed on the Computers of the "Norddeutscher Verbund für Hoch- und Höchstleistungsrechnen (HLRN)."

*Corresponding author. Email address: peter.bloechl@tu-clausthal.de

[1] G.E. Moore, Proc. SPIE **2438**, 2 (1995).
[2] International Technology Roadmap for Semiconductors, 2001 ed., http://public.itrs.net/
[3] R.A. McKee, F.J. Walker, and M.F. Chisholm, Phys. Rev. Lett. **81**, 3014 (1998).
[4] R.A. McKee, F.J. Walker, and M.F. Chisholm, Science **293**, 468 (2001).
[5] H. Ishiwara and K. Azuma, in *Heteroepitaxy on Silicon: Fundamentals, Structures, and Devices*, edited by H.K. Choi *et al.*, Mater. Res. Soc. Symp. Proc. **116** (Materials Research Society, Pittsburgh, 1988), p. 369.
[6] H. Mori and H. Ishiwara, Jpn. J. Appl. Phys., Part 2 **30**, L1415 (1991).
[7] W.C. Fan, N.J. Wu, and A. Ignatiev, Phys. Rev. B **42**, 1254 (1990).
[8] R.Z. Bakhtizin, J. Kishimoto, T. Hashizume, and T. Sakurai, Appl. Surf. Sci. **94/95**, 478 (1996).
[9] R.Z. Bakhtizin, J. Kishimoto, T. Hashizume, and T. Sakurai, J. Vac. Sci. Technol. B **14**, 1000 (1996).
[10] X. Hu, Z. Yu, J.A. Curless, R. Droopad, K. Eisenbeiser, J.L. Edwards, Jr., W.J. Ooms, and D. Sarid, Appl. Surf. Sci. **181**, 103 (2001).
[11] A. Herrera-Gomez, F.S. Aguirre-Tostado, Y. Sun, P. Pianetta, Z. Yu, D. Marshall, R. Droopad, and W.E. Spicer, J. Appl. Phys. **90**, 6070 (2001).
[12] Y. Liang, S. Gan, and M. Engelhard, Appl. Phys. Lett. **79**, 3591 (2001).
[13] R.A. McKee, F.J. Walker, J.R. Conner, and R. Raj, Appl. Phys. Lett. **63**, 2818 (1993).
[14] J. Lettieri, J.H. Haeni, and D.G. Schlom, J. Vac. Sci. Technol. A **20**, 1332 (2002).
[15] D.P. Norton, C. Park, Y.E. Lee, and J.D. Budai, J. Vac. Sci. Technol. B **20**, 257 (2002).
[16] R.A. McKee, F.J. Walker, M.B. Nardelli, W.A. Shelton, and G.M. Stocks, Science **300**, 1726 (2003).
[17] T. Urano, K. Tamiya, K. Ojima, S. Hongo, and T. Kanaji, Surf. Sci. **357-358**, 459 (1996).
[18] Y. Takeda, T. Urano, T. Ohtani, K. Tamiya, and S. Hongo, Surf. Sci. **402-404**, 692 (1998).
[19] X. Hu, C.A. Peterson, D. Sarid, Z. Yu, J. Wang, D.S. Marshall, R. Droopad, J.A. Hallmark, and W.J. Ooms, Surf. Sci. **426**, 69 (1999).
[20] R.A. McKee, F.J. Walker, J.R. Conner, E.D. Specht, and D.E. Zelmon, Appl. Phys. Lett. **59**, 782 (1991).
[21] X. Yao, X. Hu, D. Sarid, Z. Yu, J. Wang, D.S. Marshall, R. Droopad, J.K. Abrokwah, J.A. Hallmark, and W.J. Ooms, Phys. Rev. B **59**, 5115 (1999).
[22] X. Hu, X. Yao, C.A. Peterson, D. Sarid, Z. Yu, J. Wang, D.S. Marshall, R. Droopad, J.A. Hallmark, and W.J. Ooms, Surf. Sci. **445**, 256 (2000).
[23] K. Ojima, M. Yoshimura, and K. Ueda, Surf. Sci. **491**, 169 (2001).
[24] K. Ojima, M. Yoshimura, and K. Ueda, Phys. Rev. B **65**, 075408 (2002).
[25] K. Ojima, M. Yoshimura, and K. Ueda, Jpn. J. Appl. Phys., Part 1 **41**, 4965 (2002).
[26] C.P. Cheng, I.H. Hong, and T.W. Pi, Phys. Rev. B **58**, 4066 (1998).
[27] A. Herrera-Gomez, P. Pianetta, D. Marshall, E. Nelson, and W.E. Spicer, Phys. Rev. B **61**, 12 988 (2000).
[28] A. Mesarwi, W.C. Fan, and A. Ignatiev, J. Appl. Phys. **68**, 3609 (1990).
[29] J. Wang, J.A. Hallmark, D.S. Marshall, W.J. Ooms, P. Ordejon, J. Junquera, D. Sanchez-Portal, E. Artacho, and J.M. Soler, Phys. Rev. B **60**, 4968 (1999).
[30] P. Hohenberg and W. Kohn, Phys. Rev. **136**, B864 (1964).
[31] W. Kohn and L.J. Sham, Phys. Rev. **140**, A1133 (1965).
[32] J.P. Perdew, K. Burke, and M. Ernzerhof, Phys. Rev. Lett. **77**, 3865 (1996).
[33] P.E. Blöchl, Phys. Rev. B **50**, 17 953 (1994).
[34] R.C. Weast, *CRC Handbook of Chemistry and Physics*, 83rd ed. (CRC Press, Boca Raton, 2002), pp. 4–164.
[35] R. Car and M. Parrinello, Phys. Rev. Lett. **55**, 2471 (1985).
[36] The characteristic k point spacing for bulk crystals is calculated as $2\pi/(\Omega N_k)^{1/3}$, where Ω is the volume of the unit cell, and as $2\pi/(AN_k)^{1/2}$ for surfaces, where A is the area of the supercell. N_k is the number of k points per unit cell or supercell. The actual number of k points used in the calculation is reduced relative to N_k by exploiting time-inversion symmetry.
[37] N.D. Mermin, Phys. Rev. **137**, A1441 (1965).
[38] M. Gillan, J. Phys.: Condens. Matter **1**, 689 (1989).
[39] C.J. Först, K. Schwarz, and P.E. Blöchl, Comput. Mater. Sci. **27**, 70 (2003).
[40] E. Zintl, Angew. Chem. **52**, 1 (1939); W. Klemm, Proc. Chem. Soc. London, 329 (1958); E. Bussmann, Z. Anorg. Allg. Chem. **313**, 90 (1961).
[41] E.I. Gladyshevskii and P.I. Kripyakevich, Zh. Strukt. Khim. **6**, 148 (1966).
[42] G.E. Pringle, Acta Crystallogr., Sect. B: Struct. Crystallogr. Cryst. Chem. **B28**, 2326 (1972).
[43] A. Currao, J. Curda, and R. Nesper, Z. Anorg. Allg. Chem. **622**, 85 (1996).
[44] B. Eisenmann, H. Schaefer, and K. Turban, Z. Naturforsch. B **29**, 464 (1974).
[45] R. Nesper and F. Zuercher, Z. Kristallogr. - New Cryst. Struct. **214**, 19 (1999).
[46] A. Widera, B. Eisenmann, and H. Schaefer, Z. Naturforsch. B **31**, 520 (1976).
[47] A. Ramstad, G. Brocks, and P.J. Kelly, Phys. Rev. B **51**, 14 504 (1994).
[48] R.A. Wolkow, Phys. Rev. Lett. **68**, 2636 (1992).
[49] S.B. Healy, C. Filippi, P. Kratzer, E. Penev, and M. Scheffler, Phys. Rev. Lett. **87**, 016105 (2001).
[50] This energy is obtained from comparing the energies of single, diagonal chains at 1/16 ML with and without buckling reversal. Without introducing a buckling reversal, one positively charged Si atom points towards the Sr atom. A buckling reversal allows to surround the Sr adatoms exclusively by negative Si atoms. The total energy of the cell with the reversed buckling has been corrected by 0.06 eV as described above.
[51] W.C. Fan and A. Ignatiev, Surf. Sci. **253**, 297 (1991).
[52] C. J. Först, C. R. Ashman, K. Schwarz, and P.E. Blöchl, Nature (London) **427**, 53 (2004).
[53] R. Droopad, Z. Yu, H. Li, Y. Liang, C. Overgaard, A. Demkov, X. Zhang, K. Moore, K. Eisenbeiser, M. Hu, J. Curless, and J.

Finder, J. Cryst. Growth **251**, 638 (2003).
[54] A.P. Smith and H. Jonsson, Phys. Rev. Lett. **77**, 1326 (1996).
[55] The adsorption energy per (1×1) unit cell is defined as $E=\{(E[\text{supercell}]-nE_0[\text{m layer}-\text{Si}-\text{slab}]/l)-E_0[\text{Sr}]\}X$, where $E[\text{supercell}]$ is the total energy of the supercell used for the specific surface reconstruction, n is the number of (1×1) surface unit cells contained in that supercell, and m is the slab thickness in units of silicon layers of the supercell. l denotes the number of Sr atoms in the supercell and X the Sr coverage for that reconstruction. This energy can be alternatively calculated using the energy per Sr atom (see, e.g., Table IV) multiplied with the coverage X. The reference energies E_0 are listed in Table I.

6.3 Phys. Rev. B 70, in press: The chemistry of La on the Si(001) surface: ab-initio electronic structure calculations

This paper explores the adsorption structures of La on Si(001). We find that the La ad-atoms behave quite similarly to Sr at low coverages (compare publication 2). Above a coverage of 1/3 ML, La is in a 2+ oxidation state and behaves identically to Sr. The La adsorbate structures, however, are only thermodynamically stable up to a coverage of 1/3 ML.

The chemistry of La on the Si(001) surface from first principles

Christopher R. Ashman,[1] Clemens J. Först,[1 2] Karlheinz Schwarz[2] and Peter E. Blöchl,[1 *]
[1] *Clausthal University of Technology, Institute for Theoretical Physics, Leibnizstr.10, D-38678 Clausthal-Zellerfeld, Germany and*
[2] *Vienna University of Technology, Institute for Materials Chemistry, Getreidemarkt 9/165-TC, A-1060 Vienna, Austria*
(Dated: August 30, 2004)

This paper reports state-of-the-art electronic structure calculations of La adsorption on the Si(001) surface. We predict La chains in the low coverage limit, which condense in a stable phase at a coverage of $\frac{1}{5}$ monolayer. At $\frac{1}{3}$ monolayer we predict a chemically rather inert, stable phase. La changes its oxidation state from La^{3+} at lower coverages to La^{2+} at coverages beyond $\frac{1}{3}$ monolayer. In the latter oxidation state, one electron resides in a state with a considerable contribution from La-*d* and *f* states.

PACS numbers: 68.43.Fg, 68.47.Fg, 71.15.Mb, 73.20.-r

I. INTRODUCTION

Device scaling has been the engine driving the microelectronics revolution as predicted by Moore's law.[1] By reducing the size of transistors, processors become faster and more power efficient at an exponential rate. Currently the main challenge in device scaling is the integration of high-k oxides as gate oxides into silicon technology.

The gate oxide is an integral part of a metal-oxide-semiconductor field-effect transistor (MOSFET). It is the dielectric of a capacitor, which is used to attract charge carriers into the channel between source and drain, and thus switches the transistor between its conducting and its non-conducting state. With a thickness of approximately 1-2 nm,[2] the gate oxide is the smallest structure of a transistor. Further scaling would result in an unacceptably high quantum mechanical leakage current and thus a large power consumption.

In current transistors, the gate oxide is made from SiO_2 and SiO_xN_y. Future transistor generations will have to employ oxides with a higher dielectric constant (high-k). This allows greater physical thicknesses and thus reduces the quantum mechanical leakage currents. The main contenders for the replacement of SiO_2 in future transistors are, from today's point of view, oxides containing alkaline earth metals like Sr or Ba, third-row elements like Y or La, forth-row elements like Ti, Zr and Hf, or mixtures thereof. Prominent examples are perovskite structures around $SrTiO_3$[3] and $LaAlO_3$[4,5,6], fluorite structures like ZrO_2 and HfO_2[7] and also Y_2O_3 and La_2O_3[8,9] or pyrochlore structures like $La_2Hf_2O_7$[10] and $La_2Zr_2O_7$.[11,12] Recently, also promising results on Pr_2O_3 have been published.[13]

While the first high-k-oxides will be grown with an interfacial SiO_2 layer, a further reduction in scale requires high-k-oxides with a direct interface to silicon. The requirement to limit interface states, and the often crystalline nature of the oxides demand an epitaxial growth of the oxides on silicon. Considering layer-by-layer growth by molecular beam epitaxy (MBE), the first growth step for high-k oxides is the deposition of the metal on silicon. Therefore we have investigated deposition of metals out of the three most relevant classes for high-k oxides on Si(001). These are the divalent alkaline-earth metals and the three- and the four-valent transition metals. The results on adsorption of Zr and Sr have been published previously.[14,15] The present paper completes the study with a description of La-adsorption on Si(001) as example of a trivalent metal.

Our previous work has shown that Zr tends to form silicides readily.[14] Silicide grains have been observed after Zr sputtering on Si(001),[16] unless silicide formation is suppressed by early oxidation which, however, leads to interfacial SiO_2. The Sr silicides are less stable in contact with silicon and due to their sizable mismatch in lattice constant, nucleation does not proceed easily. The alkaline-earth metals Sr and Ba have been used in the first demonstration of an atomically defined interface between a high-k oxide, namely $SrTiO_3$ and silicon.[3] By following through the detailed steps of the formation of this interface, starting at the low-coverage structures of metal adsorption, we were able to provide a new picture for the phase diagram of Sr on Si(001).[15] The phase diagram has been important to link the theoretical interface structure of $SrTiO_3$ on Si(001) to the experimental growth process.[15,17,18] From the interface structure and its chemistry we could show in turn that the band-offset, a critical parameter for a transistor, can be engineered to match technological requirements by carefully controlling the oxidation of the interface.[17]

Since many of the characteristics of Sr adsorption carry over to La-adsorption let us briefly summarize the main results.[15] Sr donates its electrons to the empty dangling bonds of the Si-surface. The Si-dimers receive electron pairs one-by-one, and unbuckle as they become charged. When all Si dangling bonds are filled, i.e. beyond $\frac{1}{2}$ monolayer (ML), additional electrons enter the anti-bonding states of the Si-dimers at the surface, and thus break up the Si-dimer-row reconstruction.

At low coverage, Sr forms chains running at an angle of 63° to the Si-dimer rows. As the coverage increases,

the chains condense first into structures at $\frac{1}{6}$ ML and at $\frac{1}{4}$ ML, which are determined by the buckling of the Si-dimers and their electrostatic interaction with the positive Sr ions. At $\frac{1}{2}$ ML a chemically fairly inert layer forms, where all dangling bonds are filled and all ideal adsorption sites in the valley between the Si-dimer rows are occupied.

The paper is organized similar to our previous work on Sr adsorption. In Sec. II we describe the computational details of the calculation. In Sec. III and IV we review briefly the reconstruction of the Si(001) surface and we discuss the known bulk La silicides. Sec. V, VI and VII deal with the low coverage limit, where La adatoms form dimers and chain structures. Beyond the canonical coverage of 1/3 ML (Sec. VIII) we observe a change in the oxidation state of the La ad-atoms from 3+ to 2+ (Sec. IX). The results are placed into context in Sec. X where we propose a phase diagram for La on the surface. The computational supercells used for the simulation of the low-coverage structures are shown in the appendix.

II. COMPUTATIONAL DETAILS

The calculations are based on density functional theory[19,20] using a gradient corrected functional.[21] The electronic structure problem was solved with the projector augmented wave (PAW) method,[22,23] an all-electron electronic structure method using a basis set of plane waves augmented with partial waves that incorporate the correct nodal structure. The frozen core states were imported from the isolated atom. For the silicon atoms we used a set with two projector functions per angular momentum for s and p-character and one projector per angular momentum with d-character. The hydrogen atoms saturating the back surface had only one s-type projector function. For lanthanum we treated the $5s$ and $5p$ core shells as valence electrons. We used two projector functions per magnetic quantum number for the s, p, and f angular momentum channels and one for the d channel. The augmentation charge density has been expanded in spherical harmonics up to $\ell = 2$. The kinetic energy cutoff for the plane wave part of the wave functions was set to 30 Ry and that for the electron density to 60 Ry.

A slab of five silicon layers was used as silicon substrate. This thickness was found to be sufficient in previous studies on Sr adsorption.[15] The dangling bonds of the unreconstructed back surface of the slab have been saturated by hydrogen atoms. The lateral lattice constant was chosen as the experimental lattice constant $a = 5.4307$ Å of silicon,[24] which is 1 % smaller than the theoretical lattice constant. Since we always report energies of adsorbate structures relative to the energy of a slab of the clean silicon surface, the lateral strain due to the use of the experimental lattice constant cancels out. The slabs repeat every 16 Å perpendicular to the surface, which results in a vacuum region of 9.5 Å for the clean silicon surface.

The Car-Parrinello ab-initio molecular dynamics[25] scheme with damped motion was used to optimize the electronic and atomic structures. All structures were fully relaxed without symmetry constraints. The atomic positions of the backplane of the slab and the terminating hydrogen atoms were frozen.

Many of the adsorption structures are metallic, which requires a sufficiently fine grid in k-space. We used an equivalent to twelve by twelve points per (1×1) surface unit cell. Previous studies have shown that a mesh of eight by eight k-points is sufficient.[15] We have chosen a higher density here as this allows us to use commensurate k-meshes for $3\times$ and $2\times$ surface reconstructions.

For metallic systems, the orbital occupations were determined using the Mermin functional,[26] which produces a Fermi-distribution for the electrons in its ground state. The electron temperature was set to 1000 K. In our case this temperature should not be considered as a physical temperature but rather as a broadening scheme for the states obtained with a discrete set of k-points. The Mermin functional adds an entropic term to the total energy, which is approximately canceled by taking the mean of the total energy $U(T)$ and the Mermin-free energy $F(T) = U(T) - TS(T)$ as proposed by Gillan:[27]

$$U(T = 0) \approx \frac{1}{2}(F(T) + U(T)). \quad (1)$$

The forces are, however, derived from the free-energy $F(T)$. The resulting error has been discussed previously.[15]

In order to express our energies in a comprehensible manner, we report all energies relative to a set of reference energies. This set is defined by bulk silicon and the lowest energy silicide $LaSi_2$. The reference energies are listed in Tab. I. The reference energy E_0[La] for a La atom, corresponding to the coexistence of bulk silicon and bulk La, is extracted from the energy $E[LaSi_2]$ of the disilicide calculated with a $9 \times 9 \times 3$ k-mesh for the tetragonal unitcell with $a = 4.326$ and $c = 13.840$ and the reference energy of bulk silicon E_0[Si] as

$$E_0[\mathrm{La}] = E[\mathrm{LaSi_2}] - 2E_0[\mathrm{Si}]. \quad (2)$$

The bulk calculation for silicon was performed in the two atom unit cell with a $(10 \times 10 \times 10)$ k-mesh and at the experimental lattice constant of 5.4307 Å.[24]

For the surface calculations, we always subtracted the energy of a slab of the clean (4×2) silicon surface of the same layer thickness and backplane.

III. THE SILICON SURFACE

Before discussing the adsorption of La, let us briefly summarize the chemistry of the clean (001) surface

TABLE I: Reference energies used in this paper without frozen core energy. See text for details of the calculation.

	Energy [H]
E_0[Si]	-4.0036
E_0[La]	-32.1395
$E_0^{(1\times1)}$[5 layer-Si-slab]	-21.1139

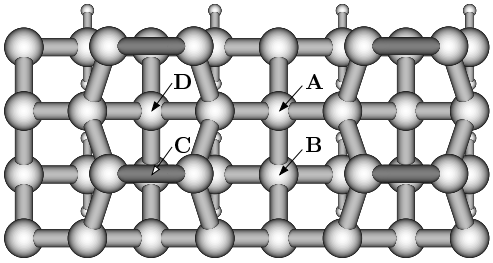

FIG. 1: Top view of the Si(001) surface and the four high symmetry positions spanning the surface irreducible (2×1) unit cell. The dimer buckling is not shown.

of silicon. A more detailed account has been given previously.[15]

On the unreconstructed silicon surface, the atoms form a square array. Due to a lack of upper bonding partners, each atom has two singly occupied dangling bonds pointing out of the surface. In order to avoid half-occupied bands, pairs of silicon atoms dimerize, using up one dangling bond per atom to form the dimer bond. This is called the dimer row reconstruction. Still, one dangling bond per silicon atom is half occupied, which drives the so-called buckled-dimer reconstruction: One atom of each dimer lifts up and the other shifts down, resulting in a "buckled" dimer. This buckling causes both electrons to localize in the upper, sp^3-like silicon atom of a dimer, whereas the other, sp^2-like silicon atom with the empty p-like dangling bond prefers a more planar arrangement.

Fig. 1 shows a ball stick model of the silicon surface and introduces the high-symmetry adsorption sites A to D, which we will refer to in the following discussion.

Filling the empty dangling bond with two electrons results in a removal of the buckling as observed in our studies on Sr adsorption.[15] As La has an odd number of valence electrons, we also examined the changes of the buckling upon filling the initially empty dangling bond with a single electron. While the difference in z coordinate of the two silicon atoms of a buckled dimer is 0.76 Å and the one of an unbuckled dimer 0.00 Å, it is 0.35 Å after donation of a single electron to a dimer. Thus the amplitude of the dimer buckling may be used as a measure for the electron count.

TABLE II: Energies per La atom of bulk silicides relative to our reference energies (Tab. I).

	E[La] [eV]
$LaSi_2$ ($I41\ amdS$)	0.00
LaSi ($Pnma$)	0.42
LaSi ($Cmcm$)	0.62
La_3Si_2 ($P4\ mbm$)	0.80

IV. BULK LA SILICIDES

In the case of Sr, the chemical interaction with silicon could be understoood by investigating the bulk Sr silicides.[15] All these structures could be explained by the Zintl-Klemm concept.[28] The electropositive Sr atoms donate their two valence electrons to the silicon atoms. Each accepted electron saturates one of silicon's four valences. A Si^- can thus form three covalent bonds, a Si^{2-} only two, a Si^{3-} only one and a Si^{4-} has a closed shell and does not form covalent bonds. This principle was found to also be valid for the surface reconstructions of Sr on Si(001).[15]

The Zr silicides on the other hand cannot be explained by the simple Zintl-Klemm concept.[14] The Zr d states also contribute to the bonding and thus retain a variable number of electrons.

Similarly, the La silicides cannot be simply explained by a quasi-ionic interaction with silicon. We find La in formal charge states between two and three (i.e. charge according to the Zintl-Klemm concept). Also the atom and angular momentum resolved density of states reveals, that La d states are partly occupied in these structures.

Fig. 2 shows the La silicides. $LaSi_2$ is the lowest energy silicide. The energies per La atom are listed in Table II.

V. AD-ATOMS AND LA DIMERS

Our search for the adsorption structures of La have been guided by the electron count rules that emerged from our investigation of Sr[15] adsorption on the same surface. The studies of Sr provided a consistent picture: The electrons from Sr are fully transfered into the Si-dimer dangling bonds of the Si substrate. The ordering of Sr atoms on the surface is determined by the electrostatic attraction between the Sr-cations and negatively charged Si-ions at the surface. The negative Si-ions are the raised atoms of buckled Si dimers and the atoms of filled, and thus unbuckled, dimers. This picture holds up to coverages where all Si-dimers are filled at 1/2 ML. Due to the different electron count of La as compared to Sr, we expect that the silicon dimers are filled already at a coverage of 1/3 ML and secondly we anticipate deviations from the above scheme.

Even though we predict La-chains to be the most stable structures in the low coverage limit, we first investigate

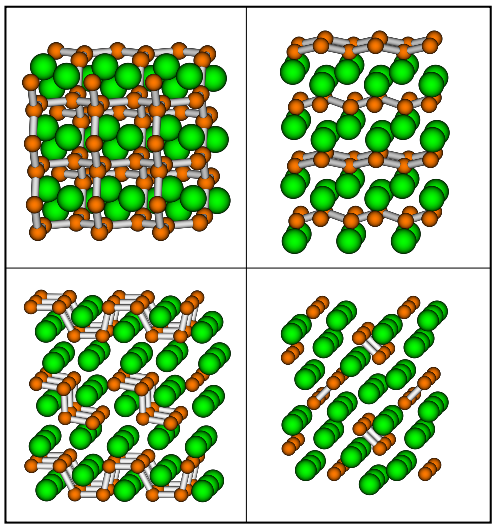

FIG. 2: (Color online) The bulk silicide structures. top left: $LaSi_2$ $I41$ $amdS$[29] (lowest energy structure); top right: LaSi $Pnma$;[30] bottom left: LaSi $Cmcm$;[31] bottom right: La_3Si_2 $P4$ mbm.[32]

isolated ad-atoms[33] and La-dimers in order to provide an understanding of the constituents of the more extended structures. Chain structures are more stable by 0.34-0.40 eV per La atom as compared to isolated ad-atoms.

Similar to Sr,[15] we find the most stable position of an isolated La atom at position A, in the center of four Si-dimers (compare Fig. 1). The position D, B and C have energies 0.23 eV, 0.51 eV and 1.70 eV higher than position A. A (4×4) supercell has been used for these calculations.

The diffusion barrier along the valley is equal to the energy difference between sites A and B, namely 0.52 eV, the one across the row is 1.31 eV and is estimated by the midpoint between the sites A and D.

The formation of La dimers lowers the energy per ad-atom by 0.10–0.18 eV compared to isolated ad-atoms. Due to the topology of the Si(001) surface, three different types of La-dimers can be formed: (1) orthogonal to the Si dimer rows, (2) parallel to the Si dimer rows and (3) diagonal to the Si dimer rows. All three structures are shown in Fig. 3. We find that the parallel La-dimer is lowest in energy, followed by the orthogonal and diagonal La-dimers. All La-dimers lie within a small energy window of 0.08 eV. Note, that we only investigated singlet states.

A pair of La atoms has six valence electrons and from the lessons learned from Sr adsorption, one would assume that three Si-dimers in the vicinity of the La-dimer get unbuckled. This is, however, not the case. Only two Si-dimers become fully unbuckled. The remaining two

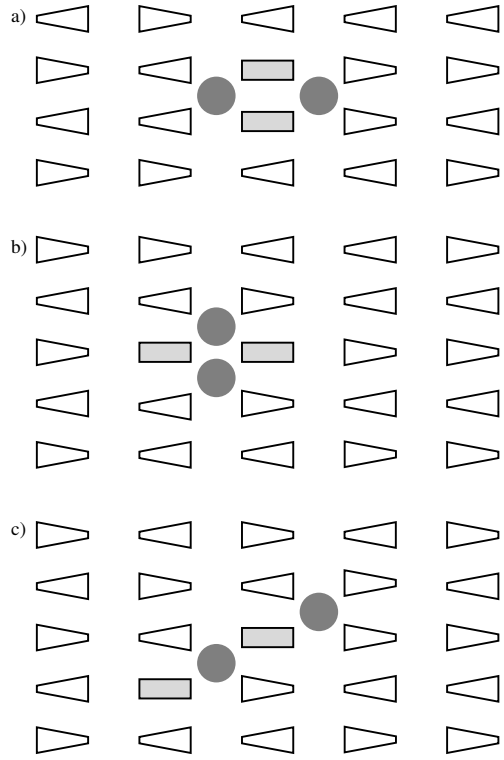

FIG. 3: Schematic representation of isolated La-dimers on the Si(001) surface. The filled circles represent the La ad-atoms, the rectangles represent a filled and therefore unbuckled Si-dimers. The triangles represent buckled Si-dimers. The flat side of a buckled dimer indicates the upper Si atom with a filled dangling bond, whereas the pointed side indicates the lower Si atom with the empty dangling bond. Only the Si-dimers which are clearly unbuckled have been drawn as rectangles. The partially unbuckled ones are represented by triangles (see discussion in section V). The supercells used for the total energy calculations are shown in Fig. 14.

electrons from the La-dimer enter into states that are derived from the upper dangling-bond band and which have an admixture of the La-d and f states.

Usually one can easily distinguish between buckled and unbuckled dimers. In the vicinity of La-dimers oriented diagonally or orthogonally, however, we also observe Si-dimers with an intermediate buckling amplitude. Thus, in these cases, the oxidation state of the La atom, namely 2+ versus 3+ cannot be attributed in a unique manner.

For the orthogonal and diagonal La-dimers we observe a tendency for the La atoms to reduce their distance compared to staying centered on A sites by 1 – 4 %. For the parallel La-dimer this effect is opposite and much larger. The distance between the two La atoms is 4.11 Å, compared to 3.84 Å between two A sites which amounts

to an expansion of 7 %. This ad-atom repulsion within one valley has already been observed in case of Sr[15] and explains the formation of isolated chains instead of condensed chains or clusters at low coverages. Nevertheless, we find the parallel dimer to be the most stable.

VI. CHAIN STRUCTURES AT LOW COVERAGES

As we combined pairs of the most favorable site for isolated La ad-atoms into dimers, we now search for ways to stack the three types of La-dimers together into more extended structures.

We systematically approached linear chain structures. Each of the three La-dimer types – parallel to the Si-dimer row, orthogonal or diagonal – has been stacked such that it shares at least one Si-dimer, so that this Si-dimer is next to two Lanthanum atoms from different La-dimers. The energetic ordering has been deduced on the basis of binding energy per La atom (compare Tab. III). Note that the binding energy per La atom for a given chain structure is slightly coverage dependent. In case of the double stepped chains (compare Fig. 4a for the structural principle) the adsorption energy varies within 0.06 eV at coverages between 1/10 and 1/5 ML. In order to ensure comparability all numbers listed here refer to a coverage of 1/6 ML.

We start our investigation with parallel La-dimers shown in Fig. 3b, which is the most stable dimer structure. The most favorable chain in this class is stacked perpendicular to the Si-dimer rows as shown in Fig. 4c. Its energy lies 0.06 eV per La atom above the lowest energy chain structure.

The most favorable chain made from orthogonal La-dimers is shown in Fig. 4a. It can also been interpreted as a variant of a chain of diagonal La-dimers (compare Fig. 3 c). This is the most favorable chain structure of La atoms on Si(001). Its chains run at an angle of about 76° to the Si-dimer row. It should be noted that it is equally possible to arrange the La-dimers in a zig-zag manner as shown in 4b. The zig-zag chain has not been explicitly calculated. The coexistence of straight and zig-zag chains has been found for Sr on Si(001), where the two modifications have been shown to be almost degenerate in energy.[15]

In all low-energy structures each La atom is thus surrounded by four silicon atoms having filled dangling bonds. Three of them are partners of filled Si-dimers while one is a buckled Si-dimer with the negative Si atom pointing towards the La ad-atom. On the basis of counting unbuckled Si-dimers, these structures are in a 3+ oxidation state.

The La-chain is the configuration with lowest energy in the low coverage limit. The lowest energy chain structures are of the order of 0.17 eV per La atom more stable than the most favorable isolated La-dimer. At elevated temperatures, entropic effects will lead to increasingly

La-dimer type	α	E[La] [eV]	panel
parallel	90	-0.30	a
parallel	63	-0.15	b
parallel	45	-0.20	c
parallel	34	-0.13	d
parallel	0	-0.07	e
orthogonal	90	-0.26	f
orthogonal/diagonal	76	-0.36	g
diagonal	63	-0.28	h

TABLE III: Energies per La atom of the chain structures at 1/6 ML. The orientation of the chain is described by the angle α (degrees) of the chain to the Si-dimer row. The supercells used for the total energy calculations are sketched in the corresponding panels of Fig. 15.

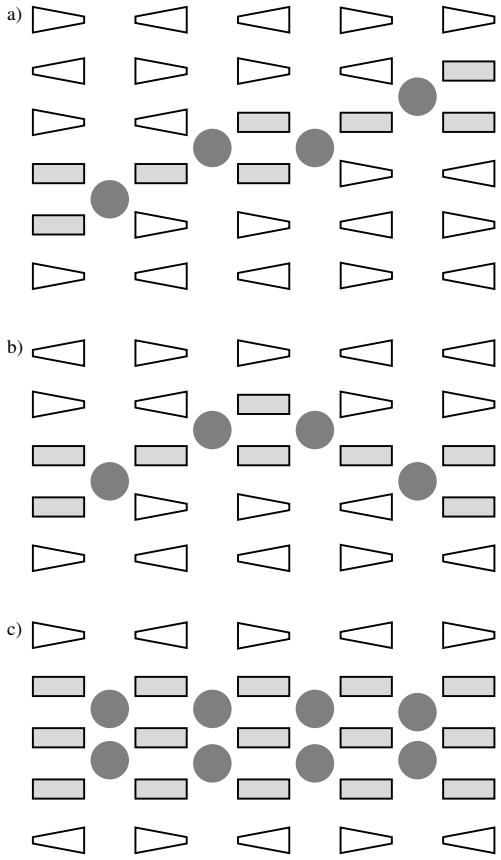

FIG. 4: Schematic representation of isolated La ad-atom chains. a) a single, double-stepped La chain. This is the energetically most favorable surface reconstruction at low coverages. A change in chain direction is realized by stacking two La-dimers with different orientation (b). Panel (c) shows the lowest energy chain structure derived from parallel dimers.

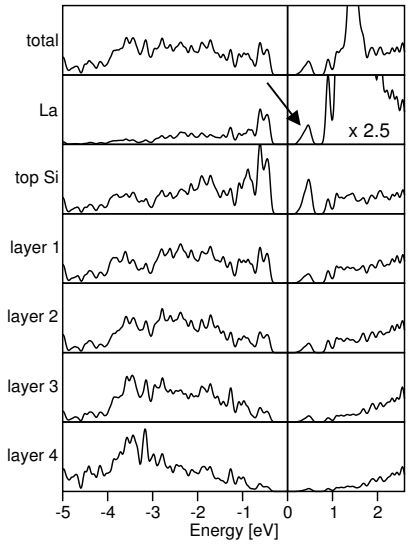

FIG. 5: Layer resolved density of states of 1/5 ML. The arrow indicates the upper dangling bond bands in the gap of silicon. The La panel was magnified by a factor of 2.5. The seemingly large gap of the silicon substrate is due to finite size effects and also found for the clean silicon surface at this slab thickness. For bulk silicon we obtain a "typical" GGA value of 0.65 eV. This DOS corresponds to the supercell outlined in Fig. 6 b.

shorter chain fragments. From the energy-difference of the linear chain and the isolated La-dimer, we obtain an estimate for the chain termination energy of approximately 0.09 eV. It should be noted, that experiments often observe shorter chain sequences than predicted from thermal equilibrium as high-temperature structures are frozen in.

The electronic structure of the La-chain is analogous to that of the Sr single chain.[15] The empty silicon surface has an occupied and an un-occupied band formed from the dangling bonds of the Si-dimers. La donates electrons into the upper dangling bond band. Those dangling bond states, which become filled, are shifted down in energy due to the change in hybridization on the one side and due to the proximity of the positive La-cations on the other side.

VII. CONDENSED CHAINS

With increasing coverage, the chains become closer packed. In the case of Sr, there was a preference for a periodicity of $(2n + 1)$ surface lattice spacings along the Si-dimer row direction.[15] This restriction has been attributed to the requirement that every cation be surrounded by four Si-atoms with filled dangling bonds, and that there is no frustration of the Si-dimer buckling, i.e. adjacent Si-dimers are buckled antiparallel.

For La the situation is more complex. Due to the longer periodicity of the La chains compared to those of Sr, there are two families of chain packing for La as shown in Fig. 6. In the first family the La chains are displaced only parallel to the Si-dimer row direction. In the second family the chains are in addition displaced perpendicular to the Si-dimer row.

The first family has a preference of $(2n + 1)$ surface lattice spacings along the dimer row as in the case of Sr adsorption. The spacing in the second family is arbitrary. The reason is that in family one, the buckling of every second Si-dimer row is pinned on both sides by two neighboring La chains (see Fig. 6a). A Si-dimer is pinned, if its buckling is determined by the Coulomb attraction of its raised, and thus negatively charged, Si atom to a nearby La ion. Since the buckling alternates along the Si-dimer row, this pinning can lead to indirect, long-ranged interaction between different La-chains.

In the second family the buckling of every Si-dimer row is pinned only at one La-chain as seen in Fig. 6b, while there is no preference of the Si-dimer buckling at the other La-chain. Thus for La we find – in contrast to Sr[15] – arbitrary chain spacings.

The closest packing of La-chains before they merge is 1/5 ML. We consider two La-chains merged if La atoms of different La chains occupy nearest-neighbor A sites within one valley. We predict a distinct phase at this coverage as seen in Fig. 12 and discussed later. This structure, shown in Fig. 6b, is derived from chains of the second family. An explanation for finding a phase at 1/5 ML is that the energy at higher coverage increases due to the electrostatic interaction of the La atoms within one valley. For the first family, the highest possible coverage before La-chains merge is 1/6 ML (Fig. 6a).

Note that the chains can change their direction without appreciable energy cost as shown in Fig. 4b. Experimentally measured diffraction patterns would reflect a configurational average.

The layer resolved density of states is shown in Fig. 5. We see that the Fermi-level lies in a band gap of the surface. Above the Fermi-level and still in the band-gap of bulk Si, surface bands are formed, which originate from the remaining empty dangling bonds of the buckled Si-dimers. As in the case of Sr, these states form flat bands in the band-gap of silicon, which approximately remain at their energetic position as the La coverage is increased. Its density of states, however, scales with the number of empty dangling bonds.

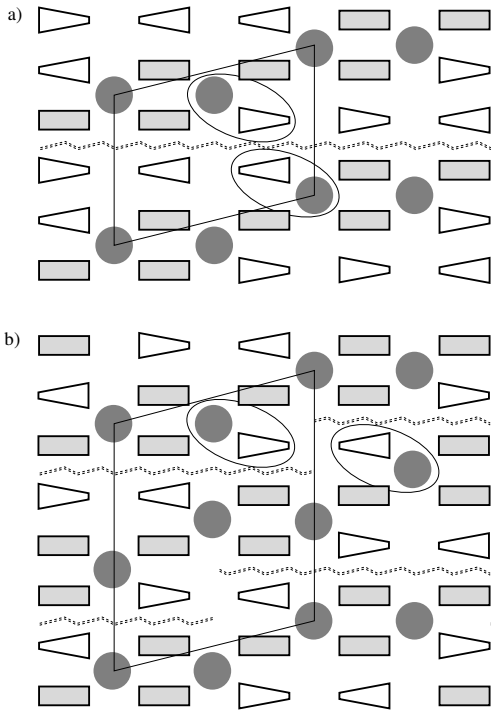

FIG. 6: Schematic representation of the two packing types of double stepped La chains at their maximum condensed coverage. The reconstruction in panel a) consists of parallel La chains. The chains in panel b) are also displaced by one valley orthogonal to the Si-dimer rows. The ovals indicate the pinning of the Si-dimer buckling by a La ad-atom. The dashed double zig-zag lines shows the positions where, in case of structure a), an even number of Si-dimers can be inserted in order to arrive at more dilute coverages. In case of structure b) an arbitrary number of Si-dimers can be inserted, as the buckling of each row is just pinned on one side. The calculational supercells are outlined.

VIII. THE CANONICAL SURFACE AT 1/3 ML COVERAGE

If the spacing of the chains is further reduced, they condense at 1/3 ML to the structure shown in Fig. 7.

There are several versions of this structure type. They have a repeating sequence of two La-atoms and one vacant A site in each valley in common. The relative displacement of this sequence from one valley to the next, however, may differ. We investigated several structures and found the one shown in Fig. 7 to be the most stable.

A structure with a sequence of four A sites occupied with metal ions separated by two empty A sites, has been the most favorable structure at this coverage in the case of Sr adsorption.[15] For La, however, this configuration is

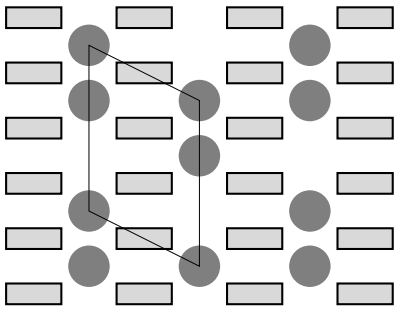

FIG. 7: Schematic representation of the most stable reconstruction at the canonical coverage of 1/3 ML. All Si-dimer dangling bonds are filled. This structure can be thought of as the condensed chain structure in Fig. 6 b) with a reduced chain spacing. The calculational supercell cell is outlined.

energetically unfavorable.

At a coverage of 1/3 ML, all silicon dangling bonds are filled due to the electrons provided by the La adatoms. This surface is isoelectronic to the Sr covered surface at 1/2 ML.[15] For the Sr-covered silicon surface, the increased oxidation resistance of the corresponding 1/2 ML structure has been observed experimentally.[34] Similarly we suggest that the surface covered with 1/3 ML of La will have an increased oxidation resistance.

In Fig. 8 we show the layer-resolved density of states of the most stable structure at 1/3 ML. In analogy to the 1/2 ML covered Sr surface, there are no surface states deep in the band gap of silicon, because all Si-dimer dangling bonds are filled and shifted into the valence band due to the electrostatic attraction of the electrons to the positive La ions. Note, however, that in contrast to the canonical surface coverage of Sr on Si(001) at a coverage of 1/2 ML, the canonical La surface exhibits vacant A-sites.

IX. TRANSITION FROM LA^{3+} TO LA^{2+} ABOVE 1/3 ML

Up to the canonical coverage of 1/3 ML, all thermodynamically stable reconstructions could be explained by La being in the 3+ oxidation state. In contrast to the isolated La-atoms and La-dimers, the oxidation state can clearly be identified from the number of unbuckled Si-dimers: Each unbuckled dimer has received two electrons. A 3+ oxidation state is also consistent with the density of states.

If we follow the picture that emerged from Sr, we would anticipate that increasing the coverage above 1/3 ML in case of La would lead to filling the Si-dimer antibonds, which results in a breaking up of the dimer bonds. For La the situation is different: the La-d band is located at much lower energies as compared to Sr. Therefore

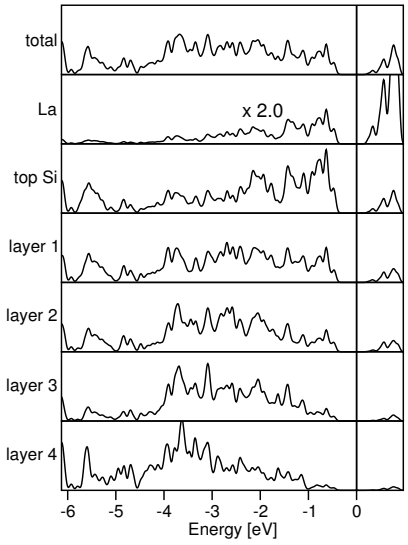

FIG. 8: Layer resolved density of states of 1/3 ML. The La panel was magnified by a factor of 2. Compare Fig. 5 for a discussion about the Si band gap. This DOS corresponds to the supercell outlined in Fig. 7.

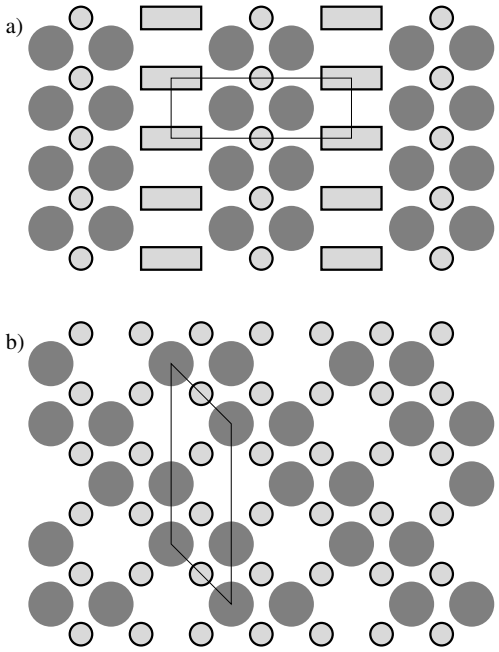

FIG. 9: The lowest energy structures at 2/3 ML in the 2+ (a) and 3+ (b) regime. The calculational supercells are outlined.

the energy to break the Si-dimer bonds is larger than that to add electrons into the La d-shell. As a result we find that La changes its oxidation state from 3+ to 2+. Oxidation states of La that are even lower are unfavorable due to the Coulomb repulsion of electrons within the La-d and f shells. Thus the structures above 1/3 ML can be explained in terms of La^{2+} ions and are similar to those found for Sr.[15]

It may be instructive to compare two structures with different oxidation states of La. A good example is found at a coverage of 2/3 ML: The lowest energy structure is a (3×1) reconstruction already found for Sr[15] and depicted in Fig. 9a. This is a clear 2+ structure. Since every Si-dimer only accepts two electrons, they can just accommodate two of the three valence electrons of La. The lowest structure with formal La^{3+} ions, which can clearly be identified as having all Si-dimer bonds broken, is shown in Fig. 9b. It has an energy which is 0.36 eV per La atom higher than the structure with La^{2+} ions.

At 1/2 ML, we find a structure where all A sites are occupied to be most stable. There the La d-states are partially occupied. We confirmed that the system is not spin polarized.

The crossover of the energy surfaces of the 2+ and the 3+ structures is shown in Fig. 10 using a set of surface reconstructions, for which the charge state can be determined unambiguously. It can be clearly seen that the 2+ structures become significantly more stable above 1/2 ML. From Fig. 11 it is apparent that the energy rises sharply as the La atoms cross over to the 2+ oxidation state beyond the canonical interface at a coverage of 1/3 ML.

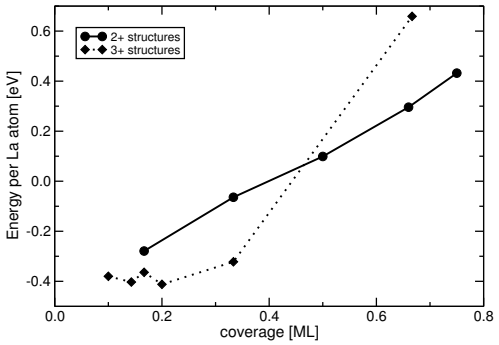

FIG. 10: Crossover of the total energy surfaces of the 2+ and 3+ regime beyond the canonical coverage of 1/3 ML.

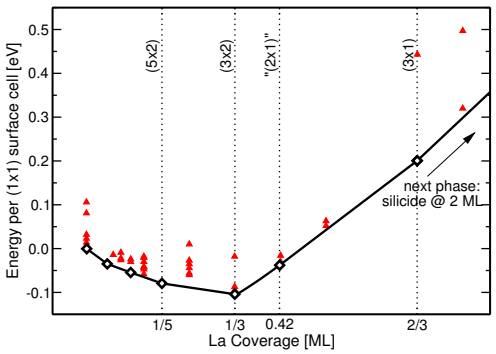

FIG. 11: (Color online) The surface energy[35] versus coverage. The open diamonds correspond to the thermodynamically accessible surface structures while the triangles mark metastable structures. Compare Figs. 6b, 7 and 9a for the structures at 1/5, 1/3 and 2/3 ML, respectively. At 0.42 ML we predict a (2×1) reconstruction which originates from the half-ML structural template with a La vacancy concentration of 17 % (see discussion in the text).

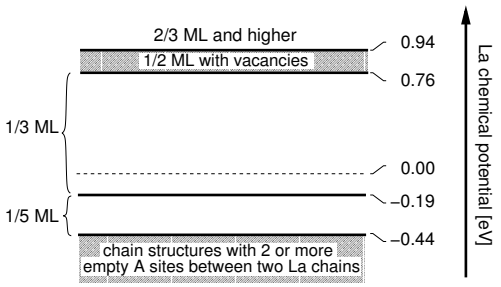

FIG. 12: The phase diagram for La adsorption on Si(001).

X. PHASE DIAGRAM

Based on the surface energies composed in Fig. 11 we extracted the zero-Kelvin phase diagram shown in Fig. 12. The slope of the line-segments of the lower envelope in Fig. 11 corresponds to the chemical potential, at which the two neighboring phases coexist (for a more elaborate discussion, refer to Ref.[15]). The stable phases are defined by the coverages where two line segments with different slopes meet. The zero for the La chemical potential has been chosen as the value at which $LaSi_2$ and silicon coexist. Consequently, all phases in regions of positive chemical potentials are in a regime where the formation of bulk silicides is thermodynamically favorable.

Below a chemical potential of -0.44 eV we expect single chain structures as described in Sec. VI. At 1/5 ML we predict a distinct phase since this is the highest possible coverage without La ad-atoms at nearest neighbor A sites (compare Fig. 6b). At a chemical potential of -0.19 eV the stability region of the 1/3 ML coverage (Fig. 7) starts.

The transition from the phase at 1/3 ML to the 2×1 reconstructed surface at 1/2 ML, where all A-sites are filled, can be described by a decrease of La-vacancies (compare Fig. 7 of this manuscript and Fig. 9 of Ref.[15]). From this point of view, the phase at 1/3 ML can be described by an ordered array of La-vacancies in the 1/2 ML structure. There is an effective repulsion between La-vacancies due to the repulsion between La-atoms on neighboring A-sites. We describe the total energy by an empirical model energy of the form $E(c_V) = E_0 + E_f \cdot c_V + \Delta \cdot c_V^2$, where c_V is the concentration of La vacancies, E_0 is the energy of the structure with all A-sites filled (1/2 ML), E_f is the formation energy of an isolated La-vacancy, and Δ describes the repulsion between vacancies. Coexistence between the two phases would result from a negative value of Δ. In that case, adding an additional ad-atom to a phase requires more energy than starting a new phase with the next higher coverage. Between 1/3 and 1/2 ML, however, Δ is positive as filling a portion of vacancies is favorable compared to creating patches of pure 1/2 ML coverage.

We calculated the energy of an adsorption structure with three La atoms on neighboring A sites separated by one vacancy within one valley. La triplets in different valleys have been arranged, so that the distance between vacancies is maximized in order to minimize the repulsive energy. Based on the energies at 1/3 and 1/2 ML as well as at the intermediate coverage of 3/8 ML just described, we can determine the three parameters E_0, E_f and Δ to be 0.05, -0.56 and 0.26 eV, respectively.

At a certain vacancy concentration of $c_V^0 = 17\,\%$ (i.e. a La-coverage of 0.42 ML) we find a phase boundary with the next stable phase at 2/3 ML at a chemical potential of 0.94 eV. According to our phase diagram, the pure surface reconstruction at 1/2 ML is never formed. The shaded region in Fig. 12 corresponds to 1/2 ML structural template with variable vacancy concentration.

As seen in the phase diagram shown in Fig. 12 bulk silicide formation becomes thermodynamically stable within the stability region of the 1/3 ML coverage. In a growth experiment we would expect the formation of bulk silicide grains to be delayed beyond a coverage of 1/3 ML. The nucleation of silicide grains may suffer from the large mismatch between bulk silicide phases and silicon. This is of particular importance during the initial stages of nucleation because the strained interface region occupies most of the volume of the grain.

Thus it may be of interest to know the stability of silicide thin films on Si(001). We found one such silicide layer which is shown in Fig. 13. It consists of a (1×1) silicon surface in contact with two La layers that sandwich a layer of Si^{4-} ions in between. While we have not performed a thorough search of other candidates, the energy of this silicide layer indicates that silicide formation will at the latest be initiated beyond a coverage of 2/3 ML.

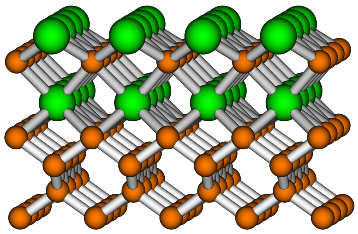

FIG. 13: (Color online) Silicide overlayer at a coverage of 2 ML.

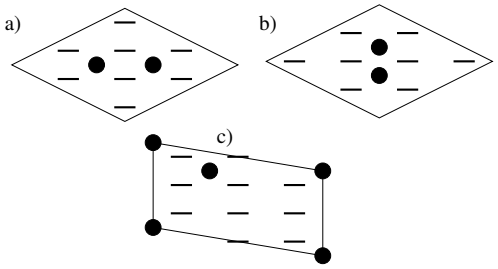

FIG. 14: Supercells used for the simulation of isolated La dimers shown in Fig. 3.

We can thus only pin down the onset of silicide formation within a coverage interval between 1/3 (thermodynamically) and 2/3 ML (including kinetic considerations).

XI. CONCLUSIONS

In this paper we have investigated the surface structures of La adsorbed on Si(001) as a function of coverage. We propose a theoretical phase diagram by relating the phase boundaries at zero temperature to chemical potentials, which can be converted into partial pressure and temperature in thermal equilibrium.

Our findings elucidate the chemistry of third row elements on Si(001) and the phases of La on Si(001), and are expected to provide critical information for the growth of a wide class of high-k oxides containing La. The phase diagram may be used as a guide for the growth of La-based oxides on Si(001).

APPENDIX A: SUPERCELLS AT DILUTE COVERAGES

Fig. 3 shows the three possible La-dimer orientations on the Si(001) surface. We did not draw the periodic images introduced by the calculational supercell in order to emphasize that fact that this local arrangement corresponds to an isolated dimer. Fig. 14 sketches the supercells used. They were chosen in order to avoid frustration of Si dimers due to periodic images.

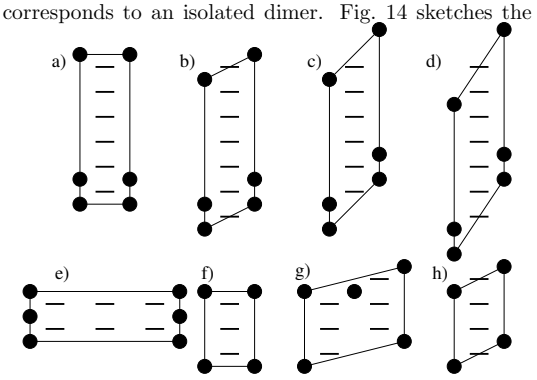

FIG. 15: Supercells used for the calculation of La chains at 1/6 ML as listed in Tab. III.

Tab. III summarizes the energetics of chains structures built from La dimers. The supercells used in the corresponding total energy calculations are sketched in Fig. 15.

Acknowledgments

We thank A. Dimoulas, J. Fompeyrine, J.-P. Loquet, G. Norga and C. Wiemer for useful discussions. This work has been funded by the European Commission in the project "INVEST" (Integration of Very High-K Dielectrics with CMOS Technology) and by the AURORA project of the Austrian Science Fond. Parts of the calculations have been performed on the Computers of the "Norddeutscher Verbund für Hoch- und Höchstleistungsrechnen (HLRN)". This work has benefited from the collaborations within the ESF Programme on 'Electronic Structure Calculations for Elucidating the Complex Atomistic Behavior of Solids and Surfaces'.

* Corresponding author: peter.bloechl@tu-clausthal.de

[1] G.E. Moore, SPIE **2438**, 2 (1995)

[2] International Technology Roadmap for Semiconductors, 2001 Ed. http://public.itrs.net/

[3] R.A. McKee, F.J. Walker and M.F. Chisholm, Phys. Rev. Lett. **81**, 3014 (1998).

[4] M. V. Cabañas, C. V. Ragel, F. Conde, J. M. González-Calbet, M. Vallet-Regí, Solid State Ionics, **101**, 191, (1997).

[5] M. Nieminen, T. Sajavaara, E. Rauhala, M. Putkonen and L. Niinistö, J. Mater. Chem., **11**, 2340, (2001).

[6] B.-E. Park and H. Ishiwara, Appl. Phys. Lett., **79**, 806, (2001).

[7] G.D. Wilk, R.M. Wallace and J.M. Anthony, J. Appl. Phys. **89**, 5243 2001.

[8] S. Guha, N.A. Bojarczuk, and V. Narayanan, Appl. Phys. Lett. **80**, 766 (2002)

[9] S. Guha, E. Cartier, M.A. Gribelyuk, N.A. Bojarczuk, and M.C. Copel, Appl. Phys. Lett. **77**, 2710 (2000)

[10] G. Apostolopoulos, G. Vellianitis, A. Dimoulas, J.C. Hooker and T. Conard App. Phys. Lett., **84**, 260 (2004).

[11] J. Fompeyrine, G. Norga, A. Guiller, C. Marchiori, J. W. Seo, J.-P. Locquet, H. Siegwart, D. Halley, C. Rossel in *Proceedings of the WODIM 2002, 12th Workshop on Dielectrics in Microelectronics* (IMEP, Grenoble, France, 2002), p. 65.

[12] J. W. Seo, J. Fompeyrine, A. Guiller, G. Norga, C. Marchiori, H. Siegwart, and J.-P. Locquet, App. Phys. Lett, **83**, 5211, (2003).

[13] H.J. Osten, J.P. Liu, H.-J. Müssig and P. Zaumseil, Microelectronics Reliability **41**, 991 (2001)

[14] C.J. Först, K. Schwarz and P.E. Blöchl, Comp. Mater. Sci. **27**, 70 (2003).

[15] C.R. Ashman, C.J. Först, K. Schwarz and P.E. Blöchl, Phys. Rev. B **69**, 75309 (2004).

[16] Y.M. Sun, J. Lozano, H. Ho, H.J. Park, S. Veldmann and J.M. White, Appl. Surf. Sci. **161**, 115 (2000)

[17] C.J. Först, C.R. Ashman, K. Schwarz and P.E. Blöchl, Nature **427**, 53 (2004).

[18] G.J. Norga, A. Guiller, C. Marchiori, J.P. Locquet, H. Siegwart, D. Halley, C. Rossel, D. Caimi, J.W. Seo, and J. Fompeyrine, Materials Research Society Symp. Proc. **786**, E 7.3.1 (2004).

[19] P. Hohenberg and W. Kohn, Phys. Rev. **136**, B864 (1964).

[20] W. Kohn and L.J. Sham, Phys. Rev. **140**, A1133 (1965).

[21] J.P. Perdew, K. Burke, and M. Ernzerhof, Phys. Rev. Lett. **77**, 3865 (1996).

[22] P.E. Blöchl, Phys. Rev. B **50**, 17953 (1994).

[23] Peter E. Blöchl, Clemens J. Först and Johannes Schimpl, Bull. Mater. Sci. **26**, 33 (2003)

[24] R. C. Weast, CRC Handbook of Chemistry and Physics, 83^{rd} ed., CRC Press, Inc., Boca Raton, 2002, p. **4**-164.

[25] R. Car and M. Parrinello, Phys. Rev. Lett. **55**, 2471 (1985).

[26] N. D. Mermin, Phys. Rev. **137**, A1441 (1965).

[27] M. Gillan, J. Phys: Cond. Mat. **1**, 689 (1989)

[28] E. Zintl, Angew. Chem. **52**, 1 (1939); W. Klemm, Proc. Chem. Soc. London **1958**, 329; E. Bussmann, Z. Anorg. Allg. Chem. **313**, 90 (1961).

[29] H. Nakano, S. Yamanaka, J. Sol. Stat. Chem. **108**, 260-266, (1994).

[30] D. Hohnke, E. Parthe, Act. Cryst. A **20**, 572-582, (1966)

[31] H. Mattausch, O. Oeckler, A. Simon, Z. Anorgan. Alg. Chemie A **625**, 1151-1154, (1999).

[32] E. I. Gladyshevskii, IVNAM **1**, 648-651, (1965).

[33] The isolated La atom has one unpaired electron. Hence the calculations have been performed spin polarized. Due to the periodic boundary conditions, the unpaired electron enters a delocalized, partially filled band. As a result most of the calculations on isolated defects produced no net spin.

[34] Y. Liang, S. Gan, and M. Engelhard, App. Phys. Lett., **79**, 3591 (2001).

[35] The adsorption energy per (1×1) unit cell is defined as $E = \left\{ \frac{1}{l} \big[E[\text{supercell}] - nE_0[\text{m layer-Si-slab}] \big] - E_0[\text{La}] \right\} \cdot X$, where E[supercell] is the total energy of the supercell used for the specific surface reconstruction, n is the number of (1×1) surface unit cells contained in that supercell and m is the slab-thickness in units of silicon layers of the supercell. l denotes the number of La atoms in the supercell and X the La coverage for that reconstruction. This energy can be alternatively calculated using the energy per La atom multiplied with the coverage X. The reference energies E_0 are listed in Tab. I.

6.4 Comp. Mat. Sci. 27, 70 (2003): Heteroepitaxial growth of high-k gate oxides on silicon: insights from first-principles calculations on Zr on Si(001)

In this publication we show that all Zr surface reconstructions are thermodynamically unstable with respect to silicide formation. At a coverage of 2 ML, the surface reconstruction contains structural elements of bulk $ZrSi_2$ which indicates a low nucleation barrier for silicide grains.

ELSEVIER

Computational Materials Science 27 (2003) 70–74

COMPUTATIONAL MATERIALS SCIENCE

www.elsevier.com/locate/commatsci

Heteroepitaxial growth of high-k gate oxides on silicon: insights from first-principles calculations on Zr on Si(0 0 1)

Clemens J. Först [a,b,*], Peter E. Blöchl [a], Karlheinz Schwarz [b]

[a] *Clausthal University of Technology, Institute for Theoretical Physics, Leibnizstr. 10, D-38678 Clausthal-Zellerfeld, Germany*
[b] *Vienna University of Technology, Institute for Materials Chemistry, Getreidemarkt 9/165-TC, A-1060 Vienna, Austria*

Abstract

Metal deposition of Zr on a Si(0 0 1) surface has been studied by state-of-the-art electronic structure calculations. The energy per Zr adatom as a function of the coverage shows, that Zr forms silicide islands even at low coverages. Adsorbed Zr is thermodynamically unstable against the formation of bulk silicide $ZrSi_2$. The observation that the islands consist of structural elements of the bulk silicide is an indication that silicide grains will form spontaneously.

PACS: 82.65.F; 31.15.A; 68.55
Keywords: High-k oxides; Heteroepitaxial growth; Si(1 0 0); Zr; DFT

1. Introduction

The scaling of the CMOS transistor has been the driving force behind the tremendous increase in microprocessor performance observed during the last decades. While the problems of the past were dominated by manufactural aspects, one now faces the first fundamental physical limitations as structures in logical devices approach atomic dimensions.

As a rule of thumb, the thickness of the gate-oxide has to be directly proportional to the channel length in a MOSFET (metal oxide silicon field effect transistor) device. In the course of the ongoing miniaturization, also the thickness of this insulating layer is being continually reduced. By the year 2007, gate-oxides in a transistor will approach a thickness of 1.5 nm [1], which corresponds to about ten atomic distances. The quantum mechanical tunneling currents through such a thin oxide are intolerable and cause increased power consumption and deteriorated switching characteristics of the transistor. Replacing SiO_2-based oxides, nowadays employed as gate dielectric, is one of the "key challenges" to the semiconductor industry [1], which has to find a solution within the next four to five years.

Employing high-k (≡large dielectric constant) oxides would allow for a greater physical thickness

* Corresponding author. Address: Clausthal University of Technology, Institute for Theoretical Physics, Leibnizstr. 10, D-38678 Clausthal-Zellerfeld, Germany.

0927-0256/03/$ - see front matter
doi:10.1016/S0927-0256(02)00427-5

while preserving the electrical properties. Possible candidates have to meet an extensive list of requirements [2] such as sufficiently large band offsets, thermodynamical stability or interface quality.

The Si–SiO_2 system meets all these requirements in an unparallelized way [3]. First attempts to grow alternative oxides on Si(0 0 1) did not yield satisfactory results for a variety of reasons—often originating in the interface region.

In the course of changing to a new gate material, one also considers to now grow crystalline oxide layers. It has been a paradigm that the gate oxide must be amorphous in order to avoid dislocations and grain boundaries, which provide natural pathways for leakage currents and atom diffusion. However, in the very small devices used in the near future, the probability for such a defect may be sufficiently small. On the other hand, epitaxial oxides bear the promise of very low defect concentrations at the interface to silicon, which is crucial for efficient device operation.

The first account of heteroepitaxial growth of a transition metal oxide has been presented by a seminal work of McKee et al. [4] who succeeded in growing $SrTiO_3$ on Si(0 0 1). For the divalent elements detailed studies have been performed [5–10]. A similar understanding does not yet exist for the technological relevant early transition metals such as zirconium. Theoretical studies on Zr are limited bulk interface calculations of silicates [11].

The deposition and formation of an interface between one of the major contenders for high-k oxides, namely zirconia (ZrO_2), and silicon has not yet been investigated with ab-initio simulations. As a first step we performed state-of-the-art electronic structure calculations of the deposition of Zr on Si(0 0 1) up to a coverage of two monolayers (MLs).

2. Computational aspects

We performed first-principles calculations within the framework of density functional theory [12,13] using the gradient corrected density functional of Perdew, Burke and Enzerhof [14]. The electronic structure problem has been solved with the projector augmented waves method [15], which uses augmented plane waves to describe the full wave-functions and densities without shape approximation. The PAW method as implemented in the CP-PAW code employs the Car–Parrinello approach [16] to minimize the total energy functional.

The core electrons are described within the frozen core approximation with the semi-core (4s and 4p) shells of the Zr atoms treated as valence electrons. Plane wave cutoffs of 30 and 60 Ry for the wave functions and the density have been used.

For metallic systems we minimized the Mermin functional with respect to the occupation numbers which yields the Fermi–Dirac distribution for the electrons. An electronic temperature of 1000 K was used. The zero-Kelvin result has been extrapolated using the method suggested by [17].

The reconstructed Si(0 0 1) surface is the template for our growth studies. It is modeled by a slab consisting of five silicon layers, where the bottom layer is saturated with two hydrogen atoms per silicon. The position of the hydrogen atoms and the lowest silicon layer has been frozen. Supercells with 16 atoms per layer have been used for the calculations of Zr in the dilute limit, 8 atoms per layer for all higher coverages. In the first case, the distance between two periodic images of an adatom is 15.36 Å. For all surface calculations the k-mesh density corresponds to 64 lateral k-points per p(1×1) surface unit cell.

3. Dilute limit

Fig. 1 shows the structure of the reconstructed Si(0 0 1) surface. Excellent accounts covering the full complexity of the surface reconstruction can be found in literature [18,19]. The resulting structure can, however, be explained by the following considerations: While every bulk silicon is 4-fold coordinated, the surface atoms lack their upper bonding partners which leaves two dangling bonds per atom, each occupied by one electron. In a first step, two neighboring silicon atoms form a dimer bond—initially parallel to the surface—which leaves one dangling bond per atom. Now both electrons are transferred into one dangling bond to

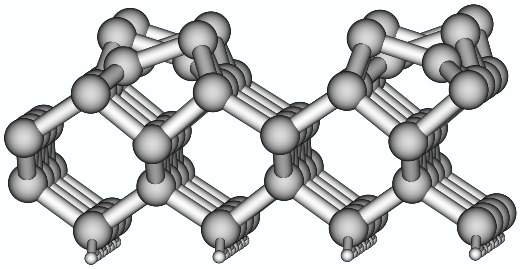

Fig. 1. Si(0 0 1) surface with c(4 × 2) reconstruction. The figure represents one supercell of the slab as used as a template in our calculations.

reduce the number of unpaired electrons to zero. This results in the buckling as the silicon with the filled dangling bond prefers a tetrahedral bonding arrangement, while the other prefers a planar sp^2 configuration. From the electrostatic point of view, the alternating buckling behavior is favorable. Our calculations readily reproduce previously reported results such as the c(4 × 2) reconstruction and the difference in *z*-coordinate of two silicon atoms within a dimer [20].

The energy surface of a Zr adatom on Si(0 0 1), has been obtained by freezing the lateral position of the adsorbed atom relative to the slab backplane, while all other degrees of freedom were fully relaxed. We used a grid of 12 Zr positions in the irreducible zone of the reconstructed p(2 × 1) silicon surface.

The resulting total energy surface for an isolated Zr on top of Si(0 0 1) is shown in Fig. 2. Two nearly degenerate positions can be identified. One is located in the valley right in the middle of two dimers of neighboring rows and the other on top of a dimer row between to adjacent dimers. A third, local minimum, is located in the valley and has an energy 0.30 eV higher relative to the most favorable positions. The diffusion is quasi one-dimensional with barriers of 0.70 eV for diffusion parallel to the dimer rows and 1.63 eV from the valley to the row.

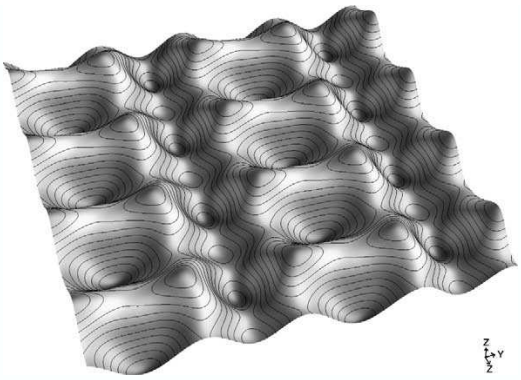

Fig. 2. The total energy surface of an isolated Zr adatom as a function of the lateral position on the Si(0 0 1) surface. The dimer silicon atoms are located at the bar-shaped maxima on this surface. The valleys in the energy map correspond to the valleys between the dimer rows.

4. Coverage of 0.25 and 0.5 monolayers

In order to investigate the formation of a continuous film, we increased the coverage. The structures with coverages of 0.25 and 0.5 ML have similar energies per Zr atom as the dilute limit (see Fig. 3). A wealth of complex structures has been found. Here, however, we only summarize the main trends of the chemical binding.

To first approximation Zr prefers a formal 4+ charge state—the projected density of states of the Zr *d*-states is located well above the Fermi level. It is well known that for transition metal cations the

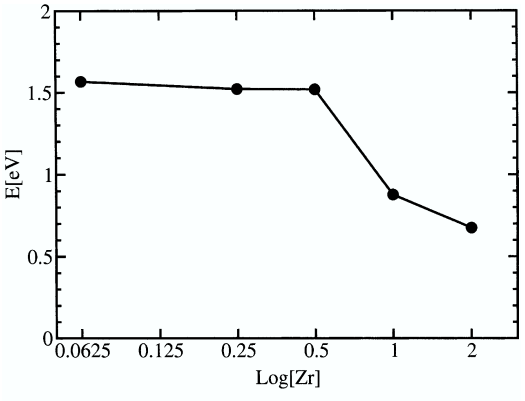

Fig. 3. The energy per Zr adatom as a function of the coverage. Energies are given relative to bulk $ZrSi_2$ and bulk Si.

s- and p-electrons are located above the *d*-states, and have only a minor effect on the occupied states. The silicon dimers at the surface accept up to two electrons in their dangling bonds. A clear structural indication that the dangling bonds are filled is the disappearance of the dimer buckling.

Further electrons that are supplied at increased coverage of Zr, occupy the anti-bonding states of the dimer bond. As a consequence the silicon dimers break up. This happens at a coverage of half a ML and above. It should be noted, however, that metallic states accept some of the electrons so that the number of broken dimers does not directly correlate with the number of Zr adatoms in the ratio one to one. As a result of the interplay between breaking dimers and metallic states we find fairly complex reconstructions of the surface structure for intermediate coverages.

5. Silicide formation

Upon increase of the coverage to a full ML, the energy drops by 0.64 eV per adatom (see Fig. 3). The stable structure with ML coverage is shown in Fig. 4. All dimer bonds of the surface layer are broken, and the Zr atoms occupy the centers of the square array of surface silicon atoms in the resulting $p(1 \times 1)$ reconstruction. Such a layer is one structural element of bulk $ZrSi_2$.

The energy gain is, however, not due to the surface geometry but can be attributed to a dimer reconstruction of the silicon subsurface. A metastable state without this reconstruction is even higher in energy than adsorbed Zr at lower coverages.

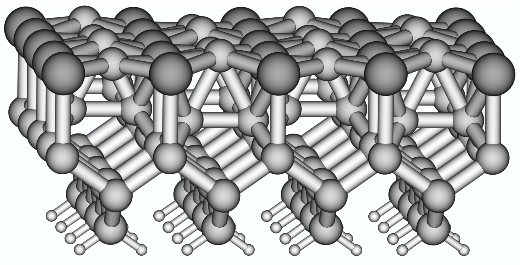

Fig. 4. The structure of a Zr monolayer. Below the silicide layer, subsurface dimers have formed.

During the reconstruction, the silicon atoms in the layer underneath the ZrSi surface layer form dimers analogous to the bare silicon surface. In contrast to the dimer row reconstruction of the silicon surface, these subsurface dimers are not buckled and are arranged in a checkerboard instead of a row pattern.

At a coverage of two MLs a second ZrSi layer is formed. This configuration is shown in Fig. 5. The second layer is nearly identical to the first, but is shifted laterally. The double layer is again a structural element of bulk $ZrSi_2$, the structure of which is shown in Fig. 6. The ZrSi double layer

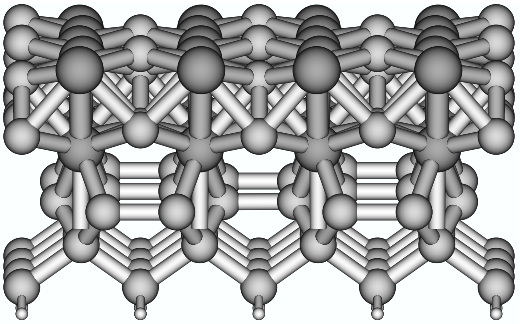

Fig. 5. Structure obtained at a structure of two monolayers of Zr. The ZrSi double layer constitutes a structural element of bulk $ZrSi_2$ (compare to Fig. 6). Note the dimer reconstruction of the silicon layer underneath the ZrSi double layer.

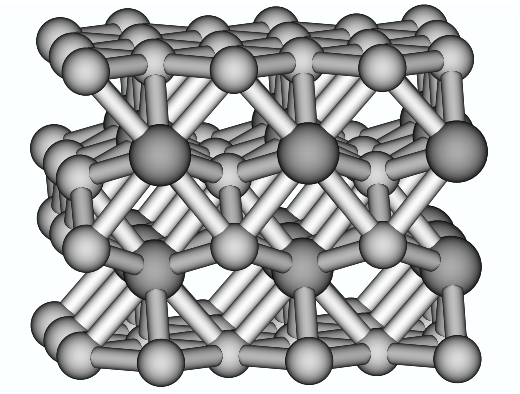

Fig. 6. Structure of $ZrSi_2$ bulk. It consists of pure silicon layers separated by a ZrSi double layers. This double layer exhibits Si zig-zag chains separated by Zr atoms.

consists of one-dimensional Si zig-zag chains separated by Zr atoms. The Zr atoms lie approximately in the plane of the upper and lower atoms of the Si chain. As for ML coverage the first silicon layer underneath the ZrSi double layer exhibits a dimer reconstruction.

Despite an additional energy gain from the ML coverage to a coverage of two MLs of 0.25 eV per adatom, even this structure is still 0.67 eV higher in energy than bulk $ZrSi_2$. While the atomic process has not yet been resolved in every detail, our findings give strong indications for the nucleation of the silicide.

6. Discussion and conclusion

We presented the results of state of the art ab-initio electronic structure calculations aiming at understanding the deposition of Zr atoms on a Si(0 0 1) surface as it is the case in an MBE reaction chamber.

Our results are summarized in Fig. 3, which shows the energy per Zr adatom as a function of the coverage. For coverages below one monolayer the energy is nearly independent of the coverage. At a coverage of 1 ML we observe a sharp drop in energy by 0.64 eV, followed by further drops in energy for higher coverages. All structures are less stable than bulk silicide.

Our findings suggest that islands with a local coverage of 1 ML or higher are formed even at low coverages. The islands contain structural elements of bulk $ZrSi_2$, which is more stable than any surface structure. Therefore a likely scenario is the formation of bulk silicide grains, that disrupt the surface morphology, and are detrimental for epitaxial growth. Modification of growth conditions, such as exposing the surface to an oxygen containing ambient, may bypass silicide formation during the first growth steps.

Acknowledgements

This work has been funded by the European Commission in the project "INVEST" (Integration of Very High-*k* Dielectrics with CMOS Technology) IST-2000-28495 and by the AURORA project (SBF F011) of the Austrian Science Fond. This work has benefited from the collaborations within the ESF Programme on 'Electronic Structure Calculations for Elucidating the Complex Atomistic Behavior of Solids and Surfaces'.

References

[1] International Technology Roadmap for Semiconductors, 2001 Ed. http://public.itrs.net/.
[2] G.D. Wilk, R.M. Wallace, J.M. Anthony, J. Appl. Phys. 89 (2001) 5243.
[3] R. Buczko, S.J. Pennycook, S.T. Pantelides, Phys. Rev. Lett. 84 (2000) 943.
[4] R.A. McKee, F.J. Walker, M.F. Chisholm, Science 293 (2001) 468.
[5] X. Yao et al., Phys. Rev. B 59 (1999) 5115.
[6] K. Ojima, M. Yoshimura, K. Ueda, Surf. Sci. 491 (2001) 169.
[7] A. Herrera-Gómez et al., Phys. Rev. B 61 (2000) 12988.
[8] R.Z. Bakhtizin et al., J. Vac. Sci. Technol. B 14 (1996) 1000.
[9] W.C. Fan, N.J. Wu, A. Ignatiev, Phys. Rev. B 42 (1990) 1254.
[10] J. Wang et al., Phys. Rev. B 60 (1999) 4968.
[11] A. Kawamoto et al., J. Appl. Phys. 90 (2001) 1333.
[12] P. Hohenberg, W. Kohn, Phys. Rev. 136 (1964) B864.
[13] W. Kohn, L.J. Sham, Phys. Rev. 140 (1965) A1133.
[14] J.P. Perdew, Y. Wang, Phys. Rev. B 45 (1992) 13244.
[15] P.E. Blöchl, Phys. Rev. B 50 (1994) 17953.
[16] R. Car, M. Parrinello, Phys. Rev. Lett. 55 (1985) 2471.
[17] M.G. Gillan, J. Phys.: Condens. Matter 1 (1989) 689.
[18] D.J. Chadi, Phys. Rev. Lett. 43 (1979) 43.
[19] S. Healy et al., Phys. Rev. Lett. 87 (2001) 16105.
[20] J.E. Northrup, Phys. Rev. B 47 (1993) 10032.

6.5 Book Chapter: Electronic structure methods: Augmented Waves, Pseudopotentials and the Projector Augmented Wave Method

This manuscript will appear in the "Handbook of Materials Modeling" of Kluwer Academic Publishers. It provides an overview over state-of-the-art electronic structure methods. Emphasis is given on the Projector Augmented Wave method [24] which has been used for the application project described in part II.

Electronic structure methods: Augmented Waves, Pseudopotentials and the Projector Augmented Wave Method

Peter E. Blöchl[1], Johannes Kästner[1], and Clemens J. Först[1 2]

[1] *Clausthal University of Technology, Institute for Theoretical Physics, Leibnizstr.10, D-38678 Clausthal-Zellerfeld, Germany and*

[2] *Vienna University of Technology, Institute for Materials Chemistry, Getreidemarkt 9/165-TC, A-1060 Vienna, Austria*

(Dated: July 30, 2004)

The main goal of electronic structure methods is to solve the Schrödinger equation for the electrons in a molecule or solid, to evaluate the resulting total energies, forces, response functions and other quantities of interest. In this paper we describe the basic ideas behind the main electronic structure methods such as the pseudopotential and the augmented wave methods and provide selected pointers to contributions that are relevant for a beginner. We give particular emphasis to the Projector Augmented Wave (PAW) method developed by one of us, an electronic structure method for ab-initio molecular dynamics with full wavefunctions. We feel that it allows best to show the common conceptional basis of the most widespread electronic structure methods in materials science.

I. INTRODUCTION

The methods described below require as input only the charge and mass of the nuclei, the number of electrons and an initial atomic geometry. They predict binding energies accurate within a few tenths of an electron volt and bond-lengths in the 1-2 percent range. Currently, systems with few hundred atoms per unit cell can be handled. The dynamics of atoms can be studied up to tens of pico-seconds. Quantities related to energetics, the atomic structure and to the ground-state electronic structure can be extracted.

In order to lay a common ground and to define some of the symbols, let us briefly touch upon the density functional theory[22,30]. It maps a description for interacting electrons, a nearly intractable problem, onto one of non-interacting electrons in an effective potential.

Within density functional theory, the total energy is written as

$$E[\Psi_n(\mathbf{r}), \mathbf{R}_R] = \sum_n f_n \langle \Psi_n | \frac{-\hbar^2}{2m_e} \nabla^2 | \Psi_n \rangle + \frac{1}{2} \cdot \frac{e^2}{4\pi\epsilon_0} \int d^3r \int d^3r' \, \frac{(n(\mathbf{r}) + Z(\mathbf{r}))\,(n(\mathbf{r}') + Z(\mathbf{r}'))}{|\mathbf{r} - \mathbf{r}'|} + E_{xc}[n(\mathbf{r})] \quad (1)$$

Here, $|\Psi_n\rangle$ are one-particle electron states, f_n are the state occupations, $n(\mathbf{r}) = \sum_n f_n \Psi_n^*(\mathbf{r})\Psi_n(\mathbf{r})$ is the electron density and $Z(\mathbf{r}) = -\sum_R \mathcal{Z}_R \delta(\mathbf{r} - \mathbf{R}_R)$ is the nuclear charge density density expressed in electron charges. $\mathcal{Z}_R$ is the atomic number of a nucleus at position $\mathbf{R}_R$. It is implicitly assumed that the infinite self-interaction of the nuclei is removed. The exchange and correlation functional contains all the difficulties of the many-electron problem. The main conclusion of the density functional theory is that E_{xc} is a functional of the density.

We use Dirac's bra and ket notation. A wavefunction Ψ_n corresponds to a ket $|\Psi_n\rangle$, the complex conjugate wave function Ψ_n^* corresponds to a bra $\langle\Psi_n|$, and a scalar product $\int d^3r \Psi_n^*(\mathbf{r})\Psi_m(\mathbf{r})$ is written as $\langle\Psi_n|\Psi_m\rangle$. Vectors in the 3-d coordinate space are indicated by boldfaced symbols. Note that we use $\mathbf{R}$ as position vector and R as atom index.

In current implementations, the exchange and correlation functional $E_{xc}[n(\mathbf{r})]$ has the form

$$E_{xc}[n(\mathbf{r})] = \int d^3r \; F_{xc}(n(\mathbf{r}), |\nabla n(\mathbf{r})|)$$

where F_{xc} is a parameterized function of the density and its gradients. Such functionals are called gradient corrected. In local spin density functional theory, F_{xc} furthermore depends on the spin density and its derivatives. A review of the earlier developments has been given by Parr[40].

The electronic ground state is determined by minimizing the total energy functional $E[\Psi_n]$ of Eq. 1 at a fixed ionic geometry. The one-particle wavefunctions have to be orthogonal. This constraint is implemented with the method of Lagrange multipliers. We obtain the ground state wavefunctions from the extremum condition for

$$F[\Psi_n(\mathbf{r}), \Lambda_{m\,n}] = E[\Psi_n] - \sum_{n\,m} [\langle \Psi_n | \Psi_m \rangle - \delta_{n\,m}] \Lambda_{m\,n} \quad (2)$$

with respect to the wavefunctions and the Lagrange multipliers $\Lambda_{m\,n}$. The extremum condition for the wavefunctions has the form

$$H|\Psi_n\rangle f_n = \sum_m |\Psi_m\rangle \Lambda_{m\,n} \quad (3)$$

3

where $H = -\frac{\hbar^2}{2m_e}\nabla^2 + v_{\text{eff}}(\mathbf{r})$ is the effective one-particle Hamilton operator. The effective potential depends itself on the electron density via

$$v_{eff}(\mathbf{r}) \;=\; \frac{e^2}{4\pi\epsilon_0}\int d^3r' \frac{n(\mathbf{r}') + Z(\mathbf{r}')}{|\mathbf{r}-\mathbf{r}'|} + \mu_{xc}(\mathbf{r})$$

where $\mu_{xc}(\mathbf{r}) = \frac{\delta E_{xc}[n(\mathbf{r})]}{\delta n(\mathbf{r})}$ is the functional derivative of the exchange and correlation functional.

After a unitary transformation that diagonalizes the matrix of Lagrange multipliers $\Lambda_{m\,n}$, we obtain the Kohn-Sham equations.

$$H|\Psi_n\rangle = |\Psi_n\rangle\epsilon_n \tag{4}$$

The one-particle energies ϵ_n are the eigenvalues of $\Lambda_{n\,m}\frac{f_n+f_m}{2f_nf_m}$[9].

The remaining one-electron Schrödinger equations, namely the Kohn-Sham equations given above, still pose substantial numerical difficulties: (1) in the atomic region near the nucleus, the kinetic energy of the electrons is large, resulting in rapid oscillations of the wavefunction that require fine grids for an accurate numerical representation. On the other hand, the large kinetic energy makes the Schrödinger equation stiff, so that a change of the chemical environment has little effect on the shape of the wavefunction. Therefore, the wavefunction in the atomic region can be represented well already by a small basis set. (2) In the bonding region between the atoms the situation is opposite. The kinetic energy is small and the wavefunction is smooth. However, the wavefunction is flexible and responds strongly to the environment. This requires large and nearly complete basis sets.

Combining these different requirements is non-trivial and various strategies have been developed.

- The atomic point of view has been most appealing to quantum chemists. Basis functions that resemble atomic orbitals are chosen. They exploit that the wavefunction in the atomic region can be described by a few basis functions, while the chemical bond is described by the overlapping tails of these atomic orbitals. Most techniques in this class are a compromise of, on the one hand, a well adapted basis set, where the basis functions are difficult to handle, and on the other hand numerically convenient basis functions such as Gaussians, where the inadequacies are compensated by larger basis sets.

- Pseudopotentials regard an atom as a perturbation of the free electron gas. The most natural basis functions are plane-waves. Plane waves basis sets are in principle complete and suitable for sufficiently smooth wavefunctions. The disadvantage of the comparably large basis sets required is offset by their extreme numerical simplicity. Finite plane-wave expansions are, however, absolutely inadequate to describe the strong oscillations of the wavefunctions near the nucleus. In the pseudopotential approach the Pauli repulsion of the core electrons is therefore described by an effective potential that expels the valence electrons from the core region. The resulting wavefunctions are smooth and can be represented well by plane-waves. The price to pay is that all information on the charge density and wavefunctions near the nucleus is lost.

- Augmented wave methods compose their basis functions from atom-like wavefunctions in the atomic regions and a set of functions, called envelope functions, appropriate for the bonding in between. Space is divided accordingly into atom-centered spheres, defining the atomic regions, and an interstitial region in between. The partial solutions of the different regions, are matched at the interface between atomic and interstitial regions.

The projector augmented wave method is an extension of augmented wave methods and the pseudopotential approach, which combines their traditions into a unified electronic structure method.
After describing the underlying ideas of the various approaches let us briefly review the history of augmented wave methods and the pseudopotential approach. We do not discuss the atomic-orbital based methods, because our focus is the PAW method and its ancestors.

II. AUGMENTED WAVE METHODS

The augmented wave methods have been introduced in 1937 by Slater[49] and were later modified by Korringa[31], Kohn and Rostokker[29]. They approached the electronic structure as a scattered-electron problem. Consider an electron beam, represented by a plane-wave, traveling through a solid. It undergoes multiple scattering at the atoms. If for some energy, the outgoing scattered waves interfere destructively, a bound state has been determined. This approach can be translated into a basis set method with energy and potential dependent

basis functions. In order to make the scattered wave problem tractable, a model potential had to be chosen: The so-called muffin-tin potential approximates the true potential by a constant in the interstitial region and by a spherically symmetric potential in the atomic region.

Augmented wave methods reached adulthood in the 1970s: O.K. Andersen[1] showed that the energy dependent basis set of Slater's APW method can be mapped onto one with energy independent basis functions, by linearizing the partial waves for the atomic regions in energy. In the original APW approach, one had to determine the zeros of the determinant of an energy dependent matrix, a nearly intractable numerical problem for complex systems. With the new energy independent basis functions, however, the problem is reduced to the much simpler generalized eigenvalue problem, which can be solved using efficient numerical techniques. Furthermore, the introduction of well defined basis sets paved the way for full-potential calculations[32]. In that case the muffin-tin approximation is used solely to define the basis set $|\chi_i\rangle$, while the matrix elements $\langle\chi_i|H|\chi_j\rangle$ of the Hamiltonian are evaluated with the full potential.

In the augmented wave methods one constructs the basis set for the atomic region by solving the radial Schrödinger equation for the spheridized effective potential

$$\left[\frac{-\hbar^2}{2m_e}\nabla^2 + v_{eff}(\mathbf{r}) - \epsilon\right]\phi_{\ell\,m}(\epsilon,\mathbf{r}) \;=\; 0$$

as function of energy. Note that a partial wave $\phi_{\ell\,m}(\epsilon,\mathbf{r})$ is an angular momentum eigenstate and can be expressed as a product of a radial function and a spherical harmonic. The energy dependent partial wave is expanded in a Taylor expansion about some reference energy $\epsilon_{\nu\,\ell}$

$$\phi_{\ell\,m}(\epsilon,\mathbf{r}) \;=\; \phi_{\nu\,\ell\,m}(\mathbf{r}) + (\epsilon-\epsilon_{\nu\,\ell})\dot{\phi}_{\nu\,\ell\,m}(\mathbf{r}) + O((\epsilon-\epsilon_{\nu\,\ell})^2)$$

where $\phi_{\nu\,\ell\,m}(\mathbf{r}) = \phi_{\ell\,m}(\epsilon_{\nu\,\ell},\mathbf{r})$. The energy derivative of the partial wave $\dot{\phi}_\nu(\mathbf{r}) = \left.\frac{\partial\phi(\epsilon\,\mathbf{r})}{\partial\epsilon}\right|_{\epsilon_{\nu,\ell}}$ solves the equation

$$\left[\frac{-\hbar^2}{2m_e}\nabla^2 + v_{eff}(\mathbf{r}) - \epsilon_{\nu\,\ell}\right]\dot{\phi}_{\nu\,\ell\,m}(\mathbf{r}) \;=\; \phi_{\nu\,\ell\,m}(\mathbf{r})$$

Next one starts from a regular basis set, such as plane-waves, Gaussians or Hankel functions. These basis functions are called envelope functions $|\tilde{\chi}_i\rangle$. Within the atomic region they are replaced by the partial waves and their energy derivatives, such that the resulting

wavefunction is continuous and differentiable.

$$\chi_i(\mathbf{r}) = \tilde{\chi}_i(\mathbf{r}) - \sum_R \theta_R(\mathbf{r})\tilde{\chi}_i(\mathbf{r}) + \sum_{R\,\ell\,m} \theta_R(\mathbf{r}) \left[\phi_{\nu\,R\,\ell\,m}(\mathbf{r})a_{R\,\ell\,m\,i} + \dot{\phi}_{\nu\,R\,\ell\,m}(\mathbf{r})b_{R\,\ell\,m\,i}\right] \quad (5)$$

$\theta_R(\mathbf{r})$ is a step function that is unity within the augmentation sphere centered at $\mathbf{R}_R$ and zero elsewhere. The augmentation sphere is atom-centered and has a radius about equal to the covalent radius. This radius is called the muffin-tin radius, if the spheres of neighboring atoms touch. These basis functions describe only the valence states; the core states are localized within the augmentation sphere and are obtained directly by radial integration of the Schrödinger equation within the augmentation sphere.

The coefficients $a_{R\,\ell\,m\,i}$ and $b_{R\,\ell\,m\,i}$ are obtained for each $|\tilde{\chi}_i\rangle$ as follows: The envelope function is decomposed around each atomic site into spherical harmonics multiplied by radial functions.

$$\tilde{\chi}_i(\mathbf{r}) = \sum_{\ell\,m} u_{R\,\ell\,m\,i}(|\mathbf{r} - \mathbf{R}_R|)Y_{\ell\,m}(\mathbf{r} - \mathbf{R}_R) \quad (6)$$

Analytical expansions for plane-waves, Hankel functions or Gaussians exist. The radial parts of the partial waves $\phi_{\nu\,R\,\ell\,m}$ and $\dot{\phi}_{\nu\,R\,\ell\,m}$ are matched with value and derivative to $u_{R\,\ell\,m\,i}(|\mathbf{r}|)$, which yields the expansion coefficients $a_{R\,\ell\,m\,i}$ and $b_{R\,\ell\,m\,i}$.

If the envelope functions are plane-waves, the resulting method is called the linear augmented plane-wave (LAPW) method. If the envelope functions are Hankel functions, the method is called linear muffin-tin orbital (LMTO) method .

A good review of the LAPW method[1] has been given by Singh[46]. Let us now briefly mention the major developments of the LAPW method: Soler[50] introduced the idea of additive augmentation: While augmented plane-waves are discontinuous at the surface of the augmentation sphere if the expansion in spherical harmonics in Eq. 5 is truncated, Soler replaced the second term in Eq. 5 by an expansion of the plane-wave with the same angular momentum truncation as in the third term. This dramatically improved the convergence of the angular momentum expansion. Singh[45] introduced so-called local orbitals, which are non-zero only within a muffin-tin sphere, where they are superpositions of ϕ and $\dot{\phi}$ functions from different expansion energies. Local orbitals substantially increase the energy transferability. Sjöstedt[47] relaxed the condition that the basis functions are differentiable at the sphere radius. In addition she introduced local orbitals, which are confined inside the sphere, and that also have a kink at the sphere boundary. Due to the large energy-cost of kinks, they

will cancel, once the total energy is minimized. The increased variational degree of freedom in the basis leads to a dramatically improved plane-wave convergence[37].

The second variant of the linear methods is the LMTO method[1]. A good introduction into the LMTO method is the book by Skriver[48]. The LMTO method uses Hankel functions as envelope functions. The atomic spheres approximation (ASA) provides a particularly simple and efficient approach to the electronic structure of very large systems. In the ASA the augmentation spheres are blown up so that their volume are equal to the total volume and the first two terms in Eq. 5 are ignored. The main deficiency of the LMTO-ASA method is the limitation to structures that can be converted into a closed packed arrangement of atomic and empty spheres. Furthermore energy differences due to structural distortions are often qualitatively incorrect. Full potential versions of the LMTO method, that avoid these deficiencies of the ASA have been developed. The construction of tight binding orbitals as superposition of muffin-tin orbitals[2] showed the underlying principles of the empirical tight-binding method and prepared the ground for electronic structure methods that scale linearly instead of with the third power of the number of atoms. The third generation LMTO[3] allows to construct true minimal basis sets, which require only one orbital per electron-pair for insulators. In addition they can be made arbitrarily accurate in the valence band region, so that a matrix diagonalization becomes unnecessary. The first steps towards a full-potential implementation, that promises a good accuracy, while maintaining the simplicity of the of the LMTO-ASA method are currently under way. Through the minimal basis-set construction the LMTO method offers unrivaled tools for the analysis of the electronic structure and has been extensively used in hybrid methods combining density functional theory with model Hamiltonians for materials with strong electron correlations[19]

III. PSEUDOPOTENTIALS

Pseudopotentials have been introduced to (1) avoid describing the core electrons explicitely and (2) to avoid the rapid oscillations of the wavefunction near the nucleus, which normally require either complicated or large basis sets.

The pseudopotential approach traces back to 1940 when C. Herring invented the orthogonalized plane-wave method[20]. Later, Phillips[43] and Antoncik[4] replaced the orthogonality condition by an effective potential, which mimics the Pauli-repulsion by the core electrons

and thus compensates the electrostatic attraction by the nucleus. In practice, the potential was modified, for example, by cutting off the singular potential of the nucleus at a certain value. This was done with a few parameters that have been adjusted to reproduce the measured electronic band structure of the corresponding solid.

Hamann, Schlüter and Chiang[18] showed in 1979 how pseudopotentials can be constructed in such a way, that their scattering properties are identical to that of an atom to first order in energy. These first-principles pseudopotentials relieved the calculations from the restrictions of empirical parameters. Highly accurate calculations have become possible especially for semiconductors and simple metals. An alternative approach towards first-principles pseudopotentials[58] preceeded the one mentioned above.

A. The idea behind Pseudopotential construction

In order to construct a first-principles pseudopotential, one starts out with an all-electron density-functional calculation for a spherical atom. Such calculations can be performed efficiently on radial grids. They yield the atomic potential and wavefunctions $\phi_{\ell\,m}(\mathbf{r})$. Due to the spherical symmetry, the radial parts of the wavefunctions for different magnetic quantum numbers m are identical.

For the valence wavefunctions one constructs pseudo wavefunctions $|\tilde{\phi}_{\ell\,m}\rangle$: There are numerous ways[6,27,35,52] to construct the pseudo wavefunctions. They must be identical to the true wave functions outside the augmentation region, which is called core-region in the context of the pseudopotential approach. Inside the augmentation region the pseudo wavefunction should be node-less and have the same norm as the true wavefunctions, that is $\langle\tilde{\phi}_{\ell\,m}|\tilde{\phi}_{\ell\,m}\rangle = \langle\phi_{\ell\,m}|\phi_{\ell\,m}\rangle$ (compare Figure 1).

From the pseudo wavefunction, a potential $u_\ell(\mathbf{r})$ can be reconstructed by inverting the respective Schrödinger equation.

$$\left[-\frac{\hbar^2}{2m_e}\nabla^2 + u_\ell(\mathbf{r}) - \epsilon_{\ell\,m}\right]\tilde{\phi}_{\ell\,m}(\mathbf{r}) = 0 \;\Rightarrow\; u_\ell(\mathbf{r}) = \epsilon + \frac{1}{\tilde{\phi}_{\ell\,m}(\mathbf{r})}\cdot\frac{\hbar^2}{2m_e}\nabla^2\tilde{\phi}_{\ell\,m}(\mathbf{r})$$

This potential $u_\ell(\mathbf{r})$ (compare Figure 1), which is also spherically symmetric, differs from one main angular momentum ℓ to the other.

Next we define an effective pseudo Hamiltonian

$$\tilde{H}_\ell = -\frac{\hbar^2}{2m_e}\nabla^2 + v_\ell^{ps}(\mathbf{r}) + \frac{e^2}{4\pi\epsilon_0}\int d^3r'\frac{\tilde{n}(\mathbf{r}') + \tilde{Z}(\mathbf{r}')}{|\mathbf{r}-\mathbf{r}'|} + \mu_{xc}([n(\mathbf{r})],\mathbf{r})$$

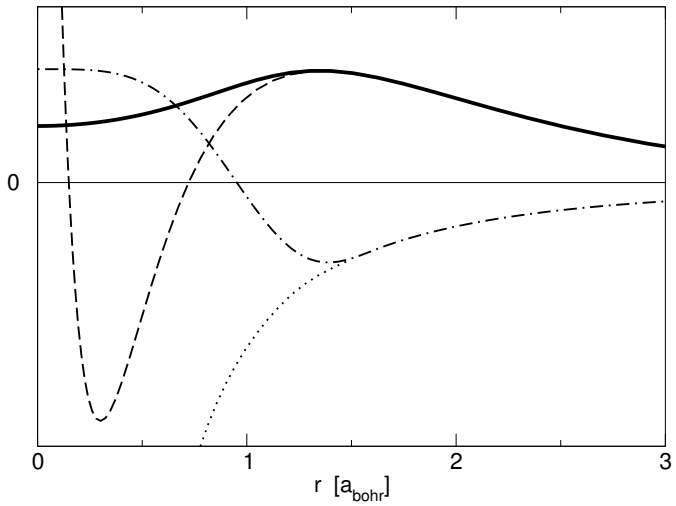

FIG. 1: Illustration of the pseudopotential concept at the example of the $3s$ wavefunction of Si. The solid line shows the radial part of the pseudo wavefunction $\tilde{\phi}_{\ell\, m}$. The dashed line corresponds to the all-electron wavefunction $\phi_{\ell\, m}$ which exhibits strong oscillations at small radii. The angular momentum dependent pseudopotential u_ℓ (dash-dotted line) deviates from the all-electron one v_{eff} (dotted line) inside the augmentation region. The data are generated by the fhi98PP code[15].

and determine the pseudopotentials v_ℓ^{ps} such that the pseudo Hamiltonian produces the pseudo wavefunctions, that is

$$v_\ell^{ps}(\mathbf{r}) \;=\; u_\ell(\mathbf{r}) - \frac{e^2}{4\pi\epsilon_0}\int d^3r'\,\frac{\tilde{n}(\mathbf{r}') + \tilde{Z}(\mathbf{r}')}{|\mathbf{r}-\mathbf{r}'|} - \mu_{xc}([\tilde{n}(\mathbf{r})],\mathbf{r}) \tag{7}$$

This process is called "unscreening".

$\tilde{Z}(\mathbf{r})$ mimics the charge density of the nucleus and the core electrons. It is usually an atom-centered, spherical Gaussian that is normalized to the charge of nucleus and core of that atom. In the pseudopotential approach, $\tilde{Z}_R(\mathbf{r})$ it does not change with the potential. The pseudo density $\tilde{n}(\mathbf{r}) = \sum_n f_n \tilde{\Psi}_n^*(\mathbf{r})\tilde{\Psi}_n(\mathbf{r})$ is constructed from the pseudo wavefunctions.

In this way we obtain a different potential for each angular momentum channel. In order to apply these potentials to a given wavefunction, the wavefunction must first be decomposed into angular momenta. Then each component is applied to the pseudopotential v_ℓ^{ps} for the corresponding angular momentum.

The pseudopotential defined in this way can be expressed in a semi-local form

$$v^{ps}(\mathbf{r},\mathbf{r}') \;=\; \bar{v}(\mathbf{r})\delta(\mathbf{r}-\mathbf{r}') + \sum_{\ell\,m}\left[Y_{\ell\,m}(\mathbf{r})\left[v_\ell^{ps}(\mathbf{r})-\bar{v}(\mathbf{r})\right]\frac{\delta(|\mathbf{r}|-|\mathbf{r}'|)}{|\mathbf{r}|^2}Y^*_{\ell\,m}(\mathbf{r}')\right] \tag{8}$$

The local potential $\bar{v}(\mathbf{r})$ only acts on those angular momentum components, not included in the expansion of the pseudopotential construction. Typically it is chosen to cancel the most expensive nonlocal terms, the one corresponding to the highest physically relevant angular momentum.

The pseudopotential is non-local as it depends on two position arguments, $\mathbf{r}$ and $\mathbf{r}'$. The expectation values are evaluated as a double integral

$$\langle\tilde{\Psi}|v_{ps}|\tilde{\Psi}\rangle \;=\; \int d^3r \int d^3r'\; \tilde{\Psi}^*(\mathbf{r})v^{ps}(\mathbf{r},\mathbf{r}')\tilde{\Psi}(\mathbf{r}')$$

The semi-local form of the pseudopotential given in Eq. 8 is computationally expensive. Therefore, in practice one uses a separable form of the pseudopotential[8,28,55].

$$v^{ps} \;\approx\; \sum_{i\,j} v^{ps}|\tilde{\phi}_i\rangle\left[\langle\tilde{\phi}_j|v^{ps}|\tilde{\phi}_i\rangle\right]^{-1}_{i\,j}\langle\tilde{\phi}_j|v^{ps} \tag{9}$$

Thus the projection onto spherical harmonics used in the semi-local form of Eq. 8 is replaced by a projection onto angular momentum dependent functions $|v^{ps}\tilde{\phi}_i\rangle$.

The indices i and j are composite indices containing the atomic-site index R, the angular momentum quantum numbers ℓ, m and an additional index α. The index α distinguishes partial waves with otherwise identical indices R, ℓ, m, as more than one partial wave per site and angular momentum is allowed. The partial waves may be constructed as eigenstates to the pseudopotential v_ℓ^{ps} for a set of energies.

One can show that the identity of Eq. 9 holds by applying a wavefunction $|\tilde{\Psi}\rangle = \sum_i |\tilde{\phi}_i\rangle c_i$ to both sides. If the set of pseudo partial waves $|\tilde{\phi}_i\rangle$ in Eq. 9 is complete, the identity is exact. The advantage of the separable form is that $\langle\tilde{\phi}v^{ps}|$ is treated as one function, so that expectation values are reduced to combinations of simple scalar products $\langle\tilde{\phi}_i v^{ps}|\tilde{\Psi}\rangle$.

B. The Pseudopotential total energy

The total energy of the pseudopotential method can be written in the form

$$E \;=\; \sum_n f_n\langle\tilde{\Psi}_n| - \frac{\hbar^2}{2m_e}\nabla^2|\tilde{\Psi}_n\rangle + E_{self} + \sum_n f_n\langle\tilde{\Psi}_n|v_{ps}|\tilde{\Psi}_n\rangle$$

11

$$+\frac{1}{2}\cdot\frac{e^2}{4\pi\epsilon_0}\int d^3r\int d^3r'\frac{\left[\tilde{n}(\mathbf{r})+\tilde{Z}(\mathbf{r})\right]\left[\tilde{n}(\mathbf{r}')+\tilde{Z}(\mathbf{r}')\right]}{|\mathbf{r}-\mathbf{r}'|}+E_{xc}[\tilde{n}(\mathbf{r})] \qquad (10)$$

The constant E_{self} is adjusted such that the total energy of the atom is the same for an all-electron calculation and the pseudopotential calculation.

For the atom, from which it has been constructed, this construction guarantees that the pseudopotential method produces the correct one-particle energies for the valence states and that the wave functions have the desired shape.

While pseudopotentials have proven to be accurate for a large variety of systems, there is no strict guarantee that they produce the same results as an all-electron calculation, if they are used in a molecule or solid. The error sources can be divided into two classes:

- Energy transferability problems: Even for the potential of the reference atom, the scattering properties are accurate only in given energy window.
- Charge transferability problems: In a molecule or crystal, the potential differs from that of the isolated atom. The pseudopotential, however, is strictly valid only for the isolated atom.

The plane-wave basis set for the pseudo wavefunctions is defined by the shortest wave length $\lambda = 2\pi/|G|$ via the so-called plane wave cutoff $E_{PW} = \frac{\hbar^2 G_{max}^2}{2m_e}$. It is often specified in Rydberg (1 Ry=$\frac{1}{2}$ H≈13.6 eV). The plane-wave cutoff is the highest kinetic energy of all basis functions. The basis-set convergence can systematically be controlled by increasing the plane-wave cutoff.

The charge transferability is substantially improved by including a nonlinear core correction[36] into the exchange-correlation term of Eq. 10. Hamann[17] showed, how to construct pseudopotentials also from unbound wavefunctions. Vanderbilt[34,55] generalized the pseudopotential method to non-normconserving pseudopotentials, so-called ultra-soft pseudopotentials, which dramatically improves the basis-set convergence. The formulation of ultra-soft pseudopotentials has already many similarities with the projector augmented wave method. Truncated separable pseudopotentials suffer sometimes from so-called ghost states. These are unphysical core-like states, which render the pseudopotential useless. These problems have been discussed by Gonze[16]. Quantities such as hyperfine parameters that depend on the full wavefunctions near the nucleus, can be extracted approximately[54]. A good review about pseudopotential methodology has been written by Payne[41] and Singh[46].

In 1985 R. Car and M. Parrinello published the ab-initio molecular dynamics method[14]. Simulations of the atomic motion have become possible on the basis of state-of-the-art electronic structure methods. Besides making dynamical phenomena and finite temperature effects accessible to electronic structure calculations, the ab-initio molecular dynamics method also introduced a radically new way of thinking into electronic structure methods. Diagonalization of a Hamilton matrix has been replaced by classical equations of motion for the wavefunction coefficients. If one applies friction, the system is quenched to the ground state. Without friction truly dynamical simulations of the atomic structure are performed. Using thermostats[12,13,24,39] simulations at constant temperature can be performed. The Car-Parrinello method treats electronic wavefunctions and atomic positions on an equal footing.

IV. PROJECTOR AUGMENTED WAVE METHOD

The Car-Parrinello method had been implemented first for the pseudopotential approach. There seemed to be unsurmountable barriers against combining the new technique with augmented wave methods. The main problem was related to the potential dependent basis set used in augmented wave methods: the Car-Parrinello method requires a well defined and unique total energy functional of atomic positions and basis set coefficients. Furthermore the analytic evaluation of the first partial derivatives of the total energy with respect to wave functions, $H|\Psi_n\rangle$, and atomic position, the forces, must be possible. Therefore, it was one of the main goals of the PAW method to introduce energy and potential independent basis sets that were as accurate as the previously used augmented basis sets. Other requirements have been: (1) The method should at least match the efficiency of the pseudopotential approach for Car-Parrinello simulations. (2) It should become an exact theory when converged and (3) its convergence should be easily controlled. We believe that these criteria have been met, which explains why the PAW method becomes increasingly wide spread today.

A. Transformation theory

At the root of the PAW method lies a transformation, that maps the true wavefunctions with their complete nodal structure onto auxiliary wavefunctions, that are numerically convenient. We aim for smooth auxiliary wavefunctions, which have a rapidly convergent plane-

wave expansion. With such a transformation we can expand the auxiliary wave functions into a convenient basis set such as plane-waves, and evaluate all physical properties after reconstructing the related physical (true) wavefunctions.

Let us denote the physical one-particle wavefunctions as $|\Psi_n\rangle$ and the auxiliary wavefunctions as $|\tilde{\Psi}_n\rangle$. Note that the tilde refers to the representation of smooth auxiliary wavefunctions and n is the label for a one-particle state and contains a band index, a k-point and a spin index. The transformation from the auxiliary to the physical wave functions is denoted by $\mathcal{T}$.

$$|\Psi_n\rangle = \mathcal{T}|\tilde{\Psi}_n\rangle \tag{11}$$

Now we express the constrained density functional F of Eq. 2 in terms of our auxiliary wavefunctions

$$F[\mathcal{T}\tilde{\Psi}_n, \Lambda_{m\,n}] = E[\mathcal{T}\tilde{\Psi}_n] - \sum_{n\,m}[\langle\tilde{\Psi}_n|\mathcal{T}^\dagger\mathcal{T}|\tilde{\Psi}_m\rangle - \delta_{n\,m}]\Lambda_{m\,n} \tag{12}$$

The variational principle with respect to the auxiliary wavefunctions yields

$$\mathcal{T}^\dagger H\mathcal{T}|\tilde{\Psi}_n\rangle = \mathcal{T}^\dagger\mathcal{T}|\tilde{\Psi}_n\rangle\epsilon_n. \tag{13}$$

Again we obtain a Schrödinger-like equation (see derivation of Eq. 4), but now the Hamilton operator has a different form, $\tilde{H} = \mathcal{T}^\dagger H\mathcal{T}$, an overlap operator $\tilde{O} = \mathcal{T}^\dagger\mathcal{T}$ occurs, and the resulting auxiliary wavefunctions are smooth.

When we evaluate physical quantities we need to evaluate expectation values of an operator A, which can be expressed in terms of either the true or the auxiliary wavefunctions.

$$\langle A\rangle \;=\; \sum_n f_n\langle\Psi_n|A|\Psi_n\rangle = \sum_n f_n\langle\tilde{\Psi}_n|\mathcal{T}^\dagger A\mathcal{T}|\tilde{\Psi}_n\rangle \tag{14}$$

In the representation of auxiliary wavefunctions we need to use transformed operators $\tilde{A} = \mathcal{T}^\dagger A\mathcal{T}$. As it is, this equation only holds for the valence electrons. The core electrons are treated differently as will be shown below.

The transformation takes us conceptionally from the world of pseudopotentials to that of augmented wave methods, which deal with the full wavefunctions. We will see that our auxiliary wavefunctions, which are simply the plane-wave parts of the full wavefunctions, translate into the wavefunctions of the pseudopotential approach. In the PAW method the

auxiliary wavefunctions are used to construct the true wavefunctions and the total energy functional is evaluated from the latter. Thus it provides the missing link between augmented wave methods and the pseudopotential method, which can be derived as a well-defined approximation of the PAW method.

In the original paper[9], the auxiliary wavefunctions have been termed pseudo wavefunctions and the true wavefunctions have been termed all-electron wavefunctions, in order to make the connection more evident. We avoid this notation here, because it resulted in confusion in cases, where the correspondence is not clear-cut.

B. Transformation operator

Sofar, we have described how we can determine the auxiliary wave functions of the ground state and how to obtain physical information from them. What is missing, is a definition of the transformation operator $\mathcal{T}$.

The operator $\mathcal{T}$ has to modify the smooth auxiliary wave function in each atomic region, so that the resulting wavefunction has the correct nodal structure. Therefore, it makes sense to write the transformation as identity plus a sum of atomic contributions $\mathcal{S}_R$

$$\mathcal{T} = 1 + \sum_R \mathcal{S}_R. \tag{15}$$

For every atom, $\mathcal{S}_R$ adds the difference between the true and the auxiliary wavefunction.

The local terms $\mathcal{S}_R$ are defined in terms of solutions $|\phi_i\rangle$ of the Schrödinger equation for the isolated atoms. This set of partial waves $|\phi_i\rangle$ will serve as a basis set so that, near the nucleus, all relevant valence wavefunctions can be expressed as superposition of the partial waves with yet unknown coefficients.

$$\Psi(\mathbf{r}) = \sum_{i \in R} \phi_i(\mathbf{r}) c_i \quad \text{for} \quad |\mathbf{r} - \mathbf{R}_R| < r_{c\,R} \tag{16}$$

With $i \in R$ we indicate those partial waves that belong to site R.

Since the core wavefunctions do not spread out into the neighboring atoms, we will treat them differently. Currently we use the frozen-core approximation, which imports the density and the energy of the core electrons from the corresponding isolated atoms. The transformation $\mathcal{T}$ shall produce only wavefunctions orthogonal to the core electrons, while the core electrons are treated separately. Therefore, the set of atomic partial waves $|\phi_i\rangle$ includes only valence states that are orthogonal to the core wavefunctions of the atom.

15

For each of the partial waves we choose an auxiliary partial wave $|\tilde{\phi}_i\rangle$. The identity

$$\begin{aligned} |\phi_i\rangle &= (1+\mathcal{S}_R)|\tilde{\phi}_i\rangle \quad \text{for} \quad i \in R \\ \mathcal{S}_R|\tilde{\phi}_i\rangle &= |\phi_i\rangle - |\tilde{\phi}_i\rangle \end{aligned} \tag{17}$$

defines the local contribution $\mathcal{S}_R$ to the transformation operator. Since $1+\mathcal{S}_R$ shall change the wavefunction only locally, we require that the partial waves $|\phi_i\rangle$ and their auxiliary counter parts $|\tilde{\phi}_i\rangle$ are pairwise identical beyond a certain radius $r_{c\,R}$.

$$\phi_i(\mathbf{r}) = \tilde{\phi}_i(\mathbf{r}) \quad \text{for} \quad i \in R \quad \text{and} \quad |\mathbf{r}-\mathbf{R}_R| > r_{c\,R} \tag{18}$$

Note that the partial waves are not necessarily bound states and are therefore not normalizable, unless we truncate them beyond a certain radius $r_{c\,R}$. The PAW method is formulated such that the final results do not depend on the location where the partial waves are truncated, as long as this is not done too close to the nucleus and identical for auxiliary and all-electron partial waves.

In order to be able to apply the transformation operator to an arbitrary auxiliary wavefunction, we need to be able to expand the auxiliary wavefunction locally into the auxiliary partial waves.

$$\tilde{\Psi}(\mathbf{r}) = \sum_{i\in R} \tilde{\phi}_i(\mathbf{r}) c_i = \sum_{i\in R} \tilde{\phi}_i(\mathbf{r}) \langle \tilde{p}_i|\tilde{\Psi}\rangle \quad \text{for} \quad |\mathbf{r}-\mathbf{R}_R| < r_{c\,R} \tag{19}$$

which defines the projector functions $|\tilde{p}_i\rangle$. The projector functions probe the local character of the auxiliary wave function in the atomic region. Examples of projector functions are shown in Figure 2. From Eq. 19 we can derive $\sum_{i\in R} |\tilde{\phi}_i\rangle\langle\tilde{p}_i| = 1$, which is valid within $r_{c\,R}$. It can be shown by insertion, that the identity Eq. 19 holds for any auxiliary wavefunction $|\tilde{\Psi}\rangle$ that can be expanded locally into auxiliary partial waves $|\tilde{\phi}_i\rangle$, if

$$\langle \tilde{p}_i|\tilde{\phi}_j\rangle = \delta_{i\,j} \quad \text{for} \quad i,j \in R \tag{20}$$

Note that neither the projector functions nor the partial waves need to be orthogonal among themselves. The projector functions are fully determined with the above conditions and a closure relation, which is related to the unscreening of the pseudopotentials (see Eq. 90 in[9]). By combining Eq. 17 and Eq. 19, we can apply $\mathcal{S}_R$ to any auxiliary wavefunction.

$$\mathcal{S}_R|\tilde{\Psi}\rangle = \sum_{i\in R} \mathcal{S}_R|\tilde{\phi}_i\rangle\langle\tilde{p}_i|\tilde{\Psi}\rangle = \sum_{i\in R} \Big(|\phi_i\rangle - |\tilde{\phi}_i\rangle\Big)\langle\tilde{p}_i|\tilde{\Psi}\rangle \tag{21}$$

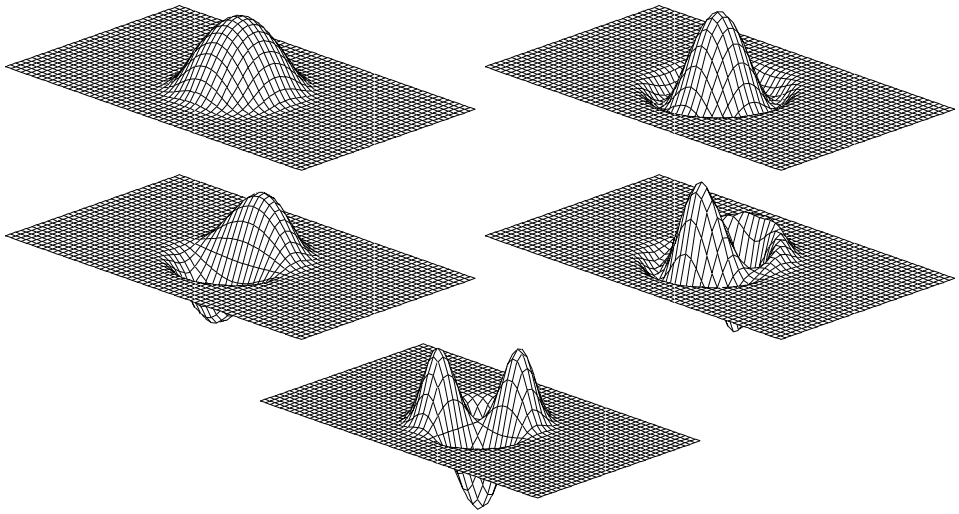

FIG. 2: Projector functions of the chlorine atom. Top: two s-type projector functions, middle: p-type, bottom: d-type.

Hence the transformation operator is

$$\mathcal{T} = 1 + \sum_i \Big(|\phi_i\rangle - |\tilde{\phi}_i\rangle \Big) \langle \tilde{p}_i | \tag{22}$$

where the sum runs over all partial waves of all atoms. The true wave function can be expressed as

$$|\Psi\rangle = |\tilde{\Psi}\rangle + \sum_i \Big(|\phi_i\rangle - |\tilde{\phi}_i\rangle \Big) \langle \tilde{p}_i | \tilde{\Psi} \rangle = |\tilde{\Psi}\rangle + \sum_R \Big(|\Psi^1_R\rangle - |\tilde{\Psi}^1_R\rangle \Big) \tag{23}$$

with

$$|\Psi^1_R\rangle = \sum_{i \in R} |\phi_i\rangle \langle \tilde{p}_i | \tilde{\Psi} \rangle \tag{24}$$

$$|\tilde{\Psi}^1_R\rangle = \sum_{i \in R} |\tilde{\phi}_i\rangle \langle \tilde{p}_i | \tilde{\Psi} \rangle \tag{25}$$

In Fig. 3 the decomposition of Eq. 23 is shown for the example of the bonding p-σ state of the Cl_2 molecule.

To understand the expression Eq. 23 for the true wave function, let us concentrate on different regions in space. (1) Far from the atoms, the partial waves are, according to Eq. 18, pairwise identical so that the auxiliary wavefunction is identical to the true wavefunction, that is $\Psi(\mathbf{r}) = \tilde{\Psi}(\mathbf{r})$. (2) Close to an atom R, however, the auxiliary wavefunction is, according to Eq. 19, identical to its one-center expansion, that is $\tilde{\Psi}(\mathbf{r}) = \tilde{\Psi}^1_R(\mathbf{r})$. Hence

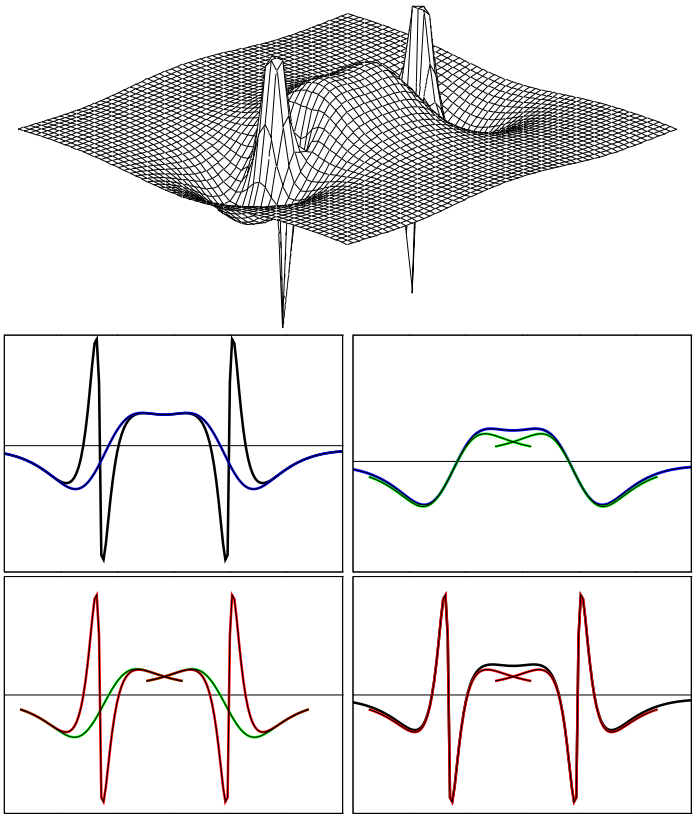

FIG. 3: Bonding p-σ orbital of the Cl_2 molecule and its decomposition of the wavefunction into auxiliary wavefunction and the two one-center expansions. Top-left: True and auxiliary wave function; top-right: auxiliary wavefunction and its partial wave expansion; bottom-left: the two partial wave expansions; bottom-right: true wavefunction and its partial wave expansion.

the true wavefunction $\Psi(\mathbf{r})$ is identical to $\Psi^1_R(\mathbf{r})$, which is built up from partial waves that contain the proper nodal structure.

In practice, the partial wave expansions are truncated. Therefore, the identity of Eq. 19 does not hold strictly. As a result the plane-waves also contribute to the true wavefunction inside the atomic region. This has the advantage that the missing terms in a truncated partial wave expansion are partly accounted for by plane-waves, which explains the rapid convergence of the partial wave expansions. This idea is related to the additive augmentation of the LAPW method of Soler[50].

Frequently, the question comes up, whether the transformation Eq. 22 of the auxiliary wave-

functions indeed provides the true wavefunction. The transformation should be considered merely as a change of representation analogous to a coordinate transform. If the total energy functional is transformed consistently, its minimum will yield auxiliary wavefunctions that produce the correct wave functions $|\Psi\rangle$.

C. Expectation values

Expectation values can be obtained either from the reconstructed true wavefunctions or directly from the auxiliary wave functions

$$\begin{aligned}\langle A\rangle &= \sum_n f_n \langle\Psi_n|A|\Psi_n\rangle + \sum_{n=1}^{N_c}\langle\phi_n^c|A|\phi_n^c\rangle \\ &= \sum_n f_n \langle\tilde{\Psi}_n|\mathcal{T}^\dagger A\mathcal{T}|\tilde{\Psi}_n\rangle + \sum_{n=1}^{N_c}\langle\phi_n^c|A|\phi_n^c\rangle \end{aligned} \tag{26}$$

where f_n are the occupations of the valence states and N_c is the number of core states. The first sum runs over the valence states, and second over the core states $|\phi_n^c\rangle$.
Now we can decompose the matrix element for a wavefunction Ψ into its individual contributions according to Eq. 23.

$$\begin{aligned}\langle\Psi|A|\Psi\rangle &= \langle\tilde{\Psi} + \sum_R(\Psi_R^1 - \tilde{\Psi}_R^1)|A|\tilde{\Psi} + \sum_{R'}(\Psi_{R'}^1 - \tilde{\Psi}_{R'}^1)\rangle \\ &= \underbrace{\langle\tilde{\Psi}|A|\tilde{\Psi}\rangle + \sum_R\Big(\langle\Psi_R^1|A|\Psi_R^1\rangle - \langle\tilde{\Psi}_R^1|A|\tilde{\Psi}_R^1\rangle\Big)}_{\text{part 1}} \\ &+ \underbrace{\sum_R\Big(\langle\Psi_R^1 - \tilde{\Psi}_R^1|A|\tilde{\Psi} - \tilde{\Psi}_R^1\rangle + \langle\tilde{\Psi} - \tilde{\Psi}_R^1|A|\Psi_R^1 - \tilde{\Psi}_R^1\rangle\Big)}_{\text{part 2}} \\ &+ \underbrace{\sum_{R\neq R'}\langle\Psi_R^1 - \tilde{\Psi}_R^1|A|\Psi_{R'}^1 - \tilde{\Psi}_{R'}^1\rangle}_{\text{part 3}}\end{aligned} \tag{27}$$

Only the first part of Eq. 27, is evaluated explicitly, while the second and third parts of Eq. 27 are neglected, because they vanish for sufficiently local operators as long as the partial wave expansion is converged: The function $\Psi_R^1 - \tilde{\Psi}_R^1$ vanishes per construction beyond its augmentation region, because the partial waves are pairwise identical beyond that region. The function $\tilde{\Psi} - \tilde{\Psi}_R^1$ vanishes inside its augmentation region, if the partial wave expansion

is sufficiently converged. In no region of space both functions $\Psi^1_R - \tilde{\Psi}^1_R$ and $\tilde{\Psi} - \tilde{\Psi}^1_R$ are simultaneously nonzero. Similarly the functions $\Psi^1_R - \tilde{\Psi}^1_R$ from different sites are never non-zero in the same region in space. Hence, the second and third parts of Eq. 27 vanish for operators such as the kinetic energy $\frac{-\hbar^2}{2m_e}\nabla^2$ and the real space projection operator $|r\rangle\langle r|$, which produces the electron density. For truly nonlocal operators the parts 2 and 3 of Eq. 27 would have to be considered explicitly.

The expression, Eq. 26, for the expectation value can therefore be written with the help of Eq. 27 as

$$\begin{aligned}
\langle A\rangle &= \sum_n f_n\Big(\langle\tilde{\Psi}_n|A|\tilde{\Psi}_n\rangle + \langle\Psi^1_n|A|\Psi^1_n\rangle - \langle\tilde{\Psi}^1_n|A|\tilde{\Psi}^1_n\rangle\Big) + \sum_{n=1}^{N_c}\langle\phi^c_n|A|\phi^c_n\rangle \\
&= \sum_n f_n\langle\tilde{\Psi}_n|A|\tilde{\Psi}_n\rangle + \sum_{n=1}^{N_c}\langle\tilde{\phi}^c_n|A|\tilde{\phi}^c_n\rangle \\
&+ \sum_R\Big(\sum_{i\,j\in R} D_{i\,j}\langle\phi_j|A|\phi_i\rangle + \sum_{n\in R}^{N_{c,R}}\langle\phi^c_n|A|\phi^c_n\rangle\Big) \\
&- \sum_R\Big(\sum_{i\,j\in R} D_{i\,j}\langle\tilde{\phi}_j|A|\tilde{\phi}_i\rangle + \sum_{n\in R}^{N_{c,R}}\langle\tilde{\phi}^c_n|A|\tilde{\phi}^c_n\rangle\Big)
\end{aligned} \tag{28}$$

where $D_{i\,j}$ is the one-center density matrix defined as

$$D_{i\,j} = \sum_n f_n\langle\tilde{\Psi}_n|\tilde{p}_j\rangle\langle\tilde{p}_i|\tilde{\Psi}_n\rangle = \sum_n\langle\tilde{p}_i|\tilde{\Psi}_n\rangle f_n\langle\tilde{\Psi}_n|\tilde{p}_j\rangle \tag{29}$$

The auxiliary core states, $|\tilde{\phi}^c_n\rangle$ allow to incorporate the tails of the core wavefunction into the plane-wave part, and therefore assure, that the integrations of partial wave contributions cancel strictly beyond r_c. They are identical to the true core states in the tails, but are a smooth continuation inside the atomic sphere. It is not required that the auxiliary wave functions are normalized.

Following this scheme, the electron density is given by

$$n(\mathbf{r}) = \tilde{n}(\mathbf{r}) + \sum_R\Big(n^1_R(\mathbf{r}) - \tilde{n}^1_R(\mathbf{r})\Big) \tag{30}$$

$$\begin{aligned}
\tilde{n}(\mathbf{r}) &= \sum_n f_n\tilde{\Psi}^*_n(\mathbf{r})\tilde{\Psi}_n(\mathbf{r}) + \tilde{n}_c \\
n^1_R(\mathbf{r}) &= \sum_{i\,j\in R} D_{i\,j}\phi^*_j(\mathbf{r})\phi_i(\mathbf{r}) + n_{c\,R} \\
\tilde{n}^1_R(\mathbf{r}) &= \sum_{i\,j\in R} D_{i\,j}\tilde{\phi}^*_j(\mathbf{r})\tilde{\phi}_i(\mathbf{r}) + \tilde{n}_{c\,R}
\end{aligned} \tag{31}$$

where $n_{c\,R}$ is the core density of the corresponding atom and $\tilde{n}_{c\,R}$ is the auxiliary core density that is identical to $n_{c\,R}$ outside the atomic region, but smooth inside.

Before we continue, let us discuss a special point: The matrix element of a general operator with the auxiliary wavefunctions may be slowly converging with the plane-wave expansion, because the operator A may not be well behaved. An example for such an operator is the singular electrostatic potential of a nucleus. This problem can be alleviated by adding an "intelligent zero": If an operator B is purely localized within an atomic region, we can use the identity between the auxiliary wavefunction and its own partial wave expansion

$$0 \;=\; \langle\tilde{\Psi}_n|B|\tilde{\Psi}_n\rangle - \langle\tilde{\Psi}^1_n|B|\tilde{\Psi}^1_n\rangle \tag{32}$$

Now we choose an operator B so that it cancels the problematic behavior of the operator A, but is localized in a single atomic region. By adding B to the plane-wave part and the matrix elements with its one-center expansions, the plane-wave convergence can be improved without affecting the converged result. A term of this type, namely $\bar{v}$ will be introduced in the next section to cancel the Coulomb singularity of the potential at the nucleus.

D. Total Energy

Like wavefunctions and expectation values also the total energy can be divided into three parts.

$$E[\tilde{\Psi}_n, R_R] \;=\; \tilde{E} + \sum_R \Big(E^1_R - \tilde{E}^1_R\Big) \tag{33}$$

The plane-wave part $\tilde{E}$ involves only smooth functions and is evaluated on equi-spaced grids in real and reciprocal space. This part is computationally most demanding, and is similar to the expressions in the pseudopotential approach.

$$\begin{aligned}\tilde{E} \;=\; & \sum_n \langle\tilde{\Psi}_n|\frac{-\hbar^2}{2m_e}\nabla^2|\tilde{\Psi}_n\rangle \\ & + \;\frac{1}{2}\cdot\frac{e^2}{4\pi\epsilon_0}\int d^3r\int d^3r'\frac{[\tilde{n}(\mathbf{r})+\tilde{Z}(\mathbf{r})][\tilde{n}(\mathbf{r}')+\tilde{Z}(\mathbf{r}')]}{|\mathbf{r}-\mathbf{r}'|} \\ & + \;\int d^3r\bar{v}(\mathbf{r})\tilde{n}(\mathbf{r}) + E_{xc}[\tilde{n}(\mathbf{r})]\end{aligned} \tag{34}$$

$\tilde{Z}(\mathbf{r})$ is an angular-momentum dependent core-like density that will be described in detail below. The remaining parts can be evaluated on radial grids in a spherical harmonics expan-

sion. The nodal structure of the wavefunctions can be properly described on a logarithmic radial grid that becomes very fine near nucleus,

$$\begin{aligned} E^1_R &= \sum_{i\,j\in R} D_{i\,j}\langle\phi_j|\frac{-\hbar^2}{2m_e}\nabla^2|\phi_i\rangle + \sum_{n\in R}^{N_{c,R}}\langle\phi^c_n|\frac{-\hbar^2}{2m_e}\nabla^2|\phi^c_n\rangle \\ &+ \frac{1}{2}\cdot\frac{e^2}{4\pi\epsilon_0}\int d^3r\int d^3r'\frac{[n^1(\mathbf{r})+Z(\mathbf{r})][n^1(\mathbf{r}')+Z(\mathbf{r}')]}{|\mathbf{r}-\mathbf{r}'|} \\ &+ E_{xc}[n^1(\mathbf{r})] \qquad (35) \\ \tilde{E}^1_R &= \sum_{i\,j\in R} D_{i\,j}\langle\tilde{\phi}_j|\frac{-\hbar^2}{2m_e}\nabla^2|\tilde{\phi}_i\rangle \\ &+ \frac{1}{2}\cdot\frac{e^2}{4\pi\epsilon_0}\int d^3r\int d^3r'\frac{[\tilde{n}^1(\mathbf{r})+\tilde{Z}(\mathbf{r})][\tilde{n}^1(\mathbf{r}')+\tilde{Z}(\mathbf{r}')]}{|\mathbf{r}-\mathbf{r}'|} \\ &+ \int d^3r\bar{v}(\mathbf{r})\tilde{n}^1(\mathbf{r}) + E_{xc}[\tilde{n}^1(\mathbf{r})] \qquad (36) \end{aligned}$$

The compensation charge density $\tilde{Z}(\mathbf{r}) = \sum_R \tilde{Z}_R(\mathbf{r})$ is given as a sum of angular momentum dependent Gauss functions, which have an analytical plane-wave expansion. A similar term occurs also in the pseudopotential approach. In contrast to the norm-conserving pseudopotential approach, however, the compensation charge of an atom $\tilde{Z}_R$ is non-spherical and constantly adapts to the instantaneous environment. It is constructed such that

$$n^1_R(\mathbf{r}) + Z_R(\mathbf{r}) - \tilde{n}^1_R(\mathbf{r}) - \tilde{Z}_R(\mathbf{r}) \qquad (37)$$

has vanishing electrostatic multi-pole moments for each atomic site. With this choice, the electrostatic potentials of the augmentation densities vanish outside their spheres. This is the reason that there is no electrostatic interaction of the one-center parts between different sites.

The compensation charge density as given here is still localized within the atomic regions. A technique similar to an Ewald summation, however, allows to replace it by a very extended charge density. Thus we can achieve, that the plane-wave convergence of the total energy is not affected by the auxiliary density.

The potential $\bar{v} = \sum_R \bar{v}_R$, which occurs in Eqs. 34 and 36 enters the total energy in the form of "intelligent zeros" described in Eq. 32

$$0 = \sum_n f_n\left(\langle\tilde{\Psi}_n|\bar{v}_R|\tilde{\Psi}_n\rangle - \langle\tilde{\Psi}^1_n|\bar{v}_R|\tilde{\Psi}^1_n\rangle\right) = \sum_n f_n\langle\tilde{\Psi}_n|\bar{v}_R|\tilde{\Psi}_n\rangle - \sum_{i\,j\in R} D_{i\,j}\langle\tilde{\phi}_i|\bar{v}_R|\tilde{\phi}_j\rangle \qquad (38)$$

The main reason for introducing this potential is to cancel the Coulomb singularity of the potential in the plane-wave part. The potential $\bar{v}$ allows to influence the plane-wave

convergence beneficially, without changing the converged result. $\bar{v}$ must be localized within the augmentation region, where Eq. 19 holds.

E. Approximations

Once the total energy functional provided in the previous section has been defined, everything else follows: Forces are partial derivatives with respect to atomic positions. The potential is the derivative of the non-kinetic energy contributions to the total energy with respect to the density, and the auxiliary Hamiltonian follows from derivatives $\tilde{H}|\tilde{\Psi}_n\rangle$ with respect to auxiliary wave functions. The fictitious Lagrangian approach of Car and Parrinello[14] does not allow any freedom in the way these derivatives are obtained. Anything else than analytic derivatives will violate energy conservation in a dynamical simulation. Since the expressions are straightforward, even though rather involved, we will not discuss them here. All approximations are incorporated already in the total energy functional of the PAW method. What are those approximations?

- Firstly we use the frozen-core approximation. In principle this approximation can be overcome.
- The plane-wave expansion for the auxiliary wavefunctions must be complete. The plane-wave expansion is controlled easily by increasing the plane-wave cutoff defined as $E_{PW} = \frac{1}{2}\hbar^2 G_{max}^2$. Typically we use a plane-wave cutoff of 30 Ry.
- The partial wave expansions must be converged. Typically we use one or two partial waves per angular momentum (ℓ, m) and site. It should be noted that the partial wave expansion is not variational, because it changes the total energy functional and not the basis set for the auxiliary wavefunctions.

We do not discuss here numerical approximations such as the choice of the radial grid, since those are easily controlled.

F. Relation to the Pseudopotentials

We mentioned earlier that the pseudopotential approach can be derived as a well defined approximation from the PAW method: The augmentation part of the total energy $\Delta E =$

23

$E^1 - \tilde{E}^1$ for one atom is a functional of the one-center density matrix $D_{i\,j\in R}$ defined in Eq. 29. The pseudopotential approach can be recovered if we truncate a Taylor expansion of ΔE about the atomic density matrix after the linear term. The term linear to $D_{i\,j}$ is the energy related to the nonlocal pseudopotential.

$$\begin{aligned}\Delta E(D_{i\,j}) &= \Delta E(D^{at}_{i\,j}) + \sum_{i\,j}(D_{i\,j} - D^{at}_{i\,j})\frac{\partial \Delta E}{\partial D_{i\,j}} + O(D_{i\,j} - D^{at}_{i\,j})^2 \\ &= E_{self} + \sum_n f_n \langle \tilde{\Psi}_n | v^{ps} | \tilde{\Psi}_n \rangle - \int d^3r \bar{v}(\mathbf{r})\tilde{n}(\mathbf{r}) + O(D_{i\,j} - D^{at}_{i\,j})^2 \qquad (39)\end{aligned}$$

which can directly be compared to the total energy expression Eq. 10 of the pseudopotential method. The local potential $\bar{v}(\mathbf{r})$ of the pseudopotential approach is identical to the corresponding potential of the projector augmented wave method. The remaining contributions in the PAW total energy, namely $\tilde{E}$, differ from the corresponding terms in Eq. 10 only in two features: our auxiliary density also contains an auxiliary core density, reflecting the nonlinear core correction of the pseudopotential approach, and the compensation density $\tilde{Z}(\mathbf{r})$ is non-spherical and depends on the wave function. Thus we can look at the PAW method also as a pseudopotential method with a pseudopotential that adapts to the instantaneous electronic environment. In the PAW method, the explicit nonlinear dependence of the total energy on the one-center density matrix is properly taken into account.

What are the main advantages of the PAW method compared to the pseudopotential approach?

Firstly all errors can be systematically controlled so that there are no transferability errors. As shown by Watson[56] and Kresse[33], most pseudopotentials fail for high spin atoms such as Cr. While it is probably true that pseudopotentials can be constructed that cope even with this situation, a failure can not be known beforehand, so that some empiricism remains in practice: A pseudopotential constructed from an isolated atom is not guaranteed to be accurate for a molecule. In contrast, the converged results of the PAW method do not depend on a reference system such as an isolated atom, because PAW uses the full density and potential.

Like other all-electron methods, the PAW method provides access to the full charge and spin density, which is relevant, for example, for hyperfine parameters. Hyperfine parameters are sensitive probes of the electron density near the nucleus. In many situations they are the only information available that allows to deduce atomic structure and chemical environment

of an atom from experiment.
The plane-wave convergence is more rapid than in norm-conserving pseudopotentials and should in principle be equivalent to that of ultra-soft pseudopotentials[55]. Compared to the ultra-soft pseudopotentials, however, the PAW method has the advantage that the total energy expression is less complex and can therefore be expected to be more efficient.
The construction of pseudopotentials requires to determine a number of parameters. As they influence the results, their choice is critical. Also the PAW methods provides some flexibility in the choice of auxiliary partial waves. However, this choice does not influence the converged results.

G. Recent Developments

Since the first implementation of the PAW method in the CP-PAW code, a number of groups have adopted the PAW method. The second implementation was done by the group of Holzwarth[23]. The resulting PWPAW code is freely available[51]. This code is also used as a basis for the PAW implementation in the AbInit project. An independent PAW code has been developed by Valiev and Weare[53]. Recently the PAW method has been implemented into the VASP code[33]. The PAW method has also been implemented by W. Kromen into the ESTCoMPP code of Blügel and Schröder.
Another branch of methods uses the reconstruction of the PAW method, without taking into account the full wavefunctions in the energy minimization. Following chemist notation this approach could be termed "post-pseudopotential PAW". This development began with the evaluation for hyperfine parameters from a pseudopotential calculation using the PAW reconstruction operator[54] and is now used in the pseudopotential approach to calculate properties that require the correct wavefunctions such as hyperfine parameters.
The implementation by Kresse and Joubert[33] has been particularly useful as they had an implementation of PAW in the same code as the ultra-soft pseudopotentials, so that they could critically compare the two approaches with each other. Their conclusion is that both methods compare well in most cases, but they found that magnetic energies are seriously – by a factor two – in error in the pseudopotential approach, while the results of the PAW method were in line with other all-electron calculations using the linear augmented plane-wave method. As a short note, Kresse and Joubert incorrectly claim that their implemen-

tation is superior as it includes a term that is analogous to the non-linear core correction of pseudopotentials[36]: this term however is already included in the original version in the form of the pseudized core density.

Several extensions of the PAW have been done in the recent years: For applications in chemistry truly isolated systems are often of great interest. As any plane-wave based method introduces periodic images, the electrostatic interaction between these images can cause serious errors. The problem has been solved by mapping the charge density onto a point charge model, so that the electrostatic interaction could be subtracted out in a self-consistent manner[10]. In order to include the influence of the environment, the latter was simulated by simpler force fields using the molecular-mechanics-quantum-mechanics (QM-MM) approach[57].

In order to overcome the limitations of the density functional theory several extensions have been performed. Bengone[7] implemented the LDA+U approach into the CP-PAW code. Soon after this, Arnaud[5] accomplished the implementation of the GW approximation into the CP-PAW code. The VASP-version of PAW[21] and the CP-PAW code have now been extended to include a non-collinear description of the magnetic moments. In a non-collinear description the Schrödinger equation is replaced by the Pauli equation with two-component spinor wavefunctions

The PAW method has proven useful to evaluate electric field gradients[42] and magnetic hyperfine parameters with high accuracy[11]. Invaluable will be the prediction of NMR chemical shifts using the GIPAW method of Pickard and Mauri[44], which is based on their earlier work[38]. While the GIPAW is implemented in a post-pseudopotential manner, the extension to a self-consistent PAW calculation should be straightforward. An post-pseudopotential approach has also been used to evaluate core level spectra[25] and momentum matrix elements[26].

Acknowledgments

We are grateful for carefully reading the manuscript to S. Boeck, J. Noffke, as well as to K. Schwarz for his continuous support. This work has benefited from the collaborations within the ESF Programme on 'Electronic Structure Calculations for Elucidating the Com-

plex Atomistic Behavior of Solids and Surfaces'.

---

[1] Andersen, O. K., 1975. Linear methods in band theory. *Phys. Rev. B* 12, 3060.

[2] Andersen, O. K. and Jepsen, O., 1984. Explicit, first-principles tight-binding theory. *Phys. Rev. Lett.* 53, 2571.

[3] Andersen, O. K., Saha-Dasgupta, T. and Ezhof, S., 2003. Third-generation muffin-tin orbitals. *Bull. Mater. Sci.* 26, 19.

[4] Antoncik, E., 1959. Approximate formulation of the orthogonalized plane-wave method. *J. Phys. Chem. Solids* 10, 314.

[5] Arnaud, B. and Alouani, M., 2000. All-electron projector-augmented-wave GW approximation: Application to the electronic properties of semiconductors. *Phys. Rev. B.* 62, 4464.

[6] Bachelet, G. B., Hamann, D. R. and Schlüter, M., 1982. Pseudopotentials that work: From H to Pu. *Phys. Rev. B* 26, 4199.

[7] Bengone, O., Alouani, M., Blöchl, P. E. and Hugel, J., 2000. Implementation of the projector augmented-wave LDA+U method: Application to the electronic structure of NiO. *Phys. Rev. B* 62, 16392.

[8] Blöchl, P. E., 1990. Generalized Separable Potentials for Electronic Structure Calculations. *Phys. Rev. B* 41, 5414.

[9] Blöchl, P. E., 1994. Projector augmented-wave method. *Phys. Rev. B* 50, 17953.

[10] Blöchl, P. E., 1995. Electrostatic decoupling of periodic images of plane-wave-expanded densities and derived atomic point charges. *J. Chem. Phys.* 103, 7422.

[11] Blöchl, P. E., 2000. First-principles calculations of defects in oxygen-deficient silica exposed to hydrogen. *Phys. Rev. B* 62, 6158.

[12] Blöchl, P. E., 2002. Second generation wave function thermostat for ab-initio molecular dynamics. *Phys. Rev. B.* 65, 1104303.

[13] Blöchl, P. E. and Parrinello, M., 1992. Adiabaticity in First-Principles Molecular Dynamics. *Phys. Rev. B* 45, 9413.

[14] Car, R. and Parrinello, M., 1985. Unified Approach for Molecular Dynamics and Density-Functional Theory. *Phys. Rev. Lett.* 55, 2471.

[15] Fuchs, M. and Scheffler, M., 1999. Ab initio pseudopotentials for electronic structure calculations

of poly-atomic systems using density-functional theory. *Comput. Phys. Commun.* 119, 67.

[16] Gonze, X., Stumpf, R. and Scheffler, M., 1991. Analysis of separable potentials. *Phys. Rev. B* 44, 8503.

[17] Hamann, D. R., 1989. Generalized norm-conserving pseudopotentials. *Phys. Rev. B* 40, 2980.

[18] Hamann, D. R., Schlüter, M. and Chiang, C., 1979. Norm-Conserving Pseudopotentials. *Phys. Rev. Lett.* 43, 1494.

[19] Held, K., Nekrasov, I. A., Keller, G., Eyert, V., Blümer, N., McMahan, A. K., Scalettar, R. T., Pruschke, T., Anisimov, V. I. and Vollhardt, D., 2002. The LDA+DMFT Approach to Materials with Strong Electronic Correlations. In: *Quantum Simulations of Complex Many-Body Systems: From Theory to Algorithms, Lecture Notes J. Grotendorst, D. Marx, A. Muramatsu (Eds.)*, vol. 10, p. 175. John von Neumann Institute for Computing, Jülich, NIC Series.

[20] Herring, C., 1940. A New Method for Calculating Wave Functions in Crystals. *Phys. Rev.* 57, 1169.

[21] Hobbs, D., Kresse, G. and Hafner, J., 2000. Fully unconstrained noncollinear magnetism within the projector augmented-wave method. *Phys. Rev. B* 62, 11556.

[22] Hohenberg, P. and Kohn, W., 1964. Inhomogeneous Electron Gas. *Phys. Rev.* 136, B864.

[23] Holzwarth, N. A. W., Mathews, G. E., Dunning, R. B., Tackett, A. R. and Zheng, Y., 1997. Comparison of the projector augmented-wave, pseudopotential, and linearized augmented-plane-wave formalisms for density-functional calculations of solids. *Phys. Rev. B* 55, 2005.

[24] Hoover, 1985. Canonical dynamics: Equilibrium phase-space distributions. *Phys. Rev. A* 31, 1695.

[25] Jayawardane, D. N., Pickard, C. J., Brown, L. M. and Payne, M. C., 2001. Cubic boron nitride: Experimental and theoretical energy-loss near-edge structure. *Phys. Rev. B* 64, 115107.

[26] Kageshima, H. and Shiraishi, K., 1997. Momentum-matrix-element calculation using pseudopotentials. *Phys. Rev. B* 56, 14985.

[27] Kerker, G. P., 1980. Non-singular atomic pseudopotentials for solid state applications. *J. Phys. C* 13, L189.

[28] Kleinman, L. and Bylander, D. M., 1982. Efficacious Form for Model Pseudopotentials. *Phys. Rev. Lett.* 48, 1425.

[29] Kohn, W. and Rostocker, J., 1954. Solution of the Schrödinger Equation in Periodic Lattices with an Application to Metallic Lithium. *Phys. Rev.* 94, 1111.

[30] Kohn, W. and Sham, L. J., 1965. Self-Consistent Equations Including Exchange and Correlation Effects. *Phys. Rev.* 140, A1133.

[31] Korringa, J., 1947. On the calculation of the energy of a bloch wave in a metal. *Physica(Utrecht)* 13, 392.

[32] Krakauer, H., Posternak, M. and Freeman, A. J., 1979. Linearized augmented plane-wave method for the electronic band structure of thin films. *Phys. Rev. B* 19, 1706.

[33] Kresse, G. and Joubert, J., 1999. From ultrasoft pseudopotentials to the projector augmented-wave method. *Phys. Rev. B* 59, 1758.

[34] Laasonen, K., Pasquarello, A., Car, R., Lee, C. and Vanderbilt, D., 1993. Implementation of ultrasoft pseudopotentials in ab-initio molecular dynamics. *Phys. Rev. B* 47, 110142.

[35] Lin, J. S., Qteish, A., Payne, M. C. and Heine, V., 1993. Optimized and transferable nonlocal separable ab initio pseudopotentials. *Phys. Rev. B* 47, 4174.

[36] Louie, S. G., Froyen, S. and Cohen, M. L., 1982. Nonlinear ionic pseudopotentials in spin-density-functional calculations. *Phys. Rev. B* 26, 1738.

[37] Madsen, G. K. H., Blaha, P., Schwarz, K., Sjöstedt, E. and Nordström, L., 2001. Efficient linearization of the augmented plane-wave method. *Phys. Rev. B* 64, 195134.

[38] Mauri, F., Pfrommer, B. G. and Louie, S. G., 1996. Ab Initio Theory of NMR Chemical Shifts in Solids and Liquids. *Phys. Rev. Lett* 77, 5300.

[39] Nosé, S., 1984. A unified formulation of the constant temperature molecular-dynamics methods. *Mol. Phys.* 52, 255.

[40] Parr, R. G. and Yang, W., 1989. *Density Functional Theory of Atoms and Molecules*. Oxford University Press.

[41] Payne, M. C., Teter, M. P., Allan, D. C., Arias, T. A. and Joannopoulos, J. D., 1992. Iterative minimization techniques for ab-initio total-energy calculations: molecular dynamics and conjugate-gradients. *Rev. Mod. Phys* 64, 11045.

[42] Petrilli, H. M., Blöchl, P. E., Blaha, P. and Schwarz, K., 1998. Electric-field-gradient calculations using the projector augmented wave method. *Phys. Rev. B* 57, 14690.

[43] Phillips, J. C. and Kleinman, L., 1959. New Method for Calculating Wave Functions in Crystals and Molecules. *Phys. Rev.* 116, 287.

[44] Pickard, C. J. and Mauri, F., 2001. All-electron magnetic response with pseudopotentials: NMR chemical shifts. *Phys. Rev. B.* 63, 245101.

[45] Singh, D., 1991. Ground-state properties of lanthanum: Treatment of extended-core states. *Phys. Rev. B* 43, 6388.

[46] Singh, S., 1994. *Planewaves, Pseudopotentials and the LAPW method*. Kluwer Academic.

[47] Sjöstedt, E., Nordström, L. and Singh, D. J., 2000. An alternative way of linearizing the augmented plane-wave method. *Solid State Commun.* 114, 15.

[48] Skriver, H. L., 1984. *The LMTO Method*. Springer, New York.

[49] Slater, J. C., 1937. Wave Functions in a Periodic Potential. *Phys. Rev.* 51, 846.

[50] Soler, J. M. and Williams, A. R., 1989. Simple Formula for the atomic forces in the augmented-plane-wave method. *Phys. Rev. B* 40, 1560.

[51] Tackett, A. R., Holzwarth, N. A. W. and Matthews, G. E., 2001. A Projector Augmented Wave (PAW) code for electronic structure calculations, Part I: atompaw for generating atom-centered functions, A Projector Augmented Wave (PAW) code for electronic structure calculations, Part II: pwpaw for periodic solids in a plane wave basis. *Computer Physics Communications* 135, 329–347, ibid. 348–376.

[52] Troullier, N. and Martins, J. L., 1991. Efficient pseudopotentials for plane-wave calculations. *Phys. Rev. B* 43, 1993.

[53] Valiev, M. and Weare, J. H., 1999. The Projector-Augmented Plane Wave Method Applied to Molecular Bonding. *J. Phys. Chem. A* 103, 10588.

[54] Van de Walle, C. G. and Blöchl, P. E., 1993. First-principles calculations of hyperfine parameters. *Phys. Rev. B* 47, 4244.

[55] Vanderbilt, D., 1990. Soft self-consistent pseudopotentials in a generalized eigenvalue formalism. *Phys. Rev. B* 41, 17892.

[56] Watson, S. C. and Carter, E. A., 1998. Spin-dependent pseudopotentials. *Phys. Rev. B* 58, R13309.

[57] Woo, T. K., Margl, P. M., Blöchl, P. E. and Ziegler, T., 1997. A Combined Car-Parrinello QM/MM Implementation for ab Initio Molecular Dynamics Simulations of Extended Systems: Application to Transition Metal Catalysis. *J. Phys. Chem. B* 101, 7877.

[58] Zunger, A. and Cohen, M., 1978. First-principles nonlocal-pseudopotential approach in the density-functional formalism: Development and application to atoms. *Phys. Rev. B* 18, 5449.

Part III

Novel Theory – Ab-Initio Atomic Fragments

Chapter 7

Why Atomic Fragments?

Nowadays, the vast majority of electronic structure calculations in materials science is done on the basis of density functional theory (compare section 2.2). Differences mostly occur in terms of the numerical representation of the wave-functions and densities. A discussion of the different flavors of basis sets is found in our publication 5, section 6.5. In a basis set representation, a wave-function is written as

$$|\psi\rangle = \sum_{i=1}^{N} |\chi_i\rangle c_i, \tag{7.1}$$

where the $|\chi_i\rangle$ are the basis functions. From now on I will make extensive use of the bra-ket notation introduced by Dirac. For a brief introduction see appendix A.2. The introduction of basis functions transform the Schrödinger equation into a matrix equation

$$\mathcal{H}|\psi\rangle = \varepsilon|\psi\rangle \quad \xrightarrow{|\chi_i\rangle} \quad \sum_{j=1}^{N} \mathcal{H}_{ij} c_j = \varepsilon c_i, \tag{7.2}$$

where matrix elements of the Hamiltonian $\mathcal{H}_{ij}$ are defined as $\langle\chi_i|\mathcal{H}|\chi_j\rangle$ and the c_i by equation 7.1. The resulting eigenvalue problem can then be solved using a series of iterative and direct numerical approaches that are available [53, 84, 54, 55, 23, 53, 56].

In the field of solid state simulations, the state-of-the-art approach is to use delocalized basis functions, mainly derived from a plane-wave (Fourier) representation. In order to obtain accurate results one needs in the order of 100 to 1000 basis functions per atom. For a 100-atom unit cell, the size of the Hamilton

matrix is thus between 10 000 by 10 000 and 100 000 by 100 000. This does not only result in a large numerical effort, but also makes the analysis of the results cumbersome. Additional techniques such as atom resolved density of states or the crystal orbital overlap population (COOP) analysis are used in order to extract information about the chemical bonding. The advantage of these basis functions, however, is that they allow for accurate and robust calculations.

A second approach uses basis functions that are localized in space. In contrast to the delocalized basis functions they are – according to O. K. Andersen [85] – "intelligible" and fast. An intelligible electronic structure method is, following his definition, a method which is based on a minimal and flexible basis of short ranged orbitals. In this context, "minimal" refers to a basis set size which corresponds to the number of orbitals needed to accommodate the valence electrons of the system. For example a minimal basis set for silicon would consist of four orbitals, one of s and three of p character.

Due to the minimal character of the basis, the basis functions have to be well adapted to the actual system. Therefore, each basis function will have a much more complex character. A review of recent approaches is given in section 9.5.

Minimal basis sets are very useful not only in connection with analysis but also for applications as the so-called order-N methods [86], which aim to scale linearly with system size in terms of numerical effort. This is in contrast to the conventional approaches which scale with N^2 to N^3 and are therefore limited to system sizes of a few hundred atoms at the moment.

The following chapters will introduce a novel scheme to construct atomic fragment orbitals from first principles. This is, to the best of our knowledge, the first time that a parameter-free construction has been proposed and implemented. Our approach is based on the construction of atomic potentials which mimic the Pauli-repulsion of the neighboring atoms and thus deform and localize the orbitals on the central atom. This results in geometry-adapted localized basis-functions. Chapter 8 introduces a novel theory which uses nodeless wave-functions and allows to calculate deformation potentials yielding the atomic fragment orbitals as solutions. Chapter 9 deals with the calculation of atomic fragment orbitals using a plane-wave basis and discusses their properties.

Chapter 8

Theory of nodeless wave-functions

This chapter describes a novel method proposed by Peter Blöchl [60] to expand atomic wave-functions in terms of nodeless basis-functions. First aspects of this new theory have already been explored in the diploma thesis of Mike Thieme [87].

8.1 Properties of an atomic fragment

When transferring an isolated atom into a crystal or molecule, its electron density experiences a deformation or contraction due to the presence of other atoms. We define an atomic fragment as a three-dimensional "puzzle piece" whose shape depends on the local atomic structure around the central atom. In the following chapters I will introduce a procedure which allows to obtain such fragments as solutions to a Schrödinger equation including a so-called deformation potential that is derived from first principles.

I will employ the frozen core approximation [88] which assumes that the core density is not affected by changes in the chemical environment. This approximation is also used in pseudo-potential and PAW [60] approaches and proves to be reliable.

Our approach is based on the following properties which an atomic fragment (valence) orbital should have, namely to

– be a solution of the atomic potential near the nucleus of the central atom and

– have the shape of the energy derivative of the valence wave-function of the neighboring atom near that nucleus.

The shape-condition at the neighboring atoms can be rationalized in terms of an expansion of a wave-function around an energy ε_0:

$$\phi(\varepsilon) = \phi(\varepsilon_0) + \dot{\phi}(\varepsilon_0)(\varepsilon - \varepsilon_0) + O\big((\varepsilon - \varepsilon_0)^2\big), \tag{8.1}$$

where $\dot{\phi}$ denotes the energy derivative of ϕ. Constructing molecular orbitals as a linear combination of atomic fragment orbitals leads to a situation, where – in the vicinity of a specified nucleus – we have a linear combination of ϕ and $\dot{\phi}$ similar to equation 8.1. Such a basis has at least the potential to solve the Schrödinger equation to linear order. In addition, the energy derivative $\dot{\phi}$ is automatically orthogonal to the core wave-functions and thus one does not need to include the core wave-functions in the basis set.

These requirements on the atomic fragments thus are a physically sensible choice. As the theory of nodeless wave-function develops we will see that this special choice leads to potential terms, which mimic the Pauli-repulsion of the neighboring atoms and thus provides a consistent physical picture.

For the construction of fragment orbitals which have these properties, we need special potential terms in order to calculate the energy derivative of the valence wave-functions as a solution to a homogeneous Schrödinger equation. The energy derivative of a wave-function, however, is defined as the solution to the following inhomogeneous Schrödinger equation:

$$\left[-\frac{1}{2}\nabla^2 + v - \varepsilon\right] |\dot{\phi}\rangle = |\phi\rangle. \tag{8.2}$$

In order to obtain $\dot{\phi}$ as the solution of a homogeneous Schrödinger equation, an additional potential term η is required:

$$\left[-\frac{1}{2}\nabla^2 + v + \eta - \varepsilon\right] |\dot{\phi}\rangle = 0$$

which is defined as

$$\eta = -\frac{|\phi\rangle}{|\dot{\phi}\rangle}.$$

Such a potential η, however, is numerically very inconvenient since the $|\dot{\phi}\rangle$ in the denominator exhibits nodes for all but the first wave-function of each angular momentum channel ($1s$, $2p$, $3d$ and $4f$).

8.2 Theory of nodeless wave-functions

The above problem was solved by Peter Blöchl who proposed the theory of nodeless wave-functions [60]. In this section I will derive the basic concept of nodeless wave-functions using a different approach as in the initial formulation [60, 87].

The underlying principle is to find a set of nodeless wave-functions $|u_i\rangle$ and their energy-derivatives $|\dot{u}_i\rangle$ from which we can construct the atomic wave-functions $|\phi_n\rangle$ and their energy derivatives $|\dot{\phi}_n\rangle$

$$|\phi_n\rangle = \sum_{i=1}^{n} |u_i\rangle c_{i,n} \tag{8.3}$$

$$|\dot{\phi}_n\rangle = \sum_{i=1}^{n} |u_i\rangle d_{i,n} + |\dot{u}_n\rangle e_n, \tag{8.4}$$

where the index n is a wave-function count for a given angular momentum ℓ. Note that the expansion for the n-th wave-function only includes the first n nodeless wave-functions.

While the expansion coefficients $c_{i,n}$ depend on the wave-function index n we require the nodeless wave-functions $|u_i\rangle$ to be a well defined basis for a given atomic species. To simplify the notation we will drop the index n for the coefficients $c_{i,n}$ from now on, implying that a set of coefficients is only valid for a given atomic wave-function $|\phi_n\rangle$ or its energy derivative $|\dot{\phi}_n\rangle$.

8.2.1 Definition of the $|u_i\rangle$

The atomic wave-functions are defined by the atomic Hamiltonian $\mathcal{H}$:

$$(\mathcal{H} - \varepsilon_i)|\phi_i\rangle = 0 \qquad \text{for} \qquad i \geq 1. \tag{8.5}$$

The first eigenfunction for each angular momentum channel ℓ, $|\phi_1\rangle$, is nodeless by definition so it is straightforward to choose

$$|u_1\rangle \equiv |\phi_1\rangle.$$

Following equation 8.3 we now make an ansatz for $|u_2\rangle$ of the form

$$|\phi_2\rangle \;=\; |u_1\rangle c_1 + |u_2\rangle c_2, \tag{8.6}$$

with $|u_2\rangle$ as well as c_1 and c_2 yet undefined and require the expansion to be a solution of the atomic Schrödinger equation (8.5):

$$\begin{aligned}
0 \quad &= \quad (\mathcal{H} - \varepsilon_2)|\phi_2\rangle \\
&\overset{\text{Eqn. 8.6}}{=} \quad c_1(\mathcal{H} - \varepsilon_2)|u_1\rangle + c_2(\mathcal{H} - \varepsilon_2)|u_2\rangle \\
&= \quad c_1\left[(\mathcal{H} - \varepsilon_1) - (\varepsilon_2 - \varepsilon_1)\right]|u_1\rangle + c_2(\mathcal{H} - \varepsilon_2)|u_2\rangle \\
&= \quad -c_1(\varepsilon_2 - \varepsilon_1)|u_1\rangle + c_2(\mathcal{H} - \varepsilon_2)|u_2\rangle.
\end{aligned}$$

The above equation still has three unknown quantities: $|u_2\rangle$, c_1 and c_2, which are, however, coupled by an inhomogeneous Schrödinger equation:

$$c_2(\mathcal{H} - \varepsilon_2)|u_2\rangle = c_1(\varepsilon_2 - \varepsilon_1)|u_1\rangle.$$

We are now free to choose the expansion coefficients c_1 and c_2. Defining c_2 as $c_1(\varepsilon_2 - \varepsilon_1)$ results in a particularly simple inhomogeneous differential equation for $|u_2\rangle$:

$$(\mathcal{H} - \varepsilon_2)|u_2\rangle = |u_1\rangle. \tag{8.7}$$

Note that via the choice of c_2, this definition of $|u_2\rangle$ is coupled to a specific expansion for $|\phi_2\rangle$:

$$|\phi_2\rangle = c_1|u_1\rangle + c_1(\varepsilon_2 - \varepsilon_1)|u_2\rangle = c_1\left[|u_1\rangle + (\varepsilon_2 - \varepsilon_1)|u_2\rangle\right]. \tag{8.8}$$

The remaining free parameter c_1 can be interpreted as a normalization constant and is undefined by construction since the norm of $|\phi_2\rangle$ is not fixed by the atomic Schrödinger equation (8.5). It can be determined by normalizing the expansion in equation 8.8. Note that any other choice for c_2 is equally possible and will result in a different scaling of $|u_2\rangle$ as well as in a more complicated form of equations 8.7 and 8.8.

Following the above principle we now expand $|\phi_3\rangle$ in terms of the already defined $|u_1\rangle$ and $|u_2\rangle$ as well as of the new quantity $|u_3\rangle$:

$$|\phi_3\rangle = |u_1\rangle c_1 + |u_2\rangle c_2 + |u_3\rangle c_3.$$

Applying the Hamiltonian to the expansion and using the knowledge of its action on $|\phi_3\rangle$ as well as on $|u_1\rangle$ and $|u_2\rangle$ we again arrive at a parametrized differential equation for $|u_3\rangle$:

$$c_3(\mathcal{H} - \varepsilon_3)|u_3\rangle = c_1 \left(\varepsilon_3 - \varepsilon_1 - \frac{c_2}{c_1}\right)|u_1\rangle + c_2(\varepsilon_3 - \varepsilon_2)|u_2\rangle,$$

By choosing

$$\frac{c_2}{c_1} = \varepsilon_3 - \varepsilon_1,$$

we can eliminate $|u_1\rangle$ from the inhomogeneity. Following the arguments related to equations 8.7 and 8.8 we again choose the parameter c_3 as

$$c_3 = c_2(\varepsilon_3 - \varepsilon_2)$$

to arrive at a possibly simple equation for $|u_3\rangle$:

$$(\mathcal{H} - \varepsilon_3)|u_3\rangle = |u_2\rangle,$$

coupled to the expansion

$$|\phi_3\rangle = c_1 \left[|u_1\rangle + (\varepsilon_3 - \varepsilon_1)|u_2\rangle + (\varepsilon_3 - \varepsilon_1)(\varepsilon_3 - \varepsilon_2)|u_3\rangle\right],$$

with the norm (c_1) again undefined.

For a general wave-function $|\phi_n\rangle$ we proceed in an analogous way. Starting from $|u_1\rangle \equiv |\phi_1\rangle$ we define the $|u_i\rangle$ for $i \leq (n-1)$ as we have just defined $|u_2\rangle$ and $|u_3\rangle$. The atomic Hamiltonian is then applied to the expansion of equation 8.3 and exploiting the action already defined for the $|u_i\rangle$ up to $(n-1)$ we arrive at the familiar parametrized differential equation for $|u_n\rangle$:

$$c_n(\mathcal{H} - \varepsilon_n)|u_n\rangle = \sum_{i=1}^{n-2} \left(\varepsilon_n - \varepsilon_i - \frac{c_{i+1}}{c_i}\right)|u_i\rangle + c_{n-1}(\varepsilon_n - \varepsilon_{n-1})|u_{n-1}\rangle.$$

Following the established principle we define the expansion coefficients by a recursive relation

$$\frac{c_{i+1}}{c_i} = (\varepsilon_n - \varepsilon_i) \qquad \text{or explicitly by} \qquad c_i = c_1 \prod_{j=1}^{i-1} (\varepsilon_n - \varepsilon_j) \tag{8.9}$$

and obtain the differential equation for a general $|u_i\rangle$

$$(\mathcal{H} - \varepsilon_i)|u_i\rangle = |u_{i-1}\rangle \qquad \text{for} \quad i \geq 1 \quad \text{and} \quad |u_0\rangle = 0. \tag{8.10}$$

8.2.2 Definition of $|\dot{u}_n\rangle$

The energy derivative of a wave-function is defined by equation 8.2. In analogy to the determination of the differential equations for the $|u_i\rangle$, we now apply the Hamiltonian to the expansion of equation 8.4:

$$(\mathcal{H} - \varepsilon_n) \left[\sum_{i=1}^{n} |u_i\rangle d_i + |\dot{u}_n\rangle e \right] = \sum_{i=1}^{n} |u_i\rangle c_i.$$

The expansion coefficients c_i as well as the action of the Hamiltonian on the $|u_i\rangle$ are already defined. Regrouping leads to a parametrized differential equation for $|\dot{u}_n\rangle$:

$$e(\mathcal{H} - \varepsilon_n)|\dot{u}_n\rangle = \sum_{i=1}^{n-1} |u_i\rangle d_i \left(\varepsilon_n - \varepsilon_i - \frac{d_{i+1}}{d_i} + \frac{c_i}{d_i} \right) + |u_n\rangle c_n.$$

A simple equation is again obtained by removing all $|u_i\rangle$ for $i \leq (n-1)$ from the inhomogeneity which defines the d_i as well as e as

$$d_{i+1} = d_i(\varepsilon_n - \varepsilon_i) + c_i \qquad \text{and} \qquad e = c_n.$$

The differential equation for $|\dot{u}_n\rangle$ is thus

$$(\mathcal{H} - \varepsilon_n)|\dot{u}_n\rangle = |u_n\rangle. \tag{8.11}$$

Table 8.1: The behavior of atomic wave-functions $|\phi_i\rangle$, the nodeless wave-functions $|u_i\rangle$ and the energy derivatives $|\dot{u}_i\rangle$ at the origin.

index i	$\|\phi_i\rangle$	$\|u_i\rangle$	$\|\dot{u}_i\rangle$
1	r^ℓ	r^ℓ	$r^{\ell+2}$
2	r^ℓ	$r^{\ell+2}$	$r^{\ell+4}$
$\vdots$	$\vdots$	$\vdots$	$\vdots$
n	r^ℓ	$r^{\ell+2(n-1)}$	$r^{\ell+2n}$

8.2.3 Properties of the nodeless wave-functions

Knowing the differential equations defining the $|u_i\rangle$ and their energy derivatives (equations 8.10 and 8.11) we can now analyze their properties at the nucleus as well as at large distances:

$\mathbf{r} \to \mathbf{0}$: The behavior of the nodeless wave-functions at the origin can be estimated using a power series expansion of the potential, the inhomogeneity and the solution. This ansatz is derived in appendix D.1. Table 8.1 summarizes the results.

Note, however, that these boundary conditions are only valid when no mixing of the true wave-function $|\phi_i\rangle$ to the nodeless ones is included. In principle, any linear combination of $|\phi_i\rangle$ and $|u_i\rangle$ is still a solution to equation 8.10, since $|\phi_i\rangle$ solves the homogeneous differential equation. However, any mixing of the atomic wave-function would inevitably introduce nodes. Therefore we suppress the $|\phi_i\rangle$ character by forcing a behavior as listed in table 8.1, that is we enforce an $r^{\ell+2(n-1)}$ behavior instead of r^ℓ. For details see appendix D.1.

$\mathbf{r} \to \infty$: At large radii the $|u_i\rangle$ become identical to the corresponding $|\phi_i\rangle$, since the $|u_j\rangle$ for $j < i$ are responsible for describing the lower and thus less extended $|\phi_j\rangle$ (equation 8.3).

nodal character: While no rigorous proof for the nodeless character of the $|u_i\rangle$ has been found so far, we could demonstrate numerically for a series of elements that the construction described so far (including the boundary conditions at the origin) yields nodeless radial solutions.

Figures 8.1 and 8.2 visualize the decomposition of the $3s$ atomic wave-function of silicon into the nodeless wave-functions and the shape of the nodeless wave-functions $|u_1\rangle$ to $|u_3\rangle$ for the silicon s channel. In the lower panel of figure 8.2 the almost perfect exponential decay of the $|u_i\rangle$ outside the corresponding maximum can be observed. Together with the r^α behavior at the origin, the nodeless wave-functions show a close connection to Slater type orbitals [89] that are frequently

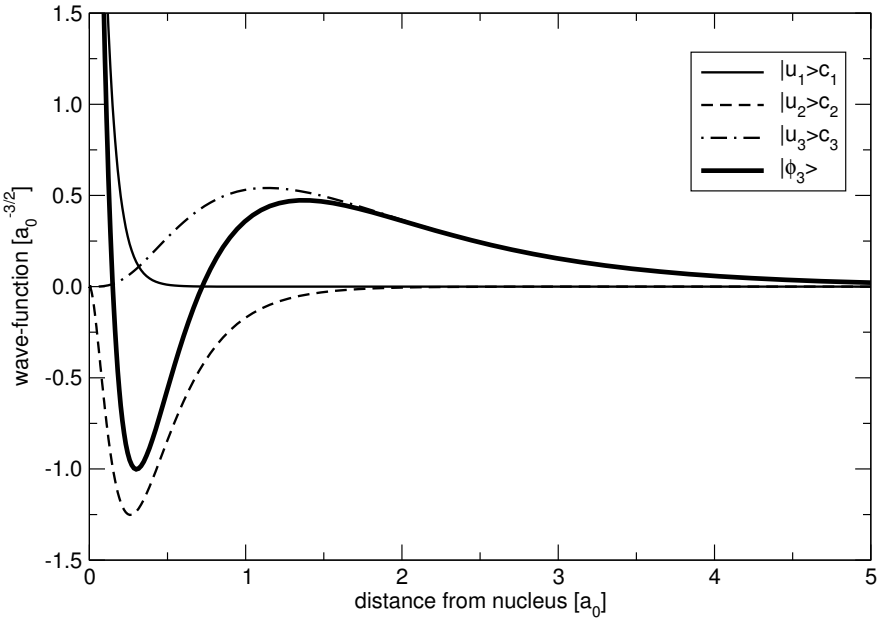

Figure 8.1: The $3s$ wave-function of silicon decomposed into the contributions from the nodeless wave-functions $|u_i\rangle$ times the corresponding weights c_i. Each nodeless wave-function is responsible for one local extremum of the atomic wave-function. The extrema of the atomic wave-function $|\phi_3\rangle$ are slightly shifted to larger r values compared those of the nodeless wave-functions.

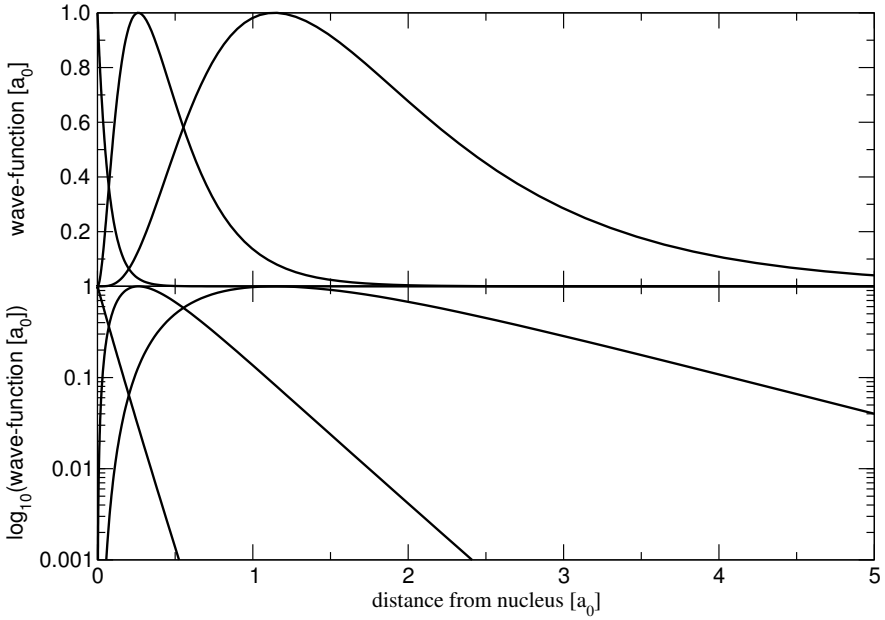

Figure 8.2: The first three nodeless wave-functions $|u_1\rangle$, $|u_2\rangle$ and $|u_3\rangle$ for the silicon s-channel scaled to have a common maximum value. $|u_3\rangle$ is the wave-function with the outermost maximum. The lower panel shows the nodeless wave-functions on a logarithmic scale.

used in quantum-chemical methods when high accuracy is needed. The possibility to parametrize these radial solutions in terms of an $A \cdot r^{\alpha} e^{-\beta r}$ ansatz has already been mentioned by Thieme [87]. Appendix D.2 discusses various fits to $|u_3\rangle$ for the Si-s channel.

8.2.4 Generalization to arbitrary energies

So far we have restricted our derivations to the atomic bound states $|\phi_n\rangle$. In a solid or molecule, however, we need to describe bonding and anti-bonding states which lie energetically below or above the atomic eigenvalue. We will now use a conceptually identical ansatz to arrive at an energy-dependent valence-nodeless wave-function $|q_n(\varepsilon)\rangle$ which will replace $|u_n\rangle$ (but not the $|u_i\rangle$ for $i < n$) in the expansion of equation 8.3.

We thus express the atomic wave-function $|\phi_n(\varepsilon)\rangle$ at an arbitrary energy

$$(\mathcal{H} - \varepsilon)|\phi_n(\varepsilon)\rangle = 0$$

by an expansion of the type

$$|\phi_n(\varepsilon)\rangle = \sum_{i=1}^{n-1} |u_i\rangle c_i + |q_n(\varepsilon)\rangle c_n.$$

Applying the Hamiltonian to the expansion and using the established procedure for removing all $|u_i\rangle$ but $|u_{n-1}\rangle$ from the inhomogeneity, we arrive at a definition for $|q_n(\varepsilon)\rangle$ (compare equation 8.10):

$$(\mathcal{H} - \varepsilon)|q_n(\varepsilon)\rangle = |u_{n-1}\rangle \tag{8.12}$$

as well as for the expansion coefficients (compare equation 8.9):

$$c_i = c_1 \prod_{j=1}^{i-1} (\varepsilon - \varepsilon_j). \tag{8.13}$$

Figure 8.3 shows the energy dependent nodeless valence wave-function for the silicon s-channel. Mind that the nodeless attribute for $|q_n(\varepsilon)\rangle$ just applies in the energy interval $\varepsilon_{n-1} \leq \varepsilon \leq \varepsilon_n$. At ε_2, $|q_3(\varepsilon)\rangle$ is identical to the energy derivative $|\dot{u}_2\rangle$ (compare equations 8.11 and 8.12). Nevertheless we will use the attribute nodeless also for the $|q_n(\varepsilon)\rangle$ in the following discussion. Upon increasing the energy starting from ε_2, the wave-function becomes initially steeper until it

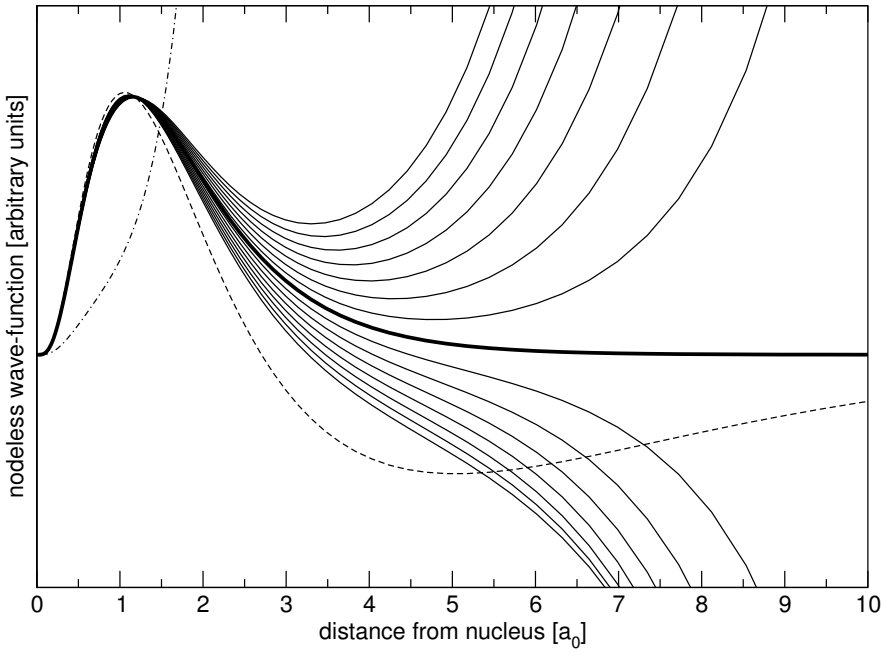

Figure 8.3: $|q_3(\varepsilon)\rangle$ for the Si s-channel in an energy window of $\pm 0.15\,\mathrm{H}$ around the atomic eigenvalue. The bound state at the atomic eigenvalue ε_3 is indicated by the bold line. The dash-dotted and dashed curves show $|q_3(\varepsilon_2)\rangle$ and $|q_3(\varepsilon_4)\rangle$, respectively.

bends down to form the inner maximum at around 1 a.u. At energies larger than ε_n, $|q_n(\varepsilon)\rangle$ exhibits a node. Upon increasing the energy above ε_3, the slope at radii outside the first extremum again increases until the second extremum is formed at around 5 a.u. The next bound state is at ε_4.

At $\varepsilon = \varepsilon_n$, $|q_n(\varepsilon_n)\rangle$ is furthermore identical to $|u_n\rangle$ and the coefficients are identical to the ones derived for the bound states (compare equation 8.9).

Furthermore it can be shown that the j^{th} energy derivative of the energy dependent wave-function $|q_{n+1}(\varepsilon)\rangle$ at $\varepsilon = \varepsilon_n$ is identical to the $j + 1^{\mathrm{st}}$ derivative of $|q_n(\varepsilon)\rangle$ at $\varepsilon = \varepsilon_n$, a relation which will be needed for the construction of the potential terms:

$$\begin{aligned} |q_{n+1}^{(j)}(\varepsilon_n)\rangle &= \frac{1}{j+1}|q_n^{(j+1)}(\varepsilon_n)\rangle \\ &= \frac{1}{j+1}|u_n^{(j+1)}\rangle. \end{aligned} \tag{8.14}$$

This relation is evident for $j = 0$ by comparing equations 8.11 and 8.12 bearing in mind that $|q_n(\varepsilon_n)\rangle$ is identical to $|u_n\rangle$. The proof for the general expression of equation 8.14 is given in appendix D.3.

8.3 Potentials for nodeless wave-functions

The ability to expand atomic wave-functions at arbitrary energies into a set of nodeless wave-functions now allows us to construct numerically convenient ab-initio pseudo-potentials $\eta_n(\varepsilon)$ for the a nodeless wave-function as already outlined in section 8.1. We rewrite the inhomogeneous Schrödinger equation

$$(\mathcal{H}-\varepsilon)|q_n(\varepsilon)\rangle = \left[-\frac{1}{2}\nabla^2 + v_{\mathrm{AE}} - \varepsilon\right]|q_n(\varepsilon)\rangle = |u_{n-1}\rangle$$

into a homogeneous one

$$\left[-\frac{1}{2}\nabla^2 + v_{\mathrm{AE}} + \eta_n(\varepsilon) - \varepsilon\right]|q_n(\varepsilon)\rangle = 0,$$

which defines $\eta_n(\varepsilon)$ as

$$\eta_n(\varepsilon) = \frac{|u_{n-1}\rangle}{|q_n(\varepsilon)\rangle}.$$

The additional potential term $\eta_n(\varepsilon)$ now mimics the presence of the lower shells. We can thus identify $\eta_n(\varepsilon)$ with a "Pauli-repulsion potential" for the energy dependent nodeless wave-function $|q_n(\varepsilon)\rangle$. The reconstruction of the $|\phi_n\rangle$ from the from $|q_n(\varepsilon)\rangle$ and the fixed $|u_i\rangle$, $i<n$ can be performed via the expansion coefficients of equation 8.13 or, alternatively, by an orthogonalization of $|q_n(\varepsilon)\rangle$ to the $|u_i\rangle$ for $i<n$.

The potential term $\eta_n(\varepsilon)$ is, however, energy dependent which renders the numerical solution of the Schrödinger equation cumbersome. We thus expand $\eta_n(\varepsilon)$ around some energy ε_ν (not necessarily the energy of the bound state ε_n):

$$\begin{aligned}\eta_n(\varepsilon) &= \eta_n(\varepsilon_\nu) + \eta_n'(\varepsilon_\nu)(\varepsilon-\varepsilon_\nu) + O(\varepsilon-\varepsilon_\nu)^2 \\ &= \underbrace{\eta_n(\varepsilon_\nu) - \eta_n'(\varepsilon_\nu)\cdot\varepsilon_\nu}_{v_n(\varepsilon_\nu)} + \underbrace{\eta_n'(\varepsilon_\nu)}_{-o_n(\varepsilon_\nu)}\cdot\varepsilon + O(\varepsilon-\varepsilon_\nu)^2,\end{aligned}$$

where $\eta_n'(\varepsilon_\nu) = \left.\frac{\partial\eta_n(\varepsilon)}{\partial\varepsilon}\right|_{\varepsilon_\nu}$. The expansion is then truncated after the linear term and rewritten into an energy independent part $v_n(\varepsilon_\nu)$ and an energy dependent part $o_n(\varepsilon_\nu)\cdot\varepsilon$, the so-called overlap times the energy. The linearized Schrödinger equation thus reads like

$$\left[-\frac{1}{2}\nabla^2 + v_{\mathrm{AE}} + v_n(\varepsilon_\nu) - \varepsilon\big(1+o_n(\varepsilon_\nu)\big)\right]|q_n(\varepsilon)\rangle = 0. \tag{8.15}$$

The corresponding Rayleigh quotient

$$\varepsilon = \frac{\langle q_n(\varepsilon)| - \frac{1}{2}\nabla^2 + v_{\mathrm{AE}} + v_n(\varepsilon_\nu)|q_n(\varepsilon)\rangle}{\langle q_n(\varepsilon)|1 + o_n(\varepsilon_\nu)|q_n(\varepsilon)\rangle)}$$

justifies the identification of $o_n(\varepsilon_\nu)$ with an overlap operator.

Such a linearization of an energy dependent potential is common practice in many electronic structure methods. The introduction of the overlap term changes the eigenvalue problem, associated with solving a Schrödinger equation without overlap, into a so-called generalized eigenvalue problem [53], for which, however, efficient numerical libraries exist [53, 56].

8.3.1 On-site Pauli-repulsion potentials

At the central atom of the atomic fragment we need to use a potential yielding the energy-dependent valence wave-function $|q_n(\varepsilon)\rangle$ as a solution. $\eta_n(\varepsilon)$ and $\eta'_n(\varepsilon)$ are therefore given by

$$\begin{aligned} \eta_n(\varepsilon_\nu) &= -\frac{|u_{n-1}\rangle}{|q_n(\varepsilon_\nu)\rangle} \qquad \text{and} \\ \eta'_n(\varepsilon_\nu) &= \frac{|\dot{q}_n(\varepsilon_\nu)\rangle|u_{n-1}\rangle}{|q_n^2(\varepsilon_\nu)\rangle}. \end{aligned}$$

Note that $|u_{n-1}\rangle$ is considered to be a fixed quantity within the assumed frozen-core approximation and therefore has a zero energy derivative. In the following we will choose the expansion energy ε_ν to be equal to the eigenvalue of the bound valence state ε_n. Note, however, that any other choice is equally possible. The linearized potential $v_n(\varepsilon_n)$ and overlap $o_n(\varepsilon_n)$ are thus given by

$$v_n(\varepsilon_n) = -\frac{|u_{n-1}\rangle}{|q_n(\varepsilon_n)\rangle}\left[1 + \varepsilon_n\frac{|\dot{q}_n(\varepsilon_n)\rangle}{|q_n(\varepsilon_n)\rangle}\right] = -\frac{|u_{n-1}\rangle}{|u_n\rangle}\left[1 + \varepsilon_n\frac{|\dot{u}_n\rangle}{|u_n\rangle}\right] \tag{8.16}$$

$$o_n(\varepsilon_n) = -\frac{|\dot{q}_n(\varepsilon_n)\rangle|u_{n-1}\rangle}{|q_n^2(\varepsilon_n)\rangle} = -\frac{|\dot{u}_n\rangle|u_{n-1}\rangle}{|u_n^2\rangle}. \tag{8.17}$$

8.3.2 Off-site Pauli-repulsion potentials

On all other but the central atom of a specific fragment orbital, the wave-function should experience the Pauli-repulsion from the core and valence shells. Based on

the potential and overlap terms of equations 8.16 and 8.17 we thus have to shift the wave-function index n by +1. The index n of the expansion energy is, however, not changed since the incoming wave will be at an energy near the valence bound state ε_n. It is only natural to expand all potential terms in the system around the same energy. We thus arrive at the following expressions for potential and overlap:

$$v_{n+1}(\varepsilon_n) = -\frac{|u_n\rangle}{|q_{n+1}(\varepsilon_n)\rangle}\left[1+\varepsilon_n\frac{|\dot{q}_{n+1}(\varepsilon_n)\rangle}{|q_{n+1}(\varepsilon_n)\rangle}\right] \overset{8.14}{=} -\frac{|u_n\rangle}{|\dot{u}_n\rangle}\left[1+\varepsilon_n\frac{|\ddot{u}_n\rangle}{2|\dot{u}_n\rangle}\right] \quad (8.18)$$

$$o_{n+1}(\varepsilon_n) = -\frac{|\dot{q}_{n+1}(\varepsilon_n)\rangle|u_n\rangle}{|q^2_{n+1}(\varepsilon_n)\rangle} \overset{8.14}{=} -\frac{|\ddot{u}_n\rangle|u_n\rangle}{2|\dot{u}^2_n\rangle}. \quad (8.19)$$

By comparing these two equations with the definition of the energy derivative of the nodeless wave-functions (equation 8.11) we observe that we would have obtained the same expressions if we had directly constructed potentials for the energy derivative $|\dot{q}_n(\varepsilon_n)\rangle = |\dot{u}_n\rangle$. At this point we now see that the puzzle pieces assembled so far really fit together to form a consistent physical picture. The Pauli-repulsion of the neighboring atoms results in the character of an energy derivative, which was initially postulated (compare equation 8.1 and related text). Note, however, that this assumption did not enter the construction of the potential terms.

To have a comparable degree of approximation at the central atom and at the neighboring atoms we will, however, not use the linearization for the repulsive potentials. The tails on the neighboring atoms contribute only in the linear part of the Taylor expansion of the atomic wave-function (compare equation 8.1 and related text). We will thus use the following potential and overlap terms in all applications:

$$v_{n+1}(\varepsilon_n) = -\frac{|u_n\rangle}{|q_{n+1}(\varepsilon_n)\rangle} = -\frac{|u_n\rangle}{|\dot{u}_n\rangle} \quad (8.20)$$

$$o_{n+1}(\varepsilon_n) = 0. \quad (8.21)$$

8.3.3 Properties of the Pauli-repulsion potentials

The on- and off-site valence potentials $v_{3/4}(\varepsilon_3)$ as well as the corresponding overlap terms $o_{3/4}(\varepsilon_3)$ for the silicon s and p channels are potted in figure 8.4.

If $|q_n(\varepsilon)\rangle$ does not exhibit nodes, which is the case in an energy interval from ε_{n-1} to ε_n, the resulting potential terms will not have any singularities except at the

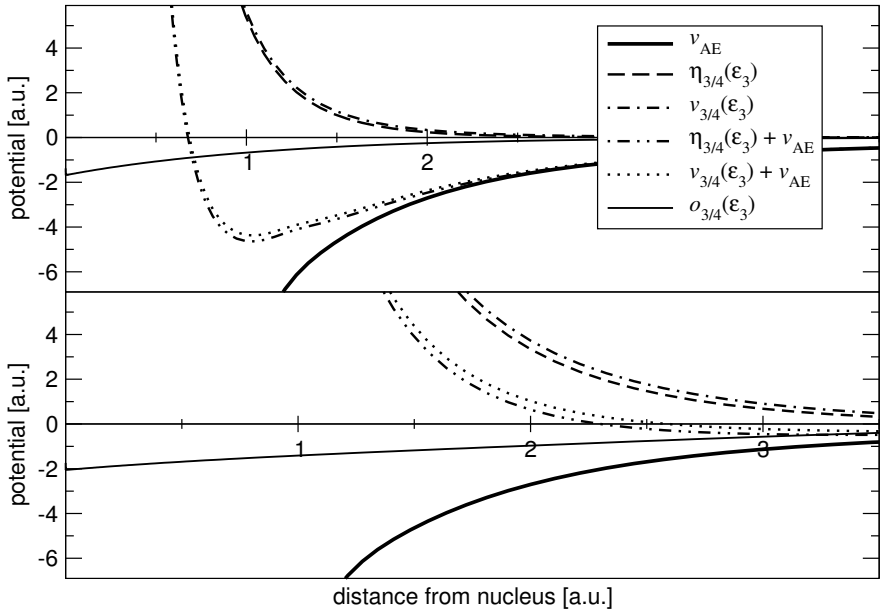

(a) Silicon s channel. Upper panel: on-site components; lower panel: off-site components.

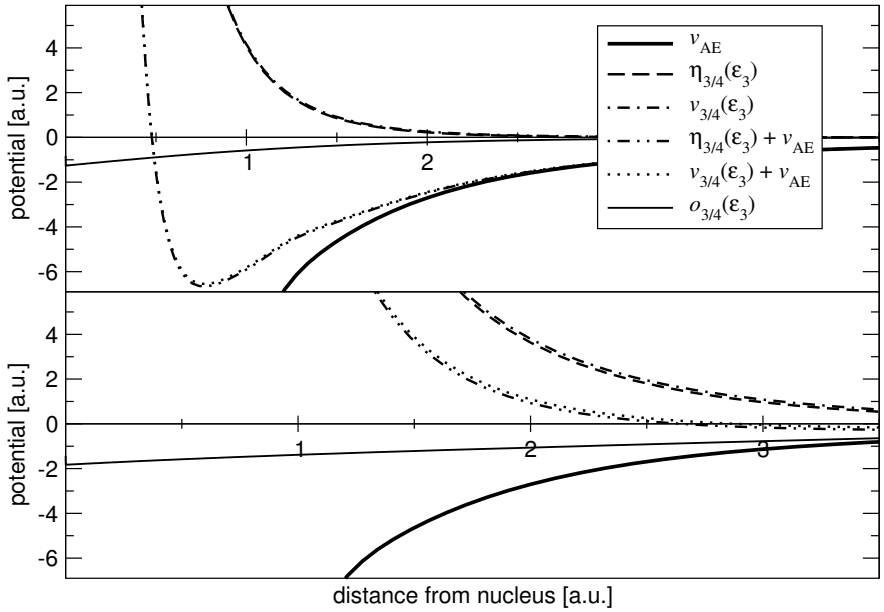

(b) Silicon p channel. Upper panel: on-site components; lower panel: off-site components.

Figure 8.4: Valence ($n = 3$) potential and overlap terms for silicon. The covalent radius of silicon is 2.1 a.u., the nearest neighbor atom in a silicon crystal would be at around 4.3 a.u.

origin (compare equations 8.16 and 8.18). There the potential exhibits an $1/r^2$ behavior (compare table 8.1 and equations 8.16 and 8.18). The overlap terms approach a constant value at the origin.

At large radii, all potential and overlap terms show an exponential decay determined by the difference in decay constants of the corresponding nodeless wave-functions. As evident from figure 8.4, both, potential and overlap terms, extend far away from the nucleus, well into the atomic region of neighboring atoms.

The potential and overlap terms derived in this section constitute "perfect" pseudo-potentials (compare our publication 5, section 6.5) in a sense that they mimic the exact Pauli-repulsion from the frozen core states. Unfortunately, the singularity at the origin as well as the long-range behavior are numerically cumbersome as will be discussed in the next chapter.

Chapter 9

Calculation of Atomic Fragment Orbitals

Figure 9.1 shows the basic idea behind the calculation of atomic fragment orbitals: For a specific central atom, an electron "sees" the core electrons of that atom but the core plus valence electrons on the neighboring atoms. With the potential terms of the previous chapter (compare equations 8.16 to 8.19) we do have potentials at hand which mimic exactly these two situations. On the basis of a given molecular or crystal potential, we can now add the atom-centered potentials and overlap terms of the last chapter to arrive at a total potential which yields fragment orbitals as solutions to the corresponding Schrödinger equation. In the following we will denote the atom-centered potential and overlap terms as "Pauli-repulsion" terms and the sum of the molecular potential as well as the Pauli-repulsion terms will be called "deformation potential".

An atomic fragment calculation thus consists of two steps which will be discussed in the following two sections:

- an atomic calculation to determine the on- and off-site Pauli-repulsion terms for all species involved (equations 8.16 to 8.19);

- the determination of the fragment orbitals as a solution to the deformation potential.

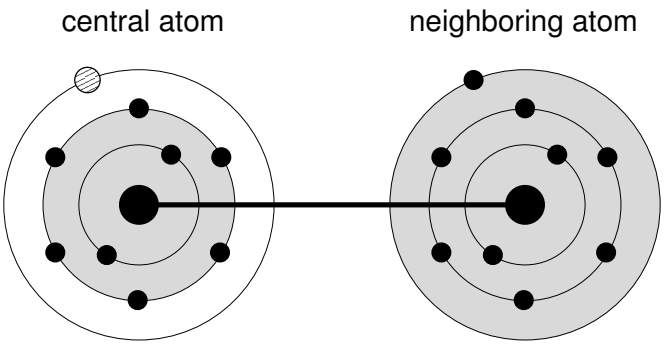

Figure 9.1: Sketch of the basic idea behind the generation of atomic fragment orbitals. The large black dots indicate the nuclei whereas the small black dots refer to electrons. The circles correspond to electronic shells. The open circle denotes the electron for which we want to create a fragment orbital.

9.1 Atomic calculations to extract the deformation potential

In the derivations of chapter 8 we have only considered a specific angular momentum number ℓ at a time, the wave-function indices i and n have thus only been used within one specified ℓ-channel. This nomenclature is valid for an atom since, in a spherically symmetric atomic potential, we can write each eigenstate as a radial times an angular momentum dependent part:

$$\phi_{\ell m}(r) = \phi_{\ell m}(|r|)Y_{\ell m}(\hat{r}).$$

$\phi_{\ell m}(|r|)$ is a so-called radial function which just depends on the magnitude of r. In a non-magnetic system, the radial functions are furthermore independent of m. $Y_{\ell m}$ is the spherical harmonic corresponding to the quantum numbers ℓ and m. $Y_{\ell m}$ is potential independent and has the angular direction of r as an argument. For a non-magnetic case, it is therefore sufficient to solve a radial Schrödinger equation for $\phi_\ell(|r|)$:

$$\left[-\frac{1}{2}\partial_{|r|}^2 + \frac{\ell(\ell+1)}{2r^2} + v(|r|) - \varepsilon\right] |r|\phi_\ell(|r|) = |r|\varphi_\ell(|r|), \tag{9.1}$$

where $\varphi_l(|r|)$ denotes an inhomogeneity which we will need in order to calculate the nodeless wave-functions and their derivatives (compare equations 8.10 and 8.11). The three-dimensional problem is thus reduced to a one-dimensional one.

This type of equation is usually solved on a radial grid, where the ith grid point is defined as

$$r_i = r_1 e^{\alpha(i-1)}, \tag{9.2}$$

with r_1 being the innermost grid point and α the so-called logarithmic spacing. Such grids are very fine near the origin, where the wave-functions exhibit their strong oscillations, and become exponentially wider at larger distances. For a given set of boundary conditions at the nucleus (compare table 8.1) as well as at large distances from the nucleus, it is then straightforward to solve a Schrödinger equation of type 9.1. The numerical implementation described in the diploma thesis of Mike Thieme [87] has also been used in the context of this thesis.

This atomic code calculates, for a given atomic species, the Pauli-repulsion potential and overlap terms of equations 8.16 to 8.19 for each angular momentum channel ℓ on radial grids.

9.2 From a single atom to a solid

The spherical symmetry of an atomic calculation is of course lost in a solid or molecule. The solutions to the Schrödinger equation are therefore superpositions of several angular momentum components. We thus have to set up a potential which probes the angular-momentum character of the wave-function and then provides the correct radial potentials. In order to simplify the notation we will now use the index i as an atomic index which also specifies whether the corresponding potential or overlap term is on- or off-site. The Pauli-repulsion potential for atom i is thus given by

$$v_i^{\text{Pauli}} = \sum_{\ell m} |Y_{\ell m}\rangle v_{i,\ell m}^{\text{Pauli}} \langle Y_{\ell m}|.$$

This type of potential is called "non-local" potential since it depends on two position arguments:

$$v_i^{\text{Pauli}}(r, r') = \langle r|v_i^{\text{Pauli}}|r'\rangle = \sum_{\ell m} Y_{\ell m}(\hat{r}) \left(v_{i,\ell m}^{\text{Pauli}}(|r|) \cdot \frac{\delta(|r| - |r'|)}{r^2} \right) Y_{\ell m}^*(\hat{r}'),$$

where $\hat{r}$ denotes the direction of the vector r and the superscript '*' denotes the complex conjugate. For a set of atoms at positions R_i, the total Pauli repulsion potential is written as

$$
\begin{aligned}
v^{\text{Pauli}}(r,r') &= \sum_i v_i^{\text{Pauli}}(r,r') \\
&= \sum_i \sum_{\ell m} Y_{\ell m}(\widehat{r-R_i}) \\
&\qquad \left(v_{i,\ell m}^{\text{Pauli}}(|r-R_i|) \cdot \frac{\delta(|r-R_i|-|r'-R_i|)}{|r-R_i|^2} \right) Y_{\ell m}^*(\widehat{r'-R_i}).
\end{aligned}
$$

This expression can directly be translated for the overlap terms. It is common practice to separate the non-local potential into a local and a non-local part:

$$
\begin{aligned}
v^{\text{Pauli}}(r,r') &= \sum_i v_{i,\text{loc}}^{\text{Pauli}}(|r-R_i|)\delta(r-r') + \sum_{i=1}^{N_{\text{atoms}}} \sum_{\ell m} Y_{\ell m}(\widehat{r-R_i}) \\
&\qquad \left(\left[v_{i,\ell m}^{\text{Pauli}}(|r-R_i|) - v_{i,\text{loc}}^{\text{Pauli}}(|r-R_i|) \right] \cdot \frac{\delta(|r-R_i|-|r'-R_i|)}{|r-R_i|^2} \right) \\
&\qquad Y_{\ell m}^*(\widehat{r'-R_i}). \qquad (9.3)
\end{aligned}
$$

Potentials of this form also occur in the pseudo-potential approach which is reviewed in our publication 5, section 6.5 as well as in references [23, 90].

Since plane-waves constitute a very flexible basis set which is numerically convenient to handle, we decided to base the first implementation of the atomic fragment orbitals on a plane-wave representation [23, 90]. This allowed us to benefit from the approaches already developed in the context of pseudo-potentials. There are basically two schemes available which allow to incorporate non-local potentials as those of equation 9.3 into a Schrödinger equation:

- direct evaluation of the matrix elements $\langle G|v^{\text{Pauli}}|G'\rangle$ (compare equation 7.2 and corresponding text) in a plane-wave basis [91];
- transformation into separable potentials [92, 93].

In the course of this thesis I have developed two plane-wave codes to calculate the atomic fragments. The initial one followed the first approach. While it is well known, that the use of separable potentials is numerically by far more efficient, the long-range behavior of our potential and overlap terms (compare section 8.3.3) initially seemed to be a showstopper for this approach as discussed in section 9.3.3.

Via a specific choice of the local potential (compare equation 9.3), however, we found a way to also construct separable potentials. Both implementations will shortly be reviewed in the following sections.

9.2.1 The nonlocal pseudo-potential code

The total Hamiltonian of a molecule or solid including the Pauli repulsion potential is given by

$$\mathcal{H} = -\frac{1}{2}\nabla^2 + v^{\text{crystal}}(r) + v^{\text{Pauli}}(r, r').$$

We now have to calculate the matrix elements $\langle G| - \frac{1}{2}\nabla^2|G'\rangle$, $\langle G|v^{\text{crystal}}|G'\rangle$ and $\langle G|v^{\text{Pauli}}|G'\rangle$ (compare equation 7.2 and related text).

The first one is straightforward to evaluate in reciprocal space, since

$$\langle G| - \frac{1}{2}\nabla^2|G'\rangle = \langle G|G'\rangle\frac{1}{2}|G'|^2 = \delta_{G,G'}V\frac{1}{2}|G'|^2,$$

if we follow the definition of a plane-wave given in appendices A.2 and E. V denotes the unit cell volume.

The matrix elements of the crystal potential v^{crystal} as well as of the local potential of v^{Pauli} have the form

$$\langle G|v^{\text{crystal}}|G'\rangle = Vv^{\text{crystal}}(G - G'),$$

where $v^{\text{crystal}}(G)$ is the Fourier transform of $v^{\text{crystal}}(r)$ (refer to appendix E.3 for details). Analysis of this term reveals, that the Fourier expansion of the potential must include a larger number of components compared to the wave-functions since $|G - G'|$ can be twice as long as the maximum wave-vector $|G_{\text{max}}|$ of the wave-function expansion:

$$|\psi\rangle = \sum_{G,|G|\leq|G_{\text{max}}} |G\rangle c_G.$$

This forces us to use two grids, one for the wave-functions and another, finer one for the potential.

In the current implementation we have used a superposition of atomic potentials as a guess for the crystal potential. While such a superposition is definitely not equal to the self-consistent potential, it is a valid choice to explore the effect of the Pauli repulsion potentials and will be used throughout this thesis.

Before using the Pauli-repulsion potentials $v^{\text{Pauli}}(|r|)$ (compare equation 9.2) given on a radial grid, we first have to perform a Bessel transform (compare appendix E.2) which leads to a logarithmically spaced grid in reciprocal space

$v^{\text{atom}}(|G|)$. For each matrix element $\langle G|v^{\text{atom}}|G'\rangle$ we then have to interpolate the corresponding value of $v^{\text{atom}}(|G-G'|)$.

After this step we have only calculated the matrix elements of a potential at the origin, since $v^{\text{Pauli}}(|r|)$ is an atom-centered potential. In Fourier representation it is, however, straightforward to shift any function by multiplying it with so-called "structure-factors". Shifting a function $f(r) = \sum_G e^{iGr} f(G)$ by a vector R translates into a multiplication of each component of its Fourier transform $f(G)$ by a phase factor e^{-iGR}:

$$f(r-R) = \sum_G e^{iG(r-R)} f(G) = \sum_G e^{iGr} e^{-iGR} f(G) = \sum_G e^{iGr} \bar{f}(G).$$

$\bar{f}(G)$ is thus the Fourier transform of the shifted function. We now use the same scheme to shift the atomic potential to any point in space. The final crystal potential matrix element is thus given by

$$\langle G|v^{\text{crystal}}|G'\rangle = \sum_{i=1}^{N_{\text{atoms}}} \langle G|v_i^{\text{crystal}}|G'\rangle e^{i(G-G')R_i}.$$

The most tricky part are the nonlocal potential matrix elements which, for a given ℓ are calculated as:

$$\sum_{m=-\ell}^{\ell} \langle G|v_{i,\ell m}^{\text{Pauli}}|G'\rangle = 4\pi(2\ell+1) P_\ell(cos\gamma) \int_0^\infty d|r| r^2 j_\ell(|G||r|) v_{i,\ell}(|r|) j_\ell(|G'||r|),$$

where $P_\ell(\alpha)$ is a Legendre polynomial and the $j_\ell(|r|)$ are Bessel functions. γ is defined as

$$\gamma = \frac{G \cdot G'}{|G||G'|}.$$

A detailed derivation of this expression is given in appendix E.4. The matrix elements are then again shifted to the positions of the corresponding atoms using structure factors. Expressions for the ℓ-dependent overlap terms are obtained by replacing $v_{i,\ell}(|r|)$ by $o_{i,\ell}(|r|)$.

Finally we have to solve the Matrix equation (compare equation 7.2).

$$\langle G|\mathcal{H}|G'\rangle\langle G'|\psi\rangle = \varepsilon\langle G|\mathcal{O}|G'\rangle\langle G'|\psi\rangle$$

which is done using numerical libraries [84] or, alternatively, iterative approaches as discussed in section 3.1 and appendix C.

While the non-local pseudopotential code was a valuable tool to explore the effect of the deformation potential, it did not prove to be efficient enough to perform accurate calculations in terms of a large plane-wave cutoff. The quality of a plane-wave basis is defined by $|G_{\max}|$ via the corresponding kinetic energy $E^{\mathrm{PW}} = \frac{1}{2}V|G_{\max}|^2$. To calculate the fragment orbitals, the cells have to be large enough to ensure that there is no interaction between periodic images. Even a memory of 2 GB allowed us to only go up to a plane-wave cutoff of 7 Ry for the smallest reasonable simulation cell. Typical pseudo-potential or PAW [24] calculations use a cutoff energy between 20 to 30 Ry. Irrespective of the memory argument, a single calculation took up to several hours on a state-of-the-art microprocessor. The majority of the time was spent in setting up the matrix elements.

9.2.2 The separable pseudo-potential code

The deficiencies of the nonlocal pseudo-potential approach mentioned above have led to the development of separable potentials [92] in the eighties. This approach has later been extended independently by Blöchl [93] and Vanderbilt [94]. The underlying principle will now directly be introduced at the example of the linearized Schrödinger equation for the nodeless wave-functions (compare equation 8.15).

In contrast to equation 8.15, we will now, however, also include local potential and overlap terms, denoted $v_{\mathrm{loc}}^{\mathrm{Pauli}}$ and $o_{\mathrm{loc}}^{\mathrm{Pauli}}$, as in the previous sections. In the following paragraphs we will only consider the atomic case for a specified angular momentum channel and thus drop the indices i, ℓ and m. Our Schrödinger equation reads

$$\left[-\frac{1}{2}\nabla^2 + v^{\mathrm{atom}} \;+\; v_{\mathrm{loc}}^{\mathrm{Pauli}} + \left(v^{\mathrm{Pauli}}(\varepsilon_n) - v_{\mathrm{loc}}^{\mathrm{Pauli}}\right) \right. \\ \left. -\; \varepsilon\left[1 + o_{\mathrm{loc}}^{\mathrm{Pauli}} + \left(o^{\mathrm{Pauli}}(\varepsilon_n) - o_{\mathrm{loc}}^{\mathrm{Pauli}}\right)\right]\right] |q_n(\varepsilon)\rangle = 0.$$

In the following derivation and also in all the calculations in section 9.3 we have used the energy of the atomic eigenvalue ε_n as expansion energy ε_ν (compare equations 8.16 to 8.19). We know that $|q_n(\varepsilon_n)\rangle = |u_n\rangle$ is an exact solution to this linearized Schrödinger equation. We can use this information, the so-called "closure relation", to obtain an expression for the non-local potential:

$$\Big[-\frac{1}{2}\nabla^2 + v^{\text{atom}} + v_{\text{loc}}^{\text{Pauli}} - \varepsilon_n\big(1 + o_{\text{loc}}^{\text{Pauli}}\big)\Big]\,|u_n\rangle + \underbrace{\Big[\big(v^{\text{Pauli}}(\varepsilon_n) - v_{\text{loc}}^{\text{Pauli}}\big) - \varepsilon_n\big(o^{\text{Pauli}}(\varepsilon_n) - o_{\text{loc}}^{\text{Pauli}}\big)\Big]\,|u_n\rangle}_{|p(\varepsilon_n)\rangle c(\varepsilon_n)} = 0. \tag{9.4}$$

The second term, or alternatively the negative of the first term is now identified to be proportional to a so-called "projector function" $|p(\varepsilon_n)\rangle$ which we will abbreviate in the following as $|p\rangle$. The constant $c(\varepsilon_n)$, short c, is determined by requiring that

$$\langle p|u_n\rangle = 1$$

and thus

$$c = \langle u_n|\big[v^{\text{Pauli}}(\varepsilon_n) - v_{\text{loc}}^{\text{Pauli}}\big) - \varepsilon_n\big(o^{\text{Pauli}}(\varepsilon_n) - o_{\text{loc}}^{\text{Pauli}}\big)\big]\,|u_n\rangle.$$

Using the projector function, the Schrödinger equation for $|u_n\rangle$ can now be written as

$$\Big[-\frac{1}{2}\nabla^2 + v^{\text{atom}} + v_{\text{loc}}^{\text{Pauli}} - \varepsilon_n\big(1 + o_{\text{loc}}^{\text{Pauli}}\big) + |p\rangle\underbrace{\langle u_n|\big[v^{\text{Pauli}}(\varepsilon_n) - v_{\text{loc}}^{\text{Pauli}}\big] - \varepsilon_n\big[o^{\text{Pauli}}(\varepsilon_n) - o_{\text{loc}}^{\text{Pauli}}\big]|u_n\rangle}_{c}\langle p|\Big]\,|u_n\rangle = 0.$$

It can be shown by insertion that $|u_n\rangle$ is indeed a solution and the linearized Schrödinger equation for arbitrary energies ε now reads as

$$\Big[-\frac{1}{2}\nabla^2 + v^{\text{atom}} + v_{\text{loc}}^{\text{Pauli}} - \varepsilon\big(1 + o_{\text{loc}}^{\text{Pauli}}\big) + |p\rangle\langle u_n|\big[v^{\text{Pauli}}(\varepsilon_n) - v_{\text{loc}}^{\text{Pauli}}\big] - \varepsilon\big[o^{\text{Pauli}}(\varepsilon_n) - o_{\text{loc}}^{\text{Pauli}}\big]|u_n\rangle\langle p|\Big]\,|q_n(\varepsilon)\rangle = 0. \tag{9.5}$$

The potential energy operator is thus defined as

$$v = v^{\text{atom}} + v_{\text{loc}}^{\text{Pauli}} + |p\rangle\langle u_n|\big[v^{\text{Pauli}}(\varepsilon_n) - v_{\text{loc}}^{\text{Pauli}}\big]u_n\rangle\langle p|$$

and the overlap operator similarly as

$$o = 1 + o_{\mathrm{loc}}^{\mathrm{Pauli}} + |p\rangle\langle u_n|\left[o^{\mathrm{Pauli}}(\varepsilon_n) - o_{\mathrm{loc}}^{\mathrm{Pauli}}\right]|u_n\rangle\langle p|.$$

Note that the two matrix elements $\langle u_n|\cdots|u_n\rangle$ above are constant and can be precalculated on radial grids. The interaction of a wave-function with the nonlocal potential has thus been reduced to a simple scalar-product between a projector function and the wave-function. However, equation 9.5 is only correct to linear order around ε_n. To enhance energy transferability it is possible to include more projector functions for each angular momentum channel [93, 94]. We have, however, only used one projector function per angular momentum quantum number in the context of this thesis.

The separable form has two major advantages compared to the nonlocal form. First of all the numerical effort to evaluate the non-local potential is very small compared to the setup of the nonlocal potential matrix as will be discussed below. The second advantage is the memory requirement. While the full Hamilton and overlap matrices have to be stored in the nonlocal approach, it is sufficient to store the projector functions, equivalent to wave-functions, in the separable code. The local potential is evaluated in real space and only requires a grid-representation of the potential, which requires a similar amount of memory as a wave-function (it is actually more since we have to use a finer grid for the potential as discussed above).

To determine $\mathcal{H}|\psi\rangle$ in the separable code we

- calculate $\langle G| - \frac{1}{2}\nabla^2|\psi\rangle = \frac{1}{2}V|G|^2\langle G|\psi\rangle$ in the plane-wave representation. This operation just involves to multiply each Fourier component by the kinetic energy of the corresponding plane-wave as well as the unit-cell volume.
- make a fast-Fourier transform [95] to real space and evaluate the interaction of the wave-function with the local potential. Numerically this corresponds to a product of two functions on a regular grid. Another fast-Fourier transform transfers the result back to reciprocal space.
- compute the projections $\langle p|\psi\rangle$ in reciprocal space and add the contributions from the nonlocal potential (compare equation 9.5). This again only involves wave-functions and no matrix-vector operations.

The sum of the three contributions above gives $\mathcal{H}|\psi\rangle$. The procedure is analogous for the overlap operator. The knowledge of $\mathcal{H}|\psi\rangle$ and $\mathcal{O}|\psi\rangle$ allows us to employ iterative minimization schemes such as steepest descent, conjugate gradient or molecular dynamics (compare chapter 3 for an introduction). For the present case I have implemented a state-by-state conjugate gradient minimization scheme. Details of the conjugate gradient technique are described in appendix C.

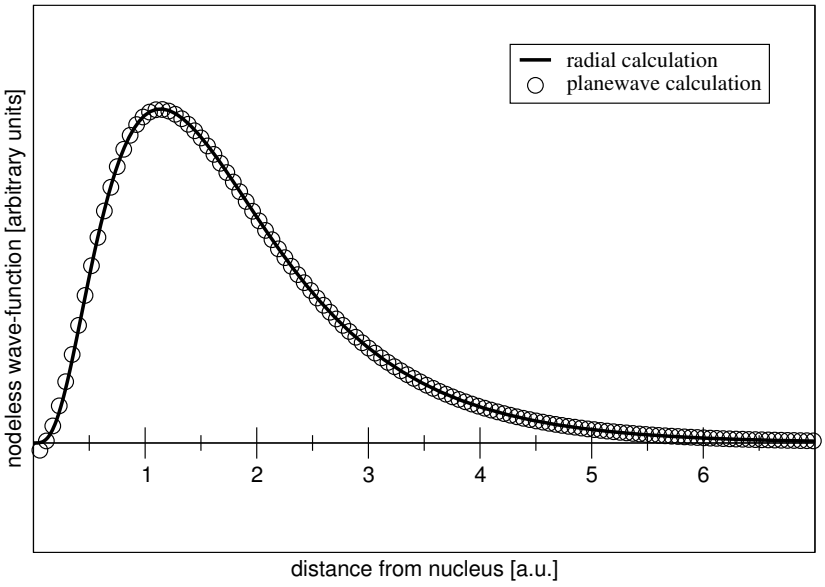

Figure 9.2: 1D-plot of the silicon $3s$ nodeless wave-function obtained from a radial atomic calculation and from a 3D plane-wave calculation. Note that the circles do not represent points from the real-space grid, which is much more coarse, but are interpolated from the plane-wave expansion.

9.3 The First Atomic Fragments

The atomic fragment orbitals and densities presented in this section are calculated using the separable code introduced in section 9.2.2. The higher efficiency in terms of memory and microprocessor requirements allowed us to use larger plane-wave cutoffs and thus to obtain better quality images. All pictures were obtained with a cutoff of 30 Ry. The potential for $\ell = 1$ has been used as the local potential.

9.3.1 The free silicon atom

As a first test system we have performed calculations on an isolated atom in an FCC cell with a lattice constant of 20 a.u. Figure 9.2 shows an overlay of the silicon $3s$ nodeless wave-function as obtained from the radial Schrödinger equation (compare section 9.1) and from a plane-wave calculation (compare section 9.2.2). The radial solution is to be considered as the exact one. It can nicely be observed that we obtain a good match between both solutions. Differences only occur at the nucleus where the plane-wave solution goes to slightly negative values. This can be attributed to our finite plane-wave cutoff. A discussion of the numerical challenges is given in section 9.3.3.

The plane-wave code also reproduces the atomic eigenvalues to within a few tenth of a milli-Hartree at the selected plane-wave cutoff.

9.3.2 The atomic fragment orbitals in bulk silicon

To explore the deformation of the free silicon atom by neighboring atoms, we performed calculations in a 16 atom bulk FCC supercell. One silicon atom, the central atom, displayed its core-repulsion potential (on-site, compare equations 8.16 and 8.17) while all the others displayed the Pauli repulsion from their valence shells (off-site, compare equations 8.18 and 8.19).

Figure 9.3 shows silicon s and p fragment orbitals. In figure 9.3(a) and 9.3(a) one clearly observes, that the spherical symmetry of the s orbital as well as the rotational symmetry of the p orbital is broken due to the repulsive potentials on the neighboring atoms. Panels 9.3(c) and 9.3(d) show a contour plot in a plane which goes through the central atom and two of the neighboring atoms. It can again nicely be observed, that neighboring atoms deform the orbital. Panels 9.3(e) and 9.3(f) finally show the difference in electronic density of the fragment orbitals and the corresponding orbitals of an isolated silicon atom. Be aware, however, that this is just a qualitative comparison, since the long-range nature of the atomic overlap operators (compare figure 8.4) results in different definitions of the norm for the isolated and deformed silicon atom. Nevertheless, the two panels show that the electron density is depleted in the region of the neighboring atoms and accumulated near the nucleus at the center.

Figure 9.4 shows the same kind of plots for an sp^3 bond orbital pointing towards the neighboring silicon atom in the [111] direction [96]:

$$|sp^3\rangle = \frac{1}{2}\big(|s\rangle + |p_x\rangle + |p_y\rangle + |p_z\rangle\big).$$

The isosurface plot nicely shows a deformation along the bond to the silicon atom to the right which corresponds to the [111] direction. Figure 9.4(b) shows a cut through a plane going through the central silicon atom and the one along [111] but through neither of the two other ones displayed. Figure 9.4(c) shows the difference in electron density between the sp^3 fragment orbital and the corresponding orbital of an isolated atom. We again observe the depletion of electrons in the region of the neighboring atom and an accumulation near the central atom. Figure 9.4(d) finally shows a cut through the plane which also includes the upper silicon atom. One now observes a clear asymmetry in the back-lobe of the sp^3 orbital and also a slight asymmetry in the front lobe near the upper silicon atom. This is due to the Pauli repulsion of that silicon atom.

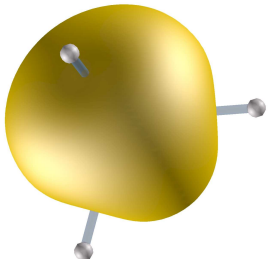

(a) Isosurface of s orbital at 10 % of the maximum value.

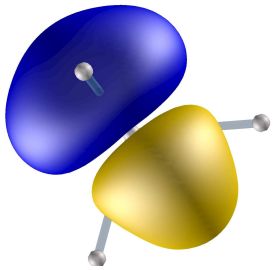

(b) Isosurface of p orbital at 10 % of the maximum value.

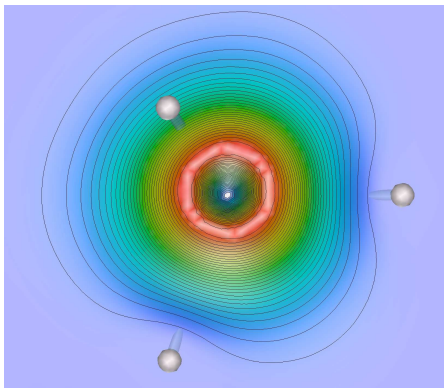

(c) Contour plot of the s orbital. Amplitude range: 0 to 0.19 .

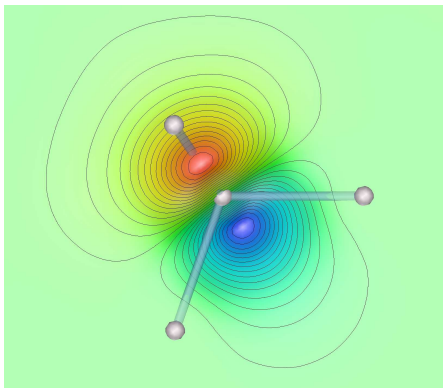

(d) Contour plot of the p orbital. Amplitude range: -0.24 to 0.24.

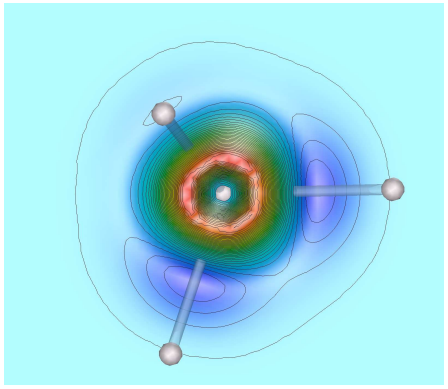

(e) Difference density to isolated atom for the s orbital. Amplitude range: $-1.9 \cdot 10^{-3}$ to $1.2 \cdot 10^{-2}$.

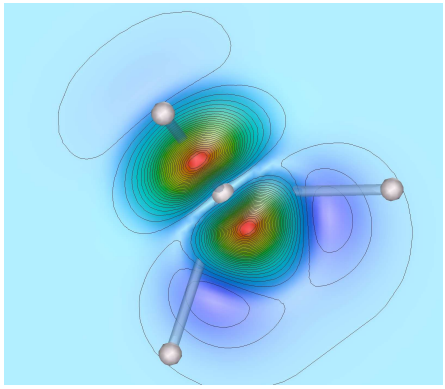

(f) Difference density to isolated atom for the p orbital. Amplitude range: $-2.9 \cdot 10^{-3}$ to $2.4 \cdot 10^{-2}$.

Figure 9.3: The silicon atomic fragment orbital. Only the first nearest neighbor shell is visualized. The plots are orientated so that the central atom as well as the atom on the bottom and to the right lie in the plane. All contour plots show 30 equispaced lines between the maximum and minimum values listed.

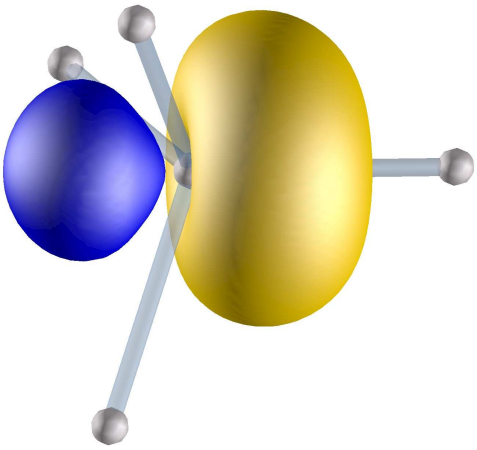

(a) Isosurface plot of an sp^3 orbital at 10 % of the maximum value.

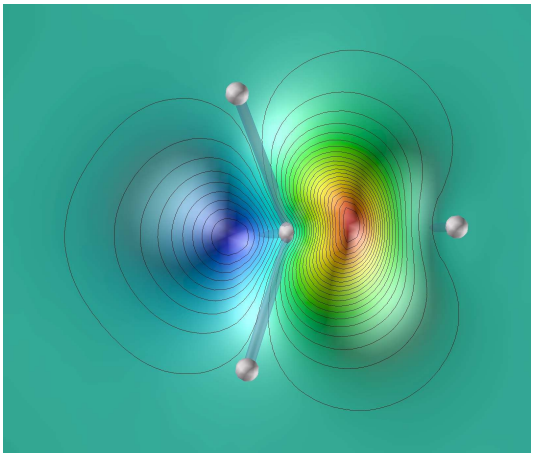

(b) Contour plot of an sp^3 orbital – view I. The amplitude ranges from −0.12 to 0.30. The two silicon atoms on the left stick out of the plane, the central and right one are in the plane.

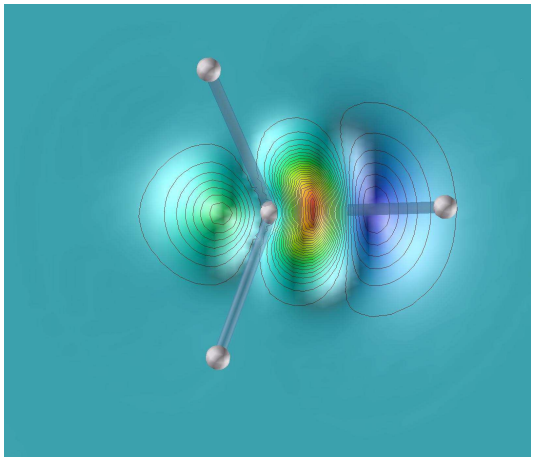

(c) Difference density to isolates Si atom – view I. Amplitude ranges between $-8.2 \cdot 10^{-3}$ and $3.2 \cdot 10^{-2}$.

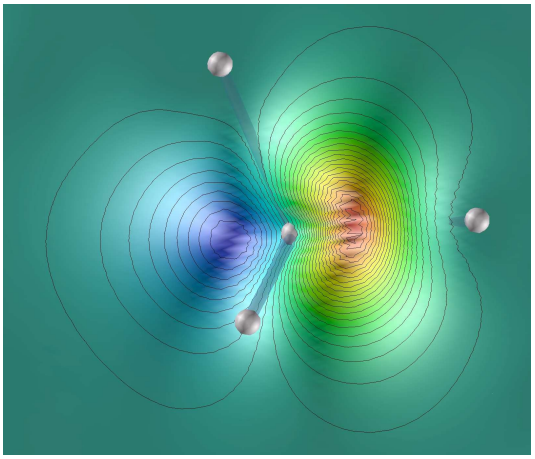

(d) Contour plot of an sp^3 orbital – view II. The amplitudes and contour lines are identical to figure 9.4(b). In this picture, the central, as well as the upper and left silicon atoms are within the plane. Amplitude range as in panel b. The bad quality of the interpolation is due to the special choice of the plane.

Figure 9.4: The silicon sp^3 atomic fragment orbital. Only the first nearest neighbor shell is visualized. The contour plots contain 30 equispaced lines between the maximum and minimum values listed.

In summary figures 9.3 and 9.4 show the deformation of the atomic orbitals due to presence of neighboring atoms. The Pauli repulsion creates atomic fragment orbitals which can be thought of as geometry adapted "puzzle pieces" holding the promise to be a well suited as a basis for condensed matter calculations. As a matter of construction, these fragment orbitals fulfill the two requirements postulated at the beginning of section 8.1, namely the behavior of an energy derivative near the neighboring atoms and the behavior of an atomic wave-function near the central atom. In order to make the calculations numerically feasible, we have switched to the nodeless wave-functions which can, however, be used to construct the physical all-electron wave functions (compare section 8.2).

9.3.3 Open issues

In the previous sections I have demonstrated the feasibility to calculate atomic fragment orbitals using the Pauli repulsion potentials derived in chapter 8. The specific form of the Pauli repulsion potentials, however, introduces numerical difficulties due to:

- the singularity at the origin and
- the long-range behavior.

Compare section 8.3.3 and figure 8.4 for a discussion and illustration.

The singularity of the potential at the origin leads to very steep projector functions in that region (compare equation 9.4). While the projector functions can be calculated to high accuracy on radial grids, they have to be Fourier transformed since the projections are evaluated in reciprocal space. Due to the finite plane-wave cutoff, the Fourier transform is not exact and the high-wavevector components are lost. This effect is called "Fourier filtering" since all frequencies above the plane-wave cutoff are "filtered" out. Figure 9.5 shows the exact projector function as well as the projector function after Fourier filtering at a series of plane-wave cutoffs. The difference is sizable. The good agreement of the plane-wave eigenvalues and eigenfunctions for the isolated atom (compare section 9.3.1), however, indicate that the results are not significantly affected by this error in the projector functions.

The second problem is the long range behavior of the potential and overlap terms which range far into the regions of neighboring atoms. Long-ranging nonlocal terms result in correspondingly long-ranging projector functions. The projector functions, however, must not overlap significantly, since the overlap region would then be probed twice which results in a double-counting. Via choosing one of the nonlocal potentials as the local one, we can, however, significantly reduce the

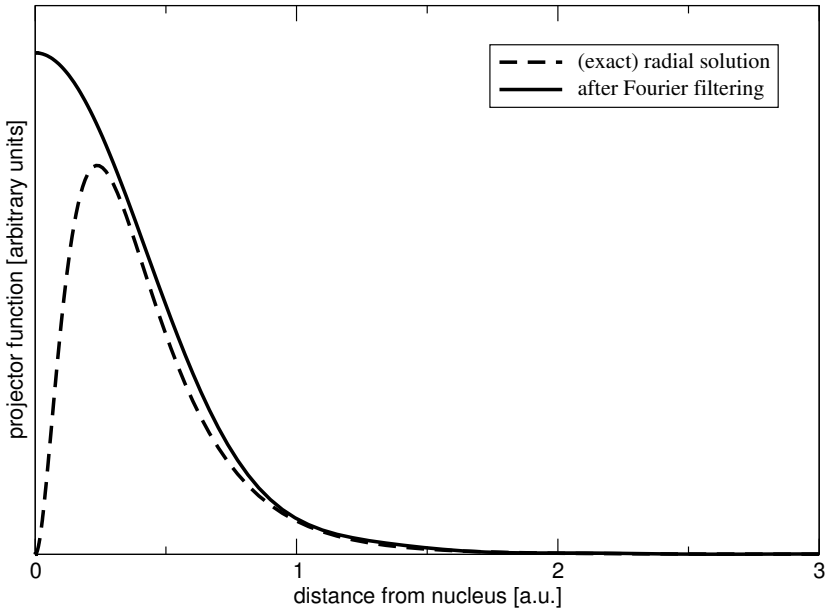

Figure 9.5: The silicon s projector function as calculated on a radial grid as well as after a Fourier transform at different plane-wave cutoffs.

extent of the projector functions (compare figures 8.4 and 9.5 as well as equation 9.4). This allowed us to do calculations using separable pseudo-potentials. Nevertheless, the long-range behavior of the Pauli repulsion terms may result in a bad energy transferability since they range far into the bonding region.

Further development of the Pauli repulsion potentials will have to focus on these two issues. The construction of the potential terms as well as the application to silicon has, however, been demonstrated and so far the results are promising.

9.4 Tight binding with atomic fragment orbitals

As a first application for the atomic fragment orbitals I have developed a tight-binding code to calculate band-structures for an fixed input potential. Tight-binding is the extension of the LCAO (linear combination of atomic orbitals) approach to solids. We start out from an infinite lattice as sketched in figure 9.6. The lattice points R are defined as

$$R = \alpha_1 t_1 + \alpha_2 t_2 + \alpha_3 t_3,$$

where the t_i are the lattice vectors and the α_i are integer numbers. The coordinates of the individual atoms of one lattice site, the so-called basis, is denoted by

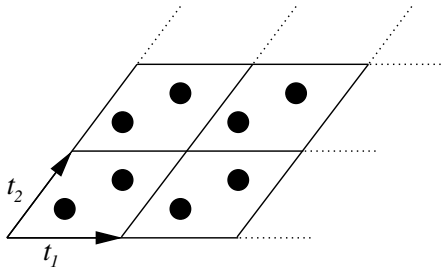

Figure 9.6: Sketch of a two-dimensional lattice.

r^j. The absolute position r of atom j on lattice site R is thus given as $r = r^j + R$. Be aware that R is used as a vector towards a lattice site and the corresponding index at the same time.

A localized atomic wave-function i on atom j, $|\chi_i^j\rangle$, in our context this will be an atomic fragment orbital, is now expanded into a Bloch wave:

$$\Xi_{i,k}^j(r) = \sum_R \chi_i^j(r - r^j - R) \cdot e^{ikR}.$$

The k-vector dependent matrix element of any operator $\mathcal{A}$ can now be evaluated via

$$\begin{aligned}
A_{i,i',k}^{j,j'} &= \langle \Xi_{i,k}^j | \mathcal{A} | \Xi_{i',k}^{j'} \rangle \\
&= \sum_{R,R'} \iint dr dr' e^{-ikR} \chi_i^{j^*}(r - r^j - R) A(r,r') \chi_i^j(r' - r^{j'} - R') e^{ikR'} \\
&= \sum_{R,R'} \iint dr dr' \chi_i^{j^*}(r - r^j - R) A(r,r') \chi_i^j(r' - r^{j'} - R') e^{ik(R'-R)} \\
&= \sum_R \left[\sum_{\Delta R = R' - R} \iint dr dr' \chi_i^{j^*}(r - r^j - R) A(r,r') \cdot \right. \\
&\qquad \left. \cdot \chi_i^j\big(r' - r^{j'} - (R + \Delta R)\big) e^{ik\Delta R} \right] \\
&= M \left[\sum_{\Delta R} \underbrace{\iint dr dr' \chi_i^{j^*}(r - r^j) A(r,r') \chi_i^j(r' - r^{j'} - \Delta R)}_{A_{i,i'}^{j,j'}(\Delta R)} e^{ik\Delta R} \right],
\end{aligned}$$

where M denotes the number of lattice sites. Since this factor occurs in all matrix elements it is not considered. The expression for $A_{i,i',k}^{j,j'}$ still includes an infinite

sum over ΔR. Assuming a purely local operator $\mathcal{A}$, $A(r,r')\delta(r-r')$ in real space, all but a few elements of this sum will be zero, if the atomic wave-functions $\chi_i^j(r)$ are localized. All operators under consideration, namely kinetic energy, potential and overlap, are de-facto local. The non-locality of the potential is restricted to small regions around each atom and the infinite sum is therefore reduced to a few elements.

Furthermore it is important to notice that the $A_{i,i'}^{j,j'}(\Delta R)$ are k-independent and thus have to be evaluated only once. The k-dependent matrix elements $A_{i,i',k}^{j,j'}$ are obtained by multiplying each sub-element with the corresponding phase factor $e^{ik\Delta R}$ and performing the sum over all ΔR.

To set up a tight-binding Hamilton or overlap matrix we first of all have to map all atomic basis functions of all atoms onto a single index. The total dimension of the matrix is

$$N_{\text{dim}} = \sum_j n^j,$$

where n^j denotes the number of basis functions for a specific atom j. In a second step, all sub-matrix elements $A_{i,i'}^{j,j'}(\Delta R)$ are set up. For a given k-point it is then straightforward to set up the k-dependent tight-binding matrix which can be diagonalized using numerical libraries [84].

As a first application we have calculated the band-structure for the 2-atom FCC unit cell of silicon. Figure 9.7(a) shows the result. We observe a nice qualitative agreement with the self-consistent result of figure 9.7(b). Note that the tight-binding calculation was performed in a non-selfconsistent potential derived from a superposition of atomic potentials. Therefore it can not be expected that the bandstructure matches quantitatively.

In the implementation of the tight-binding code, there is still a numerical problem with the integration routine since the lowest two bands are not degenerate between the k-points X and W.

9.5 Relation of our theory to previous approaches

The idea of deformed ions traces back to Finnis [97], who tried to construct a well adapted input density in the context of the non-selfconsistent Harris-Foulkes functional (compare appendix F). Realizing that the Harris-Foulkes functional yields poor surface energies for Al when using a superposition of atomic densities,

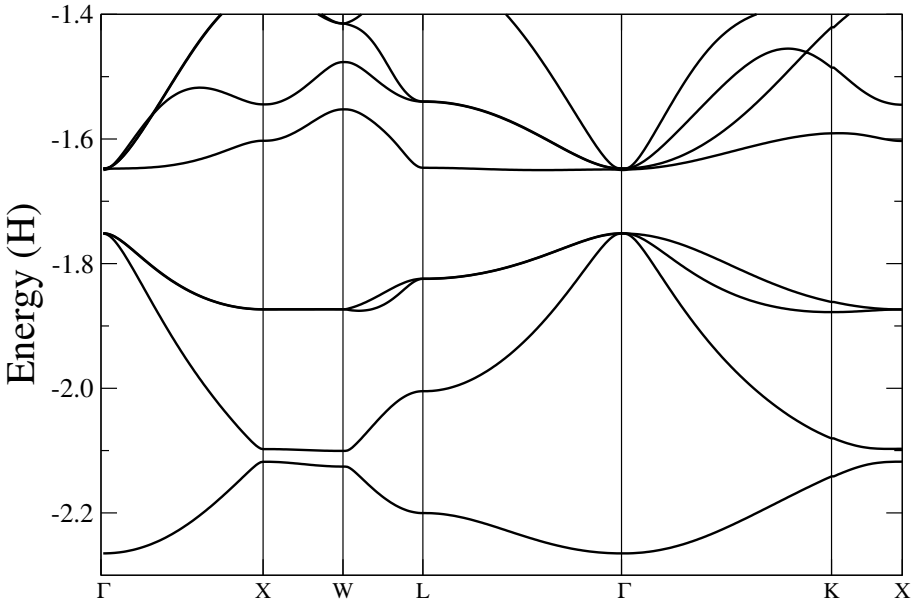

(a) Band structure obtained with a minimal basis of atomic fragment orbitals and a superposition of atomic potentials.

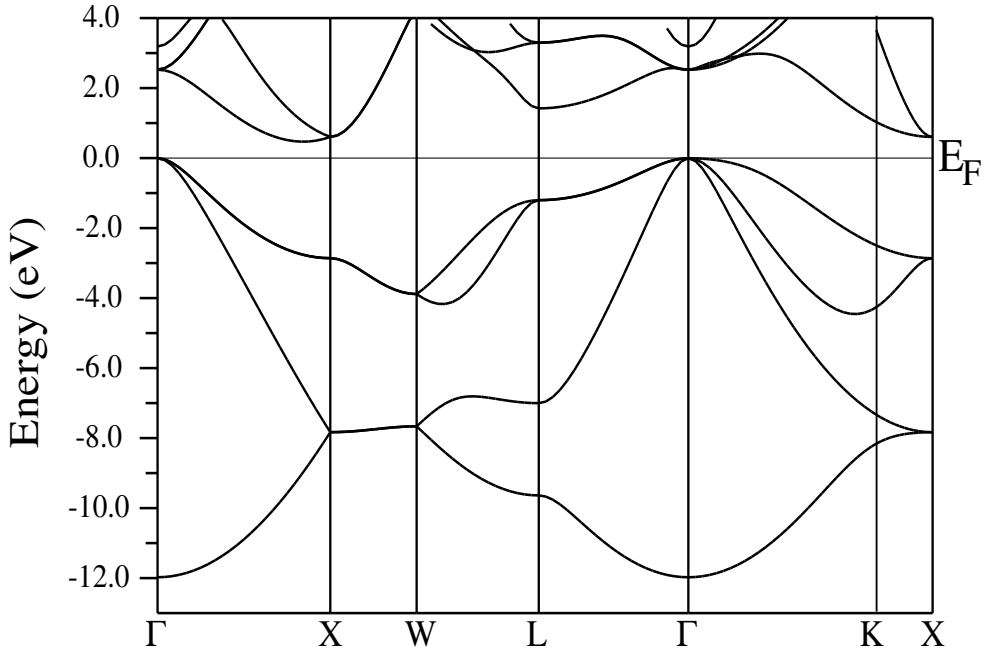

(b) Band structure obtained from a self-consistent LAPW calculation [26]. Figure courtesy of Peter Blaha, Vienna University of Technology, Austria.

Figure 9.7: Bandstructure of a silicon 2-atom FCC unit cell.

he introduced a two-parameter cutoff function to contract the density. Later, Chetty and co-workers [98] used the following relationship to extracted the Fourier components of a deformed ion out of the self-consistent density of a homo-nuclear system:

$$\rho^{\text{total}}(G) = \rho^{\text{deformed atom}}(G) \sum_{i=1}^{N_{\text{atoms}}} S_i(G),$$

where $S_i(G)$ denotes the structure factor (compare section 9.2.1) for atom i and plane-wave G. For a given $\rho^{\text{total}}(G)$ and atomic positions, it is therefore possible to obtain $\rho^{\text{deformed ion}}$ for all G where the sum over the structure factors is non-zero. The authors report a contraction of the density, similar to the approach of Finnis.

A more recent approach are the third generation muffin tin orbitals developed by Ole Andersen and co-workers with a review given in reference [85]. Their fragment orbitals are constructed as a superposition of typically three so-called "kinked partial waves", obtained at different energies. A kinked partial wave

- is a solution to the muffin-tin potential within a hard sphere around the central atom;
- is zero in the hard spheres of all other atoms;
- is a screened spherical wave in the so-called interstitial region, subject to the constraint that it must match in value the partial solutions inside the atomic spheres. Since the derivatives need not to match, the resulting joint wave-functions carry the attribute "kinked". A screened spherical wave is a solution to the differential equation

$$-\nabla^2|\phi(\varepsilon)\rangle = \varepsilon|\phi(\varepsilon)\rangle.$$

While the solution inside the central sphere has a well defined (ℓ, m) character, it contains a mixture of different angular momenta components in the interstitial region. At least in terms of the character of the wave-functions in the two kinds of atomic spheres, this approach conceptually fulfills the two requirements of section 8.1, namely $|\phi\rangle$ character in the central sphere and $|\dot{\phi}\rangle$ character in the other spheres. The first requirement is fulfilled exactly, the second on an approximate level: The energy derivative of a wave-function has only a very small amplitude near the nucleus and then diverges exponentially at some point. Similarly, the kinked partial waves are zero in the vicinity of the neighboring nucleus and then adopt the form of a spherical partial wave. On the basis of this argument, both approaches aim at a similar character of the atomic fragment. Andersen and co-workers use, however, full wave-functions including nodes. Furthermore their

construction is based on joining solutions in different regions of space whereas our approach relies on the design of potential terms which yield the atomic fragments as a solution to a single Schrödinger equation.

In the context of tight-binding and order-N approaches [86] it is furthermore common practice to construct basis functions which are zero beyond a certain radius. This is done via geometrical constraints or artificial confinement potentials. For a review of recent developments refer to references [99, 100, 101].

In terms of nodeless wave-functions there have been first approaches in the context of pseudo-potential generation [102, 103, 104]. These constructions were based on a mixing of core states into the valence states in order to obtain

- smooth pseudo wave-functions,
- minimal core overlap, and
- minimal radial kinetic energy.

The main difference between this and our approach is, that we propose a direct construction without any fitting procedure.

9.6 Outlook

In the third part of this thesis I have introduced a novel concept of nodeless wave-functions which allows us to calculate atomic potentials which mimic the Pauli-repulsion of the core or valence electrons. These potential terms have then been used to construct atomic fragments, which are atomic orbitals and densities that are adapted to a specific atomic neighborhood. While there is still work to be done in terms of numerics and self-consistency, the results obtained so far are very promising although primarily qualitative.

Appendices

Appendix A

Notation

A.1 Atomic units

Atomic units have been introduced as a convenient system of units in quantum mechanics. Fundamental constants are chosen to be equal to unity which significantly reduces the effort of writing formulae. The table below lists the values for the most important quantities:

Quantity	atomic unit	SI value	
mass	electron mass $m_e = 1$	$9.10938 \cdot 10^{-31}$	kg
charge	electron charge $e = 1$	$1.60218 \cdot 10^{-19}$	C
length	Bohr radius $a_0 = 1$	$5.29177 \cdot 10^{-10}$	m
energy	Hartree $\frac{e^2}{4\pi\varepsilon_0 a_0} = 1$	$4.35974 \cdot 10^{-18}$	J
angular momentum	$\hbar = 1$	$1.05457 \cdot 10^{-34}$	Js

The single particle Schrödinger equation is thus simplified from

$$\left[-\frac{\hbar^2}{2m_e}\nabla^2 - \frac{1}{4\pi\varepsilon_0}\frac{Ze^2}{r}\right]\psi = \varepsilon\psi$$

to

$$\left[-\frac{1}{2}\nabla^2 - \frac{Z}{r}\right]\psi = \varepsilon\psi.$$

A.2 Dirac's bra-ket notation

The bra-ket or Dirac notation was introduced by Paul Dirac and has become the standard notation in quantum mechanics. This appendix only introduces the concepts relevant to this thesis and is meant to provide an intuitive picture. A more in-depth discussion can be found in any modern textbook on quantum mechanics.

In the bra-ket notation, a quantum mechanical state is denoted by a so-called *ket*:

$$|\psi\rangle,$$

where ψ is the label identifying the state. A ket has to be considered as an abstract object. Consider a vector in real space, which specifies a direction, as an analogue. Only in connection with a basis it is possible to assign numerical values, in this case an n-tuple of numbers, to this abstract object. The numerical values of this n-tuple are defined as the scalar products onto the corresponding basis vectors. Similarly we can only assign a numerical value to the ket $|\psi\rangle$ by evaluating a scalar product with another state. The real space representation of a wave-function $|\psi\rangle$, for example, is obtained as a scalar product with the *bra* $\langle r|$, being an eigenstate of the position operator:

$$\psi(r) = \langle r|\psi\rangle.$$

The complex conjugate $\psi^*(r)$ is defined as

$$\psi^*(r) = \langle \psi|r\rangle.$$

In a more mathematical way, the bra $\langle\psi|$ is an element of the "dual space" of the Hilbert space containing the ket $|\psi\rangle$. The dual space is the set of linear functionals from the Hilbert space to the complex numbers. In the picture of a vector-space, the row vectors constitute the dual space to the column vectors.

Apart from real space, another popular choice of representation is the momentum space. Plane waves $|G\rangle$ are eigenfunctions of the momentum operator, $\hat{p}|G\rangle = \hbar G|G\rangle$. In the course of this thesis, their real space representation is defined as:

$$\langle r|G\rangle = e^{iGr}.$$

Plane-waves constitute an orthogonal basis:

$$\langle G|G'\rangle = V\delta_{G,G'}.$$

Be aware that in some text-books, $\langle r|G\rangle$ is defined as $\sqrt{\frac{1}{V}}e^{iGr}$ for periodic systems, where V denotes the volume of periodicity. The pre-factor thus results in a normalization, and the set of $|G\rangle$ is orthonormal.

The unity operator in these two representations is thus defined as

$$1 = \int_V dr\ |r\rangle\langle r| = \sum_G\ |G\rangle\frac{1}{\langle G|G\rangle}\langle G| = \frac{1}{V}\sum_G\ |G\rangle\langle G|,$$

where the sum in the last term must be replaced by an integral for non-periodic systems. A scalar product between two states ψ and ϕ in the two representations is therefore evaluated as

$$\langle\psi|\phi\rangle = \int_V dr\ \langle\psi|r\rangle\langle r|\phi\rangle = \sum_G\langle\psi|G\rangle\frac{1}{\langle G|G\rangle}\langle G|\phi\rangle,$$

again assuming periodic boundary conditions and thus discrete values of G.

Consistently, the Fourier expansion of a real-space function $\psi(r)$ is obtained via

$$\psi(r) = \langle r|\psi\rangle = \frac{1}{V}\sum_G\langle r|G\rangle\langle G|\psi\rangle = \sum_G e^{iGr}\psi(G),$$

where $\psi(G)$ is the Fourier transform of $\psi(r)$ and defined as $\frac{1}{V}\langle G|\psi\rangle$. Mind that this definition is tied to the previous definition of $\langle r|G\rangle$.

The expectation value of an operator in bra-ket notation is written as

$$\langle A\rangle = \langle\psi|\hat{A}|\psi\rangle,$$

where the rules for evaluation in specific representations is obtained by inserting the corresponding unity operator as demonstrated for the scalar product.

Appendix B

Analysis used for publications of part II

This appendix contains details on the analysis performed for our publications attached in chapter 6.

B.1 Surface phase diagrams

This section describes how to calculate the surface phase diagrams based on the adsorption energy per ad-atom. We have used this analysis in our publications 2 and 3 attached in chapter 6.

For the derivation we start out from a macroscopic number of m $Si^{(1\times1)}$ surface unit cells and two phases a and b which share a common phase boundary. For the moment let us assume that we already know the phase diagram. Later in this section we will show how to derive it from a set of surface reconstructions. At a coverage θ_a, corresponding to phase a, the number of atoms at the surface N_a and the energy $E(N_a)$ is given by:

$$\begin{aligned} N_a &= m\theta_a \\ E(N_a) &= N_a E_a = m\theta_a E_a = m E_a^{(1\times1)}, \end{aligned}$$

where E_a is the energy per ad-atom in phase a and $E_a^{(1\times1)} = \theta_a E_a$ the corresponding energy per (1×1) surface unit cell. Adding more ad-atoms to the surface will lead to the nucleation of islands of phase b and a reduction of the area covered by phase a. For N atoms on the surface, $N_a \leq N \leq N_b$, there is a coexistence of phases a and b, with m_a/m_b surface unit cells covered by phase a/b:

$$N = m_a\theta_a + (m - m_a)\theta_b \quad \longrightarrow \quad m_a = \frac{N - m\theta_b}{\theta_a - \theta_b} = \frac{N - N_b}{\theta_a - \theta_b}.$$

The surface energy for a general N between N_a and N_b can now be written as

$$\begin{aligned}
E(N) &= m_a\theta_a E_a + (m - m_a)\theta_b E_b \\
&= m_a E_a^{(1\times1)} + (m - m_a)E_b^{(1\times1)} \\
&= \frac{N - N_b}{\theta_a - \theta_b}E_a^{(1\times1)} + mE_b^{(1\times1)} - \frac{N - N_b}{\theta_a - \theta_b}E_b^{(1\times1)} \\
&= mE_b^{(1\times1)} + \frac{E_a^{(1\times1)} - E_b^{(1\times1)}}{\theta_a - \theta_b}(N - N_b) \\
E^{(1\times1)}(\theta) &= E_b^{(1\times1)} + \frac{E_a^{(1\times1)} - E_b^{(1\times1)}}{\theta_a - \theta_b}(\theta - \theta_b) \\
&= E_a^{(1\times1)} + \frac{E_b^{(1\times1)} - E_a^{(1\times1)}}{\theta_b - \theta_a}(\theta - \theta_a).
\end{aligned}$$

The chemical potential in the coverage range between θ_a and θ_b is therefore given by

$$\mu = \frac{\partial E(N)}{\partial N} = \frac{\partial E^{(1\times1)}(\theta)}{\partial \theta} = \frac{E_a^{(1\times1)} - E_b^{(1\times1)}}{\theta_a - \theta_b} = \frac{E_b^{(1\times1)} - E_a^{(1\times1)}}{\theta_b - \theta_a} \tag{B.1}$$

and thus constant. Instead of using the coverage θ, this insight now allows us to draw a phase diagram as a function of the chemical potential. The phase boundary between two phases a and b is then defined by the chemical potential of equation B.1, since it corresponds to a coexistence of both phases. Chemical potentials can then be related to process parameters such as partial pressure and temperature using approaches of statistical mechanics (compare chapter 4 and [70, 71, 72, 73]).

The chemical potential defining a phase boundary corresponds to the slope of a line connecting the two phases in an surface energy per (1×1) unit cell versus coverage plot as for example in figure 5.7. While the phase boundary is characterized by a specific chemical potential, a phase is characterized by a range of chemical potentials between the phase boundaries to the phases at lower and higher coverages.

So far we have assumed to already know the thermodynamically stable phases. Based on the formalism just derived it is now straightforward to unambiguously

identify the phases from the low energy surface reconstructions at various coverages. Imagine we have found surface reconstructions a to e as sketched in figure B.1. Each of the reconstructions is the lowest energy structure of the corresponding coverage but, as we will see, not necessarily thermodynamically stable.

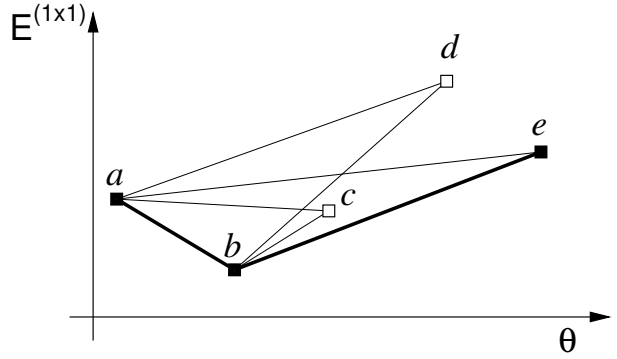

Figure B.1: Illustration of the search for phases out of a set of surface reconstructions.

We now start by connecting reconstruction a with all other reconstructions and compute the chemical potential at which these pairs would coexist. The next phase is then the reconstruction, which is connected to phase a by the lowest chemical potential. This can be rationalized by imagining to increase the chemical potentials starting at minus infinity. At some point, ad-atom adsorption will become thermodynamically favorable and phase a will be formed. Upon further increase the phase-boundary between a and b will be crossed and phase b will form.

Repeating the same procedure for phase b now gives reconstruction e as the next phase which means that c and d will not be observed in thermodynamical equilibrium and are hypothetical structures.

To compute $\mu(N,T)$, the energies $E_{a/b}$ have to be replaced by $E_{a/b}(T)$. See chapter 4 for a discussion.

B.2 Calculation of band offsets

In the context of heterostructures it is often of importance to calculate the relative position of the bandstructures of the two materials joined. In the context of high-k oxides these so-called band offsets are a crucial parameter for device application as outlined in section 5.3.4.

The most straightforward way to determine the band offsets is to plot a layer-resolved density of states as in figure B.2. One can then measure the valence band

offset as the difference of the two valence band maxima. While this is a convenient and quick way to obtain a first estimate, it is not a very accurate scheme. First of all the k-mesh used in interface calculations is usually just sufficiently dense to give reliable total energies and cannot reveal every feature of the band-structure. It is therefore likely, that the valence band minimum is not precisely reproduced. Secondly, the bandstructure can be spread out due to finite size effects. Finally it is often difficult to distinguish the bulk band edge from surface states.

The correct procedure is to use well k-converged bulk calculations of the two materials and relate them to the interface calculation via the potential. As outlined in equation F.1 on page 207 the effective potential of the Kohn-Sham equations is only defined to within a constant. The choice of this constant has no effect on charge-neutral cells since the effect of the potential on the electrons is canceled by the same effect on the positive nuclei. This constant shift of the potential does, however, shift the Kohn-Sham eigenvalues and therefore the bandstructure. A direct comparison of band edges from two different bulk calculations is thus not possible.

We can, however, relate the band edges of the bulk calculation to the corresponding electrostatic potential. It is then possible to determine the offsets of the bulk electrostatic potentials to the electrostatic potential of the interface calculations [105]. The position of the band edges of the bulk systems can now be shifted by exactly these offsets to give DFT band offsets at the interface. In the example of figure B.3, the offset for Si is $-1.08\,\mathrm{V}$ and for $SrTiO_3$ $1.88\,\mathrm{V}$. The bulk band structures thus have to be shifted by 1.08 and $-1.88\,\mathrm{eV}$.

The above scheme allows us to reliably determine the DFT band-offsets. In order to arrive at the true band-offsets we still have to make two approximations.

1. We assume that the DFT valence band maxima are reproduced correctly and the DFT valence band offsets are thus equal to the true valence band offsets. This condition is automatically fulfilled in exact DFT since the highest occupied orbital determines the decay of the density into the vacuum and is therefore directly connected to the electron density [41]. In practical DFT calculations this is not automatically fulfilled since we have to approximate the exchange-correlation functional. GW calculations indicate that the shifts in valence band maxima can be decisive [106, 107]. The inclusion of so-called "vertex corrections" to GW, however, shift the valence band maximum again up towards the LDA value [108]. At least for silicon these comparisons have shown that GW calculations do not necessarily yield better results for the position of valence band maxima. Using DFT valence band offsets therefore seems to be an equally valid choice.

2. We have to deal with the well-known band-gap problem of DFT (compare chapter 2.3 for a discussion). The Kohn-Sham eigenvalues are just La-

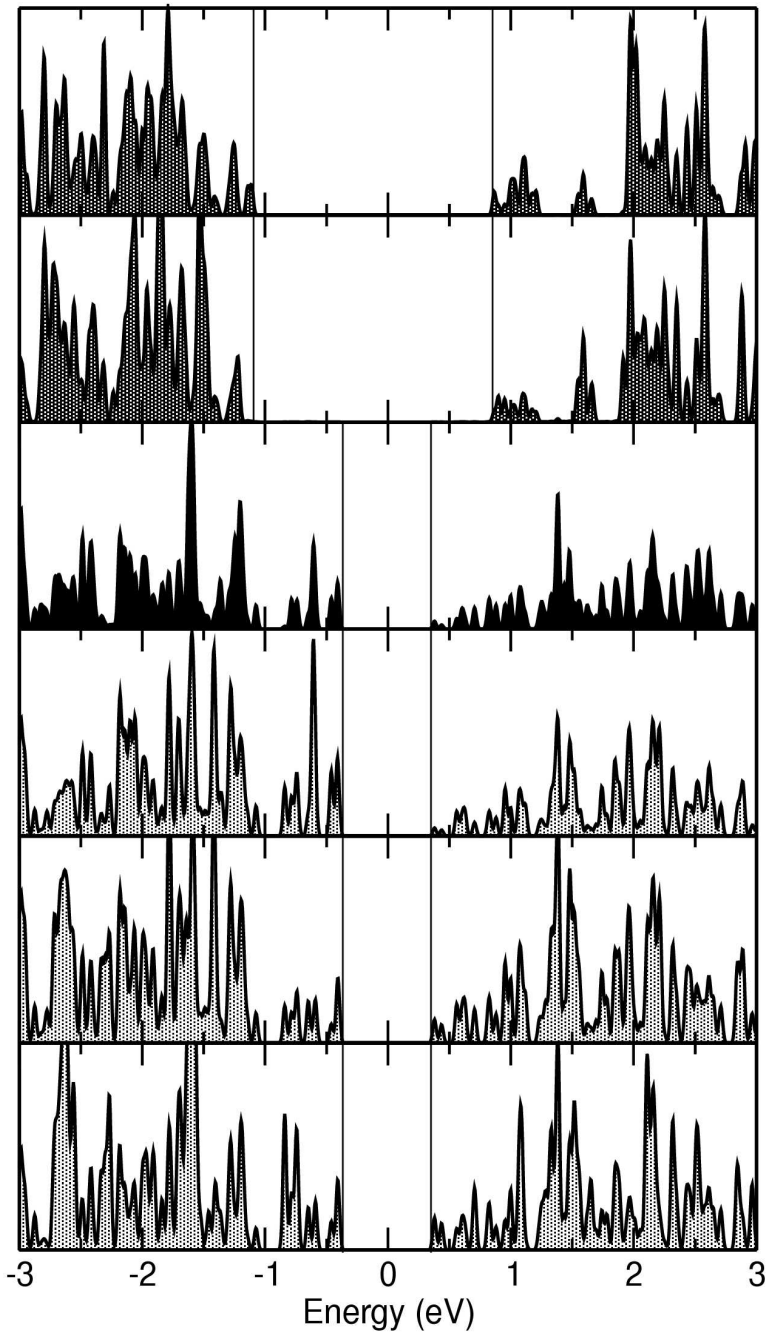

Figure B.2: Layer resolved density of states for the oxidized interface (compare right panel of figure 5.15). The lower three panels are the first three silicon layers, not including the dimer silicon atoms. The top two layers are the first two unit cells of $SrTiO_3$ and the remaining, fully blackened density of states corresponds to the interfacial layer consisting of the dimer silicon atoms and the 1/2 ML of Sr. The valence band maxima and the conduction band minima in both regions are marked by vertical lines.

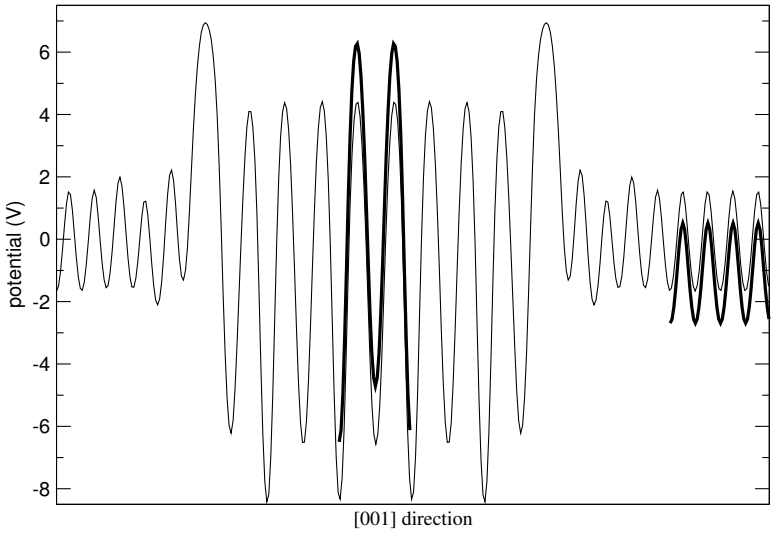

Figure B.3: Overlay of the plane-wave part of the electrostatic potential of a calculation where $SrTiO_3$ is sandwiched between silicon as well as bulk $SrTiO_3$ and Si calculations. The characteristics of these potential curves are discussed in figure 5.18.

grange multipliers to enforce the orthogonality of the wave-functions and have no physical meaning. Nevertheless it has turned out that DFT band-structures are qualitatively correct. The largest deviation from the true band-structure is the underestimation of the band-gap by up to a factor of two. Bulk silicon, for example, has an experimental gap of 1.17 eV. Using state-of-the-art gradient corrected functionals we get a gap of just 0.65 eV in DFT. For $SrTiO_3$ we obtain 1.93 eV instead of 3.32 eV. As a result, the DFT conduction band offsets have to be corrected to account for DFT's underestimation of band gaps. In the present example the conduction band offset had to be increased by 0.78 eV.

Appendix C

The Conjugate Gradient minimization scheme

This appendix contains a derivation of the conjugate gradient minimization scheme [54, 55, 23, 53, 56]. In order to enhance readability I will first show the basic principles at the example of the minimization of some abstract functional E. We will also assume that we know the gradient operator $\mathcal{G}$ which allows us to compute the gradient of the functional. The gradient operator $\mathcal{G}$ is furthermore assumed to be constant which translates into an harmonic functional E. We will later apply these results to the minimization of the Hohenberg-Kohn-Sham energy functional. Mind that a variety or different flavors of the conjugate gradient scheme are available and in use today [23, 56, 109]. In this appendix I will only derive the underlying ideas and introduce the concepts needed in part III of this thesis.

C.1 Steepest descent revisited

The starting point is the steepest descent algorithm already introduced in section 3.1. The basic principle is again visualized in figure C.1. Starting from an initial guess point $|x_1\rangle$ we compute the gradient $|g_1\rangle = \mathcal{G}|x_1\rangle$ and minimize E along $|g_1\rangle$. Such a one-dimensional minimization is called line-minimization. Finding the minimum of E along $|g_1\rangle$ is equivalent to finding a point $|x_2\rangle = |x_1\rangle + |g_1\rangle\alpha_1$, where the gradient $|g_2\rangle = \mathcal{G}|x_2\rangle$ is orthogonal to $|g_1\rangle$. In other words: the minimum along a line is found at the point where the equipotential line is parallel to the direction of minimization.

In the sequence of line-minimizations of the two-dimensional example of figure C.1, all even and all odd search directions are parallel. We are thus repeatedly

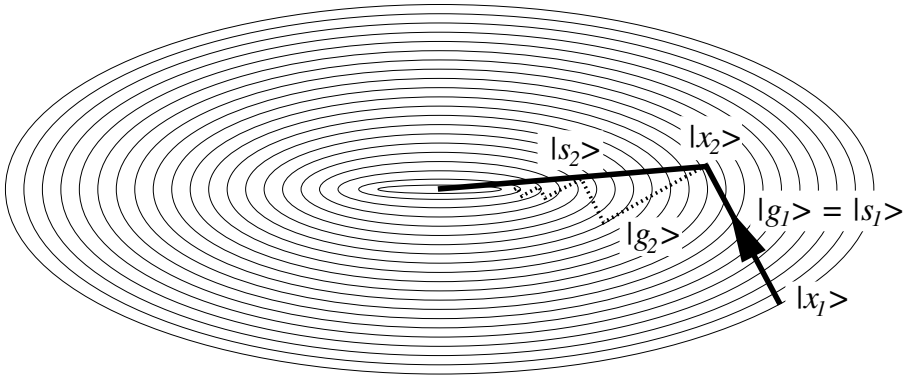

Figure C.1: Conjugate Gradient (thick line) versus steepest descent (dotted line) at the example of a two-dimensional energy surface. The labels are explained in the text.

minimizing along directions which have already been minimized before. As a result we will need an infinite number of iterations to arrive at the exact minimum, even for this simple, two-dimensional example.

C.2 Construction of "conjugated" gradients

Theoretically, it is possible to find the exact minimum of an N-dimensional harmonic potential with N minimization steps. The problem of the steepest descent approach is related to the fact that gradients become linearly dependent on their predecessors. The idea behind "conjugated" gradients, or better, "conjugated" search directions, is to circumvent exactly this linear dependence. In the following discussion, we will distinguish between gradients $|g_i\rangle = \mathcal{G}|x_i\rangle$ and search directions $|s_i\rangle$. Both are equal in the steepest descent approach.

The first conjugate gradient iteration is equal to the first steepest descent step and the search direction $|s_1\rangle$ is thus equal to the gradient $|g_1\rangle$. From then on we define the search direction to be a linear combination of the gradient and all previous search directions:

$$|s_n\rangle = |g_n\rangle + \sum_{i=1}^{n-1} |s_i\rangle\beta_i,$$

where the β_i are determined by the condition that the gradient at point $|x_{n+1}\rangle = |x_n\rangle + |s_n\rangle\alpha_n$ is orthogonal to all previous search directions. At every "new" point of the sequence, the gradient will thus point into a direction which has not been minimized before.

C.2.1 First iteration

The first step of a conjugate gradient minimization is identical to steepest descent, that is, the first search direction $|s_1\rangle$ is identical to the gradient $|g_1\rangle$. The minimum of the first line-minimization $|x_2\rangle$ is thus found according to

$$|x_2\rangle = |x_1\rangle + |s_1\rangle\alpha_1. \tag{C.1}$$

Mathematically, a line-minimization corresponds to determine $|x_{n+1}\rangle$ as

$$|x_{n+1}\rangle = |x_n\rangle + |s_n\rangle\alpha_n, \tag{C.2}$$

where α_n is defined by the condition that

$$0 = \langle s_n|g_{n+1}\rangle = \langle s_n|\mathcal{G}|x_{n+1}\rangle \overset{C.2}{=} \langle s_n|g_n\rangle + \langle s_n|\mathcal{G}|s_n\rangle\alpha_n \tag{C.3}$$

and therefore

$$\alpha_n = -\frac{\langle s_n|g_n\rangle}{\langle s_n|\mathcal{G}|s_n\rangle}. \tag{C.4}$$

C.2.2 Second iteration

After obtaining $|x_2\rangle$ analogous to the first steepest descent step, the search for $|x_3\rangle$ is again written as a line minimization

$$|x_3\rangle = |x_2\rangle + |s_2\rangle\alpha_2 \tag{C.5}$$

with

$$|s_2\rangle = |g_2\rangle + |s_1\rangle\beta_1. \tag{C.6}$$

Note that $|s_2\rangle$ still needs to be defined. The steepest descent approach is recovered by setting β_1 equal to zero. In the conjugate gradient approach, however, we will use this additional degree of freedom to require that $|g_3\rangle = \mathcal{G}|x_3\rangle$ is not only orthogonal to $|s_2\rangle$ (condition for line-minimization, compare equations C.2 to C.4) but also to $|s_1\rangle$. This excludes the possibility of a linear dependence to $|s_1\rangle$ as in the case of the steepest descent approach. Using the expansion of

equation C.5 we can now determine α_2 according to equation C.4. Secondly, we enforce the orthogonality of $|g_3\rangle$ to $|s_1\rangle$:

$$0 = \langle s_1|g_3\rangle = \langle s_1|\mathcal{G}|x_3\rangle \overset{C.5}{=} \underbrace{\langle s_1|g_2\rangle}_{\overset{C.3}{=}0} + \langle s_1|\mathcal{G}|s_2\rangle\alpha_2. \tag{C.7}$$

Since α_2 is finite, we must choose β_1 and thus $|s_2\rangle$ so that

$$0 = \langle s_1|\mathcal{G}|s_2\rangle \overset{C.6}{=} \langle s_1|\mathcal{G}|g_2\rangle + \langle s_1|\mathcal{G}|s_1\rangle\beta_1 \tag{C.8}$$

and therefore

$$\beta_1 = -\frac{\langle s_1|\mathcal{G}|g_2\rangle}{\langle s_1|\mathcal{G}|s_1\rangle} \overset{C.4}{=} \alpha_1 \frac{\langle s_1|\mathcal{G}|g_2\rangle}{\langle s_1|g_1\rangle} \overset{C.1}{=} \frac{\langle g_2|g_2\rangle - \langle g_1|g_2\rangle}{\langle s_1|g_1\rangle}. \tag{C.9}$$

In the second substitution we have expressed $\langle s_1|$ in the numerator in terms of $\langle x_2|$ and $\langle x_1|$ according to equation C.1. We can furthermore show that the second term of the numerator is zero:

$$\langle g_1|g_2\rangle = \langle g_1|\mathcal{G}|x_2\rangle \overset{C.1}{=} \langle g_1|g_1\rangle + \alpha_1\langle g_1|\mathcal{G}|s_1\rangle \overset{C.4}{=} 0. \tag{C.10}$$

In the last equality we have used that $|g_1\rangle = |s_1\rangle$. We will later show, that $\langle g_n|\mathcal{G}|s_n\rangle = \langle s_n|\mathcal{G}|s_n\rangle$ for arbitrary n. The mixing coefficient β_1 of equation C.6 is thus given as

$$\beta_1 = \frac{\langle g_2|g_2\rangle}{\langle s_1|g_1\rangle}.$$

C.2.3 Third iteration

In order to clarify the procedure, let us also analyze the third step for finding $|x_4\rangle$ using

$$|x_4\rangle = |x_3\rangle + |s_3\rangle\alpha_3 \qquad \text{and} \qquad |s_3\rangle = |g_3\rangle + |s_2\rangle\beta_2 + |s_1\rangle\beta_1. \tag{C.11}$$

α_3 is again found in the course of a line-minimization using equation C.4. β_1 and β_2 are then determined to ensure orthogonality of $|g_4\rangle$ with respect to $|s_1\rangle$ to $|s_2\rangle$ (orthogonality to $|s_3\rangle$ is enforced in the course of the line-minimization). Let us first calculate β_2 via

$$\langle s_2|g_4\rangle = \langle s_2|\mathcal{G}|x_4\rangle \overset{C.11}{=} \underbrace{\langle s_2|g_3\rangle}_{\overset{C.3}{=}0} + \langle s_2|\mathcal{G}|s_3\rangle\alpha_3. \tag{C.12}$$

The condition that $\langle s_2|\mathcal{G}|s_3\rangle = 0$ can be reformulated:

$$0 = \langle s_2|\mathcal{G}|s_3\rangle \overset{C.11}{=} \langle s_2|\mathcal{G}|g_3\rangle + \underbrace{\langle s_2|\mathcal{G}|s_1\rangle}_{\overset{C.8}{=}0}\beta_1 + \langle s_2|\mathcal{G}|s_2\rangle\beta_2.$$

Following equation C.9, β_2 can now be written as

$$\beta_2 = \frac{\langle g_3|g_3\rangle - \langle g_2|g_3\rangle}{\langle s_2|g_2\rangle}, \tag{C.13}$$

where the second term in the nominator again vanishes due to

$$\langle g_2|g_3\rangle = \langle g_2|\mathcal{G}|x_3\rangle \overset{C.5}{=} \langle g_2|g_2\rangle + \alpha_2\langle g_2|\mathcal{G}|s_2\rangle \overset{C.4}{=} 0, \tag{C.14}$$

since

$$\langle g_2|\mathcal{G}|s_2\rangle \overset{C.6}{=} \langle s_2|\mathcal{G}|s_2\rangle - \beta_1\langle s_1|\mathcal{G}|s_2\rangle \overset{C.8}{=} \langle s_2|\mathcal{G}|s_2\rangle. \tag{C.15}$$

To determine β_1 we demand orthogonality between $|g_4\rangle$ and $|s_1\rangle$:

$$0 = \langle s_1|g_4\rangle \overset{C.11}{=} \underbrace{\langle s_1|g_3\rangle}_{\overset{C.7}{=}0} + \langle s_1|\mathcal{G}|s_3\rangle\alpha_3.$$

Since $\alpha_3 \neq 0$, this equation translates into

$$0 = \langle s_1|\mathcal{G}|s_3\rangle \overset{C.11}{=} \langle s_1|\mathcal{G}|g_3\rangle + \underbrace{\langle s_1|\mathcal{G}|s_2\rangle\beta_2}_{\overset{C.8}{=}0} + \langle s_1|\mathcal{G}|s_1\rangle\beta_1,$$

and therefore

$$\beta_1 = -\frac{\langle s_1|\mathcal{G}|g_3\rangle}{\langle s_1|\mathcal{G}|s_2\rangle} \overset{C.1}{=} \frac{1}{\alpha_1\langle s_1|\mathcal{G}|s_2\rangle}\Big[\langle g_2|g_3\rangle - \langle g_1|g_3\rangle\Big] \overset{C.14}{=} 0. \tag{C.16}$$

Since each gradient can be expressed in terms of search directions (compare for example equation C.11), it can easily be verified, that any scalar product $\langle g_i|g_j\rangle$ is

zero for $i \neq j$ and not only for $i = j-1$ as can be generalized from equation C.14. The third search direction $|s_3\rangle$ is therefore given by

$$|s_3\rangle = |g_3\rangle + |s_2\rangle \frac{\langle g_3|g_3\rangle}{\langle g_2|g_2\rangle}.$$

Analysis of the equations leading to β_1 and β_2 reveals that, for the definition of $|s_n\rangle$, only $\beta_{n-1} \neq 0$ since the corresponding equation (C.13) also contains the scalar product $\langle g_{n-1}|g_{n-1}\rangle$ in the nominator. The expressions for all other β_i contain only scalar products of the form $\langle g_i|g_j\rangle$, $i \neq j$ which are zero as a matter of construction (see discussion after equation C.16).

C.2.4 Generalization and Summary

The scheme sketched above yields the following relations:

$$\langle s_i|\mathcal{G}|s_j\rangle \overset{C.8}{=} \delta_{ij} \cdot \text{const.} \tag{C.17}$$

$$\langle s_i|\mathcal{G}|g_j\rangle \overset{C.8+C.15}{=} (\delta_{ij} + \delta_{i,j+1}) \cdot \text{const.} \tag{C.18}$$

$$\langle s_i|g_j\rangle \overset{C.3,C.7,C.12}{=} \delta_{ij} \cdot \text{const.}, \qquad \text{for} \quad i < j \tag{C.19}$$

$$\langle g_i|g_j\rangle \overset{C.14}{=} \delta_{ij} \cdot \text{const.} \tag{C.20}$$

It is straightforward to see that the above equations, although derived only for $i \leq 4$, can be generalized for any index number since the rules needed for an index i trace back to rules already established for indices smaller than i and the condition of line-minimization for index i.

We can thus conclude that a conjugate gradient minimization determines its search directions via

$$|s_{n+1}\rangle \overset{C.16}{=} |g_{n+1}\rangle + |s_n\rangle\beta_n \tag{C.21}$$

with

$$\beta_n = \frac{\langle g_{n+1}|g_{n+1}\rangle}{\langle s_n|g_n\rangle} \overset{C.20+C.21}{=} \frac{\langle g_{n+1}|g_{n+1}\rangle}{\langle g_n|g_n\rangle}.$$

The fact that all β_i except β_n vanish (generalize equation C.16) is the key to the success of conjugate gradient approaches. The general expansion for $|s_{n+1}\rangle$ (compare for example equation C.11)

$$|s_{n+1}\rangle = |g_{n+1}\rangle + \sum_{i=1}^{n} |s_i\rangle\beta_i$$

thus reduces to equation C.21. It is thus only necessary to save the last search direction in order to conjugate the new gradient to *all* previous search directions. As a matter of construction, the search directions are linearly independent since each of them includes a gradient which is orthogonal to all previous search directions (compare equation C.21). Assuming an N-dimensional harmonic functional, the $(N+1)$st gradient must therefore be zero since it it is orthogonal to the N previous, linearly independent search directions.

C.3 Back to simulation

So far we have considered an abstract functional. We can now apply the conjugate gradient scheme in order to minimize the degrees of freedom in our models. In terms of the nuclei, the gradient is equal to the force and an implementation of the algorithm is straightforward.

Things get more involved when dealing with wave-functions. For the optimization of a single wave-function (state-by-state minimization) we need to minimize the Rayleigh quotient

$$\varepsilon(|\psi_n\rangle) = \frac{\langle\psi_n|H|\psi_n\rangle}{\langle\psi_n|O|\psi_n\rangle}$$

subject to the constraint that $|\psi_n\rangle$ is orthogonal to all lower wave-functions. The minimum condition disregarding the constraints yields

$$|\bar{g}_n\rangle = \left[H - \varepsilon(|\psi_n\rangle)O\right]|\psi_n\rangle.$$

$|\bar{g}_n\rangle$ is then orthogonalized to all lower bands and the current one:

$$|g_n\rangle = \left[1 - \sum_{l\leq n} |\psi_l\rangle\langle\psi_l|O\right]|\bar{g}_n\rangle$$

and can then be used as an input into the conjugate gradient scheme.

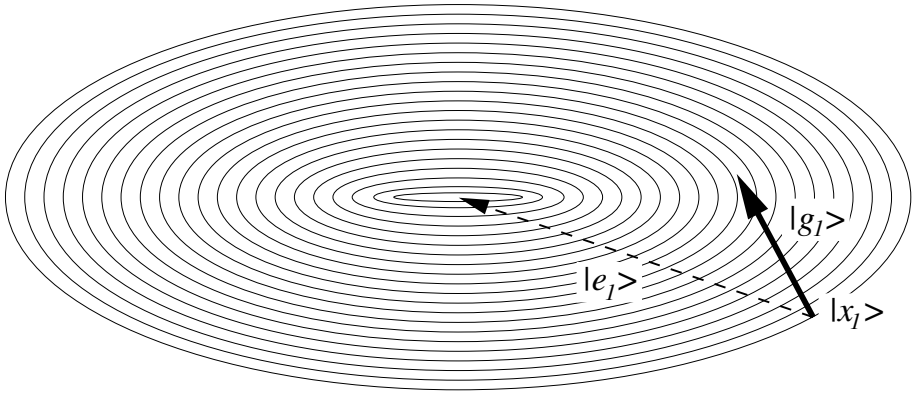

Figure C.2: Gradient vector and error vector in a general harmonic potential.

C.4 Preconditioning

We now have a scheme at hand which allows us to exactly minimize a N-dimensional harmonic functional in N steps. This large improvement compared to the steepest descent approach would still not be enough to render conjugate gradient to a useful scheme to minimize, for example, the electronic structure in an ab-initio calculation. Typically, such calculations use a basis set size between 10.000 and 100.000. This would thus translate into a corresponding number of minimization steps.

The reason why usually just in the region of 20 steps are needed is called "preconditioning". Figure C.2 again shows the familiar two-dimensional harmonic energy surface. For a general, that is non-spherical, potential, the gradient vector is not parallel to the error vector defined as the difference between the actual position and the minimum value. The gradient is dominated by the "hardest mode", in the example of figure C.2 the vertical one. On the basis of the knowledge of the direction of the error vector, it would be possible to minimize every functional with just one line minimization.

Imagine for a moment that we know the shape of the energy surface,

$$E(x, y) = ax^2 + by^2,$$

in our example. The error vector at any point is thus given as

$$|e\rangle = \begin{pmatrix} x \\ y \end{pmatrix},$$

whereas the gradient vector is given by

$$|g\rangle = \begin{pmatrix} 2ax \\ 2by \end{pmatrix}.$$

A precondition matrix of the form

$$K = \begin{pmatrix} \frac{1}{2a} & 0 \\ 0 & \frac{1}{2b} \end{pmatrix} \propto \begin{pmatrix} \frac{1}{a} & 0 \\ 0 & \frac{1}{b} \end{pmatrix} \tag{C.22}$$

would transform the gradient vector onto the error vector allowing for an exact minimization using only one line-minimization, independent of the dimensionality.

In practical calculations we do, of course, not know the exact form of the energy functional. Otherwise a numerical minimization would not be necessary. Nevertheless it is in many cases possible to gain some approximate information about the energy surface. Note that only the relative magnitude of the matrix elements is important as indicated in equation C.22.

Using a plane-wave derived basis set for the numerical representation of the wavefunctions one exploits the fact that the kinetic energy of a vast majority of basis functions is larger than their potential energy in a pseudized potential (compare our publication 5, section 6.5). The Hamilton matrix element for plane-waves is given as

$$\mathcal{H}_{G,G'} = \langle G| -\frac{1}{2}\nabla^2 + \hat{v}|G'\rangle = \frac{1}{2}V|G|^2\delta_{G,G'} + \langle G|\hat{v}|G'\rangle.$$

If the kinetic energy is dominating, the Hamilton matrix becomes diagonally dominant. One therefore uses a preconditioning matrix K which has the form of

$$K_{G,G'} \approx \frac{1}{|G|^2}\delta_{G,G'}$$

for large $|G|$. Teter et al. [55] have introduced a polynomial form for the diagonal elements which additionally approaches one for small wave-vectors where the matrix is not diagonally dominant anymore. A refinement has later been proposed by Kresse et al. [56].

For minimizing an energy functional with respect to nuclear coordinates, we can employ a lower level energy functional to gain some information about the energy surface. To get a reasonable preconditioning for a DFT structure optimization one could use a parametrized energy functional to obtain a harmonic approximation of the energy surface around each atom. The inverse of each force constant then defines a diagonal preconditioning matrix element.

Appendix D

Derivations and proofs for the atomic fragment formalism

This appendix contains derivations and proofs related to part III of this thesis.

D.1 Power series ansatz for nodeless wavefunctions and their energy derivatives

The full Schrödinger equation in a spherically symmetric potential including an inhomogeneity $|\varphi\rangle$

$$\left[-\frac{1}{2}\nabla^2 + v - \varepsilon\right]|\phi\rangle = |\varphi\rangle$$

can be split into an angular momentum dependent and a radial part. In this context we assume that the potential is spherically symmetric and that the inhomogeneity $|\phi\rangle$ has the same angular momentum quantum numbers ℓ, m as the solution $|\phi\rangle$. The solutions to the angular momentum dependent part are the spherical harmonics which are independent of the potential $v(|r|)$. The radial Schrödinger equation is given by

$$\left[-\frac{1}{2}\partial_r^2 + \frac{\ell(\ell+1)}{2r^2} + v(|r|) - \varepsilon\right]|r|\phi(|r|) = r\varphi(|r|). \tag{D.1}$$

To estimate the behavior of the solution near the origin we now expand the potential (assuming the most simple C/r shape, which is, however, a good ap-

proximation in the vicinity of the nucleus) and the solution in terms of a power series:

$$\begin{aligned} v(|r|) &= Cr^{-1} \\ \phi(r) &= \sum_{j=0}^{\infty} a_j r^j \qquad \text{and} \\ \varphi(r) &= \sum_{k=0}^{\infty} b_k r^k \end{aligned}$$

From now on we will simply write r instead of $|r|$ in order to enhance readability. For the solution $\phi(r)$ we only consider positive exponents since any negative exponents would lead to a divergence at the origin and thus to a non-normalizable wave-function. In our context we can apply the same restriction to the inhomogeneity.

Equation D.1 thus translates into

$$\begin{aligned} 0 &= \left[-\frac{1}{2}\partial_r^2 + \frac{\ell(\ell+1)}{2r^2} + Cr^{-1} - \varepsilon\right] \sum_j a_j r^{j+1} - \sum_k b_k r^{k+1} \\ &= \sum_j \left[-\frac{j(j+1)}{2} a_j r^{j-1} + \frac{\ell(\ell+1)}{2} a_j r^{j-1} + C a_j r^j - \varepsilon a_j r^{j+1}\right] - \sum_k b_k r^{k+1} \\ &= \sum_j -r^{j-1}\left[(j-\ell)(j+\ell+1)a_j - 2C a_{j-1} + 2\varepsilon a_{j-2}\right] - 2\sum_k b_k r^{k+1} \\ &= \sum_j -r^{j-1}\left[(j-\ell)(j+\ell+1)a_j - 2C a_{j-1} + 2\varepsilon a_{j-2} + 2b_{j-2}\right]. \end{aligned} \tag{D.2}$$

Since the set of $\{r^j\},\ j \geq 0$ constitutes a linearly independent polynomial basis, equation D.2 is only fulfilled if the expression in square brackets vanishes for every j. This condition determines the coefficients a_j:

$$(j-\ell)(j+\ell+1)a_j = 2C a_{j-1} + 2\varepsilon a_{j-2} + 2b_{j-2}. \tag{D.3}$$

The homogeneous differential equation: to calculate the atomic eigenfunctions we have to solve the homogeneous differential equation where the inhomogeneity $|\varphi\rangle$ and thus all b_j are zero. We have demanded above that $a_j = 0$ for all negative j. Since only coefficients a_i with $i < j$ enter into the definition of a_j,

the first non-zero a_j to solve equation D.3 can only occur in connection with the following term being zero:

$$(j - \ell)(j + \ell + 1) = 0,$$

which is the case for $j = \ell$ and $j = -\ell - 1$. The latter can be excluded since all a_j for negative j are zero by definition. Therefore, all atomic eigenfunctions exhibit an r^ℓ behavior at the origin.

The inhomogeneous differential equation: for the calculation of the $|u_i\rangle$ and $|\dot{u}_n\rangle$ we have to solve an inhomogeneous differential equation. Starting with $|u_2\rangle$ we have to use $|u_1\rangle \equiv |\phi_1\rangle$ with an r^ℓ behavior as inhomogeneity. The first non-zero coefficient b_ℓ is, however, shifted in index by -2 since b_{j-2} enters the definition of a_j (equation D.3). Therefore, the leading two components of $|u_2\rangle$, namely r^ℓ and $r^{\ell+1}$ are equal to the first two coefficients of $|\phi_2\rangle$, a_ℓ and $a_{\ell+1}$.

It can easily be verified that any linear combination of $|u_2\rangle$ and $|\phi_2\rangle$ is still a solution of the inhomogeneous Schrödinger equation defining $|u_2\rangle$. Via appropriate boundary conditions at the origin we can enforce a zero-mixing of $|\phi_2\rangle$ which cancels the first two expansion coefficients. The resulting $|u_2\rangle$ thus shows an $r^{\ell+2}$ behavior determined by the inhomogeneity. The same arguments can be used to arrive at the $r^{\ell+2(i-1)}$ behavior of a general $|u_i\rangle$.

Within the above choice of the $|u_n\rangle$, the Schrödinger equation for the energy derivative $|\dot{u}_n\rangle$ has an inhomogeneity with an $r^{\ell+2(i-1)}$ behavior. The $|\dot{u}_n\rangle$ therefore start with $r^{\ell+2i}$, if we again require a zero-mixing of the atomic eigenfunction.

D.2 Parametrization of nodeless wave-functions

Figure 8.2 on page 142 suggests a straightforward parametrization of the nodeless wave-functions by Slater type orbitals of the form

$$u(|r|) \propto |r|^\alpha e^{-\beta|r|}, \tag{D.4}$$

where α should be close to the analytical behavior at the origin listed in table 8.1 on page 141 while $-\beta$ should lie in a region around the atomic eigenvalue.

Figure D.1 shows various fits to the third nodeless wave-function for the silicon s channel using functional forms related to equation D.4. It can clearly be observed that the simple approach of equation D.4 does not give a satisfactory fit, especially at large r. The parameters α and β are 2.46 and 2.03. The introduction

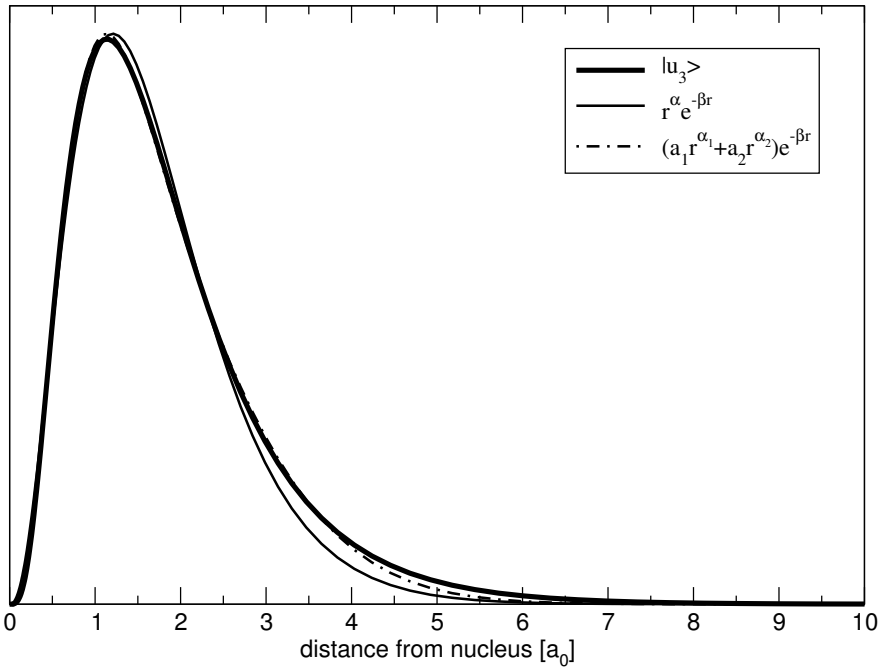

Figure D.1: Various fits to the third (=valence) nodeless wave-function $|u_3\rangle$ of the silicon s-channel.

of a second polynomial or exponential term improves the result (last curve in figure D.1). Only the fit with two polynomial and two exponential parameters (not shown in the figure) is indistinguishable from the correct $|u_3\rangle$ on the scale of figure D.1.

D.3 Algebra for energy-dependent nodeless wave-functions

In section 8.2.4 the concept of energy-dependent nodeless wave-functions $|q_n(\varepsilon)\rangle$ has been introduced to expand atomic wave-functions at arbitrary energies. An energy-dependent nodeless wave-function is defined by the inhomogeneous differential equation

$$(\mathcal{H} - \varepsilon)|q_i(\varepsilon)\rangle = |u_{i-1}\rangle \tag{D.5}$$

and can alternatively be written as

$$|q_{n+1}(\varepsilon)\rangle = \Big[|q_n(\varepsilon)\rangle - |q_n(\varepsilon_n)\rangle\Big] \frac{1}{\varepsilon - \varepsilon_n}. \tag{D.6}$$

Substitution into equation D.5 shows that the above expression is indeed a solution. We now insert the Taylor expansion of $|q_n(\varepsilon)\rangle$ around $\varepsilon = \varepsilon_n$

$$\begin{aligned} |q_n(\varepsilon)\rangle &= \sum_{j=0}^{\infty} \frac{1}{j!}(\varepsilon - \varepsilon_n)^j |q_n^{(j)}(\varepsilon_n)\rangle \\ &= \sum_{j=0}^{\infty} \frac{1}{j!}(\varepsilon - \varepsilon_n)^j |u_n^{(j)}\rangle \end{aligned}$$

into equation D.6:

$$\begin{aligned} |q_{n+1}(\varepsilon)\rangle &= \left[\left(\sum_{j=0}^{\infty} \frac{1}{j!}(\varepsilon - \varepsilon_n)^j |u_n^{(j)}\rangle\right) - |u_n\rangle\right] \frac{1}{\varepsilon - \varepsilon_n} \\ &= \sum_{j=1}^{\infty} \frac{1}{j!}(\varepsilon - \varepsilon_n)^{j-1} |u_n^{(j)}\rangle. \end{aligned}$$

Note that $|\alpha^j\rangle$ denotes to the j^{th} power of a ket $|\alpha\rangle$, whereas $|\alpha^{(j)}\rangle$ refers to the j^{th} energy derivative. The above expression can be generalized to an arbitrary derivative of $|q_{n+1}(\varepsilon)\rangle$:

$$\begin{aligned} q_{n+1}^{(k)}(\varepsilon)\rangle &= \sum_{j=k+1}^{\infty} \frac{1}{j!} \frac{(j-1)!}{(j-k-1)!}(\varepsilon - \varepsilon_n)^{j-k-1} |u_n^{(j)}\rangle \\ &= \sum_{j=k+1}^{\infty} \frac{1}{j \cdot (j-k-1)!}(\varepsilon - \varepsilon_n)^{j-k-1} |u_n^{(j)}\rangle. \end{aligned} \tag{D.7}$$

At $\varepsilon = \varepsilon_n$ equation D.7 is reduced to the simple form

$$|u_{n+1}^{(k)}\rangle = \frac{1}{k+1} |u_n^{k+1}\rangle,$$

which is the expression postulated in equation 8.14.

Appendix E

Calculating Atomic Fragments

This appendix contains several derivations that are needed in the context of the plane-wave codes developed to calculate atomic fragment orbitals.

E.1 Prerequisites

Definition of a Fourier transform: As already discussed in appendix A.2, this definition is not the only possible one. V denotes the volume of periodicity.

– for periodic systems we choose:

$$\begin{aligned}
\langle r|G\rangle &= e^{iGr} \\
1 &= \sum_G |G\rangle \frac{1}{\langle G|G\rangle}\langle G| = \frac{1}{V}\sum_G |G\rangle\langle G| \\
\phi(r) = \langle r|\phi\rangle &= \frac{1}{V}\sum_G \langle r|G\rangle\langle G|\phi\rangle = \frac{1}{V}\sum_G e^{iGr}\int_V d^3r e^{-iGr}\phi(r) \\
&= \sum_G e^{iGr}\underbrace{\left[\frac{1}{V}\int_V d^3r e^{-iGr}\phi(r)\right]}_{\phi(G)}
\end{aligned}$$

– for non-periodic systems we have to deal with continuous G vectors and the $1/V$ term transforms into a $dG/(2\pi)^3$ term:

$$\begin{aligned}
\phi(r) &= \int_\infty d^3G\phi(G)e^{iGr} \\
\phi(G) &= \frac{1}{(2\pi)^3}\int_\infty d^3r\phi(r)e^{-iGr}
\end{aligned}$$

Expanding a plane-wave into spherical harmonics and Bessel functions

$$\begin{aligned} e^{iGr} &= 4\pi \sum_{\ell,m} i^{\ell} j_{\ell}(|G||r|) Y^{*}_{\ell m}(\hat{G}) Y_{\ell m}(\hat{r}) \\ e^{-iGr} &= 4\pi \sum_{\ell,m} \left(i^{\ell}\right)^{*} j_{\ell}(|G||r|) Y_{\ell m}(\hat{G}) Y^{*}_{\ell m}(\hat{r}) \end{aligned}$$

Formulas related to spherical harmonics

$$\begin{aligned} P_{\ell}(\cos\gamma) &= \frac{4\pi}{2\ell+1} \sum_{m=-\ell}^{\ell} Y^{*}_{\ell m}(\hat{G}) Y_{\ell m}(\hat{G'}) \\ \cos\gamma &= \frac{G \cdot G'}{|G||G'|} \\ Y_{\ell m}(G) &= (-1)^{m} \sqrt{\frac{2\ell+1}{4\pi} \frac{(\ell-m)!}{(\ell+m)!}} sin^{m}\theta_{G} \times \\ & \quad \frac{d^{m}}{d(\cos\theta_{G})^{m}} P_{\ell}(\cos\theta_{G}) e^{im\phi_{G}} \end{aligned}$$

E.2 From radial grids to a plane-wave representation

This section shows how a function that is given in terms of a radial part times spherical harmonics

$$f(r) = \sum_{\ell m} f_{\ell m}(|r|) Y_{\ell m}(\hat{r})$$

can be transformed into G space

$$f(r) = \int d^{3}G f(G) e^{iGr}.$$

Note that at this point we are using a continuous set of G vectors, since we do not require periodic boundary conditions.

Using the prerequisites introduced so far we write

$$
\begin{aligned}
f(G) &= \frac{1}{(2\pi)^3}\int_\infty d^3r f(r) e^{-iGr} \\
&= \frac{4\pi}{(2\pi)^3}\int_\infty d^3r \left[\sum_{\ell m} f_{\ell m}(|r|)Y_{\ell m}(\hat{r})\right]\left[\sum_{\ell' m'}(-i)^{\ell'} j_{\ell'}(|G||r|)Y_{\ell' m'}(\hat{G})Y^*_{\ell' m'}(\hat{r})\right] \\
&= \frac{4\pi}{(2\pi)^3}\sum_{\ell' m'}(-i)^{\ell'}\left[\int_\infty d^3r \sum_{\ell m} f_{\ell m}(|r|)j_{\ell'}(|G||r|)Y_{\ell m}(\hat{r})Y^*_{\ell' m'}(\hat{r})\right] Y_{\ell' m'}(\hat{G}) \\
&= \frac{4\pi}{(2\pi)^3}\sum_{\ell' m'}(-i)^{\ell'}\left[\sum_{\ell m}\underbrace{\int_\infty d\Omega Y_{\ell m}(\hat{r})Y^*_{\ell' m'}(\hat{r})}_{\delta_{\ell\ell'}\delta_{mm'}}\right. \\
&\qquad\qquad \left.\int_0^\infty d|r|r^2 f_{\ell m}(|r|)j_{\ell'}(|G||r|)\right] Y_{\ell' m'}(\hat{G}) \\
&= \frac{4\pi}{(2\pi)^3}\sum_{\ell' m'}(-i)^{\ell'}\left[\int_0^\infty d|r|r^2 f_{\ell' m'}(|r|)j_{\ell'}(|G||r|)\right] Y_{\ell' m'}(\hat{G}).
\end{aligned}
$$

The expression for a periodic function and thus discrete G vectors is obtained by multiplying with

$$\frac{(2\pi)^3}{V}.$$

The final expression for a case with periodic boundary conditions is thus

$$f(G) = \frac{4\pi}{V}\sum_{\ell' m'}(-i)^{\ell'}\left[\int_0^\infty d|r|r^2 f_{\ell' m'}(|r|)j_{\ell'}(|G||r|)\right] Y_{\ell' m'}(\hat{G}).$$

In the applications of part III, all functions which need to be transformed can be expressed in terms of a single radial times spherical harmonics expression. In this case the sum over ℓ' and m' is thus removed. The expression in square brackets is called spherical Bessel transform of order ℓ and is calculated on radial grids [110].

E.3 The local potential in reciprocal space

In this section I derive the expression for a matrix element of a local potential in G space.

$$\begin{aligned}
\langle G|v_{loc}|G'\rangle &= \iint_V d^3r\, d^3r' \langle G|r\rangle\langle r|v_{loc}|r'\rangle\langle r'|G'\rangle \\
&= \int_V d^3r\, \langle G|r\rangle\langle r|v_{loc}|r\rangle\langle r|G'\rangle \\
&= \int_V d^3r\, v_{loc}(r) e^{i(G'-G)r} \\
&= \int_V d^3r\, v_{loc}(r) e^{-i(G-G')r} \\
&= V v_{loc}(G-G'),
\end{aligned}$$

where V is the unit-cell volume and $v_{\mathrm{loc}}(G)$ is the Fourier transform of $v_{\mathrm{loc}}(r)$ (compare appendix E.2).

E.4 The nonlocal potential in reciprocal space

This section derives the expression for a matrix element of the non-local potential in reciprocal space.

$$
\begin{aligned}
\langle G|\hat{v}_l|G'\rangle &= \iint_V d^3r d^3r' \langle G|r\rangle\langle r|\hat{v}_l|r'\rangle\langle r'|G'\rangle \\
&= \iint_V d^3r d^3r' (4\pi)^2 \sum_{l'l''m'm''} \\
&\quad \left(i^{l'}\right)^* j_{l'}(|G||r|) Y_{l'm'}(\hat{G}) Y^*_{l'm'}(\hat{r}) \\
&\quad \sum_m Y_{\ell m}(\hat{r}) v_l(|r|) \frac{\delta(|r|-|r'|)}{r^2} Y^*_{\ell m}(\hat{r'}) \\
&\quad i^{l''} j_{l''}(|G'||r'|) Y^*_{l''m''}(\hat{G'}) Y_{l''m''}(\hat{r'}) \\
&= (4\pi)^2 \sum_{l'l''m'm''} \left(i^{l'}\right)^* i^{l''} \left[\iint d|r|d|r'|r^2 r'^2 \right. \\
&\quad j_{l'}(|G||r|) v_l(|r|) \frac{\delta(|r|-|r'|)}{r^2} j_{l''}(|G'||r'|) \\
&\quad \sum_m \Bigg[\underbrace{\int d\Omega_r Y^*_{l'm'}(\hat{r}) Y_{\ell m}(\hat{r})}_{\delta_{ll'}\delta mm'} \underbrace{\int d\Omega_{r'} Y^*_{\ell m}(\hat{r'}) Y_{l''m''}(\hat{r'})}_{\delta_{ll''}\delta_{mm''}} \\
&\quad \left. Y_{l'm'}(\hat{G}) Y^*_{l''m''}(\hat{G'}) \Bigg] \right] \\
&= \underbrace{\left(i^l\right)^* i^l}_{1} (4\pi)^2 \int d|r| r^2 j_l(|G||r|) v_l(|r|) j_l(|G'||r|) \\
&\quad \underbrace{\sum_m Y_{lm}(\hat{G}) Y^*_{lm}(\hat{G'})}_{\frac{2l+1}{4\pi} P_l(cos\gamma)} \\
&= 4\pi(2l+1) P_l(cos\gamma) \int d|r| r^2 j_l(|G||r|) v_l(|r|) j_l(|G'||r|). \quad \text{(E.1)}
\end{aligned}
$$

$v_l(|r|)$ is the radial part of the potential.

Appendix F

The Harris-Foulkes Functional

The Kohn-Sham equations can only be solved iteratively, since the potential in the Hamiltonian depends on the electron density, which is itself built up from the solutions of the Kohn-Sham equations. The standard procedure to iteratively solve for the electronic ground state is the so-called self-consistency cycle visualized in figure F.1.

Starting from an input density, usually a superposition of atomic densities, the Hamiltonian is set up and the Kohn-Sham equations are solved. A new density is obtained from the occupied Kohn-Sham orbitals. This new density only equals the input density, when convergence is achieved. Otherwise, input and output densities are mixed and the cycle is started again.

J. Harris [111] and M. Foulkes [112] independently developed an energy expression closely related to the Hohenberg-Kohn-Sham formalism, which is designed to yield good approximations to the total energy but on the basis of a reasonable input density and just one self-consistency iteration.

F.1 DFT revisited

According to the Hohenberg-Kohn-Sham theorems, the many-body energy corresponding to a ground state electron density $\rho_0(r)$ is given by

$$\begin{aligned} E^{\mathrm{HKS}}[\rho_0] &= F[\rho_0] + \int v_{\mathrm{ext}}(r)\rho_0(r)dr \\ &= T_s[\rho_0] + \underbrace{E_H[\rho_0] + E_{xc}[\rho_0] + \int v_{\mathrm{ext}}(r)\rho_0(r)dr}_{E_{\mathrm{pot}}}, \end{aligned}$$

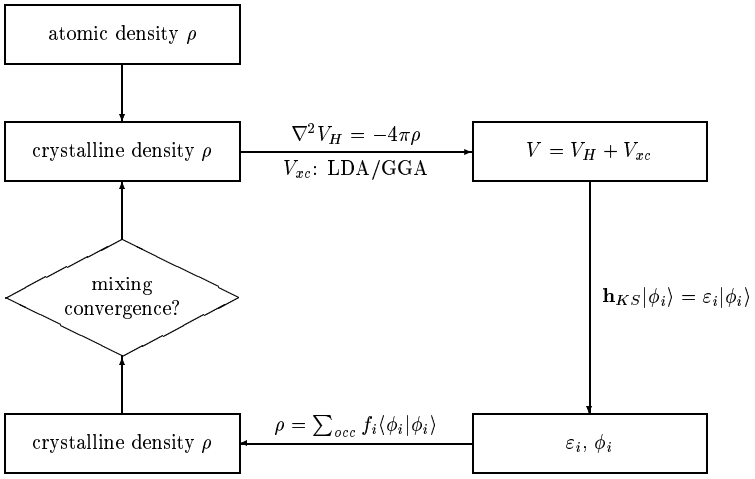

Figure F.1: A typical self-consistency cycle used in many electronic structure codes to determine the electronic ground state.

where the Hartree energy E_H is given by

$$E_H[\rho_0] = \frac{1}{2}\iint \frac{\rho_0(r)\rho_0(r')}{|r-r'|}drdr'$$

and the exchange and correlation energy E_{xc} is approximated by a local or semi-local form as discussed in section 2.2. All terms except the kinetic energy of the noninteracting system, $T_s[\rho_0]$, are denoted as $E_{\rm pot}$, ignoring that E_{xc} also includes kinetic contributions due to correlation.

The kinetic energy $T_s[\rho_0]$ is calculated from the solutions to the Kohn-Sham equations:

$$\begin{aligned}\left[-\frac{1}{2}\nabla^2 + v_{\rm eff}(r)\right]\phi_i(r) &= \varepsilon_i\phi_i(r) \qquad \text{and} \\ T_s[v_{\rm eff}] &= \sum_i f_i \int \phi_i^*(r)\left(-\frac{1}{2}\nabla^2\right)\phi_i(r)dr,\end{aligned}$$

where f_i is the occupation number of state i. In the above equation, T_s is a functional of the effective potential $v_{\rm eff}$ and not of the density. The requirement that the Hohenberg-Kohn-Sham functional becomes stationary at the ground state density relates the density and the effective potential via the so-called self-consistency condition:

$$
\begin{aligned}
v_{\text{eff}}[\rho'(r)] &= \left.\frac{\delta E_{\text{pot}}}{\delta \rho}\right|_{\rho=\rho'} + \text{const.} \\
&= \underbrace{\int \frac{\rho(r')}{|r-r'|} dr'}_{\frac{\delta E_H}{\delta \rho}} + v_{\text{ext}}(r) + \underbrace{\mu_{\text{xc}}[\rho^{\text{in}}(r)]}_{\frac{\delta E_{\text{xc}}}{\delta \rho}} + \text{const.}, \qquad \text{(F.1)}
\end{aligned}
$$

where the constant can be set to zero for a closed system. A more elaborate discussion of density functional theory and its development is found in section 2.2.

In a self-consistency cycle we usually start out with an input density ρ_{in} and construct the effective input potential

$$
v_{\text{eff}}^{\text{in}} = v_{\text{eff}}[\rho^{\text{in}}(r)] = \int \frac{\rho^{\text{in}}(r')}{|r-r'|} dr' + v_{\text{ext}}(r) + \mu_{\text{xc}}[\rho^{\text{in}}(r)],
$$

which is then used to determine the single-particle eigenvalues and -functions $\{\varepsilon_i\}$ and $\{\phi_i\}$. In this context, the density calculated from the eigenfunctions $\{\phi_i\}$ (compare equation 2.6), is denoted as $\rho^{\text{out}}(r)$ and is in general not equal to $\rho^{\text{in}}(r)$. Only for the ground-state density, input and output densities are identical and selfconsistency is achieved.

After one self-consistency cycle, the total energy $E[\rho^{\text{out}}(r)]$, can be evaluated in several ways which all give identical results:

$$
\begin{aligned}
E^{\text{HKS}}[\rho^{\text{out}}(r)] &= \sum_{i=1}^{N} f_i \int \phi_i^*(r) \left(-\frac{1}{2}\nabla^2\right) \phi_i(r) dr + E_{\text{pot}}[\rho^{\text{out}}(r)] \qquad \text{(F.2)} \\
&= \sum_{i=1}^{N} f_i\, \varepsilon_i - \int \underbrace{v_{\text{eff}}[\rho^{\text{in}}(r)]}_{\left.\frac{\delta E_{\text{pot}}}{\delta \rho}\right|_{\rho=\rho^{\text{in}}}} \rho^{\text{out}}(r) dr + E_{\text{pot}}[\rho^{\text{out}}(r)] \qquad \text{(F.3)} \\
&= \sum_{i=1}^{N} f_i\, \varepsilon_i - \left[\iint \frac{\rho^{\text{in}}(r)\rho^{\text{out}}(r')}{|r-r'|} dr dr' + \int \mu_{\text{xc}}[\rho^{\text{in}}(r)]\rho^{\text{out}}(r) dr\right] \\
&\quad + \frac{1}{2}\iint \frac{\rho^{\text{out}}(r)\rho^{\text{out}}(r')}{|r-r'|} dr dr' + E_{\text{xc}}[\rho^{\text{out}}(r)] \\
&\quad + \int v_{\text{ext}}(r)\rho^{\text{out}}(r) dr. \qquad \text{(F.4)}
\end{aligned}
$$

In equation F.2 the kinetic energy is evaluated directly, whereas in the approach of equation F.3 and F.4 one uses the sum of the Kohn-Sham eigenvalues and

subtracts out the interaction of the output density with the effective potential generated from the input density. This approach is especially useful for some augmented wave basis sets as the direct evaluation of the kinetic energy can be cumbersome.

Equations F.2 to F.4 are strictly variational which means that all non-converged energies $E[\rho^{\text{out}}(r)]$ are above the converged result $E[\rho_0(r)]$. The total energy at the ground-state density is then, in the notation of equation F.4, given as

$$\begin{aligned} E^{\text{HKS}}[\rho_0(r)] &= \sum_{i=1}^{N} f_i\,\varepsilon_i - \frac{1}{2}\iint \frac{\rho_0(r)\rho_0(r')}{|r-r'|}drdr' - \int \mu_{\text{xc}}[\rho_0(r)]\rho_0(r)dr \\ &\quad + E_{\text{xc}}[\rho_0(r)]. \end{aligned}$$

F.2 Non-selfconsistent DFT calculations

Three groups of authors independently approached the topic of non-selfconsistent density functional calculations. The first have been Wendel and Martin [113] in the context of a calculation on silicon. Harris [111] wanted to calculate the interaction energy of weakly interacting systems. He assumed that the density of the two systems in contact is very close to the sum of the density of the two isolated systems. Foulkes and Haydock [112] connected density functional theory and non-selfconsistent tight-binding calculations. Independently they all arrived at the same expression which will be derived following Foulkes and Haydock [112].

All three groups of authors considered the energy expressions F.2 to F.4 as too cumbersome to evaluate for a single-cycle calculation since $\rho^{\text{out}}(r)$ has to be evaluated. Foulkes and Haydock started from an expression corresponding to equation F.3 and expanded $E_{\text{pot}}[\rho^{\text{out}}(r)]$ in terms of $E_{\text{pot}}[\rho^{\text{in}}(r)]$:

$$\begin{aligned} E_{\text{pot}}[\rho^{\text{out}}(r)] &= E_{\text{pot}}[\rho^{\text{in}}(r)] + \int \left.\frac{\delta E_{\text{pot}}}{\delta\rho}\right|_{\rho^{\text{in}}} \Delta\rho(r)\; dr \\ &\quad + \frac{1}{2}\iint \left.\frac{\delta^2 E_{\text{pot}}}{\delta\rho^2}\right|_{\rho^{\text{in}}} \Delta\rho(r)\;\Delta\rho(r')drdr' + O[(\Delta\rho)^3], \quad \text{(F.5)} \end{aligned}$$

where $\Delta\rho(r) = \rho^{\text{out}}(r) - \rho^{\text{in}}(r)$. Substituting the expansion of $E_{\text{pot}}[\rho^{\text{out}}(r)]$ into equation F.3, using $v_{\text{eff}}[\rho^{\text{in}}(r)] = \left.\frac{\delta E_{\text{pot}}}{\delta\rho}\right|_{\rho^{\text{in}}}$ and truncating the expansion after the linear term leads to

$$\begin{aligned} E^{\mathrm{HKS}}[\rho^{\mathrm{out}}(r)] &\approx \sum_{i=1}^{N} f_i\,\varepsilon_i - \int v_{\mathrm{eff}}[\rho^{\mathrm{in}}(r)]\rho^{\mathrm{in}}(r)dr + E_{\mathrm{pot}}[\rho^{\mathrm{in}}(r)] \\ &\stackrel{!}{\equiv} E^{\mathrm{HF}}[\rho^{\mathrm{in}}(r)], \end{aligned} \tag{F.6}$$

the so-called Harris-Foulkes functional. It differs from the corresponding Hohenberg-Kohn-Sham expression only in terms quadratic in $\Delta\rho(r)$. At the ground state density the Harris-Foulkes functional is also stationary and identical to the Hohenberg-Kohn-Sham functional, since $\Delta\rho^{\mathrm{out}}(r) = \Delta\rho^{\mathrm{in}}(r)$.

One can also expand $E^{\mathrm{HKS}}[\rho^{\mathrm{out}}(r)]$ and $E^{\mathrm{HF}}[\rho^{\mathrm{in}}(r)]$ in terms of the ground state energy $E^{\mathrm{HKS}}[\rho_0(r)] = E^{\mathrm{HF}}[\rho_0(r)]$:

$$\begin{aligned} E^{\mathrm{HKS}}[\rho^{\mathrm{out}}(r)] &= E^{\mathrm{HKS}}[\rho_0(r)] + \frac{1}{2}\iint \left.\frac{\delta^2 E^{\mathrm{HKS}}}{\delta\rho^2}\right|_{\rho_0} \Delta\rho^{\mathrm{out}}(r)\;\Delta\rho^{\mathrm{out}}(r')drdr' + \ldots \\ E^{\mathrm{HF}}[\rho^{\mathrm{in}}(r)] &= E^{\mathrm{HKS}}[\rho_0(r)] + \frac{1}{2}\iint \left.\frac{\delta^2 E^{\mathrm{HKS}}}{\delta\rho^2}\right|_{\rho_0} \Delta\rho^{\mathrm{in}}(r)\;\Delta\rho^{\mathrm{out}}(r')drdr' + \ldots, \end{aligned}$$

where $\Delta\rho^{\mathrm{in/out}}(r) = \rho^{\mathrm{in/out}}(r) - \rho_0(r)$. The second functional derivative of the Hohenberg-Kohn-Sham functional at the ground-state density is positive due to the variational principle. Since $\Delta\rho^{\mathrm{out}}\Delta\rho^{\mathrm{out}}$ is also non-negative, $E^{\mathrm{HKS}}[\rho^{\mathrm{out}}(r)]$ is above the ground state energy and thus the expression is variational. $E^{\mathrm{HF}}[\rho^{\mathrm{in}}(r)]$ also depends on $\Delta\rho^{\mathrm{in}}$ and the product $\Delta\rho^{\mathrm{in}}\Delta\rho^{\mathrm{out}}$ is not necessarily non-negative. In fact it turns out to be negative in most cases duo to the so-called "overshooting" [112, 97]: the output density usually "overcompensates" the errors of the input density. As a result, $\Delta\rho^{\mathrm{in}}\Delta\rho^{\mathrm{out}}$ is negative in many regions of space and the Harris functional acts like a lower bound to the self-consistent energy whereas the $E^{\mathrm{HKS}}[\rho^{\mathrm{out}}(r)]$ is an upper bound. The Harris-Foulkes functional is thus only stationary and not variational at the ground-state density.

Since this method is only used for single-cycle calculations, the non-variational character does not matter at all. The stationary character, however, ensures that the eigenvalues obtained are better than the density from which they were obtained. It is a-priori unclear whether one of the two functional expressions is in general superior over the other. By construction they both have very similar error expressions. Empirically one has, however, observed, that usually the Harris-Foulkes functional is a better approximation to the self-consistent energy [97].

Indices

List of Figures

Bibliography

[1] J. Lettieri, J. H. Haeni, and D. G. Schlom: Critical issues in the heteroepitaxial growth of alkaline-earth oxides on silicon. *J. Vac. Sci. Techn. A* **20**(4), 1332 (2002).

[2] S. A. Chambers: Epitaxial growth and properties of thin oxides. *Surf. Sci. Rep.* **39**, 105 (2000).

[3] R. A. McKee, F. J. Walker, and M. F. Chisholm: Crystalline oxides on silicon: the first five monolayers. *Phys. Rev. Lett* **81**, 3014–3017 (1998).

[4] A. Ohtomo, D. A. Muller, J. L. Grazul, and H. Y. Hwang: Artificial charge-modulation in atomic scale perovskite titanate superlattices. *Nature* **419**, 378 (2002).

[5] K. Ojima, M. Yoshimura, and K. Ueda: Observation of the Si(100)"1×2"-Ba surface by scanning tunneling microscopy. *Phys. Rev. B* **65**, 75408 (2002).

[6] C. Klein, A. Eichler, E. L. D. Hebenstreit, G. Pauer, R. Koller, A. Winkler, M. Schmid, and P. Varga: When Scanning Tunneling Microscopy Gets the Wrong Adsorption Site: H on Rh(100). *Phys. Rev. Lett.* **90**, 176101 (2003).

[7] R. Biwas and D. Hamann: Interatomic potentials for silicon structural energies. *Phys. Rev. Lett* **55**, 2001 (1985).

[8] K. Reuter, C. Stampfl, and M. Scheffler: Ab initio atomistic thermodynamics and statistical mechanics of surface properties and functions. *arxiv:cond-mat/0404510* (2004).

[9] A. Szabo and N. S. Ostlund: *Modern Quantum Chemistry* Dover Publications, Inc. (1996).

[10] F. Jensen: *Introduction to Computational Chemistry* John Wiley & Sons (1999).

[11] P. Hohenberg and W. Kohn: Inhomogeneous Electron Gas. *Phys. Rev.* **136**, B864 (1964).

[12] M. Levy: Universal variational functionals of electron densities, first order density matrices, and natural spin-orbitals and solution of the v-representability problem. *Proc. Nat. Acad. Sci* **76**, 6062 (1979).

[13] L. H. Thomas: The calculation of atomic fields. *Proc. Cambridge Philos. Soc.* **23**, 542 (1927).

[14] E. Fermi: A statistical method for the determination of some atomic properties and the application of this method to the theory of the periodic system of elements. *Z. Phys.* **48**, 73 (1928).

[15] P. A. M. Dirac: Note on exchange phenomena in the Thomas atom. *Proc. Cambridge Phil. Soc.* **26**, 376 (1930).

[16] W. Kohn and L. J. Sham: Self-Consistent Equations Including Exchange and Correlation Effects. *Phys. Rev.* **140**, A1133 (1965).

[17] R. O. Jones and O. Gunnarsson: The density functional formalism, its applications and prospects. *Rev. Mod. Phys.* **61**, 689 (1989).

[18] R. M. Dreizler and E. K. U. Gross: *Density Functional Theory* Springer, Berlin (1990).

[19] W. Yang R G. Parr: *Density-Functional Theory of Atoms and Molecules* Oxford University Press (1994).

[20] W. Kohn: Nobel Lecture: Electronic structure of matter–wave functions and density functionals. *Rev. Mod. Phys.* **71**, 1253 (1999).

[21] A. D. Becke: Density-functional thermochemistry. I. The effect of exchange-only gradient correction. *J. Chem. Phys.* **96**, 2155 (1992).

[22] A. D. Becke: Density-functional thermochemistry. II. The effect of the Perdew-Wang generalized-gradient correlation correction. *J. Chem. Phys.* **97**, 9173 (1992).

[23] M. C. Payne, M. P. Teter, D. C. Allan, T. A. Arias, and J. D. Joannopoulos: Iterative minimization techniques for ab initio total-energy calculations: molecular dynamics and conjugate gradients. *Rev. Mod. Phys.* **64**, 1045 (1992).

[24] P. E. Blöchl: Projector augmented-wave method. *Phys. Rev. B* **50**, 17953 (1994).

[25] CP-PAW code, `http://www.pt.tu-clausthal.de/~paw/`.

[26] Wien2k code, `http://www.wien2k.at`.

[27] VASP code, `http://cms.mpi.univie.ac.at/vasp/`.

[28] ABINIT code, `http://www.abinit.org/`.

[29] SFHIngX code, `http://www.sfhingx.de/`.

[30] CASTEP code,
`http://www.accelrys.com/mstudio/ms_modeling/castep.html`.

[31] SIESTA code,
`http://www.uam.es/departamentos/ciencias/fismateriac/siesta/`.

[32] B. G. Pfrommer and S. G. Louie: Density-functional study of the magnetic and metal-insulator transition of bcc hydrogen. *Phys. Rev. B* **58**, 12680 (1999).

[33] M. Imada, A. Fujimori, and Y. Tokura: Metal-insulator transitions. *Rev. Mod. Phys.* **70**, 1039 (1998).

[34] J. P. Perdew and A. Zunger: Self-interaction correction to density-functional approximations for many-electron systems. *Phys. Rev. B* **23**, 5048 (1981).

[35] J. P. Perdew: Size-Consistency, Self-Interaction Correction, and Derivative Discontinuity in Density Functional Theory. *Adv. Quantum Chem.* **21**, 113 (1990).

[36] V. I. Anisimov, J. Zaanen, and O. K. Andersen: Band theory and Mott insulators: Hubbard U instead of Stoner I. *Phys. Rev. B* **44**, 943 (1991).

[37] W. Metzner and D. Vollhardt: Correlated Lattice Fermions in $d = \infty$ Dimensions. *Phys. Rev. Lett.* **62**, 324 (1989).

[38] A. Georges, G. Kotliar, W. Krauth, and M. J. Rozenberg: Dynamical mean-field theory of strongly correlated fermion systems and the limit of infinite dimensions. *Rev. Mod. Phys.* **68**, 13 (1996).

[39] F. Aryasetiawan and O. Gunnarsson: The GW method. *Rep. Prog. Phys.* **61**, 237 (1998).

[40] J. F. Janak: Proof that $\partial E/\partial n_i = \varepsilon$ in density functional theory. *Phys. Rev. B* **18**, 7165 (1978).

[41] C. O. Almbladh and U. von Barth: Exact results for the charge and spin densities, exchange-correlation potentials, and density-functional eigenvalues. *Phys. Rev. B* **31**, 3231 (1985).

[42] Walter Kohn, International Conference on Applied Density Functional Theory, January 14–17 2001 Vienna/Austria.

[43] L. Hedin: New Method for Calculating the One-Particle Green's Function with Application to the Electron-Gas Problem. *Phys. Rev.* **139**, A796 (1965).

[44] T. Klüner, N. Govind, Y. A. Wang, and E. A. Carter: Prediction of Electronic Excited States of Adsorbates on Metal Surfaces from First Principles. *Phys. Rev. Lett.* **86**, 5954 (2001).

[45] J. P. Perdew and M. Levy: Physical content of the exact Kohn-Sham orbital energies: band gaps and derivative discontinuities. *Phys. Rev. Lett.* **51**, 1884 (1983).

[46] L. J. Sham and M. Schlüter: Density-Functional Theory of the Energy Gap. *Phys. Rev. Lett.* **51**, 1888 (1983).

[47] E. Runge and E. K. U. Gross: Density-Functional Theory for Time-Dependent Systems. *Phys. Rev. Lett.* **52**, 997 (1984).

[48] H. Hellmann: in Einführung in die Quantenchemie. Deuticke, Leipzig (1937).

[49] R. P. Feynman: Forces in Molecules. *Phys. Rev.* **56**, 340 (1939).

[50] M. P. Allen and D. J. Tildesley: *Computer simulation of liquids* Oxford University Press (1989).

[51] D. Frenkel and B. Smit: *Understanding Molecular Simulation* Academic Press (2001).

[52] A. R. Leach: *Molecular Modelling. Principles and Applications* Prentice Hall (2001).

[53] W. H. Press, S. A. Teulosky, W. T. Vetterling, and B. P. Flannery: *Numerial Recipies in Fortran 77* Cambridge University Press (1992).

[54] I. Stich, R. Car, M. Parrinello, and S. Baroni: Conjugate gradient minimization of the energy functional: A new method for electronic structure calculation. *Phys. Rev. B* **39**, 4997 (1989).

[55] M. P. Teter, M. C. Payne, and D. C. Allan: Solution of Schrödinger's equation for large system. *Phys. Rev. B* **40**, 12255 (1989).

[56] G. Kresse and J. Furthmüller: Efficient iterative schemes for ab-initio total-energy calculations using a plane-wave basis set. *Phys. Rev. B* **54**, 11169 (1996).

[57] L. Verlet: Computer "Experiments" on Classical Fluids. I. Thermodynamical Properties of Lennard-Jones Molecules. *Phys. Rev.* **159**, 98 (1967).

[58] S. Nose: A molecular dynamics method for simulations in the canonical ensemble. *Mol. Phys.* **52**, 255 (1984).

[59] W. G. Hoover: Canonical dynamics: Equilibrium phase-space distributions. *Phys. Rev. A* **31**, 1695 (1985).

[60] Peter Blöchl, private communication.

[61] R. Car and M. Parrinello: Unified Approach for Molecular Dynamics and Density-Functional Theory. *Phys. Rev. Lett.* **55**, 2471 (1985).

[62] K. Binder: Computersimulationen. *Physik Journal* **5**, 25 (2004).

[63] N. Metropolis, A. W. Rosenbluth, M. N. Rosenbluth, A. H. Teller, and E. Teller: Equation of state calculations by fast computing machines. *J. Chem. Phys.* **31**, 1087 (1953).

[64] K. A. Fichthorn and W. H. Weinberg: Theoretical foundations of dynamical Monte Carlo simulations. *J. Chem. Phys* **95**, 1090 (1991).

[65] G. Henkelman, G. Johannesson, and H. Jonsson: *Methods for finding saddle points and minimum energy paths* Progress on Theoretical Chemistry and Physics. Kluwer Academic, New York (2000).

[66] H. Jonsson, G. Mills, and K. W. Jacobsen: *Nudged elastic band method for finding minimum energy paths of transitions* in Classical and Quantum Dynamics in Condensed Phase Simulations. World Scientific, Singapore (1998).

[67] G. Henkelmann, B. P. Uberuaga, and H. Jonsson: A climbing image nudged elastic band method for finding saddle points and minimum energy paths. *J. Chem. Phys.* **113**, 9901 (2000).

[68] G. Henkelman and H. Jonsson: A dimer method for finding saddle points on high dimensional potential surfaces using only first derivatives. *J. Chem. Phys.* **111**, 7010 (1999).

[69] A. Poddey: A Dimer method for the determination of transition states Master's thesis Institute for Theoretical Physics at Clausthal University of Technology (2004).

[70] T. Hill: *An Introduction to Statistical Thermodynamics* Dover Publications (1986).

[71] T. Hill: *Statistical Mechanics: Principles and Selected Applications* Dover Publications (1987).

[72] D. Chandler: *Introduction to Modern Statistical Mechanics* Oxford University Press (1987).

[73] J. M. Seddon and J. D. Gale: *Thermodynamics and Statistical Mechanics* Wiley-RSC (2002).

[74] G. E. Moore: Cramming more components onto integrated circuits. *Electronics* **38**(8), 114–117 (1965).

[75] D. L. Critchlow: MOSFET Scaling – The Driver of VLSI Technology. *Proceedings of the IEEE* **87**(4), 659–665 (1999).

[76] R. H. Dennard, F. H. Gaensslen, H. Yu, V. L. Rideout, E. Bassous, and A. R. Leblanc: Design of Ion-Implanted MOSFETS with Very Small Physical Dimensions. *IEEE J. Solid-State Circuits* **SC-9**(5), 256–268 (1974).

[77] *International Technology Roadmap for Semiconductors at http://public.itrs.net/* International SEMATECH, Austin, Texas (2003).

[78] R. A. McKee, F. J. Walker, and M. F. Chisholm: Physical structure and inversion charge at a semiconductor interface with a crystalline oxide. *Science* **293**, 468–471 (2001).

[79] Y. M. Sun, J. Lozano, H. Ho, H. J. Park, S. Veldmann, and J. M. White: Interfacial silicon oxide formation during synthesis of ZrO_2 on Si(100). *Appl Surf. Sci.* **161**, 115 (2000).

[80] E. Zintl: Intermetallische Verbindungen. *Angew. Chemie* **52**, 1 (1939).

[81] W. Klemm: Metalloids and their compounds with the alkali metal. *Proc. Chem. Soc. London*, 329 (1958).

[82] E. Bussmann: Die Kristallstrukturen von KSi, RbSi, CsSi, KGe, RbGe und CsGe. *Z. Anorg. Allg. Chem.* **313**, 90 (1961).

[83] R. A. McKee, F. J. Walker, M. B. Nardelli, W. A. Shelton, and G. M. Stocks: The Interface Phase and the Schottky Barrier for a Crystalline Dielectric on Silicon. *Science* **300**, 1726 (2003).

[84] E. Anderson, Z. Bai, C. Bischof, J. Demmel, J. Dongarra, J. Du Croz, A. Greenbaum, S. Hammarling, A. McKenny, S. Ostrouchov, and D. Sorensen: LAPACK *Users' Guide, 3rd ed.* SIAM Press Philadelphia (1999).

[85] O. K. Andersen, T. Saha-Dasgupta, S. Ezhov, L.Tsetseris, O. Jepsen, R. W. Tank, C. Arcangeli, and G. Krier: Third-generation MTOs. ψ_k *Newsletter* **45**, 86 (2001).

[86] S. Goedecker: Linear scaling electronic structure methods. *Rev. Mod. Phys.* **71**, 1085 (1999).

[87] M. Thieme: Deformierte Ionen als Bausteine kondensierter Materie Master's thesis Institute for Theoretical Physics, Clausthal University of Technology (2003).

[88] U. von Barth and C. D. Gelatt: Validity of the frozen-core approximation and pseudopotential theory for cohesive energy calculations. *Phys. Rev. B* **21**, 2222 (1980).

[89] J. C. Slater: Atomic Shielding Constants. *Phys. Rev.* **36**, 57–64 (1930).

[90] D. Singh: *Planewaves, pseudopotentials and the LAPW method* Kluwer Academic Publishers (1994).

[91] J. Ihm, A. Zunger, and M. L. Cohen: Momentum-space formalism for the total energy of solids. *J. Phys. C* **12**, 4409 (1979).

[92] L. Kleinmann and D. M. Bylander: Efficacious Form for Model Pseudopotentials. *Phys. Rev. Lett* **48**, 1425 (1982).

[93] P. E. Blöchl: Generalized separable potentials for electronic-structure calculations. *Phys. Rev. B* **41**, 5414 (1990).

[94] D. Vanderbilt: Soft self-consistent pseudopotentials in a generalized eigenvalue formalism. *Phys. Rev. B* **41**, 7892 (1990).

[95] J. W. Cooley and J. W. Tukey: An Algorithm for the Machine Calculation of Complex Fourier Series. *Math. Comput.* **19**, 297 (1965).

[96] W. A. Harrison: *Electronic Structure and the properties of Solids* Dover Publications, Inc. (1989).

[97] M. W. Finnis: The Harris functional applied to surface and vacancy formation energies in aluminum. *J. Phys.: Cond. Mat.* **2**, 331 (1990).

[98] N. Chetty, K. W. Jacobsen, and J. K. Norskov: Optimized and transferable densities from first-principles local density calculations. *J. Phys.: Cond. Mat.* **3**, 5437 (1991).

[99] D. Bowler, T. Miyazaki, and M. Gillan: Linear scaling ab initio calculations: recent progress with the Conquest code. ψ_k *newsletter* **47**, 91 (2001).

[100] J. M. Soler, E. Artacho, J. D. Gale, A. Garcia, J. Jungquera, D. Sanches-Portal, and P. Ordejon: The Siesta method for linear scaling ab initio simulations. ψ_k *newsletter* **48**, 134 (2001).

[101] K. Koepernik, H. Eschrig, I. Opahle, U. Nietzsche, I. Chaplygin, and M. Richter: Full-potential local-orbital minimum-basis scheme FPLO. ψ_k *newsletter* **52**, 101 (2002).

[102] S. Topiol, A. Zunger, and M. A. Ratner: The use of pseudopotentials within local-density formalism calculations for atoms: Some results for the first row. *Chem. Phys. Lett.* **49**(2), 367–373 (1977).

[103] A. Zunger and M. A. Ratner: On the first principles Hartree-Fock and local density pseudopotentials. *Chem. Phys.* **30**(3), 423–443 (1978).

[104] A. Zunger and M. L. Cohen: First-principles nonlocal-pseudopotential approach in the density-functional formalism: Development and application to atoms. *Phys. Rev. B* **18**(10), 5449–5472 (1978).

[105] C. G. Van de Walle and R. M. Martin: Theoretical calculations of heterojunction discontinuities in the Si/Ge system. *Phys. Rev. B* **34**, 5621 (1986).

[106] M. S. Hybertsen and S. G. Louie: Electron correlation in semiconductors and insulators: Band gaps and quasiparticle energies. *Phys. Rev. B* **34**, 5390 (1986).

[107] A. Fleszar and W. Hanke: Spectral properties of quasiparticles in a semiconductor. *Phys. Rev. B* **56**, 10228 (1997).

[108] R. Del Sole, L. Reining, and R. W. Godby: GW Gamma approximation for electron self-energies in semiconductors and insulators. *Phys. Rev. B* **49**, 8024 (1993).

[109] S. Ismail-Beigi and T. A. Arias: New algebraic formulation of density functional calculation. *Comp. Phys. Comm.* **128**, 1 (2000).

[110] J. D. Talmann: LSFBTR: A subroutine for calculating spherical bessel transforms. *Comp. Phys. Comm.* **30**, 93 (1983).

[111] J. Harris: Simplified method for calculating the energy of weakly interacting fragments. *Phys. Rev. B* **31**(4), 1770–1779 (1985).

[112] W. M. C. Foulkes and Haydock R. Tight-binding models and density-functional theory. *Phys. Rev. B* **39**(17), 12520–12536 (1989).

[113] H. Wendel and R. M. Martin: Theory of structural properties of covalent semiconductors. *Phys. Rev. B* **19**(10), 5251–5264 (1979).

Curriculum Vitae

Clemens J. Först

Address

Voglweg 1
2620 Neunkirchen
Austria
Phone: +41-1-58801-15677
Fax: +41-1-58801-15698
Email: clemens.foerst@tuwien.ac.at

Personal Data

Sex: male
Date of Birth: 01.06.1976
Place of Birth: Neunkirchen, Austria
Marital Status: single
Parents: Hans and Monika Först
Citizenship: Austria

Education

09.1982–06.1986	Elementary School in Neunkirchen
09.1986–06.1994	Secondary School in Neunkirchen finished with honor on the 02.05.1994
10.1995–01.1996	Study of Economics at the University of Economics in Vienna
03.1996–07.2001	Study of Chemistry and Mathematics for a Secondary School Teacher Accredidation at the Vienna University of Technology finished with honor on the 05.07.2001
1997–2000	Member of the Studienkommission
10.2000–	Study of Technical Physics at the Vienna University of Technology

Professional Appointments

01.07.2001–15.03.2002 Researcher in the group of Prof. Peter Blöchl at the Institute for Theoretical Physics at the Clausthal University of Technology, Germany

15.03.2002– Researcher in the group of Prof. Karlheinz Schwarz at the Institute for Materials Chemistry at the Vienna University of Technology within the AURORA project (FWF F1108)

Research Experience Abroad

08.2002 in the group of Prof. E. A. Carter at the Department for Chemistry and Biochemistry, University of California at Los Angeles, USA

Refereeing

- Physical Review Letters
- Physical Review B
- The European Physical Journal B
- The International Journal of Quantum Chemistry

Awards

- "**Young Scientist Award in recognition of the best paper presented during E-MRS 2002 Symposium A**"
  E-MRS Spring Meeting 2002,
  Strassbourg, France; 18.-21.06.2002

Patents

- "**Struktur, insbesondere Halbleiterstruktur, sowie Verfahren zur Herstellung einer Struktur**"
  Clemens J. Först, Christopher Ashman and Peter E. Blöchl,
  German Patent Application: Aktenzeichen 103 03 875.2, 31.01.2003
  International Patent Application: WO 2004/068568 A1, 12.08.2004

Publications

Submitted/In Press

1. **"Electronic structure methods: Augmented Waves, Pseudopotentials and the Projector Augmented Wave Method"**
   Peter E. Blöchl, Johannes Kästner and Clemens J. Först
   to appear in "Handbook of Materials Modeling"; Volume 1: Methods and Models, Sidney Yip (Ed.); Kluwer Academic Publishers

2. **"The chemistry of La on the Si(001) surface from first principles"**
   Christopher R. Ashman, Clemens J. Först, Karlheinz Schwarz and Peter E. Blöchl,
   Phys. Rev. B **70**, in press

2004

3. **"First-principles calculations of strontium on Si(001)"**
   Christopher R. Ashman, Clemens J. Först, Karlheinz Schwarz and Peter E. Blöchl,
   Phys. Rev. B **69**, 075309 (2004)

4. **"The interface between silicon and a high-k oxide"**
   Clemens J. Först, Christopher R. Ashman, Karlheinz Schwarz and Peter E. Blöchl,
   Nature **427**, 53 (2004)

2003

5. **"Heteroepitaxial Growth of High-K Gate Oxides on Silicon: Insights from First-Principles Calculations on Zr on Si(001)"**
   Clemens J. Först, Peter E. Blöchl and Karlheinz Schwarz,
   Comp. Mater. Sci. **27**, 70 (2003)

6. **"The Projector Augmented Wave Method: Ab-initio Molecular Dynamics with full Wave Functions"**
   Peter E. Blöchl, Clemens J. Först and Johannes Schimpl,
   Bull. Mater. Sci. **26**, 33 (2003)

2001

7. **"Ab-initio Molecular Dynamics applied to the Nonlinear Optical Material KTP"**
   Clemens J. Först, Master Thesis TU-Wien (2001)

Presentations at Conferences

Talks

1. **The $SrTiO_3$/Si Interface: Insights from Ab-Initio Simulations**,
   CECAM Workshop on "Atomic processes at semiconductor-oxide interfaces in microelectronic devices"
   Lyon, France; 13.-15.09.2004
   invited

2. **Ab-inito simulations of the growth of high-k oxides on silicon: the SrTiO3/Si interface**,
   Institute for Semiconductor Engineering
   University of Darmstadt, Germany; 07.05.2004
   invited

3. **Materials for future transistors: The interface between silicon and strontium titanate**,
   19^{th} Workshop on "Novel Materials and Superconductors"
   Planneralm, Austria; 22.-28.02.2004
   invited

4. **Interfacing High-K Oxides with Silicon: Solutions from Ab-Initio Simulations**,
   ESF exploratory Workshop on "Growth, Structure and Electrical Properties of High-K Gate Dielectrics: Atomistic Modeling vs Experiment",
   IBM Research Labs, Ruschlikon, Switzerland; 17.-18.03.2003
   invited

5. **Initial Steps of MBE Growth of High-K Oxides on Si(001): Insights from Ab-Initio Simulations**,
   III International Workshop on Challenges in Predictive Process Simulation,
   Prague, Czech Republic; 13.-17.10.2002
   invited

6. **Introduction to the Projector Augmented Wave Method and Applications related to High-K Oxides**,
   XII Workshop on Computational Materials Science,
   Cagliari, Italy; 23.-29.09.2002
   invited

7. **"First-Principles Simulations of the Heteroepitaxial Growth of High-K Gate Oxides on Silicon"**,
   Symposium and Summer School on: Nano and Giga Challenges in Microelectronics – Research and Opportunities in Russia,
   Moskow, Russia; 10.-13.09.2002

8. **"Heteroepitaxial Growth of High-K Gate Oxides on Silicon: Insights from First-Principles Calculations"**,
   E-MRS Spring Meeting 2002,
   Strassbourg, France; 18.-21.06.2002

9. **"Introduction to ab-initio Molecular Dynamics and the PAW Method"**,
   SCIENCE Seminar, Institute for Theoretical Physics,
   University of Hamburg, Germany; 14.05.2002
   invited

10. **"Ab initio Molecular Dynamics with full Wave Functions: The PAW Method"**,
    13. Edgar Lüscher Seminar, Serneus, Switzerland; 02.-07.02.2002
    invited

Posters

- **"Growth of high-K oxides on silicon: $SrTiO_3$/Si(001)"**,
  Workshop on Application of Density-Functional Theory in Condensed-Matter Physics, Surface Physics,Chemistry, Engineering, and Biology,
  Berlin, Germany; 21.07.-30.07.03

- **"The nonlinear optics material: $KTiOPO_4$"**,
  DFT Summer School, Caramulo, Portugal; 28.08.-02.09.01

- **"The nonlinear optics material: $KTiOPO_4$"**,
  16 Workshop on Novel Materials and Superconductors, Planneralm, Austria; 04.02.-10.02.01

Attendance

- 17. Workshop on Novel Materials and Superconductors, Planneralm, Austria; 24.02.-02.03.02

- Hauptversammlung der Deutschen Bunsen-Gesellschaft, Stuttgart, Germany; 24.05.-26.05.01

- Applied DFT 2001 Conference, Vienna, Austria; 14.01.-17.01.01

Non-Scientific

10.1994–09.1995	Service in the Austrian army
09.1999	Promotion to Second Lieutenant by the Austrian President Dr. Thomas Klestil
04.1996–10.2000	Tour guide for a Viennese travel agency for the destinations Libya, Southwest USA and Canada
10.2002	Promotion to First Lieutenant by the Austrian Secretary of Defence